POLYMER NANOSPRAY INTERFACES FOR ON-LINE ELECTROCHEMICALLY INDUCED MODIFICATIONS: APPLICATION TO PROTEIN MASS SPECTROMETRY

THÈSE N^{O} 2822 (2003)

PRÉSENTÉE À LA FACULTÉ SCIENCES DE BASE

Institut de chimie moléculaire et biologique

SECTION DE CHIMIE ET GÉNIE CHIMIQUE

ÉCOLE POLYTECHNIQUE FÉDÉRALE DE LAUSANNE

POUR L'OBTENTION DU GRADE DE DOCTEUR ÈS SCIENCES

PAR

Tatiana ROHNER

ingénieure en sciences des matériaux diplômée EPF
de nationalité française et suisse, originaire d'Altstätten

acceptée sur proposition du jury:

Prof. H. Girault, directeur de thèse
Prof. R. Compton, rapporteur
Prof. G. Hopfgartner, rapporteur
Prof. S. Pitsch, rapporteur

Lausanne, EPFL
2003

Que ta vision soit à chaque instant nouvelle.

Le sage est celui qui s'étonne de tout.

André Gide

Remerciements

En premier lieu, je tiens à remercier très chaleureusement le professeur Hubert Girault pour m'avoir permis d'effectuer ce travail de thèse au sein de son laboratoire. Je lui suis sincèrement reconnaissante pour la confiance qu'il m'a accordée durant ces quatre années de labeur. Il m'a permis de me surpasser et de tirer le meilleur de mes capacités.

Je voudrais également remercier Joël Rossier, qui m'a mis sur les rails au début de ma thèse et qui, grâce à son enthousiasme et sa motivation, m'a transmis le virus du savoir. La pertinence de ses remarques m'a beaucoup aidé et ce jusqu'au terme de ce travail.

Cette thèse n'aurait sans doute pas vu le jour sans le soutien et l'amitié de Niels Lion, mais aussi de Xiaoxia Bai, Isabelle Arnaud et Sorina Ulmeanu-Plass. Ils ont partagé beaucoup de mes joies et ont tous été d'un grand secours dans les moments difficiles, et pour cela, je leur serai éternellement reconnaissante.

Je tiens aussi à remercier Henrik Jensen, qui m'a accordé un soutien sans faille durant les derniers mois, aussi bien pour des questions scientifiques que pour le moral. Je remercie également Grégoire Lagger et Jacques Josserand, dont l'amitié et l'aide m'ont été précieuses, je regretterai aussi nos longues discussions "philosophiques".

Je suis également reconnaissante à tous les autres membres du Laboratoire d'Electrochimie Physique et Analytique qui ont également contribué à la réussite de ce travail, à commencer par Christophe Roussel pour ses précieux conseils, ainsi que Loïc Dayon, Andrea Lionello et Michel Carrara pour leur aide et leur bonne humeur tout au long de ma thèse.

Je remercie également Claudine Bovey, Maria Szuman, et Anita Schori pour leur assistance, Valérie Devaud pour son aide technique, les membres du service électronique de l'institut, Gabriel Roch, Francis Trolliet, Olivier Noverraz et Gérard Ferini, sans qui ce travail n'aurait pu s'effectuer, ainsi que les collaborateurs de l'atelier de mécanique.

Enfin, je remercie du fond du cœur Agnès Marlot, dont l'amitié m'a été très précieuse pendant toutes ces années, je ne pourrai jamais lui rendre tout ce qu'elle m'a donné. Je tiens à exprimer toute ma gratitude à la famille Zinger, qui m'a accueillie, soutenue, aidée depuis de longues années maintenant. Je remercie également ma famille, et notamment mes grands-parents, qui m'ont permis d'effectuer mes études à Lausanne. Je leur dédie cette thèse.

Finalement, je tiens à remercier avec tout mon amour Olivier, qui m'a toujours épaulée, encouragée et sans qui je n'aurai accompli ni ce travail ni beaucoup d'autres choses encore.

Résumé

Ce travail de thèse est basé sur la conception et la fabrication d'une interface miniaturisée de type "électrospray", qui permet l'analyse de solutions par spectrométrie de masse en nébulisant la phase liquide grâce à l'application d'une très grande différence de potentiel entre la source et le spectromètre de masse. La source "nanospray" a été fabriquée grâce à la technique de photoablation par laser UV sur substrat polymère, qui permet de générer des microcanaux. De la même manière, des microélectrodes de carbone peuvent être intégrées au système microfluidique, permettant la génération de l'électrospray depuis la sortie du microcanal en y appliquant un très haut voltage. La première interface développée comporte un profil plat. Cependant, une interface présentant un profil en V a montré une utilisation plus aisée et une meilleure stabilité du point de vue de la détection. De plus, ce design permet d'utiliser le flux électroosmotique pour le pompage de la solution dans le canal, en appliquant le haut voltage à une électrode introduite dans un réservoir à solution.

En exploitant le comportement électrolytique intrinsèque à l'électrospray, une modification spécifique aux cystéines libres contenues dans des protéines peut être obtenue en ligne, par l'infusion d'une solution contenant de l'hydroquinone et le matériel protéique d'intérêt. Lorsque la mixture passe au-dessus de la microélectrode, la p-hydroquinone s'oxyde, ce qui génère de la p-benzoquinone protonée. Cette dernière réagit avec les groupements thiols des cystéines, suivant un mécanisme d'addition de Michael. La modification en ligne de la protéine peut être suivie par spectrométrie de masse.

Les mécanismes impliqués dans la modification électrochimiquement induite des cystéines ont été étudiés à l'aide de la voltamétrie cyclique et de simulations numériques. Le processus consiste en un mécanisme ECE, car l'adduit formé est stabilisé sous sa forme réduite et peut donc s'oxyder. En modélisant le système cystéine/p-hydroquinone, la constante de la réaction en phase homogène a pu être extraite des voltamogrames.

Des simulations par éléments finis ont également permis de mettre en évidence différents aspects mécanistiques de la modification électrochimiquement induite. L'interface nanospray a été modélisée comme une électrode microbande en canal soumise à un flux laminaire. Après la validation du modèle par rapport aux résultats expérimentaux, l'importance de la cinétique de la réaction en phase homogène et du transport de masse a été étudiée. Il a été démontré que le profil du flux ainsi que la constante cinétique ont une grande influence sur l'efficacité de la modification.

Finalement, l'utilisation d'électrodes sacrificielles pour l'électrospray comme sources d'ions métalliques a été étudié. Des électrodes de métaux de transition, tels que le cuivre, le zinc, le nickel, le fer, ainsi que l'argent, ont permis de générer en ligne des complexes metallopeptidiques. Il a été démontré que cette technique peut remplacer l'utilisation de sels métalliques pour l'étude de la formation et de la stabilité de ces complexes.

Ces études montrent que les interfaces de type nanospray en polymère peuvent être avantageusement utilisées en tant qu'instruments analytiques, en plus de leur fonction de source d'ionisation pour des analyses de protéines/peptides par spectrométrie de masse.

Abstract

The aim of this work has been to design, and fabricate a miniaturized electrospray-type interface for mass spectrometry analysis, which allows the nebulization of solutions by applying a high potential difference between the source and the mass spectrometer. The fabrication of the nanospray emitter is based on UV-laser photoablation of polymer substrates. Thick-film channel flow electrodes can be integrated in the microfluidic system, allowing the application of a high voltage to generate electrospray from the open outlet of the microchannel. The polymer-based interface first presented is characterized by a flat edge interface. However, a V-shaped nozzle has been found to present higher stability and ease of use. This design also allows the generation of spray by applying high voltage through an electrode located in a solution reservoir, thereby inducing an electroosmotic pumping.

Taking advantage of the intrinsic electrolytic behavior of electrospray, a specific electrochemically induced tagging of free cysteine residues located in proteins can be performed on-line. A p-hydroquinone buffer is used to perform a continuous infusion of protein solution. When in contact with the high-voltage microelectrode, p-hydroquinone undergoes oxidation, thereby producing protonated p-benzoquinone. The latter reacts with free cysteine residues, following a Michael-type addition. The modification of the protein can be followed thanks to MS analyses.

A complete study of the mechanisms involved in the electrochemically induced tagging with hydroquinone has been carried out by cyclic voltammetry and digital simulation. The process of the tagging consists of an ECE mechanism, since the formed adduct is stabilized in the

reduced state, and is thus free to be oxidized. The rate constant of the chemical reaction has been extracted, by performing cyclic voltammetry studies and modeling the whole system by digital simulations.

Finite element simulations have also permitted to highlight several mechanistic aspects of the electrotagging. The nanospray interface has been modeled as a channel-flow electrode cell. After validation of the model with respect to the experimental results, kinetics and mass transport conditions have been investigated. The flow profile, as well as the kinetic rate constant, has been shown to be of great importance in the electrochemically induced tagging.

The use of a sacrificial electrode as metallic ion source to generate electrospray has also been investigated. Transition metal electrodes, i.e. copper, zinc, nickel and iron, as well as silver, were used to get on-line complexation with model peptides. It has been demonstrated that the use of in-reservoir sacrificial electrode was an efficient method to generate metal ions in order to form complexes with peptides, without the addition of metallic salts.

These studies have demonstrated that polymer nanospray interfaces can be advantageously used as analytical devices, together with their primary function, i.e. ionization sources for protein analyses by mass spectrometry.

List of symbols and abbreviations

Roman alphabet

c_i	concentration of the species i	M
c_i^0	initial concentration of the species i	M
D_i	diffusion coefficient of the species i	$m^2 \cdot s^{-1}$
d	channel depth	m
d_0	distance capillary-counter electrode	m
E	applied potential at the electrode	V
E	electric field	$V \cdot m^{-1}$
E^0	standard redox potential	V
e	electronic charge	$1.60218 \times 10^{-19} C$
F	Faraday constant	$96'485 C \cdot mol^{-1}$
h	half-height of the channel	m
K	rate constant of the ECE mechanism	-
k	kinetic constant of the homogeneous reaction in an ECE mechanism	s^{-1}
k'	kinetic constant of the homogeneous reaction in an $EC_{2X}E$ mechanism	$M^{-1} \cdot s^{-1}$
i_{ES}	spray current	A
i_F	Faraday current	A
I_p	peak current for an ECE mechanism	A
I_p^0	peak current for an E mechanism	A
L	channel length	m
N	number of charges of the parent droplet	-
N_{eff}	effective number of electrons transferred during an ECE process	-
Ps	Shear Peclet number	-

Q	charge of the parent droplet	C
[Q]	excess charge concentration	M
q	charge of the offspring droplet	C
q_{Ry}	Rayleigh limit	C
R	universal gas constant	$8.314 J \cdot K^{-1} \cdot mol^{-1}$
R	radius of the parent droplet	m
r	radius of the offspring droplet	m
r_c	outer capillary radius of the electrospray emitter	m
V_0	maximum velocity	$m \cdot s^{-1}$
v_f	flow rate	$l \cdot min^{-1}$
w	channel width	m
x_e	electrode length	m

Greek alphabet

γ	surface tension of the solvent	$N \cdot m^{-1}$
ε	permittivity of the medium	$J^{-1} \cdot C^2 \cdot m^{-1}$
ε_0	permittivity of the vacuum	$8.85419 \times 10^{-12} J^{-1} \cdot C^2 \cdot m^{-1}$
ε_r	dielectric constant of the medium	-
θ_0	Taylor cone half-angle	
κ	conductivity of the solution	$\Omega^{-1} \cdot m^{-1}$
ν	scan rate	$V \cdot s^{-1}$
σ	surface charge density	$C \cdot m^{-2}$

Abbreviations

CRM	Charge Residue Model
CE	Capillary Electrophoresis

ECE	Sequence of heterogeneous/homogeneous/heterogeneous reactions
$EC_{2X}E$	Sequence of heterogeneous/homogeneous/heterogeneous reactions involving two species for the chemical step
ESI	Electrospray Ionization
IEM	Ion Evaporation Model
MS	Mass spectrometry
MS/MS	Tandem Mass Spectrometry
MALDI	Matrix Assisted Laser Desorption Ionization
m/*z*	mass-to-charge ratio
PE	Polyethylene
PET	Polyethylene Terephthalate
SHE	Standard Hydrogen Electrode
SCE	Standard Calomel Electrode
TIC	Total Ion Current [counts·s^{-1}]

Table of contents

Remerciements i

Résumé iii

Abstract v

List of symbols and abbreviations vii

Chapter I : Introduction 1

1. Proteomics: a new challenge 1

2. Towards miniaturization 7

3. Objective of the work 9

4. References 10

Chapter II : Electrospray Ionization 13

1. Electrospray as an ionization method 13

2. Overview of the electrospray process 13

3. Emission and fission of the droplets 16

3.1 Electrospray onset 17

3.2 The Taylor cone 20

3.3 The Rayleigh limit 23

3.4 Droplet fission 25

4. Gas-phase ion generation 27

4.1 Ion Evaporation Model 28

4.2 Charge Residue Model. 38

4.3 Very final stage of gas-phase ion generation. 39

5. From solution to gas-phase 40

5.1 Effect of the solution composition 40

5.2 Relating composition to detection 42

6. Mass spectrum features 46
7. Conclusions 48
8. References 49
Chapter III : Characterization of the nanospray interface 55
1. Electrospray as an on-line interface 55
2. State-of-the art in nanospray interface designs 57
3. Microfabrication technologies 59
3.1 Photoablation applied to polymers 60
3.2 Sealing of the structures 64
4. Fabrication of the nanospray interface 65
5. Experimental Set Up 68
6. Nanospray in operation 69
7. Stability in ESI-MS 70
8. Calibration of the nanospray 72
9. New interface design 75
10. Conclusion 78
11. References 79
Chapter IV : On-line electrochemically induced tagging of free cysteines 85
1. Electrolytic behavior of the electrospray 85
1.1 Faraday and spray current 85
1.2 Electrochemical ionization 87
1.3 Analytical implications 89
2. Protein modification: what for? 90
3. On-line tagging of free cysteines with p-hydroquinone 92
3.1 Experimental description 92
3.2 Results and discussion 93
4. Mechanistic investigation of the electrochemically induced tagging 99
4.1 Electrochemical reaction studies 100
4.2 Study of the L-cysteine/hydroquinone reaction 108
4.3 Kinetic aspect of the tagging 113

5. Conclusions 117
6. References 118
Chapter V : Numerical Investigation of an Electrochemically Induced Tagging 121
1. Introduction 121
2. Theoretical description of the problem 122
3. Numerical description 126
4. Results and discussion 128
4.1 Model validation 128
4.2 Model assessment according to the experimental case 130
4.3 Description of the phenomena 132
4.4 Kinetic and convective aspects of the tagging 135
5. Conclusions 139
6. References 140
Chapter VI : Peptide on-line complexation with transition metal ions 143
1. Introduction 143
2. Complexation 144
2.1 Metal-ligand interaction 144
2.2 Affinity chromatography 145
2.3 ESI-MS for complexes elucidation 146
2.4 ESI as ionization source for complex studies 149
3. Experimental 149
4. Results 151
4.1 Tandem MS on native peptides 151
4.2 On-line complexation with Copper electrode 153
4.3 On-line complexation with Zinc electrode 159
4.4 On-line complexation with Nickel electrode 164
4.5 On-line complexation with Iron electrode 170
4.6 On-line complexation with Silver electrode 175
4.7 Summary and discussion 178
5. Conclusions 181

6. References....182
Chapter VII : Conclusions and perspectives....185
Appendix 1: Numerical formulation....191
Appendix 2: Model validation....195
Appendix 3: Ion trap scheme....199
Curriculum Vitae....201

Chapter I : Introduction

1. Proteomics: a new challenge

In 2003, the 50th anniversary of the discovery of the structure of DNA molecule by Crick and Watson has been celebrated. However, only 48 years after this breakthrough, a working draft of the human genome has been completed in the framework of the Human Genome Project, launched in 1990. The most striking result of the sequencing was the low number of genes composing the human genome, i.e. only 30'000 genes. Thus, the scientific community had to face up to the fact that this knowledge was equivalent to have all the words of a book without knowing their repetition and position. If the human genome contains roughly 30'000 genes, the human body may contain more than half a million different proteins having slightly or very different functions.[1] In addition, gene regulation is one of the most complex molecular processes known, involving up to 10% of the proteins that our cells produce. The transcriptome, consisting of the messenger RNA (mRNA) expression profiles, gives the full information on individual gene expression and regulation in a given cell state or cell type.[2] However, the steady-state levels of mature gene products are subject to additional mechanisms, and quite often mRNA and protein levels are not correlated.[3] In addition, the modifications occurring on the proteins after the translation of the mRNA, namely the post-translational modifications (PTM), are known to play a key role in protein regulation, and so in the whole functioning of cells, are not taken into account by this methodology. Therefore, the proteome, defined by Wilkins in 1995 as "the study of proteins expressed by a genome, and the systematic analysis of protein profiles in tissues",[4] is of utmost importance for the discovery of new disease markers or drug targets. Contrary to the genome, the proteome of one living entity

is completely different from a cell to another, and changes during its whole life. The coming task is therefore tremendous compared to the genome sequencing, due to the enormous population of proteins, the wide range of physical and chemical properties they present. In addition, the impossibility to amplify a specific signal, as it is the case for DNA via Polymerase Chain Reaction (PCR), and the dynamic nature of the proteome increase the complexity of the work. The development of new tools for qualitative and quantitative analysis, together with a high-throughput via automation, has become a necessity, due to the increase of interest in Proteomics and the concomitant complexity of the analysis.[5] This tendency involves high-resolution separation tools as well as very sensitive detection methods.

Proteomics, currently considered as a new scientific field in its own right, is based on two analytical tools for protein identification: the 2D gel electrophoresis and mass spectrometry. The 2D gel electrophoresis is commonly employed, despite a maximum loading of 10mg and a dynamic scale of 100, with a detection limit at the femtomole level. On a standard gel, approximately 2'000 proteins can be identified, and a maximum of 11’000 spots can be resolved on the "best gels". However, a strong discrimination against several types of proteins has been reported. First, the low-abundant proteins, which are supposed to be highly involved in the cell, are drowned out by high abundance proteins, which can be present at a 10'000 times higher concentration. In addition, hydrophobic proteins, such as the cell-membrane spanning receptor proteins, that are potential drug targets, are not identified or even detected since they even do not enter the gel. Finally, highly basic or acidic proteins are out of the isoelectric point dynamic range of the gels. Despite much refinement, it is referred to as "*...the black art or the dark force of the proteomics but a necessary evil, which requires skilled staff...*"[6] Finally, one major drawback of this method is the impossibility to study protein-protein interactions, the latter being a key issue in drug discovery.

Mass spectrometry is also an "old chemical analytical tool". The first mass spectrum was indeed recorded in 1912 by J.J. Thompson. Several mass analyzers have been developed since then, successively magnetic focusing (1918), Time of Flight (TOF) (1946) and double focusing instruments (1952), followed by quadrupole analyzers (1953-58), which include the Ion Trap (IT), and the introduction of the first triple-quadrupole in 1978, and finally Fourier Transform Ion Cyclotron Resonance (FTICR) in 1974 for the basic analyzers.

Despite these years of intense development in Mass Spectrometry (MS), the goal of analyzing large biomolecules remained elusive for 70 years. Since the late 80's implementation of two ionization techniques, the Matrix Assisted Laser Desorption Ionization (MALDI) and the Electrospray Ionization (ESI), the MS analysis has been tremendously improved in terms of sensitivity, speed and level of structural information, e.g. making possible the study of native protein complexes.[7] These ionization sources have been demonstrated to induce very low or no fragmentation on thermolabile molecules such as proteins.

Basically, MALDI is based on the use of a laser light as an ionization source.[8, 9] The sample is first mixed with a so-called matrix, characterized by a high absorption at the wavelength of the laser source. After the crystallization of the mixture on a target plate, the laser beam is shot on the target. The matrix is excited by the laser, the excitation energy is subsequently transferred to the analyte, which is then ionized and desorbed from the plate. The processes leading to the ionization of the analyte by MALDI are still under investigation, even if some routes have already been suggested.[10]

The generation of macroions thanks to electrospray ionization was first demonstrated by Dole and co-workers in 1968.[11] Pioneered earlier by the work of Zeleny[12, 13] and Taylor,[14] the electrospray principle is based on the generation of gas-phase ions from a solution flowing through a small outlet, where a high potential is applied. Once a sufficiently high voltage is supplied between the solution and the MS inlet, the solution is dispersed in fine droplets,

which undergo a succession of solvent evaporation and coulombic fissions, lastly leading to multi-charged molecular ions with intact analytes. Considering its intrinsic nature, ESI is a straightforward on-line interface between liquid phase separation systems and mass spectrometry.

The fact that the 2002 Nobel Prize in chemistry was jointly half-attributed to K. Tanaka and J.B. Fenn for their respective pioneer work on MALDI-MS and ESI-MS applied to large biomolecules analysis, indicates the high relevance of these ionization methods for life sciences. [15, 16]

The introduction of new techniques like Tandem MS, (analysis of the fragments of a chosen parent ion) and more generally MS^n ,has improved the MS analysis output, amplified by the proteomics-oriented hybrid instruments such as quadrupole-TOF (Q-TOF), or TOF-TOF during the last decade. These systems actually combine a first mass spectrometer for precursor ion selection and a second for mass analysis of fragmentation products.

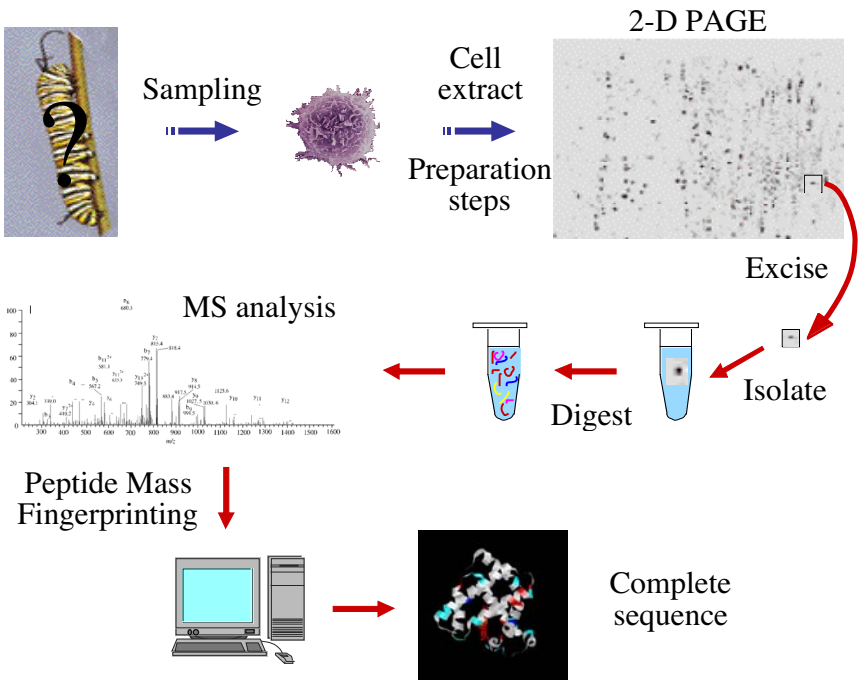

Figure I-1. *Scheme of a bottom-up approach for protein identification.*

From these technological advances, two strategies based on mass spectrometry are currently used for qualitative protein analysis. The most widespread method called "bottom-up", illustrated in Figure I-1, consists of a proteolytic digestion of a protein mixture followed by a chromatographic separation. A subsequent MS analysis employs peptide mass fingerprinting and/or tandem MS of the ion of interest. One strategy consists in running a 2D gel followed by a destaining-excision step, to recover the protein of interest andto digest it. This cumbersome method can be avoided by the molecular scanner technique.[17, 18] The 2D gel spots are electroblotted through a membrane containing immobilized trypsin. The freshly tryptic peptides are recovered, kept in their relative positions, on another membrane. The latter is then sprayed with a matrix, ready to be used for MALDI. The membrane is then automatically scanned, and a MS acquisition is done once a spot is detected.

A 2D liquid chromatography is also used, consisting in the coupling of a strong cation exchange (SCX) and a reverse-phase (RP) column, usually nano-sized, and directly connected to a MS via an ESI interface. The latter is a complete on-line method, allowing a full automation of the analysis. The high complexity of the peptide mixtures and the limited ability of the chromatographic techniques to completely separate all the components are the main limitations of this approach. The gel-based technologies allow the detection of PTM but as already mentioned, suffer from poor quantitation efficiency and are not well suited for all kinds of proteins. On the other hand, gel-free technologies are insensitive to PTM, however they do not discriminate proteins regarding to their nature and allow quantitation.

By contrast, a new trend for protein identification, the "top-down" approach, consists in gas-phase dissociation of intact protein ions without the help of proteolytic digestion prior to MS analysis. Based on the high-resolving power of a FTICR, a tandem MS is performed by using Electron Capture Dissociation (ECD) as the activation technique.[19] Due to the intrinsic nature of ECD, PTM are preserved and secondary and tertiary structure of proteins can be studied.[20]

Considering the advances in quantitative proteomics, it is evident that previous tools are not well-suited for the detection of differences between reference and altered states of a protein mixture. The techniques developed for quantitative analysis for 2D gel is based on the measurement of spot intensities, due to radioactive or fluorescent labeling or even silver staining. The ratio is then calculated between the gels representing each a different state. Unfortunately, spot detection and quantification is time-consuming and its accuracy is quite low. Recently, an improvement in the precision has been demonstrated thanks to the incorporation of an internal standard in the gel.[21] Although mass spectrometry is a powerful tool, there is a strong discrepancy in ionization efficiency for a peptidic mixture, according to the differences of chemical and physical properties. One way to overcome this difficulty is to adopt a strategy based on small-molecules MS-isotopic labeling.

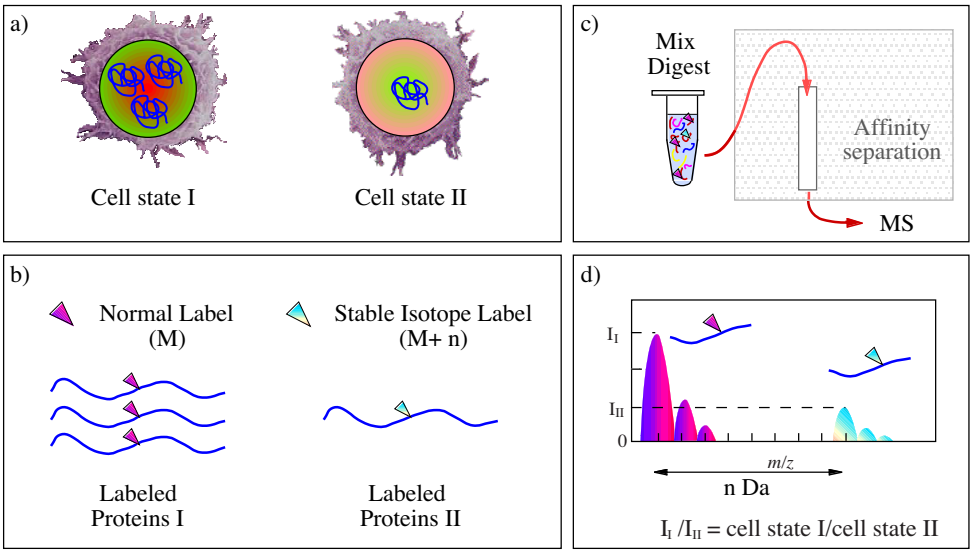

Figure I-2. *Schematic representation of quantification by isotope labeling.*

As described in Figure I-2, the two cell state proteins are labeled respectively with a small molecule and its isotopic equivalent, such as ^{15}N or deuterium. Then the two labeled solutions are mixed and digested. The mixture, which can be purified by affinity chromatography, is

then analyzed by MS. Every tryptic peptide is then related to a double distribution, corresponding to the two isotopic labeled molecules, with a shift identical to the number of nitrogen or hydrogen atoms of the probe.

The ratio of the abundance between the two states can be calculated for every peptide resulting in quantitative information of the protein regulation upon a given alteration. The Isotope Coded Affinity Tag (ICAT™) method improves the output of this method by the implementation of an affinity chromatography based on the strong interaction of the avidn-biotin complex, as schemed in Figure I-2.[22-26] The probe is indeed made up of a biotin moiety, a linker with 8 deuterium/hydrogen sites, and finally a functional group, which will react specifically with cysteine residues. The complexity of the analysis is reduced as only the cysteinyl peptides are analyzed. The major drawback of these techniques remains the wide dynamic range of protein abundance in crude mixtures. The tryptic peptides coming from the most abundant proteins dominate the whole chromatogram, resulting in poor quantification accuracy of low abundant proteins. In addition, acidic proteins are poorly detected due to their reduced tryptic cleavage sites. However, it has been demonstrated that apart form the obvious blindness to the protein lacking cysteines, a strong selectivity for proteins with very high cysteine content occurred.[27]

2. Towards miniaturization

Besides the progress in mass spectrometry, the search of new analytical tools for this huge task has naturally turned to miniaturization. This tendency is also present in numerous fields of engineering, such as microsensors, microactuators and of course microprocessors, with capabilities for low cost mass microfabrication. These microfabrication technologies pave the way for the production of inexpensive bioanalytical disposable microsystems, for instance single-use diagnostic devices.

Micro Total (chemical) Analysis Systems (μTAS), first coined by Manz and co-workers, [28] have been extensively developed for use in bioanalytical purposes.[29-31] Scaling down an apparatus presents many analytical advantages. Among them, very low analyte and solvent amounts are consumed for each run; it is therefore particularly well suited for biochemical analysis, for which very low analyte samples are available. The flows are typically laminar and can be driven by electrical means. Finally, the shorter diffusion distance leads to a drastically reduced analysis time. These potentially single-use μTAS devices can be incorporated in a fully automated analysis set-up. Miniaturized devices were first introduced as microarrays for fast and high-throughput analyses of DNA sequences.[32-34] Other devices were then developed based on separation techniques such as capillary electrophoresis and had been adapted to protein separation purposes, as the microchip shown in Figure I-3.[29-31]

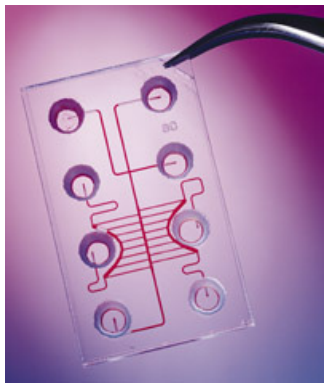

Figure I-3. *Plastic Labchip® from Caliper Technologies (Source: http://www.calipertech.com)*

The increasing implication of microchips in pharmaceutical and biochemical analyses has led to a growing demand on detection methods, to be more sensitive, more selective and able to provide structural information. A number of companies are developing chips with the hope that they will become a key technology for measuring large numbers of proteins in biological samples. Also called protein or antibody arrays, protein biochips hold the potential to measure protein-protein interactions, protein-small molecule interactions and enzyme-substrate

reactions. They hold value for identifying potential biomarkers and for pharmaceutical discovery-based research. Immunoassays have also been developed with different detection systems, but characterized by a drastically reduced incubation time.[35, 36]Prompted by the simplicity of the electrospray process and the need of more accurate detection methods, miniaturized electrospray interface fabrication has been widely investigated in order to couple analytical devices, such as CE, LC, or HPLC to mass spectrometers. It has been established that micro and nanospray interfaces (so-called for their flow rates range) provide better sensitivity than standard electrosprays.[37, 38] For the spray designs, the critical points are the application of the high voltage, the coupling to other analytical apparatus, miniaturized or not, and the dead volume minimization. The current development is oriented towards a complete integration of the ESI emitter on a microchip with several preparative and analytical devices. The coupling of glass microchips to such "macro" analyzers as MS has been successfully achieved by Karger and Ramsey group.[39, 40] Since these early proofs of principle, different designs and strategies have been investigated, and the development of these microdevices has attracted a lot of attention over.

3. Objective of the work

This work deals with the development and the characterization of a new miniaturized electrospray-type interface. Preliminary results are presented on different features of the developed nanospray interface, especially the electrolytic behavior intrinsic to ESI sources.

Chapter II describes the theory concerning electrospray generation and the physical and chemical aspects of the gas-phase ion generation. A particular attention is given to the theory of ion generation by evaporation.

After an introduction on the different strategies for the miniaturization of the electrospray source, chapter III deals with the prototyping of the nanospray interface by photoablation on polymer substrates. The microfabrication process is presented and the main characteristics of the nanospray emitter are introduced.

Chapter IV presents a new way to identify cysteine residues in proteins. The electrolytic behavior of the nanospray interface is used to generate a specific probe, which will react with the thiol moiety, just prior to MS sampling. The mechanism of the electrochemically induced tagging of cysteine is investigated thanks to cyclic voltammetry and digital simulations.

Chapter V is dedicated to a general study of the on-line tagging based on finite element simulations. Kinetic and convective aspects are investigated and a validation according to experimental results is carried out.

Chapter VI is devoted to the introduction of preliminary results on metal ion complexation with peptides using sacrificial electrodes for electrospray generation. Features of the complexation with nickel, zinc, copper, iron and silver are underlined, based on MS and MS/MS studies.

4. References

(1) Hochstrasser, D. F.; Sanchez, J. C.; Appel, R. D. *Proteomics* **2002,** *2*, 807-812.

(2) DeRisi, J. L.; Iyer, V. R.; Brown, P. O. *Science* **1997,** *278*, 680-686.

(3) Gygi, S. P.; Rochon, Y.; Franza, B. R.; Aebersold, R. *Mol. Cell. Biol.* **1999,** *19*, 1720-1730.

(4) Wasinger, V. C.; Cordwell, S. J.; Cerpapoljak, A.; Yan, J. X.; Gooley, A. A.; Wilkins, M. R.; Duncan, M. W.; Harris, R.; Williams, K. L.; Humpherysmith, I. *Electrophoresis* **1995,** *16*, 1090-1094.

(5) Figeys, D.; Pinto, D. *Electrophoresis* **2001,** *22*, 208-216.

(6) Abbott, A. *Nature* **1999,** *402*, 715-720.

(7) Aebersold, R.; Goodlett, D. R. *Chem. Rev.* **2001,** *101*, 269-295.

(8) Karas, M.; Bachmann, D.; Hillenkamp, F. *Anal. Chem.* **1985,** *57*, 2935-2939.

(9) Karas, M.; Hillenkamp, F. *Anal. Chem.* **1988,** *60*, 2299-2301.

(10) Zenobi, R.; Knochenmuss, R. *Mass Spectrom. Rev.* **1998,** *17*, 337-366.

(11) Dole, M.; Mack, L. L.; Hines, R. L.; Mobley, R. C.; Ferguson, L. D.; Alice, M. B. *J. Chem. Phys.* **1968,** *49*, 2240-2249.

(12) Zeleny, J. *The Physical Review* **1914,** *3*, 69-91.

(13) Zeleny, J. *The Physical Review* **1917,** *10*, 1-6.

(14) Taylor, G. I. *Proceedings of Royal Society of London A* **1964**, 383-397.

(15) Tanaka, k.; Waki, h.; Ido, y.; Akita, s.; Yoshida, y.; Yoshida, t. *Rapid Comm. Mass Spectrom.* **1988,** *2*, 151-153.

(16) Fenn, J. B.; Mann, M.; Meng, C. K.; Wong, S. F.; Whithouse, C. M. *Science* **1989,** *246*, 64-71.

(17) Binz, P. A.; Muller, M.; Walther, D.; Bienvenut, W. V.; Gras, R.; Hoogland, C.; Bouchet, G.; Gasteiger, E.; Fabbretti, R.; Gay, S.; Palagi, P.; Wilkins, M. R.; Rouge, V.; Tonella, L.; Paesano, S.; Rossellat, G.; Karmime, A.; Bairoch, A.; Sanchez, J. C.; Appel, R. D.; Hochstrasser, D. F. *Anal. Chem.* **1999,** *71*, 4981-4988.

(18) Müller, M.; Gras, R.; Appel, R. D.; Bienvenut, W. V.; Hochstrasser, D. F. *J. Am. Soc. Mass Spectrom.* **2002,** *13*, 221-231.

(19) Zubarev, R. A.; Kelleher, N. L.; MacLafferty, F. W. *J. Am. Chem. Soc.* **1998,** *120*, 3265-3266.

(20) Stensballe, A.; Norregaard Jensen, O.; Olsen, J. V.; Haselmann, K. F.; Zubarev, R. A. *Rapid Comm. Mass Spectrom.* **2000,** *14*, 1793-1800.

(21) Driver, S.; Ghouze, F.; Alban, A.; Orange, P.; Currie, I. *SPS'02: Applied Proteomics*, Lausanne, Switzerland 2002; FontisMedia; 53-54.

(22) Gygi, S. P.; Rist, B.; Gerber, S. A.; Turecek, F.; Gelb, M. H.; Aebersold, R. *Nat. Biotechnol.* **1999,** *17*, 994-999.

(23) Han, D. K.; Eng, J.; Zhou, H. L.; Aebersold, R. *Nat. Biotechnol.* **2001,** *19*, 946-951.

(24) Smolka, M. B.; Zhou, H. L.; Purkayastha, S.; Aebersold, R. *Anal. Biochem.* **2001,** *297*, 25-31.

(25) Smolka, M. B.; Zhou, H.; Aebersold, R. *MCP* **2002,** *1*, 19-29.

(26) Zhou, H. L.; Ranish, J. A.; Watts, J. D.; Aebersold, R. *Nat. Biotechnol.* **2002,** *20*, 512-515.

(27) Patton, W. F.; Schulenberg, B.; Steinberg, T. H. *Current Opinion in Biotechnology* **2002,** *13*, 321-328.

(28) Manz, A.; Harrison, D. J.; Verpoorte, E. M. J.; Fettinger, J. C.; Paulus, A.; Ludi, H.; Widmer, H. M. *J. Chromatogr.* **1992,** *593*, 253-258.

(29) Woolley, A. T.; Mathies, R. A. *Proc. Natl. Acad. Sci. U. S. A.* **1994,** *91*, 11348-11352.

(30) Jacobson, S. C.; Hergenroder, R.; Koutny, L. B.; Ramsey, J. M. *Anal. Chem.* **1994,** *66*, 2369-2373.

(31) Jacobson, S. C.; Hergenroder, R.; Koutny, L. B.; Ramsey, J. M. *Anal. Chem.* **1994,** *66*, 1114-1118.

(32) Strezoska, Z.; Paunesku, T.; Radosavljevic, D.; Labat, I.; Drmanac, R.; Crkvenjakov, R. *Proc. Natl. Acad. Sci. U. S. A.* **1991,** *88*, 10089-10093.

(33) Drmanac, R.; Drmanac, S.; Labat, I.; Crkvenjakov, R.; Vicentic, A.; Gemmell, A. *Electrophoresis* **1992,** *13*, 566-573.

(34) Schena, M.; Shalon, D.; Davis, R. W.; Brown, P. O. *Science* **1995,** *270*, 467-470.

(35) Rossier, J. S.; Girault, H. H. *Lab Chip* **2001,** *1*, 153-157.

(36) Rossier, J. S.; Vollet, C.; Carnal, A.; Lagger, G.; Gobry, V.; Girault, H. H.; Michel, P.; Reymond, F. *Lab Chip* **2002,** *2*, 145-150.

(37) Wahl, J. H.; Goodlett, D. R.; Udseth, H. R.; Smith, R. D. *Electrophoresis* **1993,** *14*, 448-457.

(38) Wilm, M.; Mann, M. *Anal. Chem.* **1996,** *68*, 1-8.

(39) Ramsey, R. S.; Ramsey, J. M. *Anal. Chem.* **1997,** *69*, 1174-1178.

(40) Xue, Q. F.; Foret, F.; Dunayevskiy, Y. M.; Zavracky, P. M.; McGruer, N. E.; Karger, B. L. *Anal. Chem.* **1997,** *69*, 426-430.

Chapter II : Electrospray Ionization

1. Electrospray as an ionization method

The electrospray principle has been demonstrated at the beginning of the 20th century, when Zeleny showed that a solution could be sprayed from a capillary by applying a high voltage at its outlet.[1, 2] Then, the pioneer work of Dole[3, 4] and Fenn[5] has validated electrospray as an ionization method for large compounds such as polymers and biomolecules. Since then, the processes involved in the gas-phase ion generation by this technique have been widely investigated. The electrospray is an atmospheric pressure ionization (API) source that produces gas-phase ions with a poor or without any fragmentation. With Fast Atom Bombardment (FAB), Fast Ion Bombardment (FIB), or Electron Impact (EI), the energy to generate ions is actually absorbed or transmitted directly to the analytes. In the soft ionization methods, the energy is first absorbed by an ionization "partner", the latter being the matrix in the case of MALDI, and the solution and generated droplets in the case of ESI. This ability has found its natural application to the study of proteins, including their non-denatured state[6-8] or non-covalent complexes of biomolecules.[9-12]

2. Overview of the electrospray process

The electrospray can be used either with positive or negative applied voltage. This will lead to the formation of cations (positive mode) or anions (negative mode) in the gas phase, respectively. For the electrospray onset, one can distinguish 3 stages illustrated in Figure II-1.

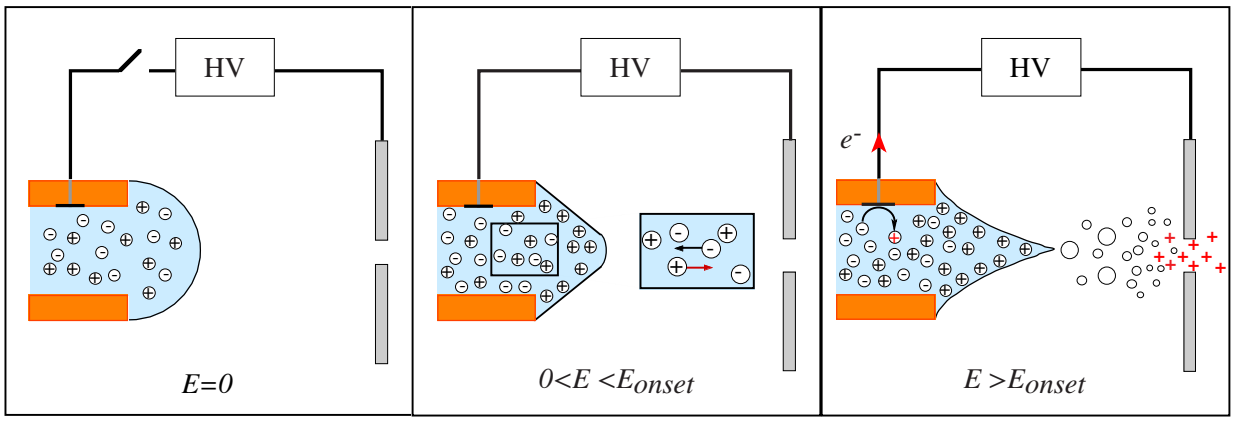

Figure II-1. *Electrospray onset.*

A power supply is connected between a solution in a capillary and a counter electrode, which can be the mass spectrometer sampler. At the first stage, when no voltage is applied, the surface tension and the pressure are the only forces that act on the liquid surface at the outlet of the capillary: the shape of the surface is hemispherical in a first approximation.

When a positive potential is supplied to the solution, the liquid/air interface presents a quasi-conical shape. This deformation is the result of the balance between the electrostatic force and the surface tension, and can be calculated considering the Laplace equation. In addition, charge movement begins to occur in the solution close to the outlet, driven by the electrophoresis of the electrolytes. Therefore, cations migrate toward the outlet, and the surface of the liquid exhibits a net positive charge, while the anions move upstream (inverse when dealing with the negative mode). When the electrostatic force and the surface tension balance perfectly, the surface is fully-conical, and is designated as the Taylor cone, due to the intensive study of this feature by Taylor.[13, 14] Some mechanistic aspects of the Taylor cone are presented in the section 3.2 below.

With a slight increase of the applied potential, the cone is destabilized. The surface tension is too low to keep the interface solution/air stable, and the latter disrupts at the tip of the cone, where the electric field is maximum. The solution is dispersed into droplets generated from the

cone apex. Two kinds of droplets are generated at this first stage: parent droplets and satellite droplets, which are directly ejected from the distorted cone surface and have a much smaller radius than the primary droplets.[15] These droplets are characterized by a net positive charge (in negative mode, the net charge is negative).

Due to evaporation of the solvent, the drops start to shrink and the charges at the surface of the droplets get closer. When the coulombic repulsion exceeds the surface tension, the drops explode in a jet-fission mode (see section 3.4 below), thereby producing a set of small progeny droplets, and one residue droplet, for each primary droplet.

The continuous generation of smaller droplets leads actually to the production of gas-phase ions, as shown schematically in Figure II-1. As the investigation of the different processes involved is still tricky and laborious, this last stage of the electrospray process is discussed in the section 4 below.

Since gas-phase ions are generated, they are guided to the counter electrode thanks to the electric field. This flow of ions induces a current i_{ES}, which has been found to be dependent on several parameters, [16] as shown in equation 1.

$$i_{ES} = \left[\left(4\pi/\varepsilon\right)^3 \left(9\gamma\right)^2 \varepsilon_0^5\right]^{1/7} \left(\kappa E\right)^{3/7} v_f^{4/7} \qquad (1)$$

where ε and ε_0 are respectively the dielectric constant of the solvent and the vacuum, γ is the surface tension of the solvent, κ is the conductivity of the infused solution and v_f is the flow rate. The above equation is based on experimental results of Pfeiffer and Hendricks[16] on electrohydrodynamic spray [(1)], and has later been supported by semi-empirical derivations.[17-20]

[(1)] This is the "under vacuum" version of the ESI, especially dedicated to high surface tension liquids, e.g. liquid metals.

Another simplified relationship has been proposed by de la Mora et al., on the basis of experimental measurements of the current the droplet sizes and charges.[21]

$$i_{ES} = f(\varepsilon_r) \cdot \left(\gamma \kappa v_f \varepsilon_r\right)^{0.5} \qquad (2)$$

where $f(\varepsilon_r)$ is a function of the solvent permittivity (it is roughly equal to 18 for $\varepsilon_r \geq 40$), such as water and methanol).[21, 22] It is worth noticing that no dependence on the electric field is considered in the last equation, unlike what has been put forward by several studies.[23-25] However for sufficiently conducting solutions, the effect of the electric field can be neglected.[20]

The spray current i_{ES} is usually below 300nA, but can rapidly equal or exceed 1μA in the case of corona discharge. This dramatic increase in current is due to a sudden drop in the gap resistance between the emitter and the counter electrode: electrons are actually field-emitted from the electrospray needle or the solution cone. These discharges are detrimental for the MS analyses: the electrons ionize the solvent, gas and other species present in the surroundings. Corona discharge is obviously more troublesome in negative mode since the field-emission of electrons is favored, but can be reduced by using for instance scavenger gases, such as SF_6 or polychlorinated hydrocarbons. O_2 is a less efficient discharge suppressor but is obviously present during electrospray ionization due to its API nature. Another possibility consists in adding in series to the electric circuit a high resistance, typically 10GΩ, to take over the gap resistance. The electrospray process will thus adjust itself to a low current, inhibiting at the same time the occurrence of discharges.[25]

3. Emission and fission of the droplets

As mentioned above, the emission of the droplets occurs at the apex of the liquid cone. From this emission depend the nature and the amount of the ionic species that will be detected by

mass spectrometry. Therefore, all phenomena and the parameters involved in the production of the primary droplets are of prime importance in the understanding of the electrospray ionization.

3.1 Electrospray onset

The striking cone shape, specific to electrospray process and characterized by a half-angle θ, has been first studied by Taylor. The development of the Laplace equation in polar coordinates permits to find the condition for which equilibrium between the pressures applying on the surface of the liquid is attained. Under the assumption that the surface of the cone is an equipotential, θ_0 is the solution for:

$$P_{1/2}(\cos\theta) = 0 \qquad (3)$$

where $P_{1/2}(\cos\theta)$ is the Legendre function of order 1/2. θ_0 has been found to be equal to 49.3° when the equilibrium between forces is obtained.[13] The complete demonstration of this calculation is given in Wilm et al.[26]

The corresponding electric field for the onset of the spray, so-called E_{onset}, has been first derived by Smith.[17] For this model, schemed in Figure II-2, the equilibrium can be expressed as follows:

$$0 = \frac{\gamma \cdot \cos\theta_0}{R_C \cdot \sin\theta_0} - \left[\frac{\varepsilon_0}{2} E_\theta^2 + \frac{(\varepsilon - \varepsilon_0)}{2} E_R^2 \right] \qquad (4)$$

where γ is the surface tension of the solvent, θ is the cone half angle, R_c is the distance between the rim of the capillary and the cone apex, E_θ and E_R are respectively the normal and the tangential component of the electric field relative to the surface of the cone. Smith has

demonstrated experimentally that the condition $1/2(\varepsilon_0 - \varepsilon) E_R << \gamma \cdot \cos\theta_0 / R_C \cdot \sin\theta_0$ was fulfilled.

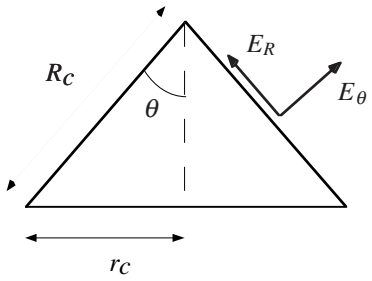

Figure II-2. *Taylor cone as the pressure balance is reached.*

As shown in Figure II-3, the tangential component of the electric field at the interface cone-air is negligible with respect to the radial one. This tendency is particularly marked close to the cone apex as demonstrated by Hayati et al.[18]

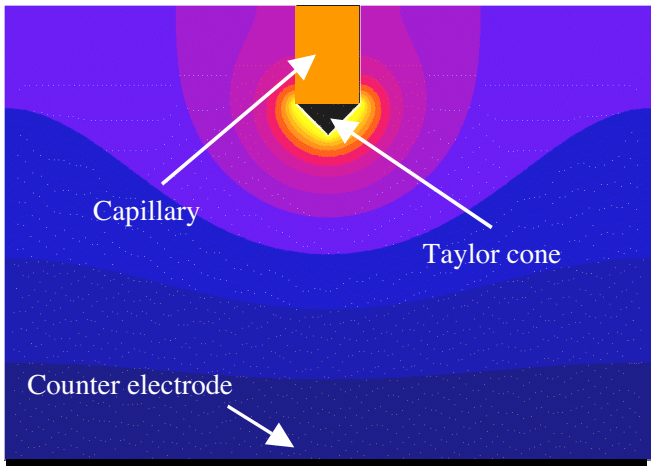

Figure II-3. *Equipotential lines at the Taylor cone. The counter electrode is located at the bottom. A potential* $\varphi = \varphi_0$ *is applied on the cone surface and the counter electrode is connected to the ground (*$\varphi = 0$*). The surface charge density is assumed to be homogeneous. The calculation is based on Laplace equation (finite element simulation with Flux-Expert®).*

From equation 4, it comes:

$$E_{\theta(R=R_C)} = E_{onset} \approx \left(\frac{2\gamma \cos\theta_0}{\varepsilon_0 r_c} \right)^{0.5} \qquad (5)$$

where r_c is the outer capillary radius. The last calculation is based on an electrostatic behavior of the system. The problem is much more complex when the spray is on, since it becomes an electrohydrodynamic state, where the viscous forces as well as the applied electric field must be taken into account.[27]

As a first approximation, the electrospray has been modeled by Eyring et al. as a system involving a metallic point, with a hyperboloid shape, and a metallic plane located at a distance d_0 from the end of the metallic point.[28] The change to hyperbolic coordinates allows the introduction of the equipotential lines in the calculation, therefore $\varphi = \varphi_0$ at the metallic point and $\varphi = 0$ at the plane. The electric field at the apex of the cone has been derived based on experimental results (see equation 6).

$$E_{ES} = \frac{2V_{ES}}{r_c \ln\left(4d_0 / r_c\right)} \qquad (6)$$

where V_{ES} is the applied voltage between the capillary and the counter electrode, d_0 is the distance between the capillary outlet and the counter electrode. A theoretical demonstration is given in the appendix of Taylor's work.[14]

The above equation shows a strong dependence of the electric field on the outer capillary radius. In Figure II-4, the electric field has been plotted versus the distance for different capillary radii following the last equation, as well as the electric field between to infinite planes.

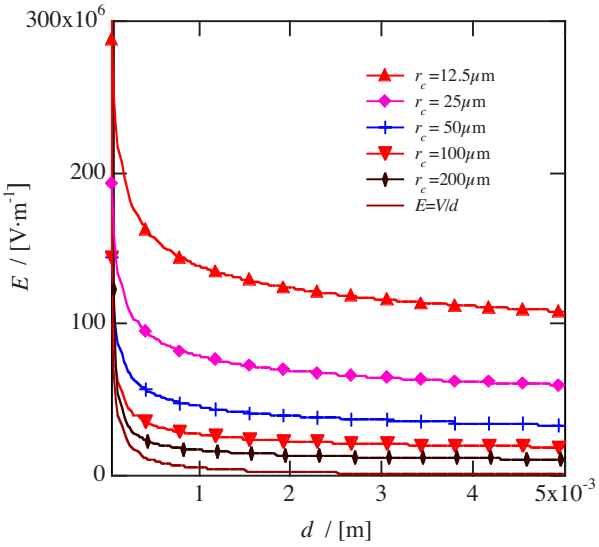

Figure II-4. *Electric fields versus the distance with different outlet outer diameters (V_{ES}=5·10^{3}V; d_0=5mm).*

Figure II-4 shows that for a given potential difference applied, the electric field distribution along the distance is similar, but the offset (at least ten times higher than the 2 infinite parallel plates) due to the decreasing outlet outer diameter is significant. This highlights the need of a sharp emitter, hence the introduction of micro and nanosprays. From a practical point of view, it allows the reduction of the applied voltage for the onset of the spray. A too high voltage value makes actually the handling of the whole system tricky.

Finally, considering equations 5 and 6, one can deduce that decreasing the outer capillary radius permits the use of solution with higher surface tension, for a given applied voltage. This last consideration is widely used for nanospray MS analyses of biocomplexes under non-denaturing conditions.[10, 29]

3.2 The Taylor cone

As the electrospray has its roots in the Taylor cone, its formation as well as its specific features has been widely investigated. First of all, the "real" geometry of a Taylor cone under electrohydrodynamic conditions can come in different modes.[30] The most interesting one is the

cone-jet mode, characterized by an extension of the cone in a jet whose breakup gives rise to the droplets. For an applied voltage above E_{onset}, one can distinguish two modes. With a low electric field, the spray is usually stable: this is the "cone-jet" mode, where only one jet of solution is observed followed by droplet formation. For high flow rates and capillary radii, the bimodal distribution of satellite and primary can be observed.[31] With a further increase in potential, several jets are formed, and the electrospray operates in the "multi-jet mode".

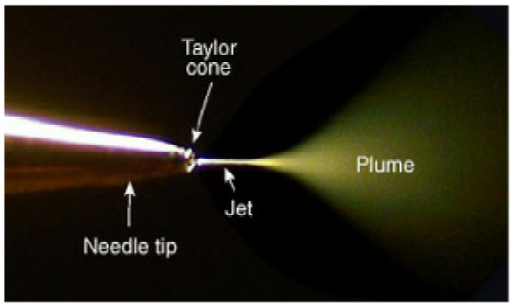

Figure II-5. *Cone-jet mode on a nanospray tip (Reprinted from New Objective, Inc. website: http://www.newobjective.com/electrospray/index.html).*

This mode is unstable and thus not used for analytical purposes. However, this cone-jet mode has been defined for large capillary outlets, and since the dimensions of the system are drastically reduced in micro and nanosprays, the study of this cone-jet mode is yet laborious, even if it has been already observed (see Figure II-5).

The hydrodynamics in the cone have also been investigated. For highly conductive and viscous solutions, a pure sink flow has been observed, related only to the flow rate.[32] When the conductivity is low, the tangential stress increases, as a result the surface velocity raises, allowing a recirculating motion in the meridional plane of the spray that was firstly reported by Hayati et al.[33] The strength of this meridional flow increases when the conductivity and the viscosity decrease. This particular flow has been also numerically simulated by Barrero et al.[32]

It consists in a motion towards the cone apex along the cone generatrix and away from it along the cone axis (see Figure II-6).

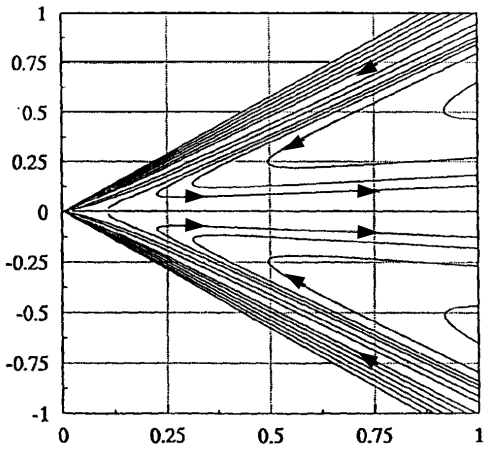

Figure II-6. *Recirculating meridional flow simulation in the Taylor cone (Reprinted from [32]).*

One explanation for this kind of motion can be given by the Electric Marangoni Effect. The Marangoni effect results from a gradient of surface tension inducing some shear stresses at a surface. The gradient of surface tension is here obtained by the gradient of electric charges along the cone generatrix.

By decreasing the viscosity and the conductivity of the solution, an intense azimuthal motion (swirl) appears in the cone in addition to the meridional motion. This kind of motion appears for very low conductivity and viscosity, i.e. for high values of Reynolds number.

These motions are driven by the tangential electrical stress $\tau_{r\theta}$ acting on the liquid-gas interface (given in equation 7) and the imposed flow rate,

$$\tau_{r\theta} = \varepsilon_0 E_\theta^g E_r \qquad (7)$$

where E_θ^g is the normal component of the electric field on the gas phase side of the interface and E_r is the tangential electric field.

A last aspect of the Taylor cone is its pulsation mode, earlier mentioned by several groups.[18, 30, 34, 35] It has been reported to occur under 2 modes: a low-frequency pulsation (few tens of Hz) which results from the mismatch between the applied flow rate and the output rate of solution ejection. The second one is in the high-frequency domain (kHz), and is the direct result of droplet ejections.[36] The latter is modulated by the former. The pulsation behavior has been underlined using parallel flash microphotographs of the Taylor cone and current monitoring. Due to these features, the electrospray can be externally pulsed, by varying the flow rate and the applied potential.[37]

3.3 The Rayleigh limit

The Rayleigh limit has been defined as the limit surface charge density, where the electrostatic force overcomes the surface tension at the surface of a droplet. The calculation takes into account the pressure p_R associated to the curvature and surface tension γ at a surface of a sphere and the electrostatic pressure p_E for a charged sphere, given in equation 8.

$$p_R = \frac{2\gamma}{R} \qquad p_E = \frac{\sigma^2}{2\varepsilon_0} \qquad (8)$$

where σ is the surface charge density.

The Rayleigh limit is therefore given by

$$q_{Ry} = 4\pi R^2 \cdot \sigma_{(p_R = p_E)} = 8\pi \cdot \left(\varepsilon_0 \gamma R^3\right)^{0.5} \qquad (9)$$

Another way to determine the limit charge has been introduced by Vonnegut and Neubauer.[38] A volume *V* of a liquid, having a surface tension γ and carrying *Q* charges is considered. Assuming that the liquid is dispersed in *N* droplets of radius *r*, each carrying *q* charges, the

total energy of the system is defined as the sum of the energy to create the droplets and the energy to charge them:

$$\Delta G = N 4\pi r^2 \gamma + \frac{N^2 q^2}{8\pi\varepsilon_0 r} \qquad (10)$$

Considering

$$V = N \cdot \frac{4}{3}\pi r^3 = \frac{4}{3}\pi R^3 \qquad (11) \quad \text{and} \quad Q = N \cdot q \qquad (12)$$

if the volume considered is initially a droplet of radius R, the equation 10 can be re-written as follows:

$$\Delta G = \frac{3V\gamma}{r} + \frac{NQ^2 r^2}{6\varepsilon_0 V} \qquad (13)$$

Assuming that the final state (N droplets are generated) corresponds to a minimum of the energy of the system, the first derivative of the total energy with respect to the initial volume gives the charge Q for which the dispersion takes place. Considering that the initial volume is contained in a sphere, it comes

$$Q = 4\sqrt{2}\pi\left(\varepsilon_0 \gamma R^3\right)^{0.5} \qquad (14)$$

The last equation, due to its derivation, can be applied to the Taylor cone instability limit, where $Q = Nq$ represents the limit charge density at which the cone will disrupt.

The comparison between the relations 9 and 14 reveals a factor $\sqrt{2}$ difference. This divergence can be explained by the way the two equations have been established. In the first case, an equilibrium condition is considered, which occurs when radially acting electric forces equal surface tension forces. In the second case, only the final state is taken into account,

which should correspond to a minimum energy of the system. It is interesting at this point to notice that the surface charge density at which coulombic fission occurs has been found to be typically around 0.7 to 0.8 q_{Ry}.[21, 39, 40] Thus, other mechanisms than the aforementioned ones may be involved in the electrospray process. However, contrary to the last model, the Rayleigh limit does not take into account the way the droplet splits, i.e. even or uneven fission (see next section).

The above calculations do not take into account an extra external potential, which is applied when droplets are electrosprayed. By means of finite element simulation, Adornato et al. demonstrated that as the external field increases, the Rayleigh limit decreases.[41] A last argument against these calculations is the fact that the surface tension of neutral solutions is considered. As putting forward by Davis and Bridges,[42] the latter is affected by the surface charge density.

3.4 Droplet fission

Droplet fission occurs at every downstream position, when the Rayleigh limit is reached, or is close to be reached. Both even and uneven fission have been found to occur. The reasons leading to a rough fission, when the droplet breaks up into a few large and unequal fragments, or a fine fission, i.e. when the drop explosion produces many very small and relatively monodisperse droplets, remain obscure, although it must be related to droplet size and a certain combination of physical properties of the liquid. It was demonstrated theoretically and later experimentally that highly conductive solutions were more predisposed to uneven fission.[43, 44]

As observed by Gomez and Tang for an uneven fission,[40] the offspring droplets are mostly ejected in the sidewise direction toward the periphery of the electrospray. This phenomenon is particularly strong at short downstream distance from the emitting cone. As illustrated in Figure II-7, the shape of an emitting droplet presents a jet from which offspring droplets are

generated. Considering the direction of the applied electric field, it is likely that other processes have to be unraveled concerning droplet fission. As proposed by Gomez and Tang, the primary droplets may vibrate just after their emission due to cone breakup, alternatively from oblate to prolate shapes, until they relax to a spherical form. This instability and deformation of the surface may lead to a local strong increase in electric field and thus the preferential side ejection. This vibration could also be transmitted to the residue droplet surface, which may disrupt in a sidewise manner. However, far from the emitter, the disruption of the droplets should occur in the same direction as the electric field.[45, 46]

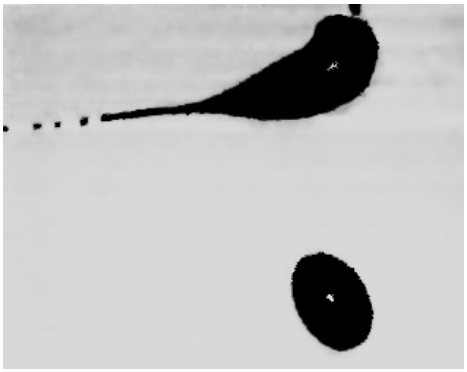

Figure II-7. *Flash shadowgraphs of the disruption of a heptane electrosprayed droplet. The direction of the electric field is top-down (Reprinted from Gomez et al.[40]).*

The study of the droplets in terms of size and charge is usually performed using Phase Doppler Interferometry or Differential Mobility Analysis techniques. In the same way as for the spray current (see equations 1 and 2), relationships relative to the size of the primary droplets have been proposed:

$$R = \left[\frac{3\varepsilon\gamma^{0.5} v_f}{4\pi\varepsilon_0^{0.5}\kappa E} \right]^{2/7} \qquad (15)$$

$$R \approx \left(v_f \varepsilon / \kappa \right)^{1/3} \qquad (16)$$

The dependence of *R* on the flow rate[10, 47] and the conductivity[48, 49] have been confirmed by others groups.

From the uneven fission, 2% of the mass and 15% of the charge of the parent droplet are transferred to the progeny droplets, characterized by a radius of roughly one tenth of the primary droplet.[39] Assuming that offspring droplets are monodisperse, and carry an equal amount of charge as demonstrated by the results of Gomez et al.,[40] Tang and Smith were able to formulate a theoretical prediction of droplet evaporation and fission.[50] They could unravel several issues about the electrospray process. First, the average number of fission events that can occur depends mainly upon the initial droplet size. Besides, both progenies and the residue parent droplet are stable, immediately after the parent droplet fission. However, progeny droplets become unstable much faster (about ten fold) than the residue droplet. Thus, they represent most likely the primary source of ions for a conventional electrospray ionization source, while the residue droplet will generate additional progeny droplets through the subsequent fission process.

4. Gas-phase ion generation

After many solvent evaporation and coulombic fission cycles undergone by the droplets, gas-phase ions are generated and guided to the counter electrode. Despite the high level of interest in ESI and the large amount of publications on this subject, the process that leads to the generation of gas-phase ions is still under investigation. As illustrated in Figure II-8, two theories are considered, the ion evaporation model (IEM)[51] and the charge residue model (CRM),[3] but it is not established which of them is predominant as the generation mechanism in the gas-phase, and at which stage it takes place, considering the size and the charge of the droplets. The distinction between the two mechanisms is also difficult to draw, because the droplets from which gas-phase ions are supposed to be generated by one of these mechanisms

have radii about tens of nm. The observation of the phenomena in which they are involved is yet difficult to achieve.

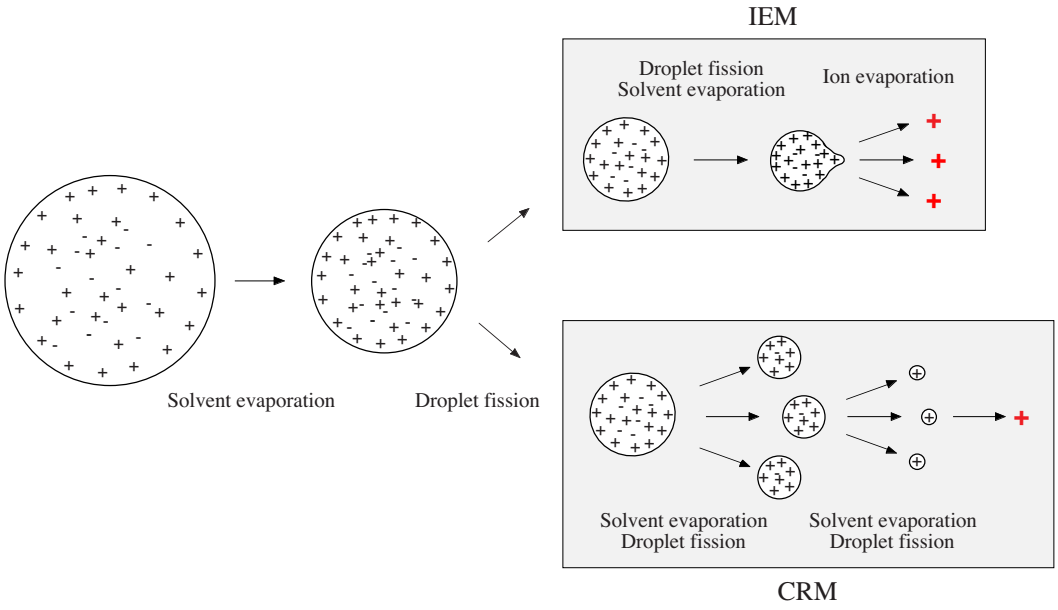

Figure II-8. *The two models for gas-phase ion generation by ESI: the Ion Evaporation Model (IEM) and the Charge Residue Model (CRM).*

4.1 Ion Evaporation Model

First introduced by Iribarne and Thomson,[51] the Ion Evaporation Model (IEM) assumes that before the droplet reaches this ultimate stage, the field on its surface becomes strong enough to overcome solvation forces and lifts a solute ion from the droplet surface into the gas medium. This mechanism is supposed to take place when droplets have a radius smaller than 10nm.

A simplified model

A first proof of principle consists in considering the dependence of each electric field, the one due the charged droplet

$$E = \frac{Ne}{4\pi\varepsilon_0 R^2} \qquad (17)$$

and the field required to get the theoretical limit of Rayleigh (see equation 9), i.e.

$$E_{Ry} = \left(\frac{4\gamma}{\varepsilon_0 R}\right)^{0.5} \qquad (18)$$

The two electric fields have been represented versus the droplet diameter in Figure II-9.

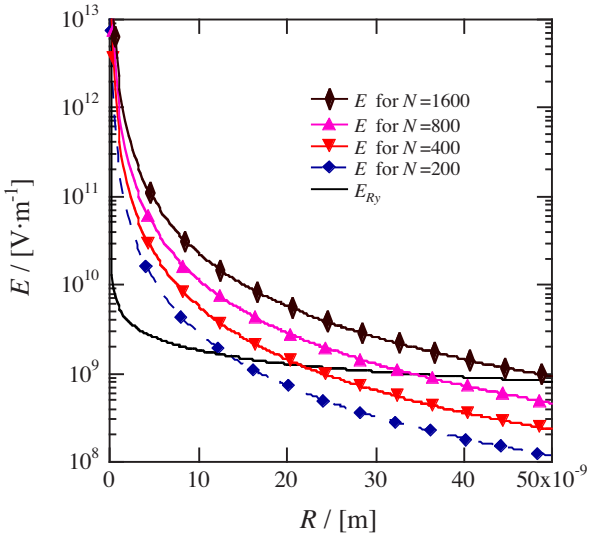

Figure II-9. *Comparison between the external field for a droplet carrying N charges (see equation 17) and the electric field at the Rayleigh limit (see equation 18).*

Thus, for an evaporating droplet carrying 200 charges, the ion evaporation is likely for radii under 12nm. In addition, if the parent droplet carries a higher number of charges, the ion evaporation is possible at an earlier stage of evaporation, e.g. for a droplet carrying 1600 charges, the ion generation by IEM is likely for a diameter of 50nm. To summarize, carrying a larger number of charges makes thus the ion evaporation possible for larger droplets. Since the droplet charge considered here is close to the statistical charge (due to the interface, some ion charges are not compensated by counter ions at the surface of the droplet), i.e. far from the

values reached for electrosprayed droplets, one expects in a first approximation that the possibility for the occurrence for an ion evaporation during ESI process is large.

Let us now consider the phenomena involved in ion evaporation. For this purpose, the Born approach can be used to model the hydration energy of the ion. It models the transfer of a bare ion from the gas-phase to a liquid drop of radius R. The energy consumed during this process can be considered as a three-step process: de-charging of the ion, transfer into the drop (formed from a liquid with a dielectric constant ε) with creation of a cavity, and lastly recharging of the ion. The resulting hydration energy is given by the equation 19.

$$\Delta G_S = 4\pi r^2\gamma - \frac{z^2e^2}{8\pi\varepsilon_0 r}\left(1-\frac{1}{\varepsilon_r}\right) \qquad (19)$$

where r is the radius of the ion, z its charge. When the droplet is charged ($Q = Ne$), an additional electrostatic work associated to the charge present at the surface of the drop has to be taken into account, i.e. the associated external potential. Therefore, the energy corresponding to the transfer of the ion into the charged droplet is given by:

$$\Delta G^{w\to g} = -4\pi r^2\gamma + \frac{z^2e^2}{8\pi\varepsilon_0 r}\left(1-\frac{1}{\varepsilon_r}\right) - \frac{zeQ}{4\pi\varepsilon_0 R} \qquad (20)$$

It can be seen from this equation that for a given charge and radius of the drop, the term $\Delta G^{w\to g}$ becomes negative indicating that an ion can evaporate.

The charge of the droplet from which an ion evaporation occurs can then be derived. The results have been reported on a graph, presented in Figure II-10. As illustrated above, this simple model indicates that the ion evaporation can occur at any stage of evaporation of the droplet.

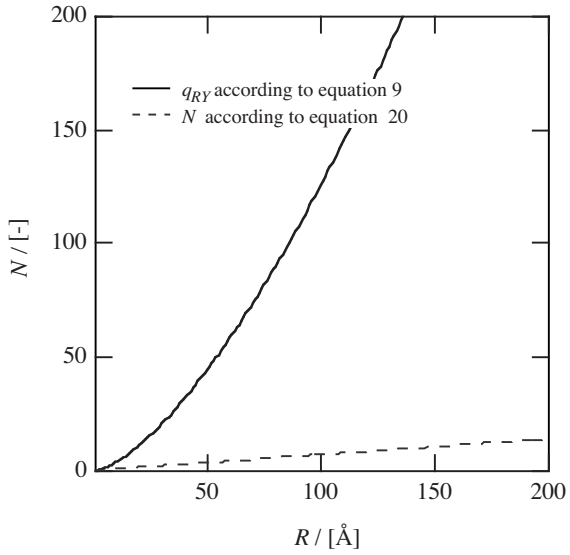

Figure II-10. *Limit charge for Rayleigh instability and the number of charges N according to the above model (r=3.85Å; z=1).*

Therefore, other electrostatic contributions have to be considered. Due to this, the problem needs to be treated following a kinetic model, for instance based on the transition state theory, which is defined by a Gibbs energy of activation, an energetic barrier which exists between the initial and the final state.

Model of Iribarne and Thomson

The ion evaporation has been treated by Iribarne and Thomson by taking into account all the interactions between the charged droplet and the ion, which is clustered with its first hydration shell. First, the electrostatic interaction due to the image charge has been taken into account (equation 21).

$$\Delta G_i = \frac{-e^2 z^2}{16\pi\varepsilon_0 x}\left(\frac{\varepsilon-\varepsilon_0}{\varepsilon+\varepsilon_0}\right) \qquad (21)$$

where x is the distance from the ion to the interface, assuming the interface is an infinite plane.

The second contribution refers to the energy difference when the ion is taken from the inner surface of the drop to a distance x outside the droplet (see equation 22). It can be interpreted also as the difference between the final and initial state of the system ion-droplet.

$$\Delta G_{d-i} = \frac{Ne^2 z}{4\pi\varepsilon_0 (R+x)} - \frac{Ne^2 z}{4\pi\varepsilon_0 (R-r)} \qquad (22)$$

The sum of all these interactions is given by the following equation.

$$\Delta G = -\Delta G_S - \Delta G_i - \Delta G_{d-i}$$

$$\Delta G = -4\pi r^2 \gamma + \frac{z^2 e^2}{8\pi\varepsilon_0 r}\left(1 - \frac{1}{\varepsilon_r}\right) + \frac{e^2 z^2}{16\pi\varepsilon_0 x}\left(\frac{\varepsilon_r - 1}{\varepsilon_r + 1}\right) + \frac{Ne^2 z}{4\pi\varepsilon_0}\left(\frac{x+r}{(R-r)(R+x)}\right) \qquad (23)$$

As the ion evaporation is treated as a spontaneous kinetic process, it is characterized by a rate constant k_{IEM}. Considering a first order reaction kinetics as a simple approach, it comes:

$$k_{IEM} = \left(\frac{kT}{h}\right) \cdot e^{-\Delta G^{\neq}/RT} \qquad (24)$$

where $\Delta G^{\neq}$ is the free energy barrier, necessary for the cluster ion to evaporate. It comes:

$$\Delta G = \Delta G^{\neq} - \Delta G_S - \Delta G_i - \Delta G_{d-i} \qquad (25)$$

Since it is a spontaneous kinetic process, the ion evaporation will take place for $\Delta G \leq 0$ and if the energy barrier is attained ($\mathrm{d}\Delta G / \mathrm{d}x = 0$). Its position x_m can thus be derived from these two conditions. The following relation is obtained:

$$x_m = \frac{R}{2\sqrt{N} - 1} \qquad (26)$$

Combining equations 25 and 26, a relationship between the charges and the radius of the droplet, for which ion evaporation occurs, is obtained. This number of charges has been represented with the Rayleigh limit versus the radius of the droplet (see Figure II-11).

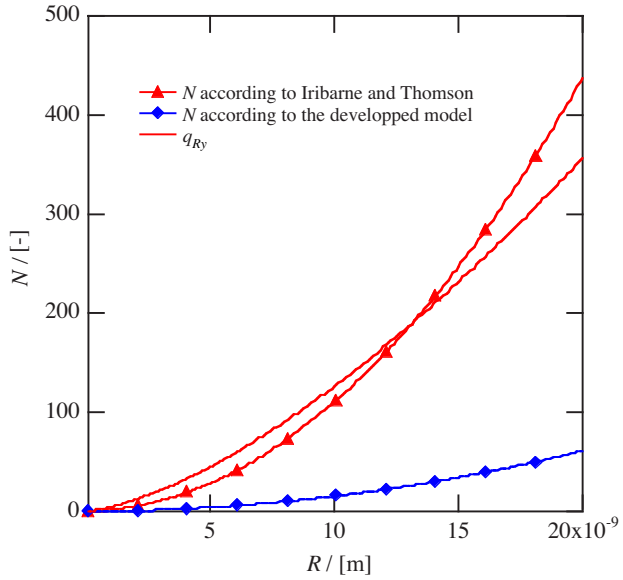

Figure II-11. *Different approaches for the ion evaporation model (r=3.85Å; z=1; γ=0.073N·m^{-1}; ε_r=80).*

For the Iribarne and Thomson curve, a solvation energy of -3.89·10^{-19}J·molecule^{-1} (-234kJ·mol^{-1}) has been considered, which corresponds to the energy required for the entering of an ion clustered with its first hydration shell based on thermodynamic quantities. The presented model takes into account the term ΔG_S based on Born's model (see equation 19), giving -1.598·10^{-19}J·molecule^{-1} considering the same radius for the cluster.(2)

For an evaporating droplet containing 300 charges, the Iribarne and Thomson model predicts droplet fission before an ion evaporation occurs. Conversely, ion evaporation will take place for a droplet carrying 100 charges, as its radius decreases by solvent evaporation. As illustrated

(2) Iribarne and Thomson gave, as a result of equation 19, 62kcal·mol^{-1}, i.e. 4.31·10^{-19}J·molecule^{-1}, which corresponds to the addition of the 2 terms and not their subtraction. This value is obtained with the correct relationship for an ion radius equal to 2.35Å.

in Figure II-11, the solvation energy affects significantly the IEM. Besides, it seems to be quite underestimated by the Born model.

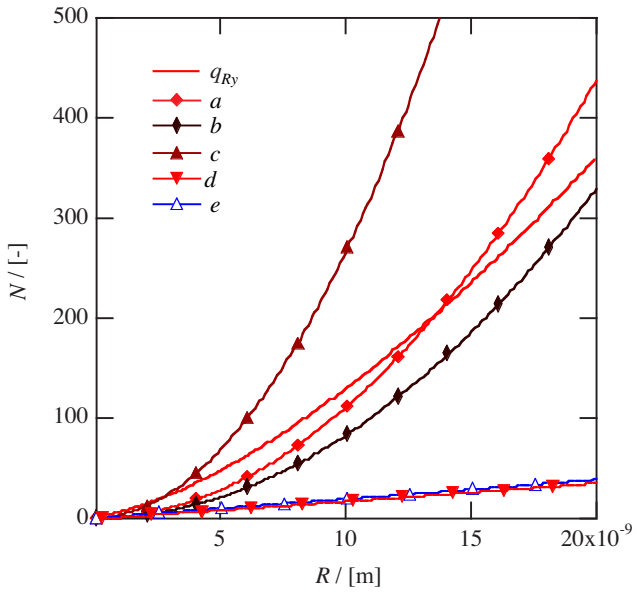

Figure II-12. *Relative contributions of the terms included in the IEM. a) N according to IEM; b) with* $\Delta G^{\neq} = 0$*; c) for* $\Delta G_i = 0$*; d) for* $\Delta G_{d-i} = -Ne^2/4\pi\varepsilon_0 R$*; e) for* $\Delta G_i = 0$ *and* $\Delta G_{d-i} = -Ne^2/4\pi\varepsilon_0 R$*.*

Apart from the influence of the solvation energy, there is a strong dependence of the model on the surface potential formulation, as illustrated in Figure II-12. However, a more complete description of the latter should consider the variation of the hydration of the ion at the boundary between two dielectric media, such as the model proposed by Kharkats and Ulstrup.[52] The equations developed by Markin and Volkov,[53] are even more adapted since they include, in addition to the last model, the image forces as well as the hydrophobic effect.

Discussion regarding the Iribarne and Thomson model

First of all, it must be noticed here that the original Iribarne-Thomson model does not consider droplets generated by electrospray, but generated by atomization. Therefore, no external field is considered, and the number of charges on the surface is underestimated. The surface tension

is therefore decreased due to a huge increase in the charge density compared to the statistically charged droplets, which has to be combined to the increase in surface charge concentration due to evaporation.

Considering the evaluation of the solvation energy by thermodynamic quantities, one has to stress the fact that the vapor pressure of the bulk water has been considered, while, more correctly, the vapor pressure of the droplet should have bee used. The vapor pressure increase due to the Kelvin effect is indeed particularly strong for radii lower than 1μm.[54]

Above all, the error on the evaluation of the solvation energy according to the Born model (see footnote 2) shows that this model is unsuitable for an ion evaporation process, since it actually underestimates the energy to transfer the ion. The Born model is indeed known to give an overestimation of the solvation energy, due to multiple assumptions on its calculation. First, the choice of a radius value for a given ion has been found to be difficult, especially for cations. Rashin et al. observed that a slight increase (7%) of the considered radius led to an excellent agreement with experimental results.[55] Since the cation is here considered with its first hydration shell, several corrections of the Born Model that could be taken into account for this specific case, such as the dielectric constant and the radius (the correction term for the transfer of the uncharged sphere into the liquid phase is already considered here),[56-59] are difficult to implement. In IEM, a slight decrease in dielectric constant (due to the rearrangement of water molecules around the cation) could be justified, however the evaluation of the right radius is here difficult to achieve, considering the hydrated cation. Anyway, all these corrections have the sole effect to lower the solvation energy derived from the Born model, and are therefore useless in the IEM evaluation. Considering the Born formulation given in equation 19, the cavity term is arguable and is not often considered when dealing with the Born model.

As it is illustrated in Figure II-13, the cavity term affects ΔG_S for radii larger than 3Å and becomes predominant for radii larger than 5Å, and therefore cannot be neglected in this study, even if some radius corrections are made.

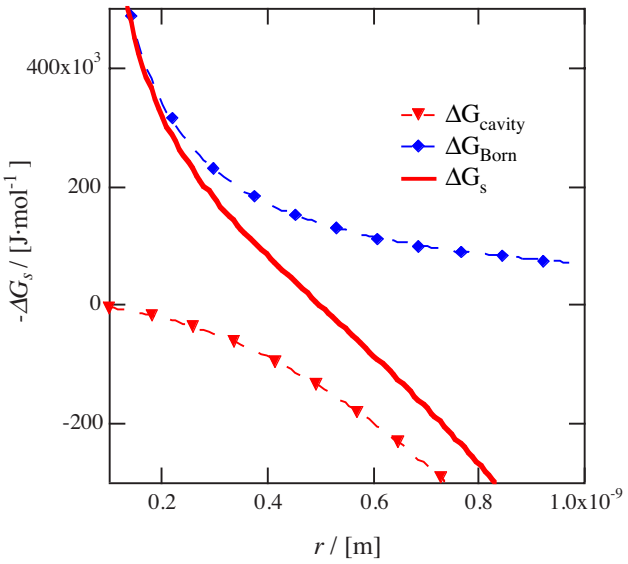

Figure II-13. *Importance of the 2 terms in Born model formulation (see equation 19) versus the ion radius.*

Finally, the fact that the interface is finite, has a curvature and a charge cannot be neglected in view of the droplet radii considered here. A model for ion evaporation, which considers the effect of the charge and radius of the emitting droplet, has been thus developed by Labowsky et al.,[60] leading to a domain (R, N), from which ion evaporation is likely to occur.

Some arguments against the formulation of the electrostatic contributions can also be raised. At least, considering that the second term of equation 22 is based on the field penetration in the droplet, it should be lowered by a ε_r factor, due to the field screening by the water molecules located at the surface of the droplet. In the other hand, this screening is important since it allows the assumption of a continuous distribution of charges even for very small droplets.

Concerning the image potential, its use is also quite controversial. The image charge has been introduced for electrons emitted from a metal surface. However, in the case of a liquid phase

the formation of a image charge requires a certain time, which is large compared to the time of presence of the escaping ion close enough to the surface to "feel" the image potential, as observed by Röllgen et al.[61] However, the attraction between the ion and the liquid surface is more likely due to the generation of a polarization potential by the microscopic reorganization of the solvent molecules, which is fast enough to interact with the escaping ion.

Finally, the IEM proposed by Iribarne and Thomson can be used only for ions with no surface activity, e.g. alkali metal ions. This shortcoming has been pointed out by Kebarle and co-workers,[62] putting forward the fact that the droplet surface can be enriched in surface-active ions, i.e. with a high affinity for liquid-air interface. Generally, ions with high surface activities, such as tetraalkylammonium ions due to their large hydrophobic groups or analytes with non-polar moieties, also have low ion solvation energies, meaning they are better suited to escape from the solvent. However, it must be stressed here that the correlation between the solvation energies and the observed relative abundances is a quite controversial issue.[63-67] The combination of several events, such as uneven droplet fission, continuous solvent evaporation, and favored formation for clusters with higher gas-phase stability could explain the interference with the solvation rank. The relation between solution composition and the relative response will be tackled in the section 5 below.

Another way to investigate the validity IEM could be to use the theory of ion transfer across liquid/liquid interfaces, since the events are in many points similar. Among all mechanisms mentioned, the theory proposed by Marcus is based on the probability to form protrusions at the interface and seems to be the most appropriate to be used for IEM.[68] The ion, which is initially in a solvent A, first attaches itself to a protrusion of solvent B to cross the interface. Since the ion is attached to the tip, it initiates the solvation by B and the desolvation from A. The ion can thus diffuse across the interface toward solvent B. The collapse of the protrusion

helps the solvation of the ion by the new solvent B, and this solvation and the desolvation from A, as the ion diffuses across the interface.

4.2 Charge Residue Model.

The CRM, first coined by Dole and co-workers,[3] for neutral macromolecules, has been extended to ions by Röllgen's group.[69] It assumes a sequence of Rayleigh instabilities driven by successive solvent evaporations and droplet fissions due to coulombic repulsions of charges at the surface of the droplet, as shown in Figure II-8. This process results in ultimate droplets, each of them containing only one molecule of solute. This molecule becomes a free gas-phase ion by retaining some of its droplet's charge as the last of its solvent molecule evaporates.

As already demonstrated for IEM, the surface activity of ions can also interfere with the CRM. These ions will tend to be the charge carriers of the droplet. They are therefore preferentially transferred to the offspring droplets, when coulombic fission occurs. Thus, these ions, as in IEM, should be highly abundant gas-phase ions.

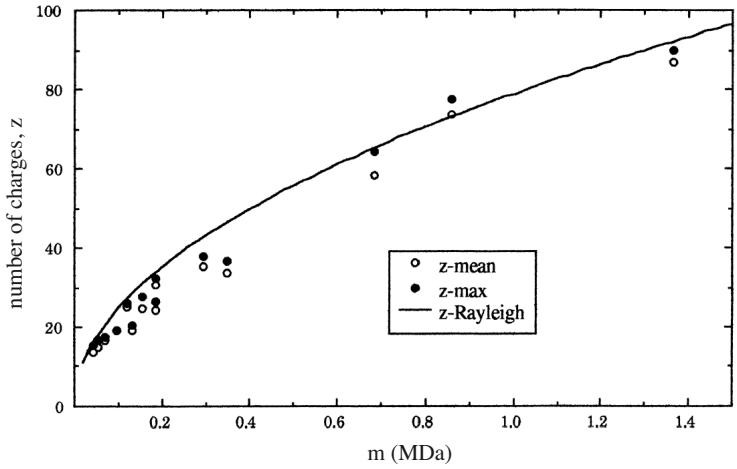

Figure II-14. *Maximum and mean charge on various native proteins compared with the Rayleigh limit given in equation 9 considering* $\rho = 1 g \cdot cm^{-3}$, $\gamma = 0.072 N \cdot m^{-1}$ *(Reprinted from [70])*

A recent study on globular proteins has shown that the number of charges observed on MS spectrum were very close and a little bit smaller than the one determined by the Rayleigh limit for a water droplet with the same diameter than the protein, as illustrated in Figure II-14.[70] These results point out that the CRM is the most likely process for these undenaturated proteins, since the criterion $q \approx q_{Ry}$ to validate this model is applicable over a wide mass range of proteins. In the same way, non-covalent complexes are more likely following the CRM.

The generation of more open multicharged structures by either CRM or IEM is still under investigation, even if some theories have been proposed for each mechanism.[70, 71]

4.3 Very final stage of gas-phase ion generation.

For very small droplets with a radius of a few nm, the Rayleigh equation cannot be considered. First, the Kelvin effect on the vapor pressure of the solvent has to be taken into account. In addition, a continuous distribution of charges is required, condition which is not fulfilled for such small droplets. However, as the solvent evaporates, the few ions are stuck in bulges, growth-enhanced by coulombic instabilities, from which single, solvated ions with or without salt addition, will finally be expelled. This process expresses more an IEM character than the CRM. Thus, these two processes are intermingled for very small droplets (R<3nm) and the tendency is now to consider a modified CRM, where IEM occurs at a very final stage, whatever the nature of analytes might be.[72]

All the above models and assumptions have been developed on an ESI basis. Nonetheless, in the case of a nanospray ionization the size of the primary formed droplet is dramatically decreased. The low surface activity of analytes is thus less problematic when dealing with nanospray, since gas-phase ions can be produced directly from the primary droplets, unlike ESI for which gas-phase ions come almost exclusively from offspring and satellite droplets.[29, 73] The ionization efficiency is in addition greatly increased because there is enough time for the

primary and residue droplet ions to be entirely transferred to the gas phase, due to their very high surface-to-volume ratios.

In conclusion, the ion evaporation mechanism remains the most likely process for gas-phase ion formation for small ions. However, the difficulty to experimentally study the droplet size and charge, and thus the accurate determination of the experimental coefficients such as the ion evaporation rate constants k', makes the determination of the occurring model uncertain.

Concerning species larger than 6500Da, de la Mora demonstrated that their transfer to gas-phase proceeded by CRM.[70]

5. From solution to gas-phase

5.1 Effect of the solution composition

Using ESI as sample introduction method, the observed MS response can be affected by a number of factors. Experimental parameters such as spray position relative to the MS entrance, spray potential, curtain gas flow rates, ionic strength and organic content of the sprayed solution have been already investigated.

The nature of the electrolytes and solvents can dramatically suppress the analyte signal or change the spectral charge distribution in the case of multiply charged ions. Either the anions[74] or the cations composing the supporting electrolytes can influence the MS analyses. Gas-phase reactions, such as proton transfer, can have a significant effect on ESI response. The proton affinity scale, which expresses the basicity, is not the same in the gas-phase and in the liquid phase. For several compounds, the order is even inversed. When dealing with these species, which includes widespread ESI solvents (water, methanol), the proton transfer in gas-phase can completely suppress analyte signal or change a charge state distribution associated to a protein.[75-77]

Some spectroscopic measurements (fluorescence, light-induced fluorescence) in a electrospray plume have permitted to highlight discrepancies in analyte solvation or protonation in solution and during the electrospray process.[78-80] In particular, the influence of the organic solvent content in the solution on the denaturation of proteins has been investigated.[81] It has been pointed out that the protein solvation was different between solution and droplets. These discrepancies were shown to be independent regarding to solvent evaporation but were certainly due to the effect of protein adsorption at the droplet/air interface. Besides, the occurrence of electrophoretic migration in the generated droplets has been investigated,[82] revealing its influence on ion response. It is worth mentioning that the time for the analytes to migrate to the surface of the droplet is shorter than the time for the droplet to reach the Rayleigh fission limit. Strong indication for axial gradients in electrosprayed droplets has indeed been pointed out by the influence of the applied voltage on ion clustering (e.g., of the form M_2X^+). Based on the high proton mobility, a hypothesis on the protein's charge insensitivity to bulk solution pH has also been presented.

Physical and chemical separations during electrospray process have first been demonstrated by Hiraoka et al.[83] The ion intensities at different axial and radial locations between the electrospray emitter and the counter electrode indicated that ions with high desorption efficiency had significantly higher abundances at the periphery of the electrospray. This was attributed to two types of droplets, satellite and progeny droplets respectively. The production of satellite droplets results from the instability of the liquid/air interface when primary droplets are generated. These droplets contain therefore an excess in hydrophobic molecules. Due to their smaller inertia and higher charge density, they are separated from the primary droplets by mutual repulsion and are expelled sidewise. The progeny droplets, which are generated from the primary droplet surface following an asymmetrical fission, are in the same way enriched in hydrophobic analytes. This striking distribution has been investigated in more details by Tang

and Smith.[84] Using a hydrophilic compound and a surfactant, a well-defined deposition pattern was revealed on the counter electrode. The center was indeed enriched with the hydrophilic colored indicator, due to the deposition of the remaining primary droplets and the residual droplets. The surfactant concentration was found to be higher on the outer part of this center region. More strikingly, the spraying process has given rise to a high concentration region, with an outer circle pattern. The first region was attributed to the deposition of the offspring droplets while the second was assigned to the satellite droplets.

5.2 Relating composition to detection

Due to the effect of solution composition on the relative response on a mass spectrum, attempts to model the ion response with respect to the initial concentrations have been carried out.

Tang and Kebarle attempt

The first approach was based on the assumption that the major mechanism for gas-phase generation is IEM.[85] The ion evaporation rate was supposed to be proportional to the ion concentration in the parent droplet. The resulting equation, for a two analytes mixture, is:

$$I_{(A^+,MS)} = pf \cdot \frac{k_A[\mathrm{A}^+]}{k_A[\mathrm{A}^+] + k_B[\mathrm{B}^+]} \cdot i_{ES} \qquad (27)$$

where $I_{(A^+,MS)}$ represents the ion current detected of the analyte A^+, k_i is the ion evaporation rate constant of the species I, p is the sampling efficiency of the system, f the fraction of the droplet charge that is converted into gas-phase ions.

Experimental results revealed two distinct behaviors according to the initial concentration. In the low range, the response curve had a linear trend in a log-log plot. In the high concentration range, the intensity was found to level off and even decrease. However, this model was found

to fail in the high concentration range, since no fit was possible with the *k* ratio used for the lower range. The ratio had to be lowered for the low concentration range. Therefore, the model was extended to include surface activity and ion solvation energies,[62, 64] that could justify the change in rate ratio depending on the considered range. However, the mathematical model (equation 27) is still not predictive.

Excess charge concentration and partition model

As underlined above, the droplet ejection is the limiting event for the electrospray current. When a droplet leaves the Taylor cone, carrying a defined number of charges, the loss of charges is compensated by oxidation (in positive mode) occurring at the spray electrode, and the rate of excess charge production is given by the spray current i_{ES}.[64] The excess charge concentration $[\mathrm{Q}]$, given by equation 28, corresponds to the number of charges leaving the capillary.

$$[\mathrm{Q}] = \frac{i_{ES}}{F.v_f} \qquad (28)$$

It is therefore the upper limit for the surface concentration of observable ions generated by the electrospray source, and the range where the analyte signal is linearly dependent on the infused concentration can thus be determined. Therefore, it equals the total concentration of cations (considering the positive mode) at the surface of the droplets, as expressed in equation 29.

$$[\mathrm{Q}] = \left[\mathrm{A}^+\right]_S + \left[\mathrm{E}^+\right]_S \qquad (29)$$

where A is the analyte and E the cation from the supporting electrolyte.

A simple model has been developed by Enke group to predict ion signal intensities, based on the definition of the charge excess concentration.[86] For this purpose, a partition ratio has been introduced. The latter determines in which ratio the analyte is located at the droplet surface (S

index) with respect to the bulk (I index), which is electroneutral. For this model, an analyte (A^+) and a supporting electrolyte (E^+) are considered, counterbalanced by the same anion (X^-). Between the surface and the bulk of the droplet, a displacement reaction can be established, as follows:

$$\left(A^+X^-\right)_I + \left(E^+\right)_S \leftrightarrow \left(E^+X^-\right)_I + \left(A^+\right)_S \qquad (30)$$

The partition coefficients are defined by the balance between dissociated cations, which are located at the surface, and clustered ions present inside the droplet. The balance can be expressed in terms of coefficient partition as follow.

$$\begin{aligned} \left(A^+X^-\right)_I &\leftrightarrow \left(A^+\right)_S + \left(X^-\right)_I \qquad K_A = \left[A^+\right]_S\left[X^-\right]_I / \left[A^+X^-\right]_I \\ \left(E^+X^-\right)_I &\leftrightarrow \left(E^+\right)_S + \left(X^-\right)_I \qquad K_E = \left[E^+\right]_S\left[X^-\right]_I / \left[E^+X^-\right]_I \end{aligned} \qquad (31)$$

It comes:

$$\frac{K_A}{K_E} = \frac{\left[E^+X^-\right]_I\left[A^+\right]_S}{\left[A^+X^-\right]_I\left[E^+\right]_S} \qquad (32)$$

Assuming that the solution concentrations remain at the same level in the generated droplets,

$$\begin{aligned} c_A &= \left[A^+\right]_S + \left[A^+X^-\right]_I \\ c_E &= \left[E^+\right]_S + \left[E^+X^-\right]_I \end{aligned} \qquad (33)$$

If it is assumed that the analyte surface fraction is very small, the inner concentrations can be taken equal to the initial concentrations. Using equations 29 and 32, the expression of the analyte response R_A is equivalent to the equation suggested by Kebarle and Tang.

$$R_A = Pf\left[A^+\right] = Pf\,\frac{c_A \cdot K_A}{c_A \cdot K_A + c_E \cdot K_E}[Q] \qquad (34)$$

However, instead of ion evaporation rates, the partition coefficients reflect information such as solvation energy, charge density and hydrophobicity of the ion, and the polarity of the solvent.

If no assumption on surface concentration is done, the combination of equations 29, 32 and 33 gives:

$$\frac{K_A}{K_E} = \frac{\left[\mathrm{A}^+\right]_\mathrm{S} \cdot \left(c_E - [\mathrm{Q}] + \left[\mathrm{A}^+\right]_\mathrm{S}\right)}{\left(c_A - \left[\mathrm{A}^+\right]_\mathrm{S}\right) \cdot \left([\mathrm{Q}] - \left[\mathrm{A}^+\right]_\mathrm{S}\right)} \qquad (35)$$

A quadratic relation between the analyte surface concentration and the initial concentrations is obtained by recombination of equation 35.

$$\left[\mathrm{A}^+\right]_\mathrm{S}^{\,2} \cdot \left(\frac{K_A}{K_E} - 1\right) - \left[\mathrm{A}^+\right]_\mathrm{S} \left[[\mathrm{Q}] \cdot \left(\frac{K_A}{K_E} - 1\right) - c_A \cdot \frac{K_A}{K_E} + c_E \right] + c_A \cdot [\mathrm{Q}] \cdot \frac{K_A}{K_E} = 0 \qquad (36)$$

For c_A much lower than $[\mathrm{Q}]$, the last equation can be reduced to:

$$\left[\mathrm{A}^+\right]_\mathrm{s} = c_A \left(\frac{K_A/K_E}{K_A/K_E - 1 + c_E/[\mathrm{Q}]} \right) \qquad (37)$$

and gives a mathematical prediction of the two regions of concentration (linear trend and saturation region), which have been corroborated by experiments for one analyte-one electrolyte system, keeping the same ratio K_A/K_E. These results confirmed the concentration-sensitive nature of the electrospray interfaces.

Considering a normal ESI use (100nA, 1μl·min^{-1}), the excess charge concentration can be estimated to be roughly 6.10^{-5}M. Therefore, for analyte concentration typically lower than this value, a linear correlation between the solution concentration and the relative abundance on the spectrum is observed, while for higher concentration, saturation occurs. This behavior has first been experimentally demonstrated by Kebarle and Tang.[34] For a system with two analytes,

competition can also occur depending on the surface activity of these compounds. It is demonstrated that matrix effects are also observed for high concentration of analytes reflecting the likelihood of every analyte to be located on the surface of the droplets.[87]

Several studies based on this model have demonstrated the possibility to extract the partition constant ratio by experimental means.[88] Depending on the nature of the analytes and the support electrolyte, the surface composition of the drop can be drastically changed, and the analyte signal can then be suppressed.[67, 89]

Several objections can be raised against this model. First, the assumption that the charges are located at the surface is arguable. As demonstrated by Myland and Oldham,[90] the ionic distribution within the droplet is analogous to the ionic distribution adjacent to a planar surface, highlighted by the theories of Debye-Hückel and Gouy-Chapman. Therefore, a correction factor should be taken into account for the surface concentration of the different ions considered. In addition, the dissociation equilibrium can be shifted due to the second Wien effect, also called dissociation field effect. Theoretically demonstrated by Onsager,[91] this effect has been verified in aqueous and non-aqueous media within the same range of electric field as used in ESI. Lastly, the use of more or less polar solvent mixtures has been shown to lead to a gradual enrichment of the less volatile component in the sprayed droplets.[92] This could lead to a change in surface concentrations of the different species and hence the partition scheme is changed during the electrospray process.

6. Mass spectrum features

An ESI spectrum is usually composed of protonated species, also called molecular ions. These ions can be single or multi-charged depending on the analytes. In positive mode, ESI mass spectra of small molecules are dominated by production of the protonated species ($[M+H]^+$), but also of cation-adducts ($[M+Na]^+$, $[M+K]^+$, $[M+NH_4]^+$). The spectrum of a larges

biomolecules appears usually has a multi-peak distribution, reflecting the population of differently protonated analyte molecules, which is, apart from the intrinsic nature of the analyte, highly dependent on the experimental conditions. The highest *m/z* ratios correspond to the lowest charged molecules. The multi-charging featuring electrosprayed analytes together with the softness of the ionization allows the study of non-covalent complexes consisting of up to 50 subunits and a molecular weight of 3.3MDa.[93]

In order to determine the molecular weight of an unknown protein and attribute to every peak a charge state, two successive peaks have to be considered, M_1, carrying n charges and M_2, (n+1) charges (see equation 38).

$$M_1 = \frac{(M + n \cdot H^+)}{n} \qquad M_2 = \frac{(M + (n+1) \cdot H^+)}{(n+1)} \qquad (38)$$

where H^+ is the monoisotopic atomic mass of hydrogen.

$$n = \frac{M_2 - H^+}{M_1 - M_2} \qquad (39)$$

$$M = n \cdot (M_1 - H^+) \qquad (40)$$

According to equation 39, the charge state of M_1, and so M_2 can be extracted. The molecular weight of the protein is calculated thanks to equation 40. These calculations can be done for every peak pair, ending up with a precision on the measured molecular weight with respect to the theoretical mass.

Thanks to high-resolution mass spectrometry, the isotopic distribution for every multi-charged peak is available. One peak is thus a combination of several peaks, representative of the isotope content. Since the separation between each isotopic peak is $\Delta m/z$, the charge is then

directly deduced, e.g. for a +4 charged ion, the gap is 0.25Da (the resolution has to be in this case 8000 for $m/z\,2000$, to be able to see the +4 isotopic distribution).

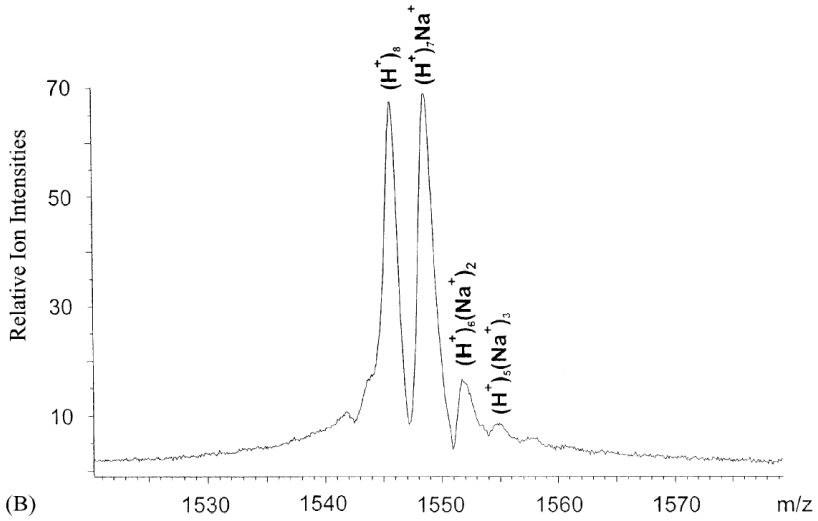

Figure II-15. *Mass spectrum of 5µM cytochrome C in NH_4Ac 0.5mM, NaCl 0.5mM aqueous solution at ph=6.8 (Reprinted from [94]).*

The same principle can be applied to the ions presenting sodium addition, even if the latter is often considered as detrimental in terms of MS analysis. Since one proton is replaced by one sodium ion, the mass difference between two adjacent peaks is therefore, in the case of a first addition, $Na^+ - H^+/n$ (see equations 38 and 39) and the charge n can be easily deduced even with a low-resolution spectrum (see Figure II-15), since the difference is roughly twenty times higher than with the isotopic distribution.

7. Conclusions

As illustrated by this chapter, the electrospray ionization is a complex process combining many mechanisms in both solution and gas-phases. From the generation of the Taylor cone, hydrodynamic, electrostatic as well as evaporation contributions have to be taken into account

for a complete description of the droplet generation. As the latter clearly represents the limiting step of the electrospray ionization, it is of utmost importance to unravel the phenomena leading to the production of the aerosol and quantify their relative importance. Actually, the droplet generation step conditions upstream phenomena, such as electrolytic events, as well as downstream gas-phase ion generation, this particular process being even nowadays a highly controversial subject. Apart from these mechanistic considerations, the composition of the sprayed solution (nature of the analytes, solvents, electrolytes, and their relative concentration) has been found to greatly influence the mass spectrometric response. A good illustration of the complexity of the electrospray ionization is the difficulty to fully understand the observed multi-charging rules applying to proteins.[95] To summarize, the electrospray ionization, even if it is a widespread technique, is by far not really understood.

8. References

(1) Zeleny, J. *The Physical Review* **1914,** *3*, 69-91.

(2) Zeleny, J. *The Physical Review* **1917,** *10*, 1-6.

(3) Dole, M.; Mack, L. L.; Hines, R. L.; Mobley, R. C.; Ferguson, L. D.; Alice, M. B. *J. Chem. Phys.* **1968,** *49*, 2240-2249.

(4) Clegg, G. A.; Dole, M. *Biopolymers* **1971,** *10*, 821-826.

(5) Fenn, J. B.; Mann, M.; Meng, C. K.; Wong, S. F.; Whithouse, C. M. *Science* **1989,** *246*, 64-71.

(6) Chowdhury, S. K.; Katta, V.; Chait, B. T. *J. Am. Chem. Soc.* **1990,** *112*, 9012-9013.

(7) Loo, J. A.; Giordani, A. B.; Muenster, H. *Rapid Comm. Mass Spectrom.* **1993,** *7*, 186-189.

(8) Babu, K. R.; Moradian, A.; Douglas, D. J. *J. Am. Soc. Mass Spectrom.* **2000,** *12*, 317-328.

(9) Loo, J. A. *Mass Spectrom. Rev.* **1997,** *16*, 1-23.

(10) Fligge, T. A.; Bruns, K.; Przybylski, M. *J. Chromatogr. B* **1998,** *706*, 91-100.

(11) Iannitti-Tito, P.; Weimann, A.; Wickham, G.; Sheil, M. M. *Analyst* **2000,** *125*, 627-633.

(12) Jiang, Y.; Wang, P. C.; Locascio, L. E.; Lee, C. S. *Anal. Chem.* **2001,** *73*, 2048-2053.

(13) Taylor, G. I. *Proceedings of Royal Society of London A* **1964**, 383-397.

(14) Taylor, G. *Proceedings of Royal Society of London A* **1969,** *313*, 453-475.

(15) Rosell-Llompart, J.; de la Mora, J. F. *Journal of Aerosol Science* **1994,** *25*, 1093-1119.

(16) Pfeifer, R. J.; Hendricks, C. D. *AIAA JOURNAL* **1968,** *6*, 496-502.

(17) Smith, D. P. H. *IEEE Trans. Ind. Appl.* **1986,** *IA-22*, 527-535.

(18) Hayati, I.; Bailey, A.; Tadros, T. F. *J. Colloid Interface Sci.* **1987,** *117*, 222-230.

(19) Juhasz, P.; Ikonomou, M. G.; Blades, A. T.; Kebarle, P. In *Methods and Mechanisms for Producing Ions from Large Molecules*; Standing, K. G., Ens, W., Eds.; Plenum press: New York, 1991.

(20) de la Mora, J. F.; Loscertales, I. G. *J. Fluid Mech.* **1994,** *260*, 155-184.

(21) de la Mora, J. F. *J. Fluid Mech.* **1992,** *243*, 561-574.

(22) Cole, R. B. *Electrospray Ionization Mass Spectrometry: Fundamentals, Instrumentation, & Applications*; John Wiley &Sons: New York, 1997.

(23) Emmett, M. R.; Caprioli, R. M. *J. Am. Soc. Mass Spectrom.* **1994,** *5*, 605-613.

(24) Wilm, M. S.; Mann, M. *Int. J. Mass Spectr. Ion Proc.* **1994,** *136*, 167-180.

(25) Jackson, G. S.; Enke, C. G. *Anal. Chem.* **1999,** *71*, 3777-3784.

(26) Wilm, M., Westfälischen Wilhelms-Universität, Münster, 1996.

(27) Cade, R. *J. Electrost.* **1995,** *35*, 279-293.

(28) Eyring, C. F.; Mackeown, S. S.; Millikan, R. A. *Physical Review* **1928,** *31*, 900-909.

(29) Karas, M.; Bahr, U.; Dulcks, T. *Fresenius Journal of Analytical Chemistry* **2000,** *366*, 669-676.

(30) Cloupeau, M.; Prunet-Foch, B. *Journal of Aerosol Science* **1994,** *25*, 1021-1026.

(31) Pantano, C.; Ganan-Calvo, A. M.; Barrero, A. *Journal of Aerosol Science* **1994,** *25*, 1065-1077.

(32) Barrero, A.; Ganan-Calvo, A. M.; Davila, J.; Palacios, A.; Gomez-Gonzalez, E. *J. Electrost.* **1999,** *47*, 13-26.

(33) Hayati, I.; Bailey, A. I.; Tadros, T. F. *Nature* **1986,** *319*, 41-43.

(34) Kebarle, P.; Tang, L. *Anal. Chem.* **1993,** *65*, 972A-986A.

(35) Charbonnier, F.; Rolando, C.; Saru, F.; Hapiot, P.; Pinson, J. *Rapid Comm. Mass Spectrom.* **1993,** *7*, 707-710.

(36) Juraschek, R.; Röllgen, F. W. *Int. J. Mass Spectrom.* **1998,** *177*, 1-15.

(37) Wei, J.; Sui, W.; Zhou, F.; Lu, Y.; Chen, K.; Xu, G.; Yang, P. *Mass Spectrom. Rev.* **2002,** *21*, 148-162.

(38) Vonnegut, B.; Neubauer, R. L. *Journal of Colloid Science* **1952,** *7*, 616-622.

(39) Taflin, D. C.; Ward, T. L.; Davis, E. J. *Langmuir* **1989,** *5*, 376-384.

(40) Gomez, A.; Tang, K. Q. *Phys. Fluids* **1994,** *6*, 404-414.

(41) Adornato, P. M.; Brown, R. A. *Proceedings of Royal Society of London A* **1983,** *389*, 101-117.

(42) Davis, E. J.; Bridges, M. A. *Journal of Aerosol Science* **1994,** *25*, 1179-1199.

(43) de la Mora, J. F. *J. Colloid Interface Sci.* **1996,** *178*, 209-218.

(44) Smith, J. N.; Flagan, R. C.; Beauchamp, J. L. *J. Phy. Chem. A* **2002,** *106*, 9957-9967.

(45) Hager, D. B.; Dovichi, N. J. *Anal. Chem.* **1994,** *66*, 1593-1594.

(46) Duft, D.; Achtzehn, T.; Müller, R.; Huber, B. A.; Leisner, T. *Nature* **2003,** *421*, 128.

(47) Wilm, M.; Mann, M. *Anal. Chem.* **1996,** *68*, 1-8.

(48) Olumee, Z.; Callahan, J. H.; Vertes, A. *J. Phy. Chem. A* **1998,** *102*, 9154-9160.

(49) Olumee, Z.; Callahan, J. H.; Vertes, A. *Anal. Chem.* **1999,** *71*, 4111-4113.

(50) Tang, K. Q.; Smith, R. D. *Int. J. Mass Spectrom.* **1999,** *187*, 97-105.

(51) Iribarne, J. V.; Thomson, B. A. *J. Chem. Phys.* **1976,** *64*, 2287-2294.

(52) Kharkats, Y.; Ulstrup, J. *Journal of Electroanalytical Chemistry* **1991,** *308*, 17-26.

(53) Markin, V. S.; Volkov, A. G. *J. Phys. Chem. B* **2002,** *106*, 11810-11817.

(54) Davies, C. N. In *Fundamentals of aerosol science*; Shaw, D. T., Ed.; Wiley Interscience: New York, 1978, pp 160.

(55) Rashin, A. A.; Honig, B. *J. Phys. Chem.* **1985,** *89*, 5588-5593.

(56) Conway, B. E.; Bockris, J. O. M. In *Modern Aspects in Electrochemistry*; Tompkins, F. C., Ed.; Academic Press: New York, 1954; Vol. 1, pp 47.

(57) Bockris, J. O. M.; Reddy, A. K. N. *Modern Electrochemistry*; Plenum Press: New York, 1977.

(58) Conway, B. E. *Ionic Hydration in Chemistry and Biophysics*; Elsevier: Amsterdam, 1981.

(59) Desnoyers, J. E.; Jolicoeur, C. In *Comprehensive Treatise of Electrochemistry*; Conway, B. E., Bockris, J. O. M., Yeager, E., Eds.; Plenum press: New York, 1985; Vol. 5.

(60) Labowsky, M.; Fenn, J. B.; de la Mora, J. F. *Anal. Chim. Acta* **2000,** *406*, 105-118.

(61) Röllgen, F. W.; Bramer-Weger, E.; Bütfering, L. *Journal de Physique* **1987,** *48*, C6-253.

(62) Kebarle, P.; Ho, Y. In *Electrospray Ionization Mass Spectrometry: Fundamentals, Instrumentation, & Applications*; Cole, R. B., Ed.; John Wiley &Sons: New York, 1997, pp 3-63.

(63) Thomson, B. A.; Iribarne, J. V. *J. Chem. Phys.* **1979,** *71*, 4451-4463.

(64) Tang, L.; Kebarle, P. *Anal. Chem.* **1993,** *65*, 3654-3668.

(65) Leize, E.; Jaffrezic, A.; Van Dorsselaer, A. *Journal of Mass Spectrometry* **1996,** *31*, 537-544.

(66) Wang, G.; Cole, R. B. *Anal. Chim. Acta* **2000,** *406*, 53-65.

(67) Cech, N. B.; Enke, C. G. *Anal. Chem.* **2000,** *72*, 2717-2723.

(68) Marcus, R. A. *J. Chem. Phys.* **2000,** *113*, 1618-1629.

(69) Schmelzeisen-Redeker, G.; Bütfering, L.; Röllgen, F. W. *Int. J. Mass Spectr. Ion Proc.* **1989,** *90*, 139-150.

(70) de la Mora, J. F. *Anal. Chim. Acta* **2000,** *406*, 93-104.

(71) Fenn, J. B. *J. Am. Soc. Mass Spectrom.* **1993,** *4*, 524-535.

(72) Kebarle, P.; Peschke, M. *Anal. Chim. Acta* **2000,** *406*, 11-35.

(73) Bahr, U.; Pfenninger, A.; Karas, M.; Stahl, B. *Anal. Chem.* **1997,** *69*, 4530-4535.

(74) Mirza, U. A.; Chait, B. T. *Anal. Chem.* **1994,** *66*, 2898-2904.

(75) Ogorzalek Loo, R. R.; Smith, R. D. *J. Am. Soc. Mass Spectrom.* **1994,** *5*, 207-220.

(76) Stephenson, J. L. J.; McLuckey, S. A. *Anal. Chem.* **1996,** *68*, 4026-4032.

(77) Amad, M. H.; Cech, N. B.; Jackson, G. S.; Enke, C. G. *J. Mass Spectrom.* **2000,** *35*, 784-789.

(78) Chillier, X. F. D.; Monnier, A.; Bill, H.; Gülaçar, F. O.; Buchs, A.; McLuckey, S. A.; Van Berkel, G. J. *Rapid Comm. Mass Spectrom.* **1996,** *10*, 299-304.

(79) Zhou, S. L.; Edwards, A. G.; Cook, K. D.; Van Berkel, G. J. *Anal. Chem.* **1999,** *71*, 769-776.

(80) Zhou, S.; Prebyl, B. S.; Cook, K. D. *Anal. Chem.* **2002**, 4885-4888.

(81) Rodriguez-Cruz, S. E.; Khoury, J. T.; Parks, J. H. *J. Am. Soc. Mass Spectrom.* **2001,** *12*, 716-725.

(82) Zhou, S. L.; Cook, K. D. *J. Am. Soc. Mass Spectrom.* **2001,** *12*, 206-214.

(83) Hiraoka, K. *Rapid Comm. Mass Spectrom.* **1992,** *6*, 463-468.

(84) Tang, K. Q.; Smith, R. D. *J. Am. Soc. Mass Spectrom.* **2001,** *12*, 343-347.

(85) Tang, L.; Kebarle, P. *Anal. Chem.* **1991,** *63*, 2709-2715.

(86) Enke, C. G. *Anal. Chem.* **1997,** *69*, 4885-4893.

(87) Constantopoulos, T. L.; Jackson, G. S.; Enke, C. G. *Anal. Chim. Acta* **2000,** *406*, 37-52.

(88) Sjoberg, P. J. R.; Bokman, C. F.; Bylund, D.; Markides, K. E. *Anal. Chem.* **2001,** *73*, 23-28.

(89) Sjoberg, P. J. R.; Bokman, C. F.; Bylund, D.; Markides, K. E. *J. Am. Soc. Mass Spectrom.* **2001,** *12*, 1002-1010.

(90) Myland, J. C.; Oldham, K. B. *J. Electroanal. Chem.* **2002,** *522*, 115-123.

(91) Onsager, L. *J. Chem. Phys.* **1934,** *2*, 599-615.

(92) Zhou, S. L.; Cook, K. D. *Anal. Chem.* **2000,** *72*, 963-969.

(93) Benjamin, D. R.; Robinson, C. V.; Hendrick, J. P.; Hartl, F. U.; Dobson, C. M. *Proc. Natl. Acad. Sci. U. S. A.* **1998,** *95*, 7391-7395.

(94) Felitsyn, N.; Peschke, M.; Kebarle, P. *Int. J. Mass Spectrom.* **2002,** *219*, 39-62.

(95) Grandori, R. *J. Mass Spectrom.* **2003,** *38*, 11-15.

Chapter III : Characterization of the nanospray interface

1. Electrospray as an on-line interface

Before the introduction of ESI, two challenging issues remained for practical mass spectrometry: the analysis of high-molecular weight compounds and an efficient interface for the coupling of Liquid Chromatography (LC). The development of ESI addressed both of them. The ionization sources used before ESI introduction were actually subject of significant drawbacks, such as sample dependence (Thermospray) or high chemical background (continuous-flow FAB or frit-FAB).

Electrospray ionization can be used over a wide range of flow rates, i.e. of instruments based on flowing solutions. High Performance Liquid Chromatography (HPLC) or LC fits well to ESI, and μLC to microspray (500nl·min^{-1} to 2μl·min^{-1}). Capillary Electrophoresis (CE) (as well as nanoLC) is more compatible to nanospray (20nl·min^{-1} to 500nl·min^{-1}) due to the intensity of electroosmotic flow. Theses features have contributed to the introduction of Electrospray ionization in analytical chemistry due to its ease of use and its flexibility.

However, commonly used solvents or compounds for separation are not always compatible with an efficient ionization. To circumvent this problem, several designs have been developed, illustrated in Figure III-1, each addressing a specific issue. The basic one (sheathless interface) consists of a sole capillary. The high voltage can be applied via a metallic junction connected

upstream. If incompatible solvents are used (high surface tension, inadequate pH), a sheath liquid can be supplied via a coaxial capillary to sustain the spray stability and efficiency. If the outer capillary is metallic, it can be used to supply high voltage to the solution. The principle is the same with the liquid junction configuration, except that the voltage connection is located far upstream in the make-up flow system, e.g. in a reservoir.

In the high-flow range, the solvent evaporation is problematic, thus a sheath gas is flowed over the sheath liquid capillary to enhance desolvation of the generated droplets. The gas flow also destabilizes the Taylor cone, therefore helping for the droplet formation. This design is also called "pneumatically assisted". Based on the same principle, an ultrasonic transducer can be used.

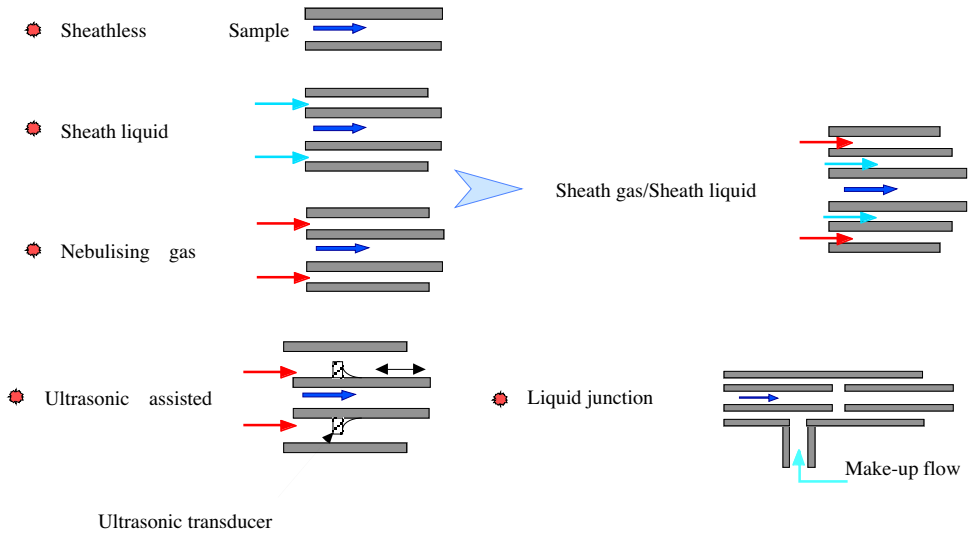

Figure III-1. *Classic ESI Designs.*

Most configurations have been developed for microspray and nanospray interfaces. The sheathless[1-5] or the liquid-junction[6-9] designs are usually employed. However, the sheathless ES interface for CE-MS coupling implies that the solution is already well suited for all the steps involved.

In the specific case of CE-MS coupling, the solution requirements for a high-resolution separation often mismatch with those for an efficient ionization and MS detection. For example, sodium or phosphate ions are known to be quite detrimental for MS analysis, even at low concentration. Their adduction on peptides leads to a difficult interpretation of spectra, not to say impossible. Moreover, the signal-to noise ratio could be drastically affected.

Decreasing the dimensions and flow rates involved is justified because it allows the formation of smaller droplets and then a more efficient solvent evaporation during the gas phase ion formation, and thus an enhanced ionization efficiency.[10] With a 5 μm diameter microspray outlet, Andren et al. obtained a zeptomole per μl sensitivity for peptides.[11] In addition, the tolerance to salts[12, 13] and non-volatile solvents is higher than with classical ESI interfaces, i.e. the signal-to-noise ratio as well as the signal stability is greatly enhanced.[14, 15] Lastly, analytes with low-surface activity are much more responsive with very-low flow interfaces, due the production of very small first generation droplets, permitting direct gas-phase ion emission.[16]

2. State-of-the art in nanospray interface designs

As mentioned earlier, the nanospray interface is characterized by a small outlet with an outer diameter of tens of μm, with associated flow rates of hundreds nl. Among all the designs, tapered glass capillary tips are widely used as sheathless emitters. It requires several steps to obtain the final shape, such as pulling and HF etching as first introduced by Gale and Smith.[17] To achieve an electrical connection on the non-conductive tips, gold is usually sputtered at the outlet of the tip.[14, 18-20] However, this conductive layer is rapidly damaged due to the high voltage applied. Several strategies have been investigated to overcome this problem. Valaskovic et al.[21] could improve the mechanical stability of the gold layer simply by overcoating the emitter with a SiOx insulating layer, inducing an extended life span. Electroplating of gold has also been used to increase the thickness and thus the robustness of

the gold layer.[22-24] Barnidge and co-workers could also obtain solid conductive coatings by fixing 2 μm gold particles with polyimide on glass tips.[25] Alternative routes for robust conductive layer deposition have been investigated, such as nickel electrodeless plating,[26] graphite layering with a colloidal suspension[27] or with a polymeric matrix.[28, 29]

For non-conducting emitters, a metallic part is often intercalated in the column with the shortcomings associated to increased "plumbing" and dead volume.[30] Other miniaturized configurations have been proposed, where the electrical connection is obtained via a metallic wire inserted at the tip.[31, 32] The drawback in this case could be the flow perturbation due to the wire and the electrochemical events that take place on it, such as bubble formation due to water oxidation and subsequent oxygen gas generation.[33] An alternative way consists of a liquid junction, through which the high voltage is applied.[34] The original design proposed by Hsieh et al. consists of a pulled capillary wherein the sheath liquid flows.[35] A tapered capillary, used for analyte delivery, is inserted, as well as a wire for the high voltage connection. The inner capillary is projected just beyond the outer capillary. In this configuration, the sheath liquid delivers high voltage to the emitter and prevents an analyte counter flow during CE experiment. In addition, no flow perturbation due to the liquid junction is observed.

Alternative materials, such as silicon[36] or silicon dioxide,[37] stainless steel machined by electrodissolution[38] or sanding[39] have been used to design sharp emitters with well-defined dimensions. The conductive nature of these tips allows the application of the high voltage via the emitter itself.[40]

Due to the emergence of separation microsystems, pioneer work on glass chips has been presented by the Karger [41] and Ramsey [42] groups for on-line coupling to mass spectrometer through nanospray interfaces. The spray was generated at an open end of a microchannel on the edge of glass chips by applying voltage at a reservoir, without any pneumatic assistance. However, they reported troubles in the spray stability due to the hydrophilic nature of the glass

substrate. Derivatization of the chip edge was found to be one way to overcome this problem.[41] Glass or silicon microchips are therefore often interfaced to a spray tip by means of glue, which yet renders the fabrication tedious.[3, 4, 43, 44] When the electrode used for electrospray generation is shared with the CE apparatus,[45] it prevents any control on the spray current and so the electrolytic events of the interface can not be unraveled from the electrophoresis apparatus. A liquid junction has also been included in several microdevices allowing the modification of solution composition prior to ionization to yield an easier spray process,[46] but also to supply the spray voltage.[6, 47]

During the last years, polymeric substrates have been also investigated. A wide range of fast prototyping techniques and materials has been used to fabricate microfluidic chips, such as replica molding,[8] soft lithography,[48] X-ray lithography,[49] hot embossing,[50] automated cutting,[51] and UV photoablation.[3, 52-55] Mass production has been also involved in emitter fabrication, such as plasma etching. [56, 57] One advantage of these substrates compared to glass or silicon, is their hydrophobic nature, which favors the spray generation. The convenience of these materials also allows the microfabrication of multichannel emitters,[51, 53, 58, 59] but also the complete integration of a sharp emitter in a microfluidic chip, in which a separation[52] or purification[55] apparatus is implemented. Among all the polymer substrates, the convenience of poly-(dimethylsiloxane) (PDMS) has permitted numerous multifunctional microchip designs, such as affinity purification associated to microdialysis apparatus,[60] or proteolysis integrated system,[61] and entire 3-D channel geometry via PDMS casting.[62]

3. Microfabrication technologies

The novel nanospray interface presented in this chapter is based on microchip designs developed previously [63, 64] and polymer photoablation. The present polymer device includes a

carbon ink microelectrode located close to the outlet of the probe, inside a sealed photoablated microchannel.

3.1 Photoablation applied to polymers

Ultraviolet (UV) photoablation on an organic polymer was first highlighted in 1982 by Srinivisan et al.[65, 66] It is based on the use of excimer lasers, which operates in the UV range. The name excimer refers to the "excited dimer" laser, such as the Xe_2* gas. Nowadays, this name is purely conventional, since rare gas monohalides form the active medium. The most commonly used lasers are Argon Fluoride (ArF, 193nm), Krypton Fluoride (KrF, 248nm), Xenon Chloride (XeCl, 308nm) and Xenon Fluoride (XeF, 351nm). Because of their short wavelength, excimer lasers feature high imaging resolution and ease of focusing. They emit pulses of UV light with a duration of about 10ns. The absorption of the UV photons is usually attributed to electronic transitions of the substrate matter. Thus, the more absorbing material at a defined wavelength will exhibit the lowest etching rate, typically between 0.1 and 1μm per pulse. Nonetheless, the resolution of the generated structures is higher, which allows a precise control of the etched depth. In addition, the UV laser ablation is characterized by a low thermal or mechanical damage of the irradiated areas. All these features make the UV excimer laser ablation an efficient microstructuration tool, particularly well suited for high-aspect ratio designs.[67]

Photoablation processes

Four different stages of interaction of a material with an excimer laser have been underlined, according to the fluence. Although these processes are found to occur one after the other, the threshold fluences are however dependent on the nature of the substrate, the wavelength and the pulse duration of the laser.

Below a defined fluence, no ablation occurs, only a surface modification is observed. Above the first threshold, the first stage corresponds to an electron excitation, due to absorption of photons corresponding to electronic transitions, followed by different relaxation processes but poor ablation is obtained. Above the second energy threshold, a mass plume is produced from the illuminated area. Due to its partial ionization by earlier electron emission, the plume strongly absorbs the light energy, resulting in a poor ablation rate. This phenomenon is called "shielding". The next stage marks the transition to the explosive ablation or phase explosion, with a high etching rate. It is characterized by a photochemical process with the generation of fragments, which undergo thermal degradation. This is typically the working stage for photoablation applied to microfabrication. Finally, with a high-energy beam, the electronic plasma is produced at early stage (on the picosecond timescale), long before the formation of the mass plume, amplifying the shielding particularly for short pulse duration. Therefore, the ablation rate is again inhibited.

Photoablation applied to microfabrication

Most of organic polymers absorb UV radiation, and their ablation rate as well as the ablated surface properties are dependent on the fluence and the wavelength of the laser as well as the surrounding atmosphere.[68] The cavity formed with a defined depth, results from the breaking of the polymer chemical bonds. The generated fragments are ejected at supersonic velocities[69, 70] up to 3.5mm[71] from the irradiated area. The ejected particle mass can be as large as 1'000 $g \cdot mol^{-1}$ and the materials ejected consist in C_2, C_3, CO CO_2, C_nH_n (n=2,..8) or monomer units.[72] The ablated surfaces are characterized by an increased roughness depending on the polymers, reliant on the laser beam fluence.[73] In addition, a lower O/C ratio has been underlined by XPS analysis on the cavity surfaces.[69, 74-77] This surface modification results in an enhanced hydrophobic behavior.[74, 75]

In the framework of plastic microstructuration, the substrates are positioned perpendicularly with respect to the laser beam. Two modes of photoablation are generally used, the static and the dynamic photoablation, both illustrated in Figure III-2. Dynamic photoablation is obtained by moving the substrate with respect to the laser beam, while no translation of the substrate is performed during the static photoablation. Most of the laser ablation features previously described have been demonstrated for the static mode. Nevertheless, different studies have demonstrated the additional decrease of O/C ratio with respect to the static photablation. [76,78,79] as well as a less homogeneous spatial distribution of crystalline phase.[73]

For microfabrication, the laser beam is used for fast prototyping of specific designs, including reservoirs, single or arrays of microholes, microchannels and intersections. Photoablation of polymers provides a good control of the width, the depth and the length of drilled microchannels by adjusting parameters such as pulse frequency, translation stage speed and laser energy.[63]

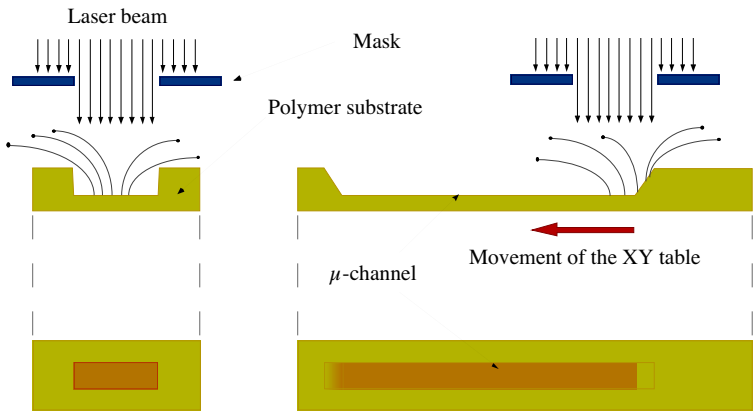

Figure III-2. *Static and dynamic photoablation mode.*

The dimensions of every item are defined by the fluence of the laser and the number of pulses on the illuminated area. The latter is delimited by the use of photomasks, made of thin molybdenum foils. In static mode, the depth of the microstructures is directly proportional to

the number of pulses. In dynamic mode, an average number of pulses is calculated taking into account the translation speed of the substrate. An illustration of the significance of the number of pulses per unit area is the aspect of the longitudinal section of a microchannel at both ends, as shown in Figure III-2. The slope results indeed from the shorter exposition of the substrate at the beginning and the end of the beam scanning.

Laser set-up

The experimental set-up for the photoablation is schemed in Figure III-3. For the fabrication of the devices, an ArF UV excimer laser (Lambda Physics LPX 205i, Germany), featuring a wavelength of 193 nm and a 23 ns pulse duration, is used to photoablate 100 μm thick PET substrates (Melinex, Dupont, US; $E_{threshold}$= 40mJ/cm^2).[80] The pulse frequency ranges from 10 to 50Hz.

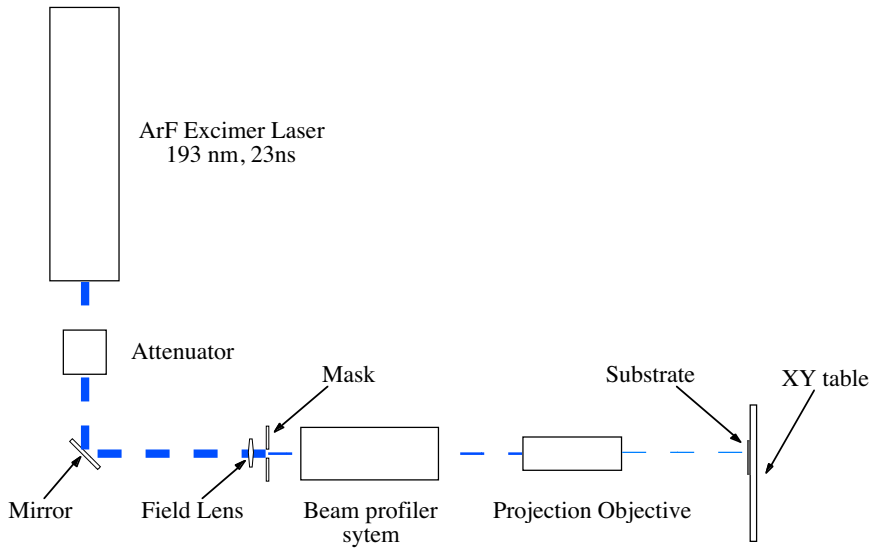

Figure III-3. *Experimental set-up for laser photoablation.*

The laser is activated with a constant output energy, allowing an invariable fluence and therefore a reproducible etching. The attenuator (Excitech, Oxford, UK) serves to work at lower energy values, which are out of range for the high voltage of laser electrodes. The field

lens is used to correct the beam divergence before the mask. The laser light passes through the beam profiler system, which helps to control the beam profile. The projection objective scales down the shaped beam by a factor of 10. For instance, a 1mm wide mask will generate a 100μm wide channel. The computer-controlled XY translation stages (Physik Instrumente, Germany) are used for a precise positioning of the substrate and its driving during the dynamic photoablation with respect to the laser beam. Before any ablation, the laser beam is focused on the exposed substrate surface.

3.2 Sealing of the structures.

In order to seal the microstructures, a 25/10μm Polyethylene/Polyethylene Terephthalate (PE/PET) composite sheet (Morane, Oxford, UK) is laminated with a standard lamination machine. The PE acts as the sealing agent due to its low melting temperature while the PET layer provides the strength of the sheet. The procedure is described in Figure III-4.

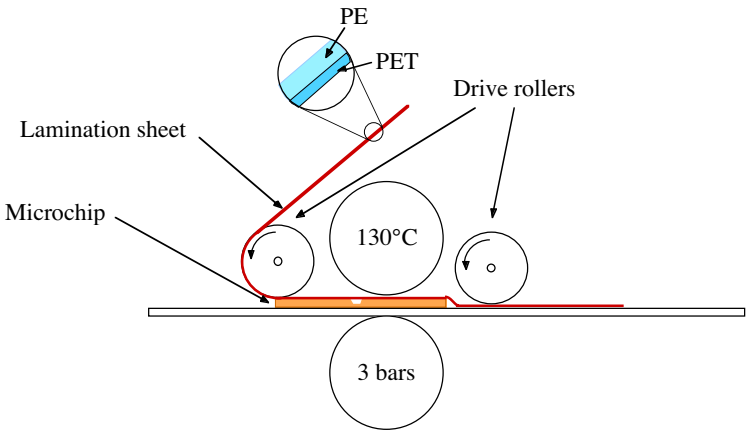

Figure III-4. *Scheme of the lamination procedure.*

The substrates are set out on a rigid support. The latter is driven by the rollers as well as the lamination sheet. By the simultaneous application of heat (130°C) and pressure (3 bars), the lamination sheet seals the microstructured substrates, and the heat exposure is less than 3s. It is

worth noticing that the microchannel is composed of different materials: PE on the top and photoablated PET at the bottom and the walls. The plasma-activated bonding has been demonstrated to be an attractive alternative to enhance the homogeneity of the structure.[79]

4. Fabrication of the nanospray interface

The objective is to get a thick-film microelectrode embedded in a microchannel, ending with a side-outlet. The complete fabrication procedure is shown in Figure III-5.

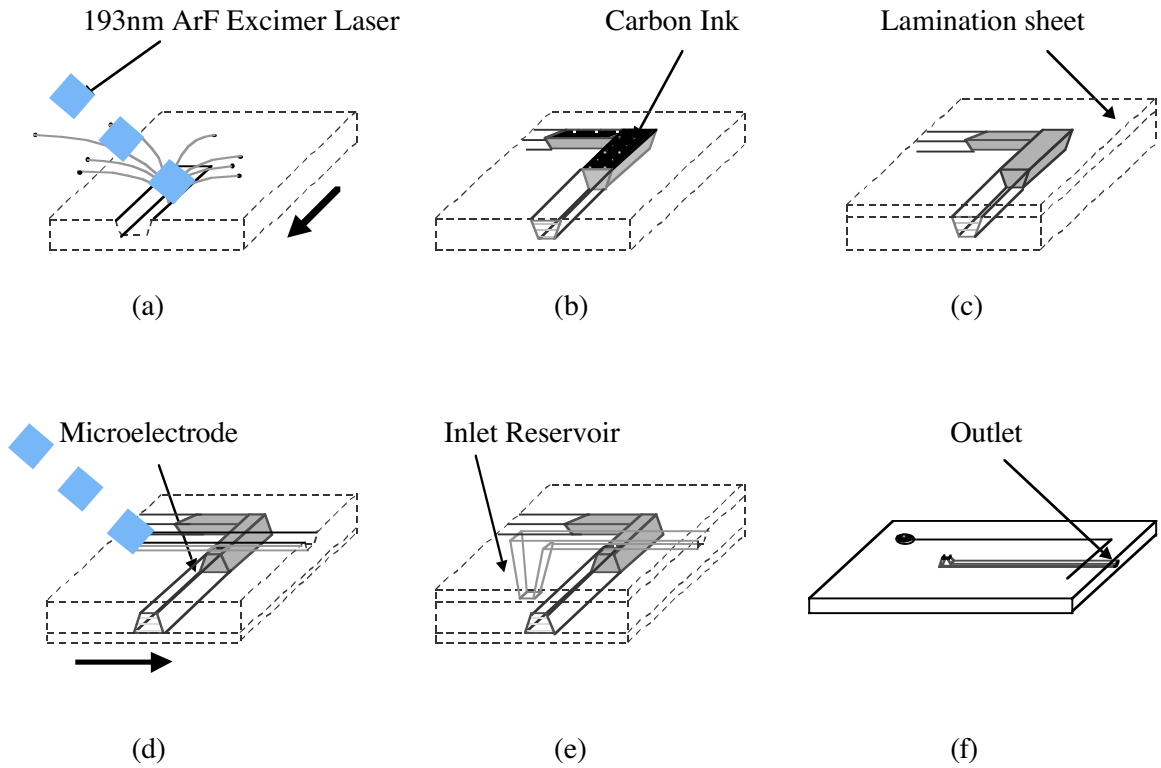

Figure III-5. *Fabrication scheme of the nanospray: [(a)] The substrate is dynamically photoablated using a rectangular mask. [(b)] It is filled with carbon ink, cured. 1 hour at 90°C. [(c)] The resulting track is sealed with a lamination sheet. [(d)] The feeding microchannel is drilled on the other side of the substrate, resulting in an embedded microelectrode. [(e)] The feeding microchannel is closed with a lamination sheet; [(f)] A photoablation is performed through all the substrate thickness, generating the nanospray outlet.*

The microelectrode is produced as previously described by Rossier et al.[64] A first microchannel is drilled on the PET substrate (200mJ, 50Hz) with a rectangular mask (1mm x 10mm by default). This channel is L-shaped, in order to have the connection of the high voltage far from the nanospray outlet. The first part is 1cm long, the second one 5cm. The microchannel is filled with carbon ink (Electrador, Electra Polymer & Chemicals Ltd., UK). It is cured during 1h at 90°C. To insure the mechanical stability and the insulation of this conductive track, the substrate is laminated, as described previously.

A second channel is drilled on the other side of the substrate, with reservoirs at both ends (mask: 0.4mm x 10mm by default). The depth is adapted in order to reach the bottom of the previous conductive channel. Thus, a microelectrode with controlled dimensions is generated at the bottom of the channel. The contact between the power supply and the generated microelectrode is obtained through the conductive track and pad. The latter is obtained after removal of a part of the lamination and the deposit of carbon ink, which is further cured.

Figure III-6 shows the generated microelectrode at the bottom of the main microchannel. Embedding the microelectrode avoids perturbations in solution flow contrary to the cases where a wire is placed in the capillary end.[31] Moreover, in this particular configuration, the electric field lines are forced through the solution, hence focusing the spray.

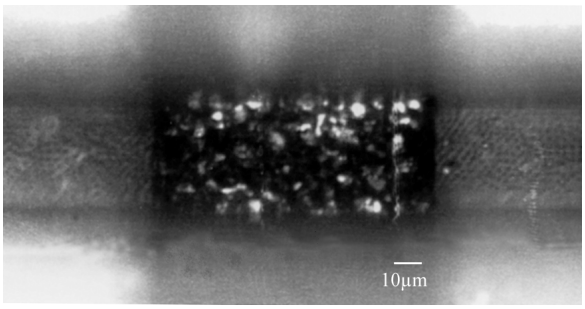

Figure III-6. *Microscope photograph of the microelectrode at the bottom of the feeding microchannel. One can distinguish the intersection between the conductive track and the main microchannel.*

The aspect of the microelectrode is observed by optical microcopy, since some irregularities of the microelectrode surface can be due to carbon ink pouring or due to laser power failure, resulting in an irregular drilling. After checking the electrode, the feeding channel is sealed by lamination. Finally, the chip edge is cut by photoablation, thereby producing the nanospray outlet as well as fixing the distance between the microelectrode and the open end. The photoablation process provides a precise positioning of the electrode with respect to the nanospray outlet.

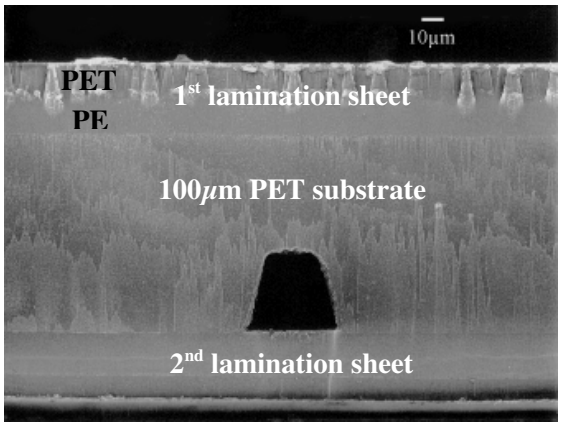

Figure III-7. *SEM picture of the nanospray outlet (Front view).*

Figure III-7 shows a SEM picture of a nanospray outlet after fabrication. The two lamination sheets are easily identified as well as the PET substrate where the feeding microchannel has been drilled. It is worth noticing the efficient sealing obtained with the lamination process. The appearance of the spray outlet is similar to the ones made in glass and presented by Ramsey et al.[42] The thickness of the substrate is less than 170 μm, which favors cone formation with a lower dead volume.

In the present nanospray, the feeding microchannel has a trapezoidal cross section, due to the photoablation process, with an average width of 35μm and 40μm deep. The distance between the microelectrode is here fixed at 2.5mm. The resulting microelectrode area is 30x85μm^2.

However, the dimensions can be varied from 200 to 8000μm^2 depending on photoablation parameters.

5. Experimental Set Up

All the experiments are carried out using the simple infusion configuration. A syringe pump is used to supply the desired flow rate to the nanospray interface.

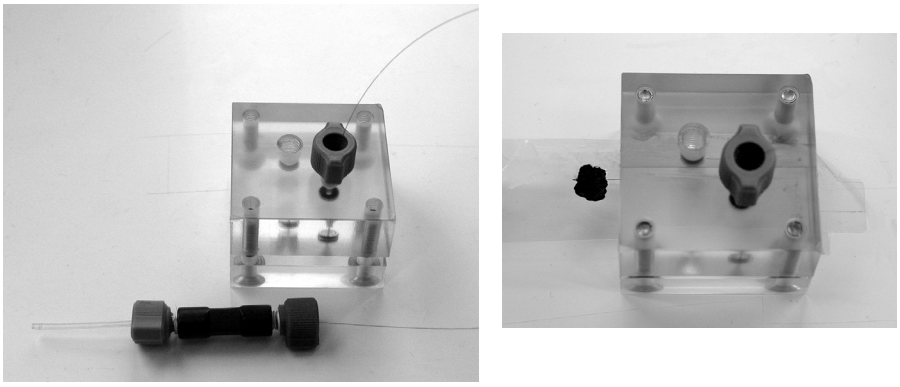

Figure III-8. *Plexiglas holder for pressure driven flow infusion in the nanospray interface and the nanospray positioned in the holder.*

The chip is inserted in a homemade Plexiglas holder to connect the infusion line to the nanospray interface, as illustrated in Figure III-8. The ESI interface of the LCQ DUO Ion Trap (Finnigan, San Jose, USA) is then removed, and the microchip holder is mounted on the probe slide adapter of the mass spectrometer without any other modification of the latter, as schemed in Figure III-9. The voltage supply of the MS is connected to the microelectrode via the carbon ink pad on the microchip using a simple crocodile clip. The applied voltage ranges from 2.5 to 8kV, resulting in a spray current about 100nA. The heated capillary of the MS is maintained at 200°C in order to enhance desolvation of cluster ions.

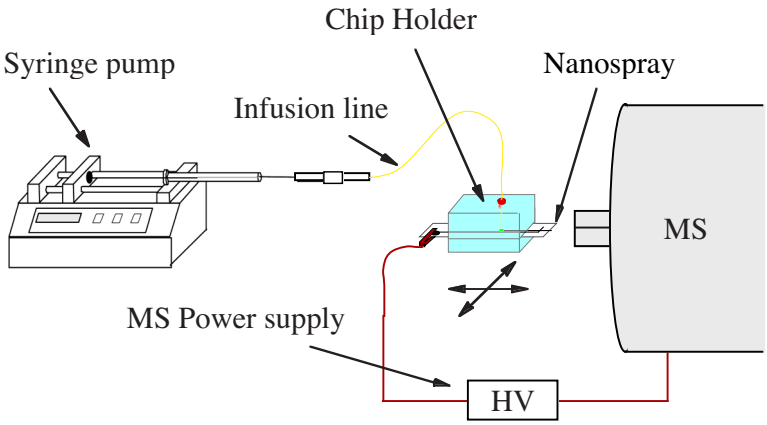

Figure III-9. *Schematic experimental set-up: the sample is introduced by simple infusion via a syringe pump. The high voltage is supplied by the LCQ Duo power supply.*

6. Nanospray in operation

Figure III-10 shows a top view of the Taylor cone obtained at the nanospray outlet. In a first approximation, the cone volume is calculated to be less than 1nl. The electrospray generation is observed to occur near to the microchannel aperture, but not at the outlet.

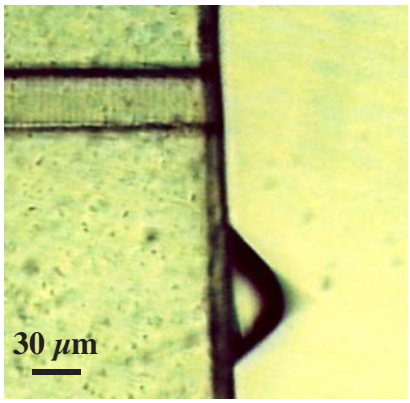

Figure III-10. *Microscope photograph of a Taylor Cone formed at the outlet of the nanospray (Top view).*

This position offset is attributed to a protruding tip on the substrate edge. The electric field is greatly increased due to the small dimensions of the tip, which acts as an “electric field

densifier". Referring to Figure III-7, the position of the cone could be determined by the rough patches observed. This cone position effect has been confirmed by Kameoka and co-workers.[81] They demonstrated the improvement of the Taylor cone confinement thanks to a thin polymer triangle tip adjusted at the outlet of the chip channel.

The hydrophobic character of the polymer body, improved by the photoablation process,[73] avoids the use of non durable derivatization which is commonly used on glass microchips to obtain a stable spray.[41] It helps to prevent solution spilling at the outlet of the chip as already mentioned. Further surface modifications, such as plasma treatment, have been shown to induce a durable enhancement of the hydrophobic nature of the polymeric substrates.[53, 82] In order to adapt it to a separation device, a main critical parameter is the cone volume, where a strong convection and mixing occur.[83] Actually, if the cone volume is too large, a well-resolved separation could be completely lost. The individual separated analytes should be sequentially spaced enough to avoid overlapping during mass analysis. Therefore, in this configuration, the injection plug size and the separation length must be adapted with this limitation.

7. Stability in ESI-MS

To demonstrate the efficiency of this interface, a solution of 5μM Myoglobin from Horse Heart (Sigma, St Louis, MO) in 50/49/1 (v/v) Methanol/Water/Acetic Acid has been infused continuously. The distance between the nanospray outlet and the MS entrance (0.5 to 2cm), the applied high voltage (2.5 to 8kV) and the flow rate (50 to 1000nl·min^{-1}) have been varied in order to obtain the best stability and the highest intensity of the base peak.

Figure III-11 shows the mass spectrum obtained in full scan mode. The charge state distribution of the protein ranges from +9 to +21, and the peak corresponding to the heme group (616.15 Da) is also observed. This is relevant from a complete denaturation of the

protein, mainly due to the large difference between the isolelectric point (PI) of the protein (9.51) and the quite acidic pH (2.8) of the solution. The deconvoluted mass is 16951.57 ± 0.94 Da (theoretical mass 16951.48 Da).

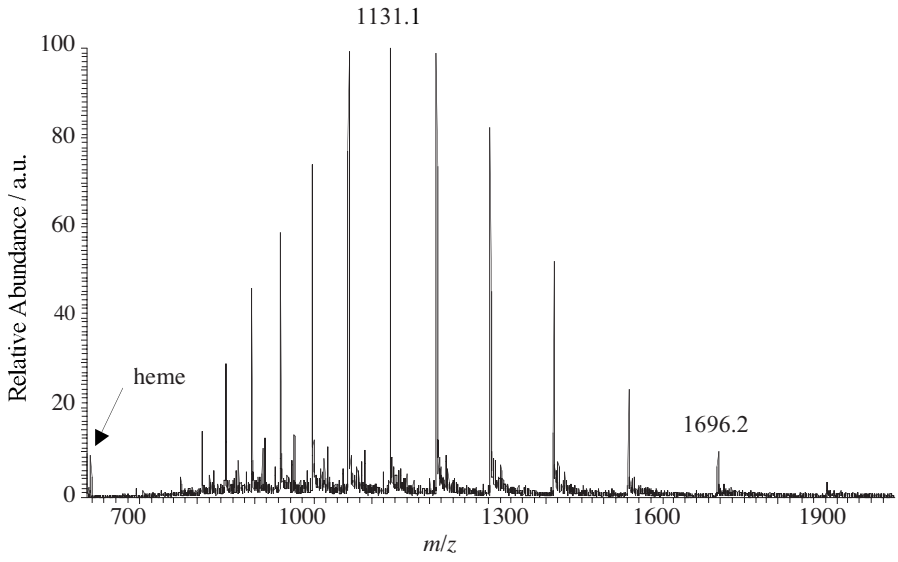

Figure III-11. *Full scan MS spectrum for 5µM Horse Heart Myoglobin infusion experiment (233 nl·min^{-1}).*

Figure III-12 illustrates the spray stability over 6 minutes by plotting the total ion current (TIC), the $[M+15H]^{+15}$ intensity, and the $[M+10H]^{+10}$ charge peak versus the acquisition time.

The Total Ion current (TIC) stays within the 95-100% full scale range, which indicates a highly stable spray process. Besides, the stability for the different peak intensities illustrates the ionization stability of the interface. It was verified that the nanospray operates for at least one hour without interruption. It can also be used several times, with different analytes, and no contamination was observed. It can be noticed that once the nanospray is on, no contamination peak due to the polymer is observed. However, if the spray current exceeds 200nA, corona discharges occur. The analyte signal is then less stable, and peaks coming from polymer decomposition can be observed.

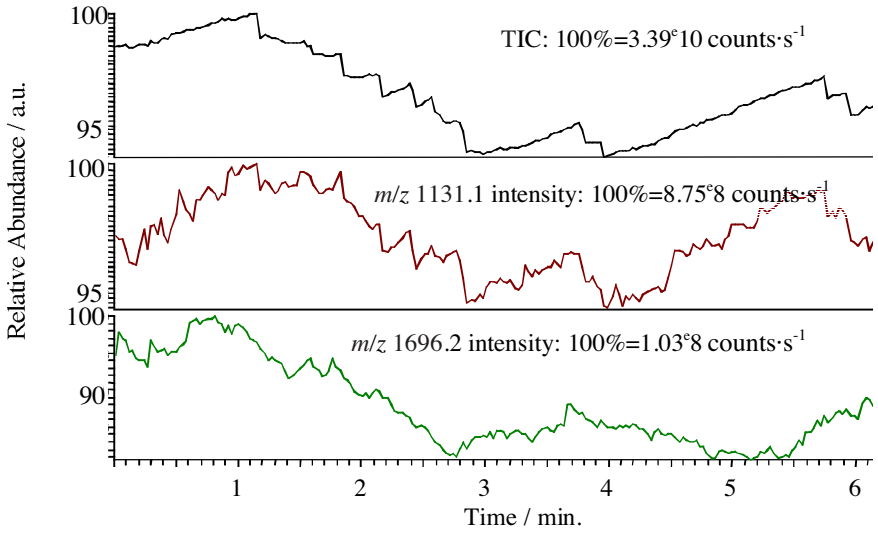

Figure III-12. *Evolution of the TIC, m/z 1131.1 peak intensity and m/z 1696.2 peak intensity over 6 minutes infusion of 5µM Horse Heart Myoglobin (233 nl·min^{-1}).*

8. Calibration of the nanospray

We also evaluated the detection limit of the device. To achieve this, solutions of different concentration of reserpine were infused. The reserpine stock solution was 1mg·ml^{-1} and fresh solutions were obtained by dilution to the desired concentrations, from 100μg·ml^{-1} to 1pg·ml^{-1} (1.64pM).

Once the nanospray was on and stable, the spectrum acquisition was done during 3 minutes. Figure III-13 shows that a good signal of the base peak $[M+H]^+$ is obtained in the full scan MS mode at the picomolar level, whilst peaks corresponding to reserpine molecular ion fragmentation are also detected. These fragment peaks can be also considered as a part of the signal due to the analyte. The same level of detection was obtained for neurotensin infusion with the microelectrospray interface developed by Andren and co-workers[11] and Lazar et al.[5] The very low field strengths used by Lazar and Andren (0.2kV·cm^{-1}) compared to our

conditions (4-8kV·cm^{-1}) could explain the fragmentation observed for low concentration infusion.

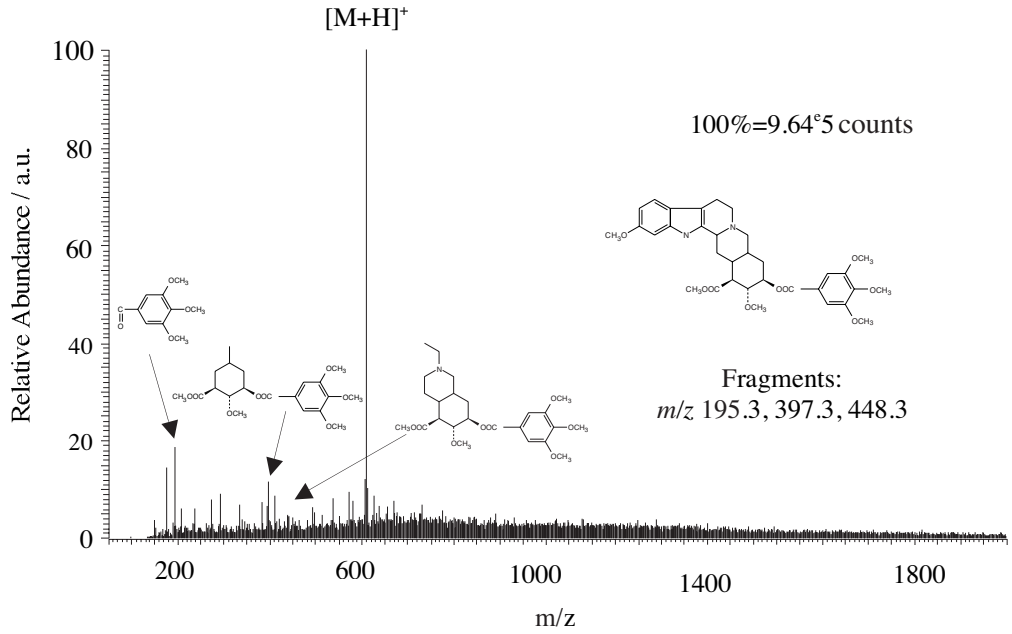

Figure III-13. *Full scan MS spectrum for 1 pg·ml^{-1} (1.64 pM) reserpine (average on 100 scans); simple infusion experiment at 200 nl·min^{-1}.*

Considering the experimental conditions and results, we are able to calculate the ion transmission ratio, i.e. the ratio between injected and detected ions. During the infusion of the 1pg·ml^{-1} solution at 200nl·min^{-1}, 3290 molecules are consumed per second by the nanospray interface. Considering a scan time of 1s, a 3x10^{5} gain value and the peak intensity (8.8x10^{5} counts), one calculate an ion transmission ratio of 9·10^{-4}, meaning that approximately 1 molecule for 1000 consumed has reached the detector. It should be pointed out that only 3.28·10^{-19}mol·min^{-1} of reserpine has been injected at that concentration, which means that sub-attomole detection has been obtained. The efficiency of the system can be attributed to the high electric field applied, inducing high electrophoretic separation close to the outlet but also to the small generated Taylor cone volume.

Results for all the concentrations tested are summarized in Figure III-15. The base peak intensity has been plotted versus concentration.

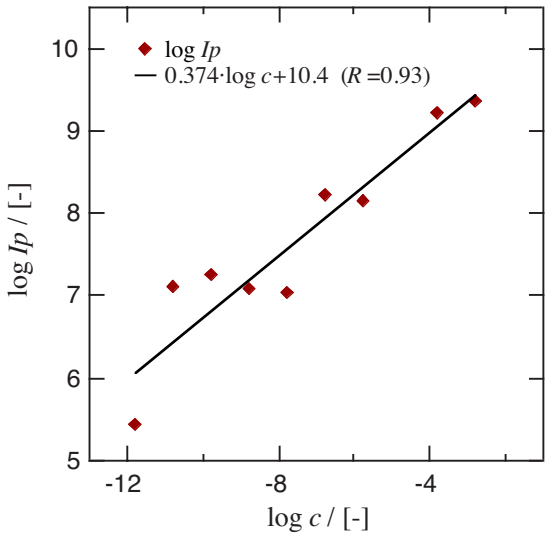

Figure III-15. *Logarithm of Base Peak Intensity versus logarithm of reserpine concentration.*

Enke and co-workers have shown that the ion response is highly dependent on flow rate and spray current i_{ES}.[84] These two parameters should be fixed at a given value for every experiment.[85] A linear trend could then be predicted for low analyte concentration compared to electrolyte. Considering the uncontrolled spray current and the varied flow rates applied, some discrepancies are observed between 10^{-5}M and 10^{-9}M. However, this model is not adapted to protonation processes and our experimental conditions, in terms of electric field, induce a non-equilibrium situation. This could explain the divergence of our calibration curve from a linear tendency.

It must be stressed here that several chips have been used and therefore an optimization procedure such as flow rate value, positioning, tuning of the MS had to be repeated for each experiment. Nonetheless, a dynamic range of 9 orders is obtained which indicates the high

integration potential of this interface. Furthermore, the injected concentration can be well evaluated.

9. New interface design

As noticed earlier, it could be useful to get a constant Taylor cone location, in the case of a multinozzle interface for instance. To obtain a precise positioning of the spray generation with respect to the mass spectrometer is also easier when its location is known before the onset. As demonstrated by Kameoka et al.,[81] the use of a pointing piece at the outlet of a microchannel is sufficient to focus the spray generation at the outlet. The configuration of integrated nozzle to a chip has been also already used by Kim and Knapp for a PDMS emitter,[48] as well as Wen et al.[52] Nonetheless, the last nozzle is multi-faced (6 sides), which could cause a misplacement of the Taylor cone, and the outer diameter is several hundreds of μm.

To get a pointing outlet, the nanospray chip has been cut in a V-shape, in order to get a nozzle, instead of a flat edge. As illustrated in Figure III-16, the Taylor cone should be therefore confined at the outlet due to the two pointing plastic pieces, resulting in a lower cone volume.

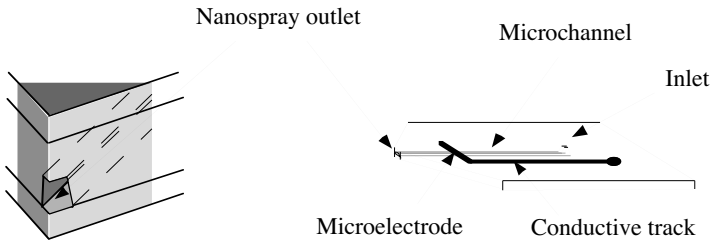

Figure III-16. *V-shaped nozzle (front view) and the new chip design.*

When working under stable conditions, no Taylor cone could be really observed with the optical microscope, due to its small dimensions but also due to its hidden location at the

nozzle. The V-shape nozzle is by far better to onset the electrospray compared to the flat edge interface. Besides, the readout of the spray current indicates a more stable electrospray process.

Under EOF pumping, the sharp design gives a stable signal and can work without any interruption, if evaporation from the reservoir is prevented. Under the same conditions, no stable spray could be established with the flat interface. The self-regulation of the nanospray interfaces can explain this failure. With the confinement of the droplet between the two pointing parts of the outlet in the V-shaped device, the spreading of the solution on the edge or the two faces is avoided. Therefore, the spray generation and the EOF can regulate each other. With the flat interface, a first auto-regulation occurs, i.e. the positioning of the Taylor cone and the subsequent spray generation at a favorable location. However, this step needs a constant flow rate at the outlet, such as a forced pressure flow. Unless the Taylor cone is stable in position, a spray is not generated. Therefore, the EOF pumping can be used only if two electrodes are located at both ends of the microchannel to apply a difference of potential, and therefore generate the EOF pumping. A decoupled electrode should be then used to spray. Another possibility is to use a thicker substrate to reduce the possibilities of the Taylor cone positioning by the confinement on the edge, such as Ramsey' group chip.[42]

This interface has also been evaluated for protein analysis. Therefore, an infusion of 5μM Myoglobin solution has been performed. Besides the enhanced stability of this interface, it is important to notice that the TIC is $9.47e^8$ counts (RSD=2.38%). When compared to the above results, the signal obtained with the flat edged interface is 35 times higher. This amplification effect could be related to the current line distribution, which is directly related to the design of the interface itself. As illustrated in Figure III-17, the tip design favors an uneven intensity of the current lines exiting from the Taylor cone, particularly from the rim of the outlet.

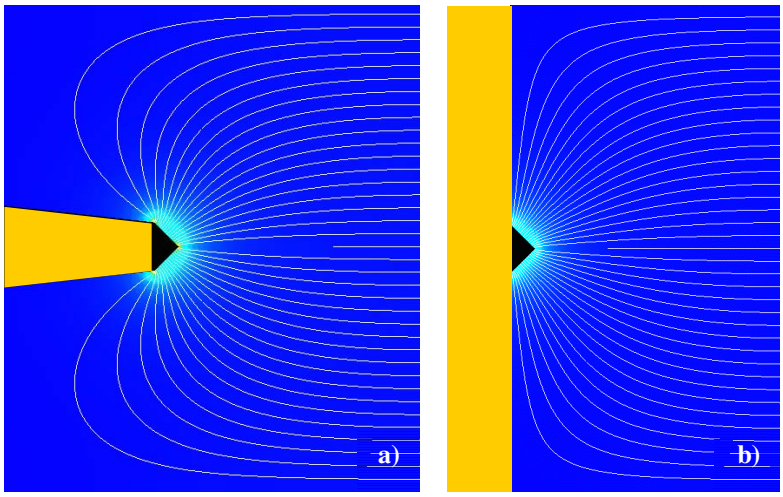

Figure III-17. *Current lines from a nanospray interface a) with tip shape; b) with a flat edge (in black the generated Taylor cone, in gray the insulating part). An non-dimensional potential* $\varphi = 1$ *is applied on the cone surface, and the counter electrode (*$\varphi = 0$*) is located on the right side (finite element simulation based on the Laplace equation with Flux-Expert* [86]*).*

In addition, some of these lines are found to be directed backwards. The combination of these two effects of the insulating part location could lead to a lower transmission of the tip-like interface. Indeed, it has been found that a multijet electrospray could be generated directly from the rim in the case of a capillary outlet, as illustrated in Figure III-18. Therefore, the droplets generated are ejected sidewise and even backwards, thus a major part of the offspring ions will not be sampled by the MS, and thus not detected. When dealing with the flat interface, there is no possibility to generate multijet due to the hindering of the insulating parts. Therefore, all the droplets and the further-generated gas-phase ions are more focused toward the MS entrance.

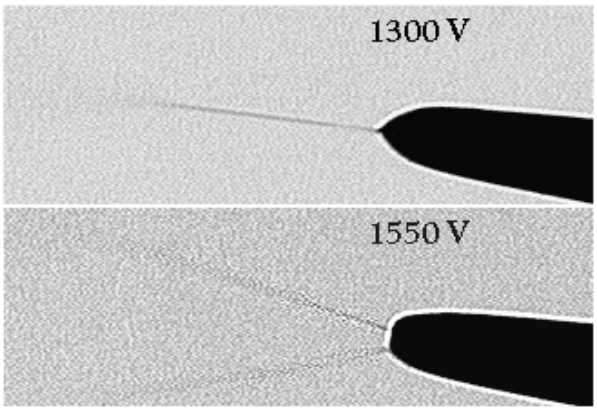

Figure III-18. *From cone-jet to multijet mode at a PicoTip™ spraying 5% Acetic acid in 30% MeOH at 200 nl/min by direct infusion from a syringe pump. The tip-to-inlet distance is approximately 5 mm (Reprinted from New Objective, Inc. web site).*

10. Conclusion

In this chapter, a novel nanospray microchip has been presented. The design is easily obtained thanks to the flexibility of the photoablation process. The interface presented here provides a highly stable and durable spray ionization, the embedded location of the microelectrode preventing flow perturbations. The detection limit with this device has been found to be at the picomolar level. A dynamic range of 9 orders of magnitude was also described. This low level of detection could be in part due to the design of the chip, as preliminary results have shown.

Taking advantage of the hydrophobic nature of PET substrates, multichannels could be drilled on a same chip to perform automated MS analyses. If the V-shaped nozzle design is used, no further surface modification of the nanospray outlet is necessary to prevent sample-to-sample cross contamination due to solution spilling, since the spray generation is confined at the nozzles.

With the presented fabrication process, several microelectrodes, including pseudo-reference electrodes, and decouplers can be added to the microchip, thereby allowing the decoupling and

the control of the different applied potentials.[87] The present interface can be integrated into a microdevice for LC or CE analysis, and a capillary for prior separation step can also be easily connected. Besides, electroosmotic flow and CE systems in photoablated PET have been previously reported,[63, 64] meaning that all the conditions are fulfilled to develop an efficient CE-nanospray chip in future works. Following the work described here, commercial chips based on the same approach are now mass-produced, and have been found to be convenient interfaces with different mass spectrometers.[56, 88, 89]

11. References

(1) Figeys, D.; Gygim, S. P.; McKinnon, G.; Aebersold, R. *Anal. Chem.* **1998,** *70*, 3728-3734.

(2) Li, J. J.; Kelly, J. F.; Chemushevich, I.; Harrison, D. J.; Thibault, P. *Anal. Chem.* **2000,** *72*, 599-609.

(3) Licklider, L.; Wang, X. Q.; Desai, A.; Tai, Y. C.; Lee, T. D. *Anal. Chem.* **2000,** *72*, 367-375.

(4) Bings, N. H.; Wang, C.; Skinner, C. D.; Colyer, C. L.; Thibault, P.; Harrison, D. J. *Anal. Chem.* **1999,** *71*, 3292-3296.

(5) Lazar, I. M.; Ramsey, R. S.; Sundberg, S.; Ramsey, J. M. *Anal. Chem.* **1999,** *71*, 3627-3631.

(6) Figeys, D.; Ning, Y. B.; Aebersold, R. *Anal. Chem.* **1997,** *69*, 3153-3160.

(7) Zhang, B.; Liu, H.; Karger, B. L.; Foret, F. *Anal. Chem.* **1999,** *71*, 3258-3264.

(8) Chan, J. H.; Timperman, A. T.; Aebersold, R. *Anal. Chem.* **1999,** *71*, 4437-4444.

(9) Li, J. J.; Thibault, P.; Bings, N. H.; Skinner, C. D.; Wang, C.; Colyer, C.; Harrison, J. *Anal. Chem.* **1999,** *71*, 3036-3045.

(10) Wahl, J. H.; Goodlett, D. R.; Udseth, H. R.; Smith, R. D. *Electrophoresis* **1993,** *14*, 448-457.

(11) Andren, P. E.; Emmett, M. R.; Caprioli, R. M. *J. Am. Soc. Mass Spectrom.* **1994,** *5*, 867-869.

(12) Juraschek, R.; Dülcks, T.; Karas, M. *J. Am. Soc. Mass Spectrom.* **1999,** *10*, 300-308.

(13) Karas, M.; Bahr, U.; Dulcks, T. *Fresenius Journal of Analytical Chemistry* **2000,** *366*, 669-676.

(14) Wilm, M.; Mann, M. *Anal. Chem.* **1996,** *68*, 1-8.

(15) Fligge, T. A.; Bruns, K.; Przybylski, M. *J. Chromatogr. B* **1998,** *706*, 91-100.

(16) Schmidt, A.; Karas, M.; Dülcks, T. *J. Am. Soc. Mass Spectrom.* **2003,** *14*, 492-500.

(17) Gale, D. C.; Smith, R. D. *Rapid Comm. Mass Spectrom.* **1993,** *7*, 1017-1021.

(18) Valaskovic, G. A.; Kelleher, N. L.; Little, D. P.; Aaserud, D. J.; Mclafferty, F. W. *Anal. Chem.* **1995,** *67*, 3802-3805.

(19) Korner, R.; Wilm, M.; Morand, K.; Schubert, M.; Mann, M. *J. Am. Soc. Mass Spectrom.* **1996,** *7*, 150-156.

(20) Bahr, U.; Pfenninger, A.; Karas, M.; Stahl, B. *Anal. Chem.* **1997,** *69*, 4530-4535.

(21) Valaskovic, G. A.; Mclafferty, F. W. *J. Am. Soc. Mass Spectrom.* **1996,** *7*, 1270-1272.

(22) Barroso, M. B.; de Jong, A. P. *J. Am. Soc. Mass Spectrom.* **1999,** *10*, 1271-1278.

(23) Kelly, J. F.; Ramaley, L.; Thibault, P. *Anal. Chem.* **1997,** *69*, 51-60.

(24) Li, J. J.; Wang, C.; Kelly, J. F.; Harrison, D. J.; Thibault, P. *Electrophoresis* **2000,** *21*, 198-210.

(25) Barnidge, D. R.; Nilsson, S.; Markides, K. E. *Anal. Chem.* **1999,** *71*, 4115-4118.

(26) Bendahl, L.; Hansen, S. H.; Olsen, J. V. *Rapid Comm. Mass Spectrom.* **2002,** *16*, 2333-2340.

(27) Zhu, X. F.; Thiam, S.; Valle, B. C.; Warner, I. M. *Anal. Chem.* **2002,** *74*, 5405-5409.

(28) Wetterhall, M.; Nilsson, S.; Markides, K. E.; Bergquist, J. *Anal. Chem.* **2002,** *74*, 239-245.

(29) Nilsson, S.; Wetterhall, M.; Bergquist, J.; Nyholm, L.; Markides, K. E. *Rapid Comm. Mass Spectrom.* **2001,** *15*, 1997-2000.

(30) Mazereeuw, M.; Hofte, A. J. P.; Tjaden, U. R.; vanderGreef, J. *Rapid Comm. Mass Spectrom.* **1997,** *11*, 981-986.

(31) Cao, P.; Moini, M. *J. Am. Soc. Mass Spectrom.* **1997,** *8*, 561-564.

(32) Fong, K. W. Y.; Chan, T. W. D. *J. Am. Soc. Mass Spectrom.* **1999,** *10*, 72-75.

(33) Smith, A. D.; Moini, M. *Anal. Chem.* **2001,** *73*, 240-246.

(34) Jussila, M.; Sinervo, K.; Porras, S. P.; Riekkola, M. L. *Electrophoresis* **2000,** *21*, 3311-3317.

(35) Hsieh, F.; Baronas, E.; Muir, C.; Martin, S. A. *Rapid Comm. Mass Spectrom.* **1999,** *13*, 67-72.

(36) Schultz, G. A.; Corso, T. N.; Prosser, S. J.; Zhang, S. *Anal. Chem.* **2000,** *72*, 4058-4063.

(37) Griss, P.; Melin, J.; Sjodahl, J.; Roeraade, J.; Stemme, G. *J. Micromech. Microeng.* **2002,** *12*, 682-687.

(38) Ishihama, Y.; Katayama, H.; Asakawa, N.; Oda, Y. *Rapid Comm. Mass Spectrom.* **2002,** *16*, 913-918.

(39) Guzzetta, A. W.; Thakur, R. A.; Mylchreest, I. C. *Rapid Comm. Mass Spectrom.* **2002,** *16*, 2067-2072.

(40) Schultz, G. A.; Corso, T. N.; Prosser, S. J. *49th ASMS conference on Mass Spectrometry and Allied Topics*, Chicago, Illinois 2001.

(41) Xue, Q. F.; Foret, F.; Dunayevskiy, Y. M.; Zavracky, P. M.; McGruer, N. E.; Karger, B. L. *Anal. Chem.* **1997,** *69*, 426-430.

(42) Ramsey, R. S.; Ramsey, J. M. *Anal. Chem.* **1997,** *69*, 1174-1178.

(43) Lazar, I. M.; Lee, M. L. *J. Am. Soc. Mass Spectrom.* **1999,** *10*, 261-264.

(44) Chen, S. H.; Sung, W. C.; Lee, G. B.; Lin, Z. Y.; Chen, P. W.; Liao, P. C. *Electrophoresis* **2001,** *22*, 3972-3977.

(45) Vrouwe, E. X.; Gysler, J.; Tjaden, U. R.; van der Greef, J. *Rapid Comm. Mass Spectrom.* **2000,** *14*, 1682-1688.

(46) Zhang, B. L.; Foret, F.; Karger, B. L. *Anal. Chem.* **2000,** *72*, 1015-1022.

(47) Deng, Y.; Henion, J.; Li, J.; Thibault, P.; Wang, C.; Harrison, D. J. *Anal. Chem.* **2001,** *73*, 639-646.

(48) Kim, J. S.; Knapp, D. R. *J. Chromatogr. A* **2001,** *924*, 137-145.

(49) Meng, Z. J.; Qi, S. Z.; Soper, S. A.; Limbach, P. A. *Anal. Chem.* **2001,** *73*, 1286-1291.

(50) Kameoka, J.; Craighead, H. G.; Zhang, H.; Henion, J. *Anal. Chem.* **2001,** *73*, 1935-1941.

(51) Yuan, C.-H.; Shiea, J. *Anal. Chem.* **2001,** *73*, 1080-1083.

(52) Wen, J.; Lin, Y. H.; Xiang, F.; Matson, D. W.; Udseth, H. R.; Smith, R. D. *Electrophoresis* **2000,** *21*, 191-197.

(53) Tang, K.; Lin, Y.; Matson, D. W.; Kim, T.; Smith, R. D. *Anal. Chem.* **2001,** *73*, 1658-1663.

(54) Xiang, F.; Lin, Y. H.; Wen, J.; Matson, D. W.; Smith, R. D. *Anal. Chem.* **1999,** *71*, 1485-1490.

(55) Xu, N. X.; Lin, Y. H.; Hofstadler, S. A.; Matson, D.; Call, C. J.; Smith, R. D. *Anal. Chem.* **1998,** *70*, 3553-3556.

(56) Gobry, V.; van Oostrum, J.; Martinelli, M.; Rohner, T. C.; Reymond, F.; Rossier, J. S.; Girault, H. H. *Proteomics* **2002,** *2*, 405-412.

(57) Rossier, J. S.; Vollet, C.; Carnal, A.; Lagger, G.; Gobry, V.; Girault, H. H.; Michel, P.; Reymond, F. *Lab Chip* **2002,** *2*, 145-150.

(58) Kim, J. S.; Knapp, D. R. *Electrophoresis* **2001,** *22*, 3993-3999.

(59) Liu, H.; Felten, C.; Xue, Q.; Zhang, B.; Jedrzejewski, P.; Karger, B. L.; Foret, F. *Anal. Chem.* **2000,** *72*, 3303-3310.

(60) Jiang, Y.; Wang, P. C.; Locascio, L. E.; Lee, C. S. *Anal. Chem.* **2001,** *73*, 2048-2053.

(61) Gao, J.; Xu, J. D.; Locascio, L. E.; Lee, C. S. *Anal. Chem.* **2001,** *73*, 2648-2655.

(62) Chiou, C. H.; Lee, G. B.; Hsu, H. T.; Chen, P. W.; Liao, P. C. *Sens. Actuator B-Chem.* **2002,** *86*, 280-286.

(63) Roberts, M. A.; Rossier, J. S.; Bercier, P.; Girault, H. *Anal. Chem.* **1997,** *69*, 2035-2042.

(64) Rossier, J. S.; Roberts, M. A.; Ferrigno, R.; Girault, H. H. *Anal. Chem.* **1999,** *71*, 4294-4299.

(65) Srinivasan, R. *Polymer* **1982,** *23*, 1863-1864.

(66) Srinivasan, R.; Leigh, W. J. *J. Am. Chem. Soc.* **1982,** *104*, 6784-6785.

(67) Lazare, S.; Lopez, J.; Weisbuch, F. *Appl. Phys. A* **1999,** *69*, S1-S6.

(68) Petit, S.; Laurens, P.; Amouroux, J.; Arefi-Khonsari, F. *Appl. Surf. Sci.* **2000,** *168*, 300-303.

(69) Srinivasan, R.; Lazare, S. *Polymer* **1985,** *26*, 1297-1300.

(70) Srinivasan, R.; Braren, B.; Dreyfus, R. W. *J. Appl. Phys.* **1987,** *61*, 372-376.

(71) Taylor, R. S.; Leopold, K. E.; Singleton, D. L.; Paraskevopoulos, G.; Irwin, R. S. *J. Appl. Phys.* **1988,** *64*, 2815-2818.

(72) Srinivasan, R.; Braren, B. *Chem. Rev.* **1989,** *89*, 1303-1316.

(73) Rossier, J. S.; Bercier, P.; Schwarz, A.; Loridant, S.; Girault, H. H. *Langmuir* **1999,** *15*, 5173-5178.

(74) Lippert, T.; Nakamura, T.; Niino, H.; Yabe, A. *Appl. Surf. Sci.* **1997,** *110*, 227-231.

(75) Watanabe, H.; Tanaka, T.; Tsuge, M. *Polymer international* **1993,** *31*, 247-254.

(76) Lazare, S.; Hoh, P. D.; Baker, J. M.; Srinivasan, R. *J. Am. Chem. Soc.* **1984,** *106*, 4288-4290.

(77) Watanabe, H.; Yamamoto, M. *J. Appl. Polym. Sci.* **1997,** *64*, 1203-1209.

(78) Bianchi, F.; Chevolot, Y.; Mathieu, H. J.; Girault, H. H. *Anal. Chem.* **2001,** *73*, 3845-3853.

(79) Wu, Z. Y.; Xanthopoulos, N.; Reymond, F.; Rossier, J. S.; Girault, H. H. *Electrophoresis* **2002,** *23*, 782-790.

(80) Lazare, S.; Srinivasan, R. *J. Phys. Chem.* **1986,** *90*, 2124-2130.

(81) Kameoka, J.; Orth, R.; Ilic, B.; Czaplewski, D.; Wachs, T.; Craighead, H. G. *Anal. Chem.* **2002,** *74*, 5897-5901.

(82) Sigurdsson, S.; Shishoo, R. *J. Appl. Polym. Sci.* **1997,** *66*, 1591-1601.

(83) Hayati, I.; Bailey, A. I.; Tadros, T. F. *Nature* **1986,** *319*, 41-43.

(84) Enke, C. G. *Anal. Chem.* **1997,** *69*, 4885-4893.

(85) Constantopoulos, T. L.; Jackson, G. S.; Enke, C. G. *Anal. Chim. Acta* **2000,** *406*, 37-52.

(86) Simulog; (www.simulog.fr) 35 Chemin du Vieux Chene 38240 Meylan Zirst - France; anne-marie.bernier@simulog.fr.

(87) Rossier, J. S.; Ferrigno, R.; Girault, H. H. *J. Electroanal. Chem.* **2000,** *492*, 15-22.

(88) Lion, N.; Gobry, V.; Jensen, H.; Rossier, J. S.; Girault, H. H. *Electrophoresis* **2002,** *23*, 3583-3588.

(89) Rossier, J. S.; Youhnovski, N.; Lion, N.; Damoc, E.; Reymond, F.; Girault, H. H.; Przybylski, M. *Angewandte Chemie-International Edition in English* **2003,** *42*, 53-58.

Chapter IV : On-line electrochemically induced tagging of free cysteines

1. Electrolytic behavior of the electrospray

A phenomenon that has to be considered in order to fully understand electrospray ionization is its electrolytic nature. This ionization source can indeed be seen as a special kind of electrolysis cell, where the anode is the emitter and the counter electrode, the cathode (reversed polarity in negative mode). The conduction through this cell is supported by the motion of the ions in the solution and then in the gas phase before reaching the counter electrode. In this electrolytic flow cell, the limiting step is the droplet ejection, and so the electrospray current i_{ES}. From an electrochemical standpoint, the ESI source can be considered as a controlled-current electrolytic cell. The charged droplet formation process is in this case the limiting step.

Due to this configuration, the faradaic current will be kept equal to the spray current by the oxidation of different species. Thermodynamically speaking, those with the lowest oxidation potential will be first oxidized, then if the current level is not sufficient after they are all consumed, the compounds with a higher oxidation potential will undergo oxidation, in order to balance the charges.

1.1 Faraday and spray current

Due to the electrospray process, ions are continuously expulsed, consisting of a net excess of cations (in positive mode). To keep the electroneutrality of the solution in the capillary, charge

compensation must take place. Thus, a net current is generated at the electrode/solution interface, where the high voltage is applied, as the excess charge continuously leaves the solution phase. In positive mode, a net anodic current is generated, leading to oxidation of electroactive species. The electrochemical reaction can be directly related to the Faraday current i_F, featuring the electron flow that leaves the ESI electrode. Considering the "cell" configuration, the relation between i_F and i_{ES} (see equation 41) is straightforward.

$$i_F = i_{ES} \qquad (41)$$

The faradaic current, at the diffusionnal limit, is given by the following equation:

$$i_F = F\Sigma n_i c_i m_i \qquad (42)$$

where n_i and m_i are respectively the number of electrons involved in the electrochemical reactions and the mass transfer coefficient of one reduced species i, and F is the Faraday constant (96'485 C·mol^{-1}). Considering the specific case of an electrospray interface, the solution flows parallel to the electrode. The latter can be either tubular in the case of a metallic needle emitter, or a ring electrode, such as the gold-sputtered nanospray tip, or even, as in the present case, a microband integrated in a channel flow cell. Therefore, the hydrodynamic regime is identical, regardless of the considered source. This feature imposes a dependence on $v_f^{1/3}$ for the limiting current, where v_f is the flow rate. The Levich relation for a channel flow cell is given by the following relation:

$$i_F = 0.925Fw\left(\frac{v_f}{h^2 d}\right)^{1/3} \sum_i n_i c_i \left(x_e D_i\right)^{2/3} \qquad (43)$$

where x_e is the electrode length, w its width, $2h$ and d are the height and the width of the channel, c_i and D_i are respectively the concentration and the diffusion coefficient of the reactant i. The last two equations highlight the concentration sensitivity of the electrospray.

The electrochemical behavior of ESI and the equivalence of the two currents (see equation 43) have been well proved by Blades et al.[2] by using a Zn capillary tip for the electrospray. By this mean, they showed that Zn^{2+} could be detected in the sprayed solution. The supplied amount of Zn^{2+} was found to be equal to the theoretical amount generated electrochemically, based on the i_{ES} measurement and calibration with known Zn^{2+} concentration solutions.

1.2 Electrochemical ionization

The ESI-MS analyses have been first limited to the analytes that are ionic in solution due to an ionic functionality or to protonation sites, such as in the proteins. Recently, the spectrum of analytes has been enlarged to non-ionic species. Due to electrochemical reactions occurring in the ESI probe, neutral electroactive analytes can converted into an ionized form. The most likely compounds, which can undergo electrochemical oxidation, have relatively low oxidation potential and structural characteristics that stabilize the formed cation. Conversely, for an efficient electrochemical ionization via reduction, the species should have a low reduction potential and form stable anions.

The evidence of the analyte oxidation has been first reported by Van Berkel's group.[3] Molecular radical cations of some divalent porphyrins were observed. However, the chemical oxidation could not be ruled out. The likely gas-phase processes and chemical oxidations were checked to be uninvolved in the detection of the ESI induced radical cations.[4] Van Berkel et al. confirmed also the dependence of the spray current on the conductivity (see equation 2 in Chapter II) by UV/visible spectra and MS.[5] By increasing κ, the amount of oxidized porphyrins has been shown to increase.

The on-line oxidation has also been observed for a series of metallocenes.[6] It was also demonstrated that the minimum voltage applied necessary to observed the radical cations increased linearly with the redox potential of the tested metallocenes. This trend established

experimentally the controlled-current electrochemical behavior, as well as the reliance of the spray current with the applied electric field, unraveled by Pfeifer and Hendricks, also later confirmed by Van Berkel et al.[7] and Bateman.[8]

The observation of dications from neutral porphyrins has first been reported by Van Berkel et al.[9] Due to the controlled-current behavior, it is worth noticing that, in order to get the second oxidation step occurrence, the neutral form has to be entirely consumed, if the latter have a lower oxidation potential than monocations.

Lastly, the analytes can be modified to exhibit an electrochemical activity. Taking advantage of the low redox potentials and the stability of the formed cation, ferrocene-based derivatives have been used to enhance the MS analysis of simple alcohols, sterols and phenols.[10]

For an efficient neutral analyte ionization and sensitive gas-phase detection, i.e. with minimized signal suppression, several requirements have to be fulfilled. The spray current must be sufficient for the oxidation of the molar equivalent of all the electroactive species available in the solution that are as easily or more easily oxidized than the target molecule, including the electrode material. This first prerequisite can be satisfied by the addition of a supporting electrolyte, which increases the conductivity of the sprayed solution, and thus the spray current. Consequently, the increased faradaic current i_F forces the oxidation reactions on the electrode. Secondly, the analyte must be available for reaction at the metal/solution interface, what is easily fulfilled by low flow rates associated to large electrochemically inert electrodes.[11] However, the above requirements must not inhibit the formation of gas-phase ions from the ions generated electrochemically.

Conversely, the analyte oxidation can be prevented by different means. First, the spray electrode can induce a redox buffering. Depending on the oxidation potential of the electrode material with respect to the analytes, the oxidation of the latter can be entirely prevented. Copper or stainless steel spray needles have been used to prevent oxidation,[12] but can also

produce chemical noise for the subsequent MS analyses, such as metal complexes of the analytes.[13] Another strategy consists in avoiding contact of the high voltage electrode with the analyte by means of membranes,[12, 14, 15] or emitter specific designs.[11]

Lastly, the definition of i_F (see equation 43) to be considered in its complete form, that is the sum of the anodic and cathodic currents. As oxidation is only required to be the dominant process on the electrode in positive mode, it has been pointed out that electrode reductions could indeed occur in the positive mode.[16]

1.3 Analytical implications

As a summary of the discussion above, it can be stated that the electrochemical reactions occuring during the electrospray process induce some changes in the solution composition. Particularly, the oxidation of water

$$2H_2O \rightarrow O_2 + 4H^+ + 4e^- \quad (E^0 = 1{,}299\text{V vs SHE}) \qquad (44)$$

induces the generation of protons, which means a decrease in pH and also an O_2 production. This pH change has been well described by Van Berkel et al.[17] It was demonstrated that this shift could attain 4 pH units decrease in an non-buffered system. This trend is highly dependent on the flow rate and i_{ES}. Typically, this electrochemically induced pH changes can cause protein unfolding.[18]

The other consequence of the oxidation of water is the production of oxygen gas. The bubble formation causes an unstable electrospray. The produced oxygen has been found to react with methionine, tryptophan, tyrosine,[19] and even leucine,[8] resulting in a +16Da modification observed by MS. This modification has been confirmed using ^{18}O labeled water, inducing a +18Da mass shift, which was inhibited by the addition of a reducing agent in the solution. Moini et al. proposed to replace this redox reaction by the oxidation of p-hydroquinone.[20]

$$H_2Q \rightarrow BQ + 2H^+ + 2e^- \quad (E^0 = 0{,}699V \text{ vs SHE}) \qquad (45)$$

This reaction leads also to the generation of protons and p-benzoquinone, and it will replace the water oxidation because of its standard potential. In addition, p-hydroquinone is a neutral species, therefore even a highly concentration will not disturb the ionization efficiency of the analytes. In terms of spray stability, Hydroquinone addition was shown to be more effective in the case of a platinum electrode.

2. Protein modification: what for?

As previously described, protein identification and quantitative analysis are performed with either 2D gel electrophoresis followed by peptide mass fingerprinting, or more recently, Isotope-coded-affinity tag (ICAT™) coupled with liquid chromatography and tandem mass spectrometry.[21] Cysteine plays an important role in both of these techniques. In the first method, the cysteine-containing proteins show a tendency to undergo reactions with either gel compounds or other cysteines. These modifications have been shown to significantly decrease the confidence of protein identification and the accuracy of quantitative analysis.[22] In the case of the ICAT™ technique, cysteinyl residues are the targets of the tagging method. The choice of this specific amino acid residue has two main advantages, apart from its well-developed alkylation chemistry: 80% of the proteins contain at least one cysteine, and yet only 10% of the peptides in the tryptic peptide mixture include this residue. As demonstrated by Sechi and Chait, if the cysteine content of a protein is known, the protein identification is tremendously improved by reducing the number of likely matching proteins.[23] Thus, following the affinity step of the ICAT protocol (see figure I-2), a large number of proteins can be quantified despite the low amount of retained peptides.

Lastly, as cysteine is intrinsically the strongest nucleophile among all amino acids, it is also involved in several important biochemical reactions. Indeed, the free sulphydryl moieties of

cysteine or even cystine-cysteine exchange reactions are important features in enzyme catalysis and in binding of metal ions to proteins.[24]

As discussed above, information on cysteine content at any stage of protein identification or quantification is of utmost importance for both of the currently important proteomics techniques. In this perspective, the development of a specific cysteine tagging method has been investigated, using MS detection coupled to electrospray ionization (ESI). Taking advantage of its electrochemical behavior previously described, an electroactive species could be chosen here so as to obtain a cysteine-specific adduct formation, immediately prior to MS analysis. The advantage of an electrochemical generation of the tag is that the occurrence and the location of the reaction can be chosen. At a post column stage and prior to MS detection, the native protein and the modified one would have the same retention time. This is not the case if the adduct formation occurs before the separation. Therefore, the identification of a biological mixture as well as the cysteine content of every analyte could be performed.

Quinonoid compounds are widely used in electrochemical studies. Furthermore, quinone-cysteine reactions have been widely investigated, particularly in toxicology,[25] because they are products of benzene metabolism.[26] The interaction of quinones with cellular nucleophiles, such as protein and non-protein sulphydryls like glutathione, induces a specific nucleophilic addition, which can prevent several physiological events. These include inhibition of microtubule formation,[27] which is involved in mitotic spindle, activity of enzymes such as ribonuclease,[28] or metabolic activation, producing nephrotoxic products.[29] Catechol addition to a thiol moiety has already been assessed for the electrochemical detection of cysteine residues in biological medium by Lawrence et al. [30]. However, this technique is difficult to implement for peptide mixture identification, since the detection does not discriminate the sources of cysteine. Nevertheless, no interference with other nucleophilic amino acids, such as lysine, tyrosine, methionine or cystine, has been reported, demonstrating the selectivity of the

reaction.[28] The specific reaction of a quinone with a cysteinyl moiety has also been studied using MS by Mason et al. in the case of 1,4-benzoquinone and peptides.[31]

3. On-line tagging of free cysteines with p-hydroquinone

ß-Lactoglobulin A from Bovine Milk containing 5 cysteine residues, four of them being involved in disulfide bonds and one presenting a free sulphydryl group, and p-hydroquinone (H_2Q), were chosen as model molecules for the quinone-cysteine reactions. The sulfurhydryl group of the protein is known to be located in a hydrophobic core, which is relatively preserved in acidic or non-aqueous medium.[32, 33] Due to the low oxidation potential of hydroquinone compared to that of water (see Table IV-1), the electrochemical reaction of this compound is sufficient to sustain the whole spray current, as demonstrated for other electroactive additives.[5] To study quinone-electrochemical tagging, two types of devices, namely the home-made nanospray interface, and a classic ESI probe, have been evaluated with respect to their adduct formation yield.

3.1 Experimental description

ß-Lactoglobulin A from Bovine Milk and Myoglobin from Horse Heart were purchased from Sigma (St. Louis, USA), p-hydroquinone (H_2Q) and p-benzoquinone (Q) from Fluka (Buchs, CH) and were used as received. Methanol (Merck, Darmstadt, Germany) and acetic acid (Fluka) were used without any further purification. Deionized water (18,5MΩ) was prepared using a Milli-Q system from Millipore (Bedford, USA). Proteins were dissolved in deionized water to a $1mg \cdot ml^{-1}$ concentration. Stock solutions of p-benzoquinone and p-hydroquinone (100mM) were freshly prepared in methanol before every experiment and used within 20 minutes. Mixtures containing 5mM of one quinone species and 3μM of protein were prepared, with a final composition of methanol/water/acetic acid 50/49/1% (v/v).

The chip was designed with the V-shape nozzle, as shown schematically in Figure III-16. The solution microchannel cross section was 35 μm average width and 40 μm depth and the channel length was 14 mm. The distance between the microelectrode (80x35μm^2) and the outlet was set to 8mm. The high voltage (U=4kV) was applied to the microelectrode from the voltage supply of the MS via the carbon ink pad on the microchip. The chip was then lined up with the entrance of the mass spectrometer and the distance between the nanospray outlet and the MS entrance (1 to 4 cm) was varied to optimize the signal and the trap injection time. The mixture solution was infused without any interruption and the MS spectra were constantly monitored. Spray currents were found to be stable during every experiment.

Experiments have been carried out with the conventional ESI interface of the LCQ DUO Ion Trap (precised in text) and the nanospray interface using the simple infusion configuration. The experimental set-up for the microfabricated interface is the same as described in the last chapter.

3.2 Results and discussion

The tagging of free cysteines with benzoquinone can be performed following different pathways. Reactions involved in the electrochemical modification of free cysteine residues are summarized in Table IV-1. Depending on the device used and the incubation conditions, every one of these reactions can take place in the tagging process.

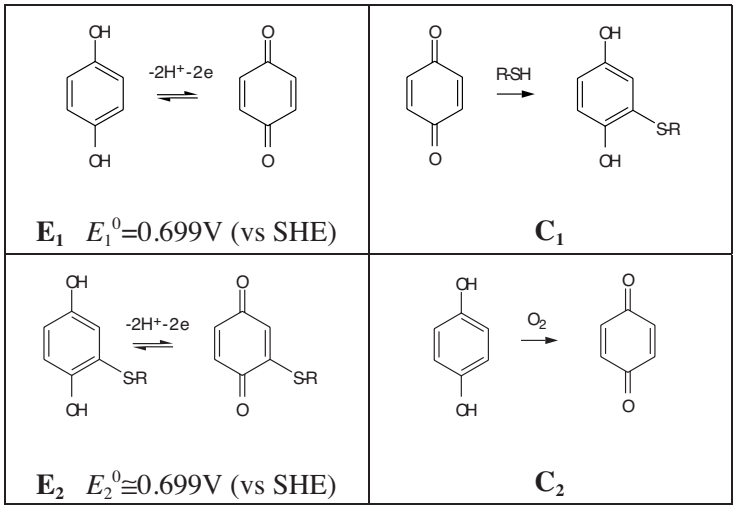

Table IV-1: *Reactions involved in electrotagging of cysteines.*

As illustrated in Figure IV-1, when the mixture of ß-Lactoglobulin and p-hydroquinone is infused, all the compounds flow over the microelectrode. Thus, p-hydroquinone undergoes an oxidation on the microelectrode due to the positive high voltage applied, thereby generating p-benzoquinone (reaction $\mathbf{E_1}$). This product diffuses in the spray channel and reacts with the free cysteine residues of the proteins in solution (reaction $\mathbf{C_1}$). As the adduct is stabilized in the reduced form, it can be oxidized (reaction $\mathbf{E_2}$, see Table IV-1).

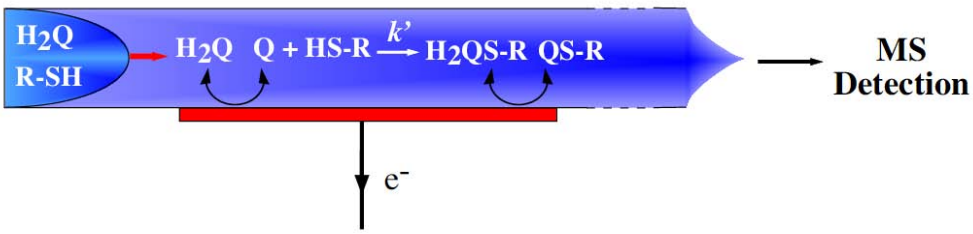

Figure IV-1. *Scheme of the on-line electrochemically induced tagging of free cysteine residues.*

The E_1C_1 modification (see Table IV-1) can be followed directly from the changes in the mass spectra. As illustrated in Figure IV-2, a new peak distribution appears under these conditions with a constant mass shift relative to native peaks, which corresponds to the addition of one molecule per protein.

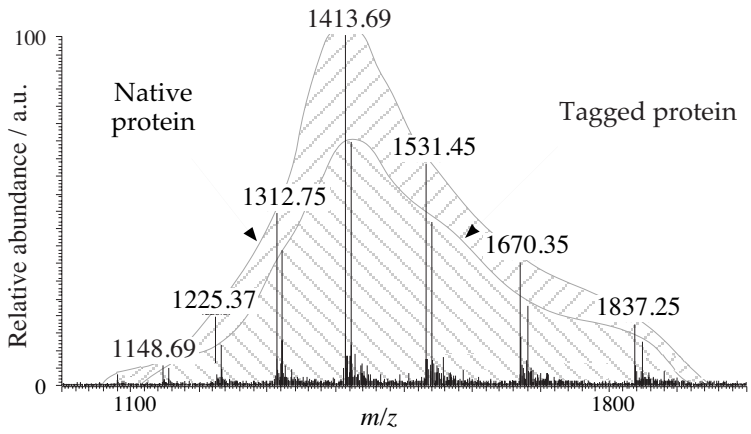

Figure IV-2. *Mass spectrum of ß-Lactoglobulin A infused with 5mM p-hydroquinone through the nanospray interface (*v*=250 nl.min^{-1}), 5 minutes after mixing. Doublet peaks appear corresponding to the distribution of the native and modified protein. This spectrum provides the number of tagged cysteines, in this case 1 because only the native plus one shifted peak are observable per pair.*

From the work of Mason et al.[31], a shift of 108 Da with respect to the native peak is expected for the addition of p-benzoquinone on peptides. However, due to the reaction E_2, the oxidized and the reduced states of the modified protein should be observable, resulting in shifts of 106 and 108 Da, respectively. Indeed, it has been shown by White et al. [34] that the product of the nucleophilic addition, which is in the reduced state, may also undergo such a heterogeneous oxidation.

The mass shift observed with respect to the native peak distribution was found to be 107.4 Da. This value is in agreement with the presence of both the reduced and the oxidized modified proteins in the sprayed solution (see Table IV-1). Nevertheless, considering the low diffusion coefficient of the proteins, the electrochemical oxidation of the adduct is unlikely (see Figure IV-1). The multiply-charged peak distribution and the low resolution of the spectra are undoubtedly at the root of the observed shift, since the 2 Da difference is not resolved, e.g. for the peak $[M+10H]^+$, the difference could be 0.2.

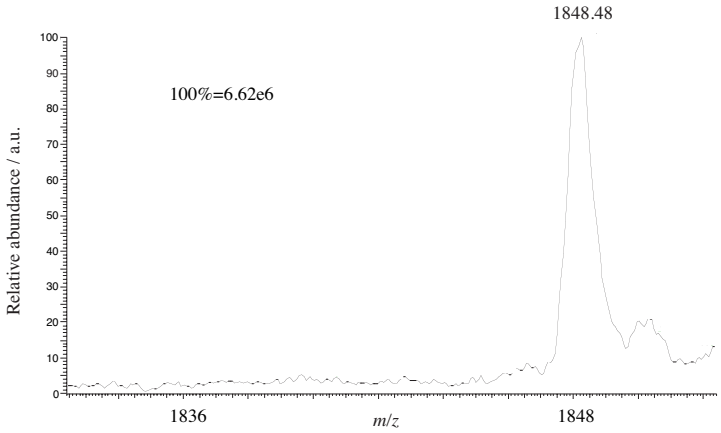

Figure IV-3. *Mass spectrum of ß-Lactoglobulin A infused with 5mM p-benzoquinone through the nanospray interface (v_f =250nl.min^{-1}). The native peak for [M+10H]$^{+10}$ corresponding to the unmodified protein is completely vanished. All the protein molecules have been tagged with one p-benzoquione.*

To corroborate this E_1C_1 mechanism, a solution containing the protein and p-benzoquinone, i.e. the oxidized form of p-hydroquinone, was infused and analyzed. As illustrated in Figure IV-3, an instant and complete modification of the protein was observed, exhibiting the same shift in the MS spectra. Moreover, the modification of a protein without any cysteine residues, namely Horse Heart Myoglobin, was also attempted. No tagging was observed in this case, highlighting the specificity of the quinone addition on the free cysteines.

The efficiency of the tagging is evaluated by considering one paired peak (here the $[M+10H]^+$). Referring to Figure IV-4a, a yield of 35% is obtained with the nanospray interface. The corresponding yield obtained when using the ESI interface is only 4% (see Figure IV-4b). To explain this difference, the behavior of each interface can be characterized by the generated spray current. This current reflects the amount of species that have undergone an electrochemical reaction, which is often called the excess charge concentration in the electrospray literature. In steady state conditions, i.e. constant flow rate and spray current, the so-called excess charge concentration remains constant.

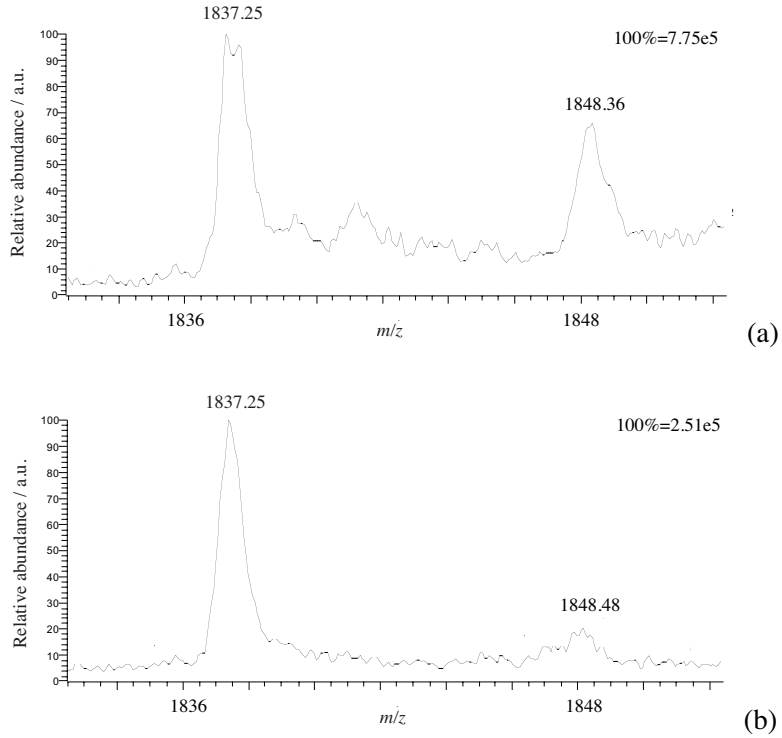

Figure IV-4. *Mass spectrum of ß-Lactoglobulin A infused with 5mM p-hydroquinone (only the $[M+10H]^{+10}$ region is shown); (a) through the nanospray interface (v_f=250nl.min^{-1}), (b) through ESI interface (v_f=2.5µl.min^{-1}), 15min after mixing. While the modification is efficient with the nanospray, the yield obtained with the ESI interface is low and close to the background level.*

Therefore, the spray current was monitored during the whole duration of every experiment and the excess charge concentration, as well as the amount of electrogenerated BQ, was calculated (see Table IV-2). Assuming that only the E_1 reaction (see Table IV-1) takes place on the microelectrode, the same amount of benzoquinone was electrogenerated for the two types of interface. Nevertheless, due to the coaxial configuration of the needle and the infusion capillary, benzoquinone is produced very close to the ESI outlet.

Furthermore, due to the large diameter of the latter, the time for benzoquinone to diffuse to the center is drastically reduced at the ESI outlet, therefore the effective number of proteins able to react with the electrogenerated benzoquinone is dramatically reduced. This leads to a situation in which protein and benzoquinone molecules are in contact only in the Taylor cone and not

during a sufficient time to react in an efficient manner, resulting thus in a very low reaction yield.

	i_{ES} / [nA]	[Q] / [μM]	[BQ] / [μM]
ESI 2.5μl·min^{-1}	1400	348	174
Nanospray 250nl·min^{-1}	150	374	187

Table IV-2. *Spray current generated i_{ES} and corresponding excess charge concentration [Q] according to Equation 28 (Chap. II). [BQ] is equal to half the excess charge concentration, since the oxidation of p-hydroquinone involves 2 electrons.*

When dealing with oxygenated solutions, hydroquinone can be directly oxidized by dissolved oxygen, thereby generating benzoquinone (see mechanism C_2 in Table IV-1). In order to demonstrate this pathway, a continuous infusion of the solution was performed with the nanospray interface until a complete modification of the protein occurred. In the case of ESI infusion, the mixture solution was kept in an Eppendorf™ tube and sampled at different incubation times. As shown in Figure IV-5, a second source of benzoquinone is available, resulting in an increase of the different yields despite a constant excess charge concentration. As illustrated above, a complete modification is almost achieved within 2 hours with the miniaturized interface. The design of the latter is certainly more suited to the electrochemical tagging compared to the ESI geometry. These results corroborate that the "electrochemical cell" design of the interface is a key issue.

Referring to all the reactions summarized in Table IV-1, two pathways have to be taken into account. For the heterogeneous pathway, the mechanism follows the $E_1C_1E_2$ pathway, which is favored by the use of nanospray.

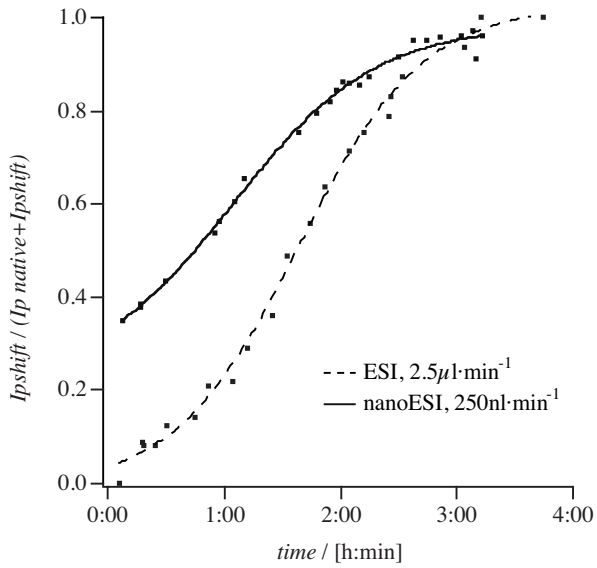

Figure IV-5. *Modification yield of ß-Lactoglobulin A infused with 5mM p-hydroquinone with the two different interfaces (same conditions as in Figure IV-4. Calculation of the yields was done using the peak intensities of the +10 charged paired-peak (modified and unmodified).*

In the presence of dissolved oxygen in the solvents, the $C_2C_1E_2$ mechanism should also be considered for long duration experiments. The optimization of the nanospray device should be focused on the mechanism E_1C_1, in order to maximize the amount of modified proteins. By increasing the yield of modification, the detection limit could be therefore decreased, allowing the detection of proteins containing several free cysteine residues.

4. Mechanistic investigation of the electrochemically induced tagging

To fully understand and thus optimize the efficiency of the on-line tagging, the study of the electrochemical behavior of the system is of utmost importance. As illustrated by the following paragraphs, the study of coupled reactions involving heterogeneous charge transfer is quite laborious.

4.1 Electrochemical reaction studies

Electrode reactions

The electrochemical processes can involve several steps, each of them presenting a time or kinetic dependence, as illustrated by Figure IV-6. Side reactions may occur at or close to the surface of the electrode surface, such as catalysis, adsorption or polymerization. Chemical reactions can also interfere in the whole mechanism.

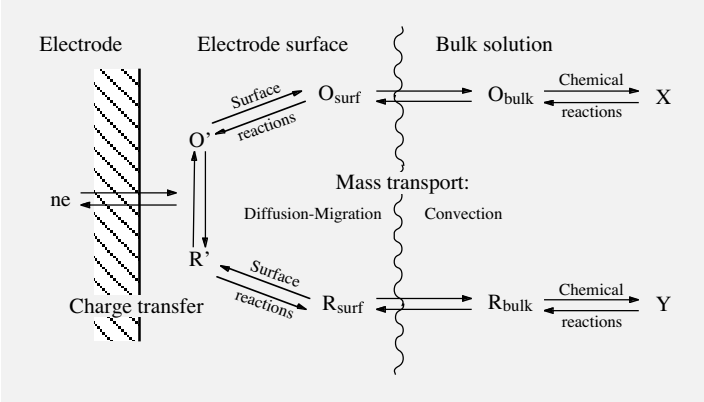

Figure IV-6. *Overview of a general electrode reaction*

Therefore, a classification of the electrode reaction has been established according to the relative importance of the rate of mass transport of the reactants and products and the charge transfer. To describe the behavior of an electrochemical system, a reversibility concept has been introduced. If the heterogeneous electron transfer is fast compared to the mass transport of the reactants and the products, then the mechanism is called reversible. The reaction is termed irreversible when the heterogeneous charge transfer is the limiting step. If the reaction moves away from this two distinct cases, the mass transport and the charge transfer occur at comparable rates, the mechanism is described as quasi-reversible.

Let us consider the following reaction:

$$\mathrm{O} + ne \underset{k_c}{\overset{k_a}{\rightleftharpoons}} \mathrm{R} \qquad (46)$$

When an irreversible process is assumed, the limiting case is the charge transfer reaction at the electrode. The total current is given by the sum of the anodic and cathodic currents:

$$i_F = i_a + i_c = nFA\left[k_a c_R(0,t) - k_c c_O(0,t)\right] \qquad (47)$$

where i_F is the total current, A is the electrode surface and $c_O(0,t)$ is the time dependent surface concentration. For an electrochemical system, the equilibrium can be shifted by applying an overpotential η defined by:

$$\eta = E - E_{eq} \quad \text{where} \quad E_{eq} = E^{0'} + \frac{RT}{nF}\ln\left(\frac{c_O^*}{c_R^*}\right) \qquad (48)$$

where c_O^* and c_R^* are the bulk concentrations, E_{eq} and $E^{0'}$ are respectively the equilibrium potential and the formal potential. According to transition state theory, the reaction rate constants, and the activation energies resulting from the imposed overpotential can be expressed as:

$$\begin{aligned} \Delta G_a &= \Delta G_a^{eq} - \alpha nF\eta \\ \Delta G_c &= \Delta G_c^{eq} - (1-\alpha)nF\eta \end{aligned} \qquad (49)$$

It comes:

$$\begin{aligned} k_a &= k^0 e^{\alpha n \frac{F}{RT}\left(E - E^{0'}\right)} \\ k_c &= k^0 e^{-(1-\alpha) n \frac{F}{RT}\left(E - E^{0'}\right)} \end{aligned} \qquad (50)$$

where α is the transfer coefficient and k^0 is the standard heterogeneous rate constant, corresponding to k_a and k_c at equilibrium (i.e. $E = E^{0'}$). k^0 can be interpreted as the kinetic facility of the redox couple. A system with a large k^0 value will achieve equilibrium on a short time scale, while a system with a low rate constant will be sluggish. Combining equations 47 and 50, a relationship between the electrode potential and the current is obtained:

$$i_F = nFAk^0\left[c_R(0,t)e^{\alpha n\frac{F}{RT}\left(E-E^{0'}\right)} - c_O(0,t)e^{-(1-\alpha)n\frac{F}{RT}\left(E-E^{0'}\right)}\right] \qquad (51)$$

Defining the exchange current i_0 as the current at $\eta = 0$, it comes from equations 48 and 51:

$$i_0 = nFAk^0\left(c_R^*\right)^{1-\alpha}\left(c_O^*\right)^{\alpha} \qquad (52)$$

Thus, the kinetics of the electrochemical system can be described by the Butler-Volmer equation:

$$i_F = i_0\left[\frac{c_R(0,t)}{c_R^*}e^{\alpha n\eta\frac{F}{RT}} - \frac{c_O(0,t)}{c_O^*}e^{-(1-\alpha)n\eta\frac{F}{RT}}\right] \qquad (53)$$

The last equation is based on parameters (η, i_0), which are experimentally available.

Electrode reactions with coupled homogeneous chemical reactions

Apart from the above developments, the electrode polarization can induce other electrochemical (E) or chemical (C) reactions. Actually, the immediate product of the electron transfer is known to be chemically unstable in a very large number of cases. In the case of the hydroquinone/benzoquinone couple, the electron transfer reactions are usually followed by a deprotonation, i.e. the whole process consists of an ECEC mechanism.[35] This observation has led to the development of models including homogeneous steps in the electrochemical processes.

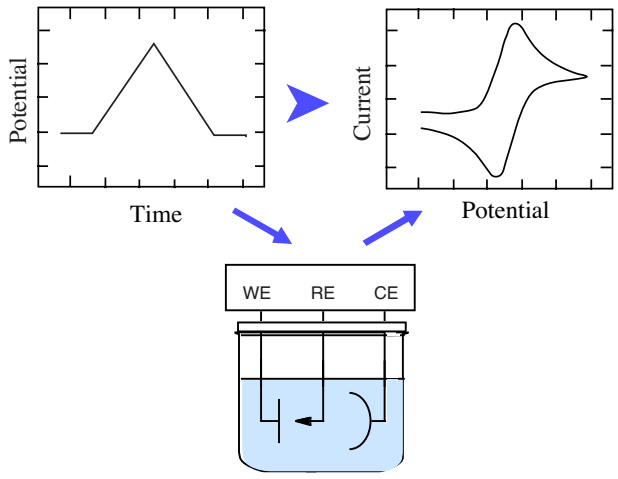

Figure IV-7. *Scheme of a cyclic voltammetry experiment.*

Generally, the mechanistic study of an electrochemical process is done using cyclic voltammetry. A potentiostat is used to control the potential difference between the working and the reference electrode immersed in the solution. The potential-time wave form is thus integrated in the potentiostat or an external input. For cyclic voltammetry, a potential sweep is performed, defined by the scan rate v, as described by Figure IV-7. The resulting current is displayed versus the potential, and the analysis of the resulting voltammogram is a way to unravel and characterize the different mechanisms involved.

A given mechanism involving electron transfer and/or chemical reaction can be described once elucidated as a combination of E and C steps. Subscripts may be used to provide additional information on the different steps. An "r" means that the reaction is reversible, i.e. both forward and backward processes are fast enough to maintain Nerstian conditions at the surface. An "i" indicates an irreversible process. Boundaries between reversible, quasi-reversible and irreversible electron transfer reactions have been suggested by Matsuda and Ayabe,[36] and are nowadays largely used. For this purpose, they introduced a dimensionless parameter Λ.

$$\Lambda = \frac{k^0}{D^{1/2}} \cdot \left(\frac{nF}{RT} \right)^{1/2} \upsilon^{1/2}$$

where υ is the scan rate. The kinetic effects are classified with respect to the relative time of experiment but also the transfer coefficient α.

These subscripts are also used to describe the kinetic aspects of the homogeneous reaction: the "r" indicates that the forward and backward reactions can take place, while the "i" specifies that the sole forward reaction is possible. A catalytic process, i.e. O is regenerated from R via a chemical reaction, is indicated with a C'.

A review of the most studied processes are listed in several book sections and papers.[37-39] However, the complexity of the mechanisms dealing with intermediate behavior (such as quasi-reversible electron transfer and/or chemical step) prevents general formulations. For simple processes, or boundary behaviors (pure diffusion controlled, pure kinetic conditions), the prediction of the shape of the voltammograms is possible and, for few cases, some analytical relations can be derived for the peak current and/or peak potential,[38, 39] which are the main valuable sources of mechanistic and kinetic information.

Formulation of an ECE mechanism

In an ECE mechanism, the product of the chemical reaction is also electroactive and can undergo oxidation (or reduction). Therefore, the anodic peak current is a direct source of information on the kinetics of the coupled chemical reaction. To model an ECE mechanism, a reversible chemical reaction, characterized by its kinetic constants k_f and k_b (here a first order), as well as a second electron-transfer reaction have to be considered:

$$A + e \rightleftharpoons B \qquad (54)$$

$$B \underset{k_f}{\overset{k_b}{\rightleftharpoons}} C \qquad (55)$$

$$C + e \rightleftharpoons D \qquad (56)$$

In addition, if the second electron transfer is much easier than the first one, i.e. $E_2^0 >> E_1^0$, a disproportionation reaction can occur, since B and C pertain the same oxidation state. Thus, the second electron transfer takes place in solution, following the reaction:

$$B+C \underset{}{\overset{k_d}{\rightleftharpoons}} A+D \qquad (57)$$

Depending on the relative importance of K and k_d, 3 limiting cases can be considered:

- ECE, where the reaction (57) infinitely slow,
- DISP1, where the reaction (55) is the limiting event, and the reaction (56) is negligible,
- DISP2, where the reaction (55) is the limiting step and the reaction (57) is negligible.

It is worth noticing that for an irreversible C step (reaction (55)), the sole transition ECE-DISP1 is possible, when k_d is increased.[40] Assuming a reversible and heterogeneous charge transfer (the reaction (57) is not considered), the problem can be then formulated as follows:

$$\begin{aligned}
\frac{\partial c_A}{\partial t} &= D\frac{\partial^2 c_A}{\partial^2 x} \\
\frac{\partial c_B}{\partial t} &= D\frac{\partial^2 c_B}{\partial^2 x} - k_b c_B + k_f c_C \\
\frac{\partial c_C}{\partial t} &= D\frac{\partial^2 c_C}{\partial^2 x} + k_b c_B - k_f c_C \\
\frac{\partial c_D}{\partial t} &= D\frac{\partial^2 c_D}{\partial^2 x}
\end{aligned} \qquad (58)$$

To describe the problem, few parameters are introduced:

$$K = k_f / k_b \qquad (59)$$

$$k = k_f + k_b \qquad (60)$$

$$\lambda = \frac{RT}{F} \cdot \frac{k}{\upsilon} \qquad (61)$$

where K is the equilibrium constant of the reaction, and λ is a dimensionless parameter describing the competition between the rates of diffusion and chemical reaction. The limiting cases can be classified for few coupled mechanisms that determine domains where relationships can be used for the peak current and the peak potential.

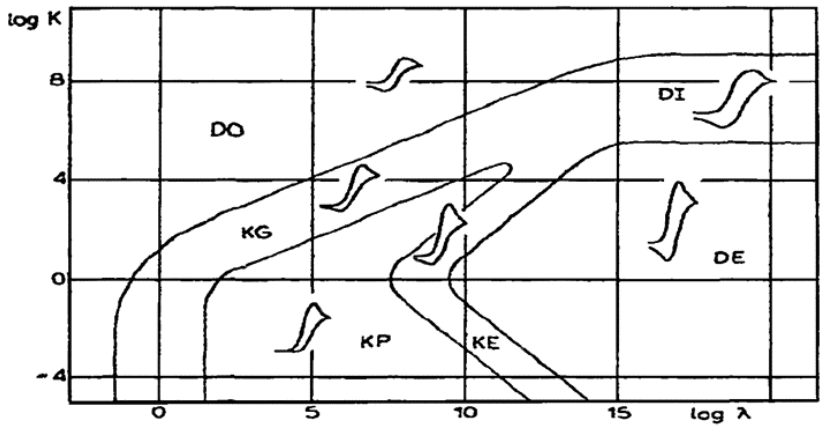

Figure IV-8. *First-order ECE mechanism (Reprinted from [41]).*

The kinetic zone diagram presented below (see Figure IV-8) shows an overview of the principal features of the voltammograms relatively to the parameters K and λ.

The ECE diagram has been first coined by Savéant et al.[42] and later extended to higher values of K and λ.[41, 43] In a log$K$ versus logλ diagram, the zones are delimited according to the particular behaviors reached for extreme values of these two parameters.

Two cases, based on the surface concentration of C, have to be considered. The condition $c_C(0,t) = 0$ is fulfilled for high scan rates and/or low kinetic constants, i.e. small λ values, here represented in the left part of the zone diagram. Three successive behaviors will be observed as λ increases:

- DO zone: the process is controlled by diffusion. The peak current is proportional to $\upsilon^{1/2}$, while the peak potential is not affected. For very small *K* and λ values, the system behaves as a one-electron process.
- KG zone: this is the general case for small λ values, featuring a peak current variation lower than a $\upsilon^{1/2}$ proportionality. It is a mixed zone, located between DO and KP zones, and for which no step is predominant.
- KP zone: the process is controlled by the kinetics of the chemical reaction. The peak current stabilizes to a given value, while the peak potential shifts cathodically by 30mV per $\log \upsilon$ unit (at 25°).

For high λ values, i.e. low scan rates and/or high kinetic rate constant, the surface concentration in C is no longer zero. Two other zones are therefore delimited:

- KE zone: this zone is the general case for high λ values, the peak current rises weakly with λ and the peak potential still varies. The system behaves as a quasi-reversible two-electron transfer.
- DE zone: the peak current and potential reach stable values corresponding to a 2-electron wave controlled by diffusion.

For high *K* values, the equilibrium is greatly right shifted, i.e. low amount of C are generated. Therefore, the DO zone appears on the top of the kinetic zone diagram, even for large λ values. Thus, a transition zone between DO and DE, called DI, is included in the diagram delimited by two horizontal lines (*K*=cst). The system exhibits a reversible behavior and the zone corresponds to the transition from the one to two-electron transfer process.

As illustrated by the zone diagram, the interpretation of a voltammogram becomes tricky, even for simple systems. For those involving non-reversible steps (which are not always all

identified) and/or a large number of processes, the numerical simulation of the process remains the main way to unravel the whole mechanism and get kinetic constants of the different steps.

4.2 Study of the L-cysteine/hydroquinone reaction

The first step of the investigation of the mechanism consists in determining the species involved in the reaction. Then, the kinetic of the different processes involved have to be determined. For this purpose, mass spectrometry and cyclic voltammetry have been chosen.

Mass spectrometry determination

The specificity of the reaction has been verified by infusing cysteine with hydroquinone with the same nanospray interface as described above. As illustrated by Figure IV-9, the adduct corresponding to the addition of the hydroquinone on the thiol moiety of the cysteine is detected. The experiment has been repeated with benzoquinone instead of hydroquinone. In this case, the sole adduct is detected and the MS/MS spectrum is identical to the insert of Figure IV-9.

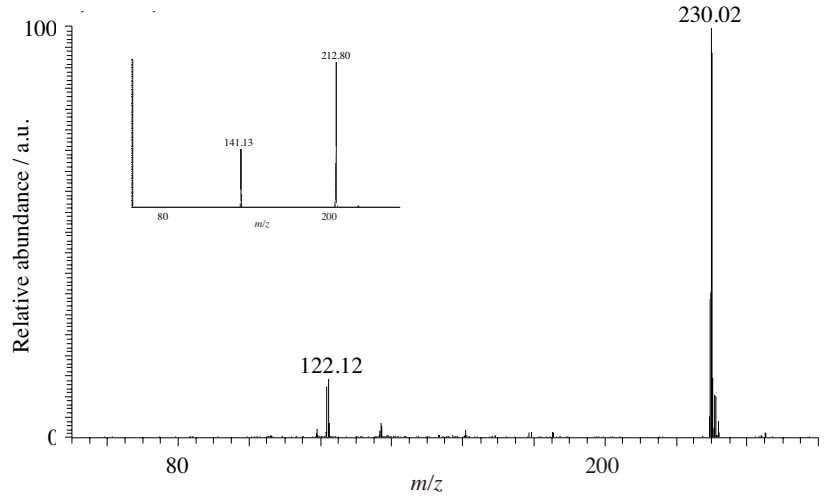

Figure IV-9. *MS spectrum of 200µM cysteine and 20mM hydroquinone in (50/49/1% (v/v) MeOH/H_2O/AcOH) infused in the nanospray interface (v_f=250nl·min^{-1}). Insert: MS/MS spectrum of the ion m/z 230.02 (collision energy 35%)*

Electrochemical measurements

The electrochemical measurements have been performed in a three-compartment cell fitted with a saturated calomel electrode (SCE) as reference electrode, a glassy carbon working electrode (Ø=3mm) and a platinum wire as counter electrode. The potentiostat was an Autolab PGSTAT 12 (Metrohm). 0.1M lithium trifluoromethanesulfonate (Fluka) have been added to the ESI medium as supporting electrolyte. For the CV obtained in basic solution, a sodium tetrafluoroborate aqueous buffer has been used (Fluka) to adjust the pH.

Hydroquinone electrochemical behavior

As the redox behavior of the quinones is known to be highly dependent on the medium,[44] especially on the proton concentration,[45] the one of hydroquinone has been studied in detail.

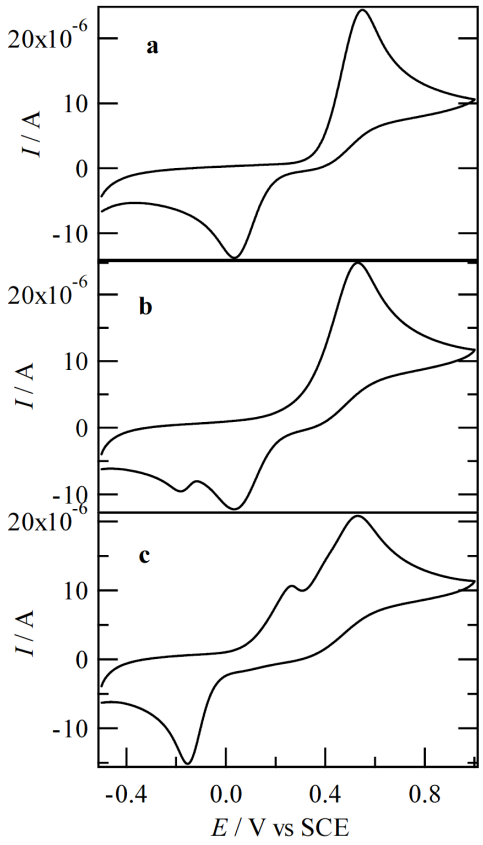

Figure IV-10. *Cyclic voltammograms of hydroquinone in 0.1mM CF_3SO_3Li solution with a) MeOH/H_2O/AcOH 50/49/1% (v/v); b) MeOH/H_2O 50/50% (v/v); (c) MeOH/H_2O 50/50% (v/v) pH=8 (ν =50mV·s^{-1}).*

As shown in Figure IV-10a, the process is irreversible, as indicated by the difference between the peak potentials (and also checked by increasing the scan rate), probably due to the 2 electrons transfer for oxidation with a combined lost of 1 or 2 protons. Considering the pH of the ESI medium, it is actually likely that protonated benzoquinone is the species generated during the forward sweep. When the proton concentration is decreased, the reduction peak disappears and a peak at a lower potential appears, which can be attributed to unprotonated benzoquinone. This behavior has already been unraveled for similar quinonoïd compounds and medium composition.[44] Therefore, protonated benzoquinone is without any doubt the species involved in the homogeneous addition on L-cysteine.

Voltammetric study of the tagging mechanism

After having checked the non-redox behavior of L-cysteine within the studied potential window (see dotted lines in Figure IV-11), a stoichiometric amount of hydroquinone has been added and different scan rates have been used. As illustrated by Figure IV-11a, the CV response is markedly changed at low scan rates, with the appearance of a cathodic peak at a higher potential than the reduction potential of protonated benzoquinone, which is still visible. In addition, the anodic peak is broadened and its intensity is higher (see Figure IV-10a and Figure IV-11c). To ascribe this peak, an equimolar solution of L-cysteine and benzoquinone was allowed to react during 10 min. in a closed vessel under nitrogen, followed by the acquisition of the cyclic voltammogram, displayed in Figure IV-12. According to the MS results and the identical position of the additional cathodic peak (E_{pc}=0.2V), the latter can be attributed to the reduction of the adduct generated through the mechanism described in Figure IV-13a.

As the scan rate is increased, this peak tends to disappear, and the electrochemical response is similar to the one observed without cysteine addition (see Figure IV-10a and Figure IV-11b).

The time for protonated benzoquinone to react with cysteine is indeed lowered and therefore the adduct is produced in smaller amount.

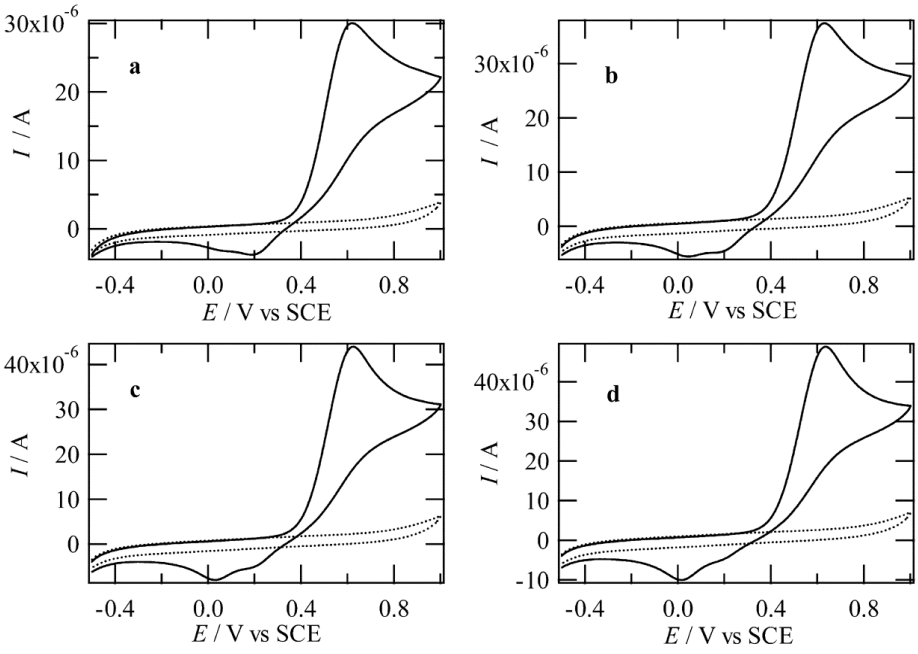

Figure IV-11. *Cyclic voltammograms of 2mM cysteine in 0.1M CF_3SO_3Li solution MeOH/H_2O/AcOH 50/49/1% (v/v) (dotted lines), with addition of 2mM Hydroquinone (plain lines) at different scan rates: a) 25mV·s^{-1}; b) 50mV·s^{-1}; 75mV·s^{-1}; d) 100mV·s^{-1}.*

At a certain scan rate (here just above 100mV·s^{-1}), the time to react is so short that the adduct cannot be generated, which causes the vanishing of the additional cathodic peak and the recurrence of the protonated benzoquinone reduction peak. Since the primary adduct is in the reduced state, it can be further oxidized and then undergo a second addition of L-cysteine.

As it can be observed in Figure IV-11, the cathodic peaks, corresponding to the reduction of the protonated benzoquinone and the adducts, are small or even absent at low scan rates. This could be attributed to side reactions, such as polymerization as previously suggested for hydroquinone[44] However, since the lowering of the peak height is only observed in the

presence of cysteine, the latter could induce or catalyze the decomposition of the protonated benzoquinone and the adducts.[46]

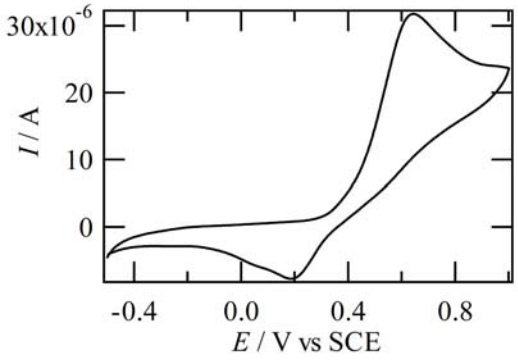

Figure IV-12. *Cyclic voltammogram of 2mM cysteine with 2mM benzoquinone in 0.1M CF_3SO_3Li solution MeOH/H_2O/AcOH 50/49/1% (v/v) (50mV·s^{-1}).*

To rule out the possibility of blocked electrode due to the adsorption of cysteine, which is known to occur on several electrode materials,[47] a series of multiscan cyclic voltammetry has been carried out. Since no change in the peak height has been observed, the catalytic role of cysteine seems to be the more likely explanation.

As described by the mechanism displayed in Figure IV-13b, the secondary adduct can also be oxidized after its generation. Since no additional anodic peak is observed, these reactions take place at a potential similar to the primary oxidation.

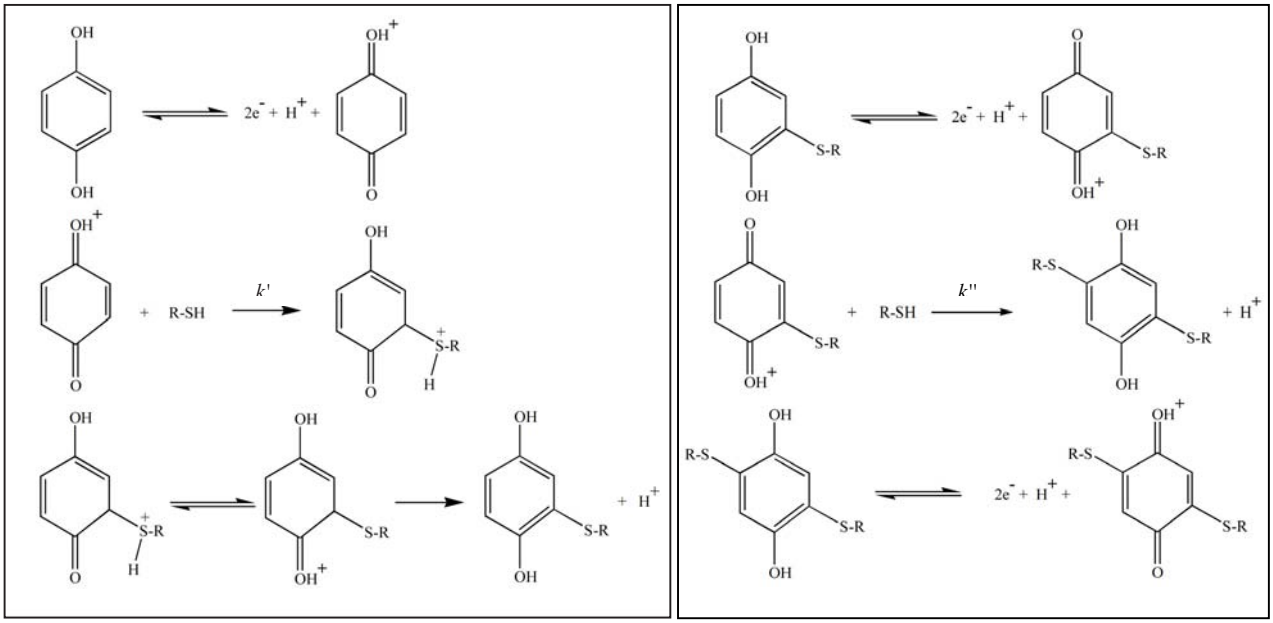

Figure IV-13. *a) Scheme of the primary mechanism for the reaction of the electrochemically generated protonated benzoquinone with L-cysteine; b) Secondary reactions following the electrochemically induced reaction of cysteine with hydroquinone.*

4.3 Kinetic aspect of the tagging

As mentioned above, the heterogeneous electron transfer taking place during the oxidation of the quinonoid compounds (hydroquinone and adducts) is sluggish. This assumption is verified since, as the scan rate is increased, the peak potential shifts toward more positive values, following the relationship for a slow electron transfer reaction. Therefore, the rate constant of the addition cannot be extracted directly from the experimental results using standard electrochemical methods.[39]

Digital simulation details and parameters

All the simulations were carried out using the commercially available software Digisim 3.0 (Bioanalytical Systems). The simulation is based on an expanding grid (expanding grid factor=0.5) and the Rudolph algorithm using voltage step of 1.8mV. The IR drop was 3kΩ. In

the case of the standard curves no IR drop was assumed. The standard potentials and standard heterogeneous rate constants of hydroquinone as well as the primary and secondary adducts were adjusted to fit the CVs, but these parameters cannot be determined individually due to the irreversible nature of the CVs at all scan rates. The dimerization rates constants of hydroquinone and the primary and secondary adduct were set to $7M^{-1}\cdot s^{-1}$, $30M^{-1}\cdot s^{-1}$ and $60M^{-1}\cdot s^{-1}$, respectively. These side reactions only had a minor effect on the standard curves, but clearly improved the agreement between experimental and simulated CVs at low scan rates.

Results

Taking into account the mechanisms unraveled by voltammetry studies, summarized in Figure IV-13, it is possible to simulate the cyclic voltammetric response and thus obtain a rate constant value for the L-cysteine-hydroquinone reaction. The simulated responses obtained for a rate constant $k'=210mM^{-1}s^{-1}$ are given in Figure IV-14b and fit well with the background-subtracted experimental voltammetric responses.

Since cysteine is not in large excess, a precise value for k'' is not essential to get an accurate value of k'. Besides, the oxidation potential for the mono- and di-substituted hydroquinones has been assumed to be equal to, or slightly lower then the unsubstituted one, and the effect on the reduction potential due to cysteine addition. Lastly, the sole dimerization of the oxidation products has been considered for side reaction, unraveled by the irreversible nature of the cyclic voltammograms at low scan rates. The last assumption gives clearly a better fit of the simulated cyclic voltammograms, while it affects only slightly the extracted rate constant for the cysteine addition.

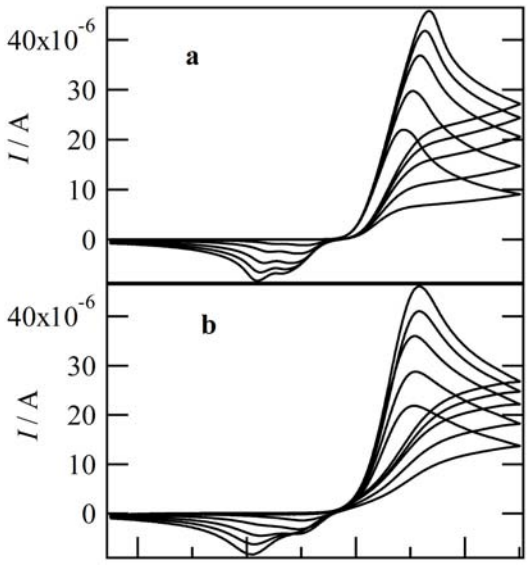

Figure IV-14. *Cyclic voltammograms at 10 mV·s^{-1}, 25mV·s^{-1}, 50mV·s^{-1}, 7 mV·s^{-1}, and 100 mV·s^{-1} a) obtained by numerical simulation; b) Background subtracted experimental CVs.*

In Figure IV-15 are displayed working curves calculated with different rate constants. These working curves are based on the decrease of the oxidation peak current with the scan rates. The oxidation peak current is composed of two contributions: one coming from the hydroquinone, one from the adduct.

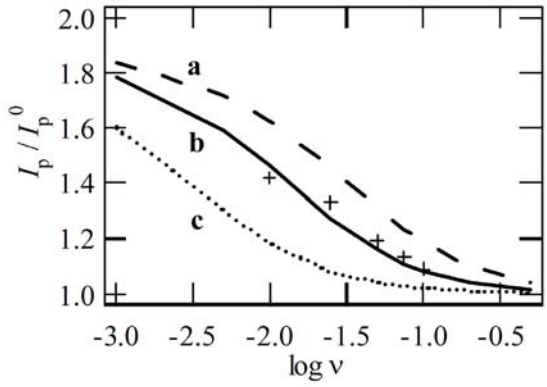

Figure IV-15. *Simulated curves corresponding to the reaction mechanism given in Figure IV-13 a) k'=500M^{-1}·s^{-1}; b) k'=210M^{-1}·s^{-1} (experimental points +); c) k'=50M^{-1}·s^{-1}.*

As the scan rate increase, the time for the homogeneous reaction to occur is decreased. Therefore, the peak current will decrease. When the scan rate is sufficiently high, the addition

does not take place and the ratio I_p/I_p^0 is 1. This behavior has been observed experimentally and simulated, as displayed in Figure IV-15. The good agreement between experimental results and the simulated curve for k'=210M^{-1}·s^{-1} increases the confidence in the extracted value.

To validate the kinetic rate constant of the cysteine tagging, working curves considering different concentration ratios have been simulated and carried out experimentally. As illustrated in Figure IV-16, the curves fit to each other quite well in all the cases, when a rate constant of 210M^{-1}·s^{-1} is considered.

Particularly observable at low scan rates, the peak current is higher when a higher concentration of cysteine is used, since there are more formed adducts that get oxidized. When a lower concentration of cysteine than hydroquinone is used, the peak current I_p is limited due to the lower production of adduct.

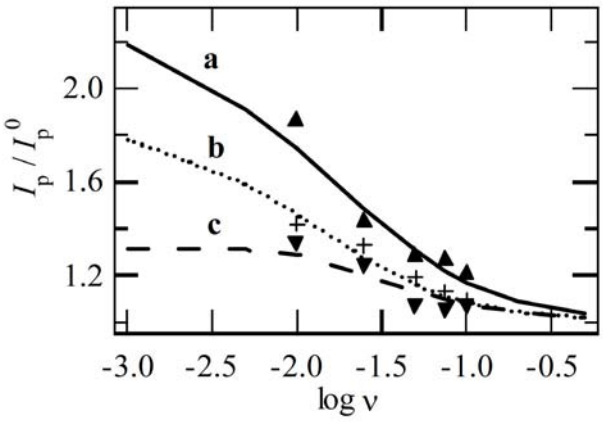

Figure IV-16. *Simulated curves corresponding to the reaction mechanism assuming k'=210M^{-1}·s^{-1} with a) 4mM cysteine with 2mM hydroquinone (experimental points ▲); b) 2mM cysteine with 2mM hydroquinone (experimental points +); a) 2mM cysteine with 6mM hydroquinone (experimental points ▼).*

Considering the experimental conditions for on-line tagging using a nanospray interface, only the primary adduct will be produced since there is a large excess of hydroquinone in the

infused solution (10^3 in the case of protein tagging). If a concentration of 5mM in hydroquinone is used, the assumption of pseudo-first order reaction leads to a rate constant of $1.1s^{-1}$.

5. Conclusions

Taking advantage of the intrinsic electrolytic behavior of electrospray interface, the electrochemical tagging of free cysteine residues of proteins could be performed. The heterogeneous oxidation of hydroquinone and the subsequent reaction with free sulphydryl groups could be demonstrated. To obtain consistent results all the solutions should be degassed in order to avoid a non-electrolytic source of the quinone tag. In addition to the efficiency of the tagging, it is also specific to the cysteine residue.

The electrochemically induced tagging of L-cysteine amino acid with hydroquinone has been studied in detail and the mechanistic and the associated kinetics aspects have been unraveled. It has been demonstrated that protonated benzoquinone is the reactant in the tagging of L-cysteines. Digital simulations could be obtained with a good agreement with the experimental results. The kinetic of the reaction is sufficiently fast to expect a complete conversion within the potential residence time range of the presented microsystem. Due to the high surface-to-volume ratio of the nanospray interface, the use of the high voltage electrode is particularly well suited to perform electrochemical modification of the analyte.

In order to enhance the tagging efficiency, the optimization of the electrochemical cell design requires taking into account the effective electrolysis time as well as the relative residence time of the proteins and the oxidized quinone in the cell. In either way the chip residence time is increased. Thus, due to the flexibility of prototyping the nanospray interfaces, several improvements can be investigated, in particular concerning geometrical parameters. Other

quinonoid compounds should also be studied, the addition of functional groups on the ring change the reactivity of the molecule, resulting in higher tagging efficiencies.

6. References

(1) Levich, V. G. *Physicochemical Hydrodynamics*: Englwood Cliffs, 1962.

(2) Blades, A. T.; Ikonomou, M. G.; Kebarle, P. *Anal. Chem.* **1991,** *63*, 2109-2114.

(3) Van Berkel, G. J.; McLuckey, S. A.; Glish, G. L. *Anal. Chem.* **1991,** *63*, 1098-1109.

(4) Van Berkel, G. J.; McLuckey, S. A.; Glish, G. L. *Anal. Chem.* **1992,** *64*, 1586-1593.

(5) Van Berkel, G. J.; Zhou, F. M. *Anal. Chem.* **1995,** *67*, 2916-2923.

(6) Xu, X.; Nolan, S. P.; Cole, R. B. *Anal. Chem.* **1994,** *66*, 119-125.

(7) Van Berkel, G. J.; Zhou, F. M. *Anal. Chem.* **1995,** *67*, 3958 - 3964.

(8) Bateman, K. P. *J. Am. Soc. Mass Spectrom.* **1999,** *10*, 309-317.

(9) Van Berkel, G. J.; Zhou, F. *J. Am. Soc. Mass Spectrom.* **1996,** *7*, 157-162.

(10) Van Berkel, G. J.; Quirke, J. M. E.; Tigani, R. A.; Dilley, A. S.; Covey, T. R. *Anal. Chem.* **1998,** *70*, 1544-1554.

(11) Van Berkel, G. J. *J. Am. Soc. Mass Spectrom.* **2000,** *11*, 951-960.

(12) Van Berkel, G. J.; Asano, K. G.; Kertesz, V. *Anal. Chem.* **2002,** *74*, 5047-5056.

(13) Kertesz, V.; Van Berkel, G. J. *J. Mass Spectrom.* **2001,** *36*, 204-210.

(14) Severs, J. C.; Harms, A. C.; Smith, R. D. *Rapid Comm. Mass Spectrom.* **1996,** *10*, 1175-1178.

(15) Severs, J. C.; Smith, R. D. *Anal. Chem.* **1997,** *69*, 2154-2158.

(16) Van Berkel, G. J.; Kertesz, V. *J. Mass Spectrom.* **2001,** *36*, 1125-1132.

(17) Van Berkel, G. J.; Zhou, F. M.; Aronson, J. T. *Int. J. Mass Spectr. Ion Proc.* **1997,** *162*, 55-67.

(18) Konermann, L.; Silva, E. A.; Sogbein, O. F. *Anal. Chem.* **2001,** *73*, 4836-4844.

(19) Morand, K.; Talbo, G.; Mann, M. *Rapid Comm. Mass Spectrom.* **1993,** *7*, 738-743.

(20) Moini, M.; Cao, P.; Bard, A. J. *Anal. Chem.* **1999,** *71*, 1658-1661.

(21) Gygi, S. P.; Rist, B.; Gerber, S. A.; Turecek, F.; Gelb, M. H.; Aebersold, R. *Nat. Biotechnol.* **1999,** *17*, 994-999.

(22) Herbert, B.; Galvani, M.; Hamdan, M.; Olivieri, E.; MacCarthy, J.; Pedersen, S.; Righetti, P. G. *Electrophoresis* **2001,** *22*, 2046-2057.

(23) Sechi, S.; Chait, B. T. *Anal. Chem.* **1998,** *70*, 5150-5158.

(24) Monks, T. J.; Lau, S. S. *Crit. Rev. Toxicol.* **1992,** *22*, 243-270.

(25) Bolton, J. L.; Trush, M. A.; Penning, T. M.; Dryhurst, G.; Monks, T. J. *Chem. Res. Toxicol.* **2000,** *13*, 135-160.

(26) Wallin, H.; Melin, P.; Schelin, C.; Jergil, B. *Chem.-Biol. Interact.* **1985,** *55*, 335-346.

(27) Pfeiffer, E.; Metzler, M. *Chem.-Biol. Interact.* **1996,** *102*, 37-53.

(28) Hanzlik, R. P.; Harriman, S. P.; Frauenhoff, M. M. *Chem. Res. Toxicol.* **1994,** *7*, 177-184.

(29) Boatman, R. J.; English, J. C.; Perry, L. G.; Fiorica, L. A. *Chem. Res. Toxicol.* **2000,** *13*, 853-860.

(30) Lawrence, N. S.; Davis, J.; Compton, R. G. *Talanta* **2000,** *52*, 771-784.

(31) Mason, D. E.; Liebler, D. C. *Chem. Res. Toxicol.* **2000,** *13*, 976-982.

(32) Babu, K. R.; Moradian, A.; Douglas, D. J. *J. Am. Soc. Mass Spectrom.* **2000,** *12*, 317-328.

(33) Uhrinova, S.; Smith, M. H.; Jameson, G. B.; Uhrin, D.; Sawyer, L.; BArlow, P. N. *Biochemistry* **2000,** *39*, 3565-3574.

(34) White, P. C.; Lawrence, N. S.; Davis, J.; Compton, R. G. *Anal. Chim. Acta* **2001,** *447*, 1-10.

(35) Laviron, E. *J. Electroanal. Chem.* **1984,** *164*, 213-227.

(36) Matsuda, H.; Ayabe, Y. *Zeitschrift für Elektrochemie* **1955,** *59*, 494-503.

(37) Hanaley, M. K.; Scott, R. L. *Anal. Chem.* **1978,** *50*, 116-137.

(38) Andrieux, C. P.; Savéant, J. M. In *Investigation of rates and mechanisms of reactions. Part II*; Bernasconi, C. F., Ed.; John Wiley & Sons: New York, 1986; Vol. 6, pp 305-390.

(39) In *Electrochemical methods: Fundamentals and applications*; Bard , A. J., Faulkner, L. R., Eds.; John Wiley and sons: New York, 1980, pp 429-487.

(40) Amatore, C. A.; Savéant, J. M. *J. Electroanal. Chem.* **1977,** *85*, 27-46.

(41) Savéant, J. M.; Andrieux, C. P.; Nadjo, L. *Electroanalytical Chemistry and Interfacial Electrochemistry* **1973,** *41*, 137-141.

(42) Savéant, J. M.; Vianello, E. *Electrochim. Acta* **1967,** *12*, 629-646.

(43) Mastragostino, M.; Nadjo, L.; Savéant, J. M. *Electrochim. Acta* **1968,** *13*, 721-749.

(44) Yamamoto, K.; Asada, T.; Nishide, H.; Tsuchida, E. *Bull. Chem. Soc. Jpn.* **1990,** *63*, 1211-1216.

(45) Hammerich, O.; Parker, V. D. *Acta Chemica Scandinavica Series B-Organic Chemistry and Biochemistry* **1982,** *36*, 63-64.

(46) Nematollahi, D.; Golabi, S. M. *J. Electroanal. Chem.* **2000,** *481*, 208-214.

(47) Ulman, A. *Chem. Rev.* **1996,** *96*, 1533-1554.

Chapter V : Numerical Investigation of an Electrochemically Induced Tagging

1. Introduction

Since the eighties, a lot of effort has been made in the numerical characterization of microband electrodes for voltammetric studies under diffusion limited[1-7] as well as diffusion convection limited mass transport.[8-19] This type of electrodes offers many advantages in terms of electrochemical behavior and their ease of fabrication (by photolithography or even simply by sealing metal films between two insulating layers) has led to applications in many analytical methods.[20] According to its electrolytic behavior, the nanospray presented previously can also be considered as a channel-flow cell with a microband electrode.

As described in Chapter IV, the electrochemically induced cysteine tagging consists in the infusion of a solution containing proteins and hydroquinone in the microchannel of the nanospray interface. Hydroquinone undergoes an oxidation at the channel electrode (A→B), and the product, benzoquinone, reacts with the free cysteines of the protein (B+X→C). The adduct is formed in a reduced state, and hence can be reoxidized at the same microelectrode (C→E). This on-line electrochemical tagging corresponds therefore to an $EC_{2X}E$ mechanism. This mechanism has been investigated for other hydrodynamic steady state techniques using finite difference modelisation.[21] Particularly, the electrochemically induced reaction of L-cysteine with acetamidophenol (paracetamol), has already been investigated and shown to follow an $EC_{2X}E$ pathway.[22] A good agreement between experimental and numerical results for

the voltammetric sensing of thiols was observed. To study the quantitative yield of the whole reaction, a finite element model of the electrochemically induced tagging in a 2D microchannel has been developed using the equation generator of the Flux-Expert® software. After initial validations, ECE and $EC_{2X}E$ mechanisms are described and the effect of the target concentration is evaluated. The present model is then checked against previous experimental results. Finally, convection and kinetic effects are investigated, unraveling all the phenomena involved in the electrochemically induced tagging.

2. Theoretical description of the problem

The phenomena described above are set out as a simplified model, where 2 species A and X are continuously introduced in a channel containing a microelectrode at the bottom as illustrated in Figure V-1.

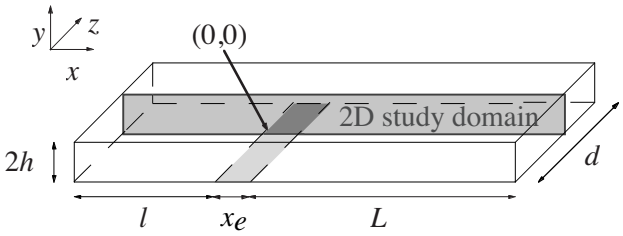

Figure V-1. *Schematic representation of the channel electrode geometry.*

A is the first species to be oxidized at the electrode, producing B (62), which will further react homogeneously with X. The produced species C can then be oxidized at the same electrode (65) said above, the (62)-(63)-(65) sequence results in an $EC_{2X}E$ mechanism, where the homogeneous reaction is characterized by a kinetic rate constant *k'*. Moreover, side reactions, which have been pointed out in the case of the cysteine with quinones tagging,[23, 24] are not taken into account in the present model.

To validate and compare the model with the literature, an ECE mechanism (62)-(64)-(65) is introduced, the chemical step being defined by k. When the $EC_{2X}E$ reaction is only limited by the concentration of B, the problem can be described using an ECE formulation, assuming a large excess of the species X and considering the relationship (66) between k and k'. The reactions (62) and (65) are assumed to be rapid and only limited by diffusion.

$$A \longrightarrow B + e \qquad (62)$$

$$B + X \xrightarrow{k'} C \qquad (63)$$

or

$$B \xrightarrow{k} C \qquad (64)$$

$$C \longrightarrow E + e \qquad (65)$$

$$k' c_X^0 = k \qquad (66)$$

Moreover, 2 kinetic constants are introduced for every redox reaction (62) and (65) in order to impose its direction, i.e. oxidation or reduction, at the microelectrode.

$$A \underset{k_{red1}}{\overset{k_{ox1}}{\rightleftharpoons}} B \qquad (67)$$

$$C \underset{k_{red2}}{\overset{k_{ox2}}{\rightleftharpoons}} E \qquad (68)$$

where k_{ox1}, k_{red1}, k_{ox2}, k_{red2} represent the respective rate constant of the oxidation and reduction of reaction (67) and (68). The complete mechanisms are schematically described in Figure V-2. The ratio k_{oxi}/ k_{redi} is maintained at 1000 in order to establish an oxidation regime at the electrode.

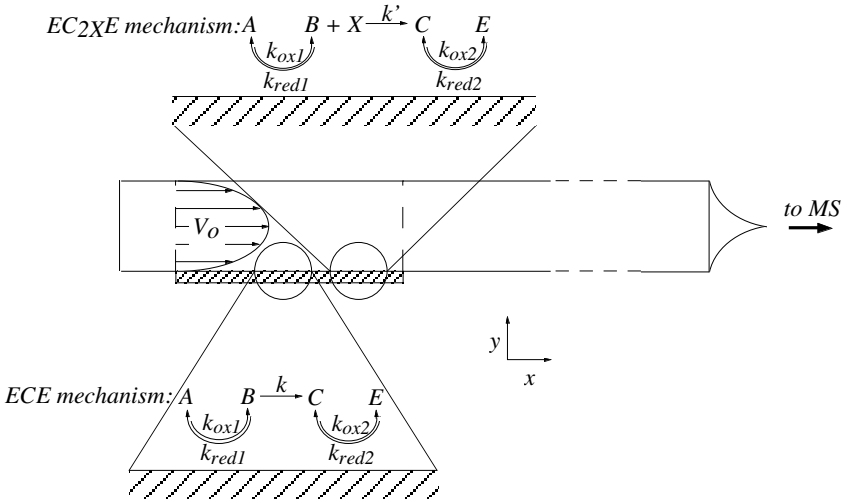

Figure V-2. *Scheme of the model including illustrations of the ECE and $EC_{2X}E$ mechanisms.*

In the present model, the convection diffusion of the 5 species is studied in a steady state regime in a 2D cross section of the geometry (see equation 69). The migration effects are neglected.

$$\frac{\partial c_i}{\partial t} + \mathbf{div}(-D_i \nabla c_i) + \mathbf{V} \cdot \nabla c_i = R_i \qquad (69)$$

where c_i is the concentration of the species i, D_i its diffusion coefficient, $\mathbf{V}$ is the fluid velocity vector and R_i is the rate of generation or consumption of the species i. The consumption and production of the different species in the domain (R_i) is implemented in the differential equation system, following the kinetics of the reactions (62) to (68). The details of the finite element integral formulation of the problem are described in Appendix 1.

The 2D geometry used in the model, assuming $w/2h \gg 1$ to neglect the velocity gradient in the third space direction (z axis), is far from the experimental dimension ($w/2h=1$). However it allows a first approach of the different phenomena involved in the present problem. Besides, the solution is supposed to be sufficiently diluted to ensure a uniform viscosity and density of the fluid, whatever the concentration gradients are. The channel walls are assumed to be

smooth and the wall capillary forces are neglected. Finally, diffusion coefficients are taken to be uniform in the entire domain and thermal effects are neglected.

The present model is based on a microband channel electrode, where x_e, d and h are defined as electrode length, channel depth, and channel half-height, respectively, as illustrated in Figure V-1. Referring to Figure V-1 and Figure V-2, we can define the following dimensionless parameters,

$$Q = \frac{4dhV_0}{3} \qquad p_1 = \frac{x_e}{h} \qquad p_2 = \frac{Q}{dD} \tag{70}$$

where Q is the volume flow rate defining the laminar flow conditions, and V_0 is the maximum fluid velocity of the corresponding fully developed Poiseuille flow profile. Several dimensionless parameters are also introduced, as described in the literature.[25] The shear rate Peclet number P_S indicates the relative importance of convection compared to diffusion. The dimensionless reaction rate and rate constant of the global ECE mechanism are given by K_{ECE} and K, respectively.

$$P_S = \frac{3}{2} p_1^{\,2} p_2 \tag{71}$$

$$K_{ECE} = \frac{kx_e^2}{D} \tag{72}$$

$$K = P_s^{-2/3} K_{ECE} \tag{73}$$

$$N_{eff} = \frac{I_K}{I_0} \tag{74}$$

N_{eff} is defined as the effective number of electrons transferred during the whole ECE (or $EC_{2x}E$) process normalized by the initial E step. I_K is the current provided by the whole ECE

(or $EC_{2X}E$) mechanism while I_0 is the current consumed for the first step (62), assuming a one-electron process for every electrochemical reaction. The current corresponding to the second electrochemical reaction (65) depends on the production of the species C. If the flow rate is high and the rate constant of the chemical step is low, the generation of C will be low giving rise to low oxidation current. In this case, N_{eff} will be close to 1 (i.e. close to a one-electron behavior) due to the almost complete inhibition of reaction (65). Conversely, if the flow rate is low and the kinetics of the homogeneous reaction fast, C will be produced in large quantities leading to an overall two-electron process (N_{eff}=2). The convection and the kinetic conditions are related to P_S and K, respectively.

To study the steady state of the on-line tagging, the transversal mean concentration of every species involved in the $EC_{2X}E$ process is calculated at a defined x position according to

$$< c_i(x) >= \frac{1}{2h}\int_0^{2h} c_i(x)\,dy \qquad (75)$$

3. Numerical description

The finite element software Flux-Expert® (Simulog)[26] is operated on a Silicon Graphics Octane 2 Unix workstation. The model is formulated in a 2D cartesian form (see Appendix 1) and calculations are based on FEM, which have been reported to extend the kinetic range for ECE and similar mechanisms.[27] Non-linear algorithms based on the Gauss inversion method are used for all the calculations. The iterative scheme is performed with a precision criterion of 1% for the convergence. A steady-state algorithm is applied in most of the cases, while a transient is chosen for low concentrations of species X on short electrode geometries. For this last case, the fulfillment of the steady state is verified with a typical duration of 0.4s, with 9 time steps from 0.02s to 0.1s (case of the short electrode calculations). Thanks to the non-linearity iterations, the mesh can be enlarged, corresponding to a more than 3 fold decrease in the

number of nodes (an error of -0.15% compared to the thinner mesh is obtained, while this error is –5.4% with the static algorithm).

In order to avoid a boundary condition conflict at the interfaces between the electrode and insulated walls concerning the flux directions, a slightly recessed geometry is used.[13] The recess size ranges from 0.1% to 0.3% depending on the electrode length. Its influence on the calculation precision is detailed in Appendix 2. The boundary conditions used are defined below.

$$\begin{aligned}
&\frac{\partial c_A}{\partial n} = \frac{\partial c_B}{\partial n} = \frac{\partial c_C}{\partial n} = \frac{\partial c_E}{\partial n} = 0, \qquad \text{for y} = 0,\ x < 0 \text{ and } x > x_e, \\
&\frac{\partial c_A}{\partial n} = \frac{\partial c_B}{\partial n} = \frac{\partial c_C}{\partial n} = \frac{\partial c_E}{\partial n} = 0, \qquad \text{for y} = 2h,\ \forall \text{x}, \\
&c_A = c_A^0, \quad c_X = c_X^0, \quad c_B = c_C = c_E = 0, \qquad \text{for } 0 < y < 2h,\ x = -l
\end{aligned} \tag{76}$$

where l is the distance between the cell inlet and the origin (electrode leading edge) as defined in Figure V-1. Furthermore, the following conditions for the consumption or production of species on the electrode are fulfilled according to the kinetic constants introduced in reactions (67) and (68).

$$\begin{aligned}
&\frac{\partial c_A}{\partial n} = k_{ox1} c_A = -\frac{\partial c_B}{\partial n} = -k_{red1} c_B \\
&\frac{\partial c_C}{\partial n} = k_{ox2} c_C = -\frac{\partial c_E}{\partial n} = -k_{red2} c_E
\end{aligned} \tag{77}$$

For the transient calculations, the initial conditions are the following:

$$c_A = c_A^0, \quad c_X = c_X^0, \quad c_B = c_C = c_E = 0 \tag{78}$$

4. Results and discussion

4.1 Model validation

The mesh parameters, i.e. recess size and electrode mesh, are validated according to literature values[28] with an error of 0.2% (see Appendix 2 for the short electrode validation), based on an E mechanism.

The model is also evaluated according to P_S values (corresponding to the convection effect). As shown in Figure V-3, the values obtained are in good agreement with the literature, except for low P_S values, for which the current is slightly over-estimated. For high P_S values, a good agreement is, however, found with an analytical model put forward by Newman and co-workers.[29]

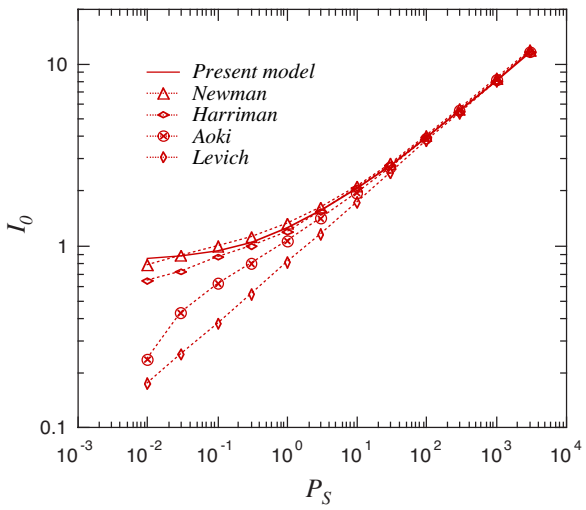

Figure V-3. *Comparison of the analytical and simulated values of the current I_0 for a range of P_S for a short electrode: Levich et al.,[30] Newman and co-workers[29] and Aoki group[31] calculated values according respectively to Equations A-10, A-11 and A-12 (see Appendix 2); simulated values of Harriman et al.,[28] (x_e=5µm, V_0=0.5m·s^{-1}, h=200µm; c_A^0=1mM; D_i=1·10^{-9} m^2·s^{-1}).*

The model is also evaluated regarding ECE and $EC_{2X}E$ mechanisms. For this purpose, a comparison is made with previous works.[32, 33] The effective transfer of electrons N_{eff} is calculated for two flow rates. The working curves are obtained in the following cases by

varying the kinetic constants k (ECE mechanism) or k' ($EC_{2X}E$ mechanism). As illustrated in Figure V-4a, the simulated results for low flow rate are very close to those of Alden and Compton, as well as those of Harriman et al. with Leveque approximation. At higher flow rate ($\log P_S$=0), the results displayed in Figure V-4b are in very good agreement with the values of ref. 32.

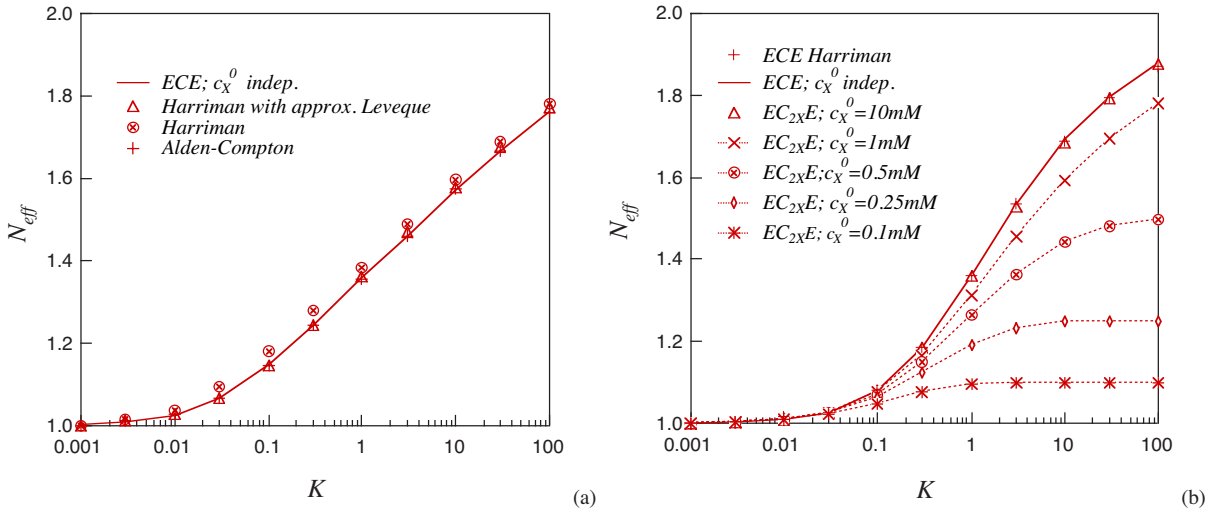

Figure V-4. *Working curves for an ECE mechanism at a short electrode (x_e=5µm, V_0=0.5m·s^{-1}, h=200µm; c_A^0=1mM; c_X^0=10mM; D_i=1·10^{-9}m^2·s^{-1}) at low flow rate, log P_S=-2.4 (a), for an ECE and an $EC_{2X}E$ mechanism at medium flow rate, log P_S=0 (b); Dotted curves represent the effect of the depletion of X on N_{eff}.*

In this case, the two mechanisms, ECE and $EC_{2X}E$, are considered in order to assess the second set of equations. To calibrate the $EC_{2X}E$ model on the ECE situation, an excess of X (c_X^0=10mM) and the relation 66 are taken into account. The errors between the two sets of results remain within –0.25%.

Figure V-4b permits a quantification of the effect of the depletion of X on the $EC_{2X}E$ phenomenon, displaying the working curves calculated for c_X^0 ranging from 0.1mM to 10 mM. For c_X^0<1mM, the convergence of the model could not be reached with the last set of equations. Therefore, a non-linear dynamic (transient) algorithm with 0.4s duration is also chosen. Referring to Figure V-4b, the depletion of X is found to have a tremendous effect on

the $EC_{2X}E$ mechanism. At low K values, the reaction 65 is kinetically limited and the effect of c_X^0 is insignificant in contrast to the situation at high K values. Thus, X is totally consumed near the electrode, and consequently the generation of C and E are strongly limited leading to the plateau characterizing the limit of diffusion control.[30]

After these initial validations, a new mesh is generated to simulate our system. The mesh is then optimized according to the same parameters as introduced above. The reference case is calculated using the following values: x_e= 100μm, V_0= 4mm·s^{-1}, h= 20μm, L= 400μm, recess size= 0.03μm, recess mesh= 0.01μm, electrode mesh size= 1.225μm (see Appendix 2 for the long electrode validation).

4.2 Model assessment according to the experimental case

For the $EC_{2X}E$ mechanism studies, the goal is usually to get the highest value for N_{eff}, because the amperometric detection of the adduct is based on the second electrochemical step (65). The purpose, here, is to optimize the yield of the adduct formation, in both reduced (C) and oxidized (E) states. Since both forms can be detected by MS, the ratio $\left(c_C + c_E\right)/c_X^0$ will therefore be considered throughout this study. For all the calculations presented below, the P_S value is kept constant (P_S=4000; logP_S=3.6) corresponding to a high flow rate regime. For this geometry, the corresponding velocity is one of the lowest that can be used in an actual experiment. Indeed, below a certain flow rate (150 nl·min^{-1}), it becomes difficult to obtain an efficient and stable nanospray, which is of utmost importance for MS analysis.

The present model is evaluated considering the experimental conditions used for the electrochemically induced tagging of proteins in the present nanospray. [24] For this purpose the ratio c_A^0/c_X^0 is set to 10^3, the channel length is extended to L=7.9·10^{-3} m and the rate constant k' is equal to the one determined for the addition of cysteine to protonated benzoquinone (k'=0.21

$mM^{-1}\cdot s^{-1}$).[23] The depletion of X implies that the second electrochemical step is largely inhibited compared with the first one, and so N_{eff} remains close to 1 even for relative high k' values (for $k'=10^4$ $mM^{-1}\cdot s^{-1}$, K=397). Furthermore, due to the large size of the electrode, a static algorithm is found to converge, despite the low values of c_X^0. The diffusion coefficients are assumed to be equal for all the species ($D_i=1\cdot10^{-9}$). It will be demonstrated in the next section that the diffusion coefficient of the target does not affect the tagging yield significantly. As illustrated in Figure V-5, the tagging for relatively low rate constants is still efficient if a sufficiently long channel is used. Considering an electroosmotic flow (EOF) profile (V_0/V_{mean}=1), 65% of the target species are tagged, versus 52% in the case of a pressure driven flow (PDF) profile (V_0/V_{mean}=1.5). This result points out the influence of the flow profile on the final tagging efficiency. Referring to the experimental case,[24] a final yield of 30% is expected.

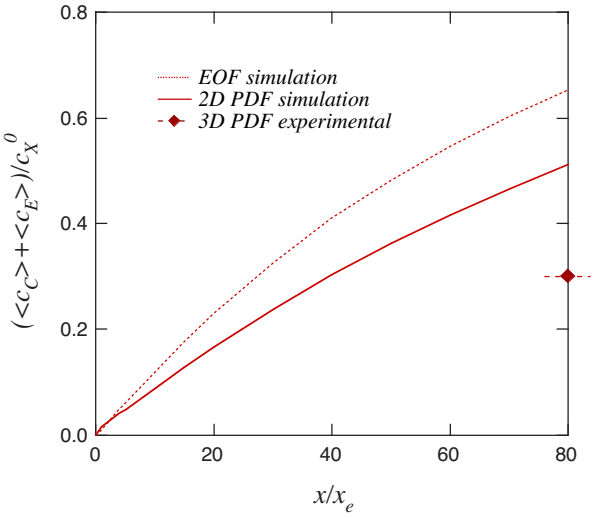

Figure V-5. *Distribution of the mean concentration of the total adduct amount along the x axis in the experimental conditions described in [24] and [23]($c_A^0/c_X^0=10^3$, $k'=0.21$ $mM^{-1}\cdot s^{-1}$, $L=7.9\cdot10^{-3}$ m). Comparison between EOF (dotted curves) and PDF for the same flow rate ($V_0^{EOF}=2.67\cdot10^{-3}m\cdot s^{-1}$, $V_0^{PDF}=4\cdot10^{-3}m\cdot s^{-1}$, $x_e=100\mu m$, $h=20\mu m$; $c_A^0=10mM$; $c_X^0=0.01mM$; $D_i=1\cdot10^{-9}m^2\cdot s^{-1}$).*

This difference can be explained considering the 3D geometry effects on the experimental flow profile. The channel geometry in the photoablated microstructures has a trapezoidal cross

section with a *w*/*2h* ratio close to 1. The resulting PDF profile is thus warped and characterized by a higher V_0/V_{mean} ratio. Relatively to the two parallel plates (present model), the other asymptotic case of the geometry is the tube, which is defined by $V_0/V_{mean}=2$. However, the axisymetric geometry would imply a ring electrode, which is not compatible with the present situation. The effect of the flow profile is investigated in detail in the next section, in order to highlight and characterize the different phenomena involved in the tagging process. According to Figure V-5, the 2D calculations considering PDF and EOF profiles allow the extrapolation of the experimental final tagging efficiency. Nevertheless, a 3D simulation study could give a more accurate evaluation of the latter.

4.3 Description of the phenomena

To make possible comparison with the experimental case,[23] the ratio c_A^0/c_X^0 is chosen to be 0.01. Furthermore, a shorter channel length is taken into account (L=400 μm), in order to focus on the phenomena involved in the surroundings of the electrode, i.e. the area where all the reactions of the $EC_{2X}E$ occur. This approach is also relevant for the experimental situation where the adducts are not stable and need to be analyzed by MS immediately after their generation.

First, the case of a specific rate constant is studied. As illustrated by the isovalues presented in Figure V-6a and Figure V-6b, a homogeneous reaction having a rate constant of $k'=10^3$ $mM^{-1}\cdot s^{-1}$ ensures the complete consumption of X at the end of the channel and consequently the maximum production of C. Concurrently, there is a huge depletion of the latter species at the electrode due to the second electrochemical step (reaction (4)). Figure V-6c shows the resulting localized distribution of E at the electrode. It is worth noticing that the concentration of C exceeds that of E at the end of the channel, since the production zone for E is confined to the microelectrode surroundings, while C is produced in the entire channel.

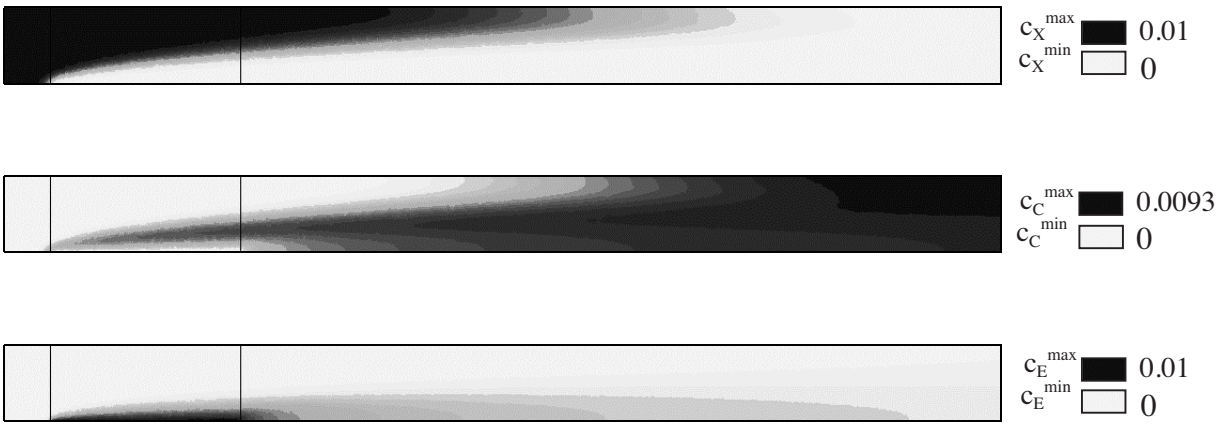

Figure V-6. *Isovalues of c_X (a), c_C (b), c_E (c) for $k'=10^3 mM^{-1}\cdot s^{-1}$ ($x_e=100\mu m$, $V_0=4\cdot10^{-3} m\cdot s^{-1}$, $h=20\mu m$; $c_A^0=1mM$; $c_X^0=0.01mM$; $D_i=1\cdot10^{-9} m^2\cdot s^{-1}$).*

In Figure V-7 are shown the relative concentration profiles along the y axis of the 5 species at the end of the electrode considering a rate constant $k'= 10^3$ $mM^{-1}\cdot s^{-1}$. For $y/2h<0.15$, half of the total amount of A is consumed, but it can be noted that c_A remains unchanged for $y/2h>0.5$. In other words, the consumption of A is not optimized. However, the residence time cannot be extended experimentally by a diminution of the velocity value, as already mentioned above. As illustrated in Figure V-7a, a smaller channel height would thus be more appropriate, to increase the probability of B and X to react.

As expected, the same depletion zone is found for X (see Figure V-7b). Due to the $EC_{2X}E$ process, a part of the adduct C undergoes an oxidation, thereby producing the species E. This effect is particularly observed in the solution surrounding the electrode ($y/2h\leq0.25$). For $y/2h>0.7$, the initial concentrations remain unchanged. This distribution suggests that h is optimized when an X depletion is observed along the entire channel depth.

When considering the nature of the targets for an electrochemically induced tagging, such as amino acids, peptides and proteins, the diffusion coefficient are considerably different. Therefore, this effect is studied by using lower diffusion coefficient values for the target X as

well as the 2 adducts C and E (down to D= $5\cdot10^{-11}m^2\cdot s^{-1}$, which corresponds to the diffusion coefficient of Myoglobin, 17kDa[34]). The mesh is also refined to keep the Peclet mesh number sufficiently low to ensure that the error is less than 0.01% (mesh size= 3μm; Reynolds mesh number= 0.03; Peclet mesh number= 12 with D= $1\cdot10^{-9}m^2\cdot s^{-1}$, i.e. for A and B species, Peclet mesh number= 240 with D=$5\cdot10^{-11}m^2\cdot s^{-1}$, for X, C and E species). For mixing situation, the critical value of the Peclet mesh number is around 100.[35]

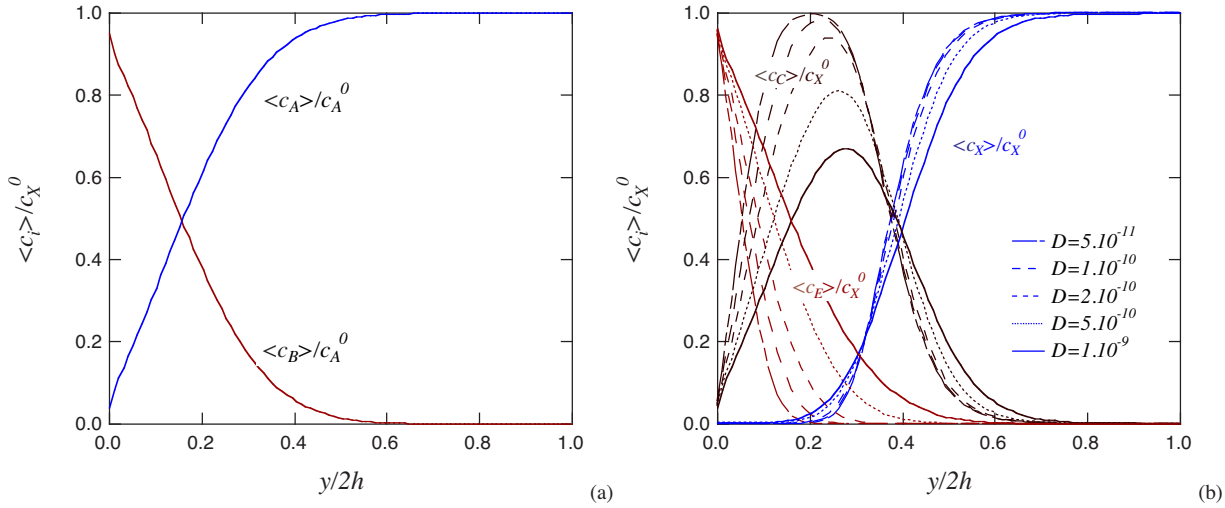

Figure V-7. *Transversal concentration profiles of species A and B (a), X, C and E (b) at the end of the electrode (x/x_e=1) at different diffusion coefficients (k'=$10^3 mM^{-1}\cdot s^{-1}$, x_e=100μm, V_0=$4\cdot10^{-3}m\cdot s^{-1}$, h=20μm; c_A^0=1mM; c_X^0=0.01mM).*

As illustrated by the transversal concentration profiles displayed in Figure V-7, the diminution of the diffusion coefficient of the target induces a more accentuated confinement for the latter as well as for the tagged species. The concentration profiles of the adducts C and E are thus shifted to the lower part of the channel, while the limit of consumption of X is more abrupt. The flux of C to feed the electrode reaction is reduced resulting in an increase in its local concentration. As pointed out by the unchanged profiles in Figure V-7a, the decrease of the diffusion coefficient of the target does not affect the concentration of the species A and B, due to their high relative concentration value ($c_{A,B}/c_X^0$=100).

Considering the effect of the diffusion coefficient on the mean transversal concentration of X, C and E at the channel outlet (x/x_e=5), it is worth noticing that the X consumption is relatively unaffected, as well as the total adduct amount, according to the values given in Table V-1.

D / $[m^2 \cdot s^{-1}]$	$1 \cdot 10^{-9}$	$5 \cdot 10^{-11}$
$<c_X>/c_X^0$	0.007	0.014
$<c_C>/c_X^0$	0.878	0.958
$<c_E>/c_X^0$	0.114	0.028
$(<c_C>+<c_E>)/c_X^0$	0.992	0.986

Table V-1. *Effect of the diffusion coefficient on the transversal mean concentration and yield at the channel outlet* (x/x_e=5) ($k'=10^3\ mM^{-1} \cdot s^{-1}$, $x_e=100\mu m$, $V_0=4 \cdot 10^{-3} m \cdot s^{-1}$, $h=20\mu m$; $c_A^0=1mM$; $c_X^0=0.01mM$).

It can be explained by the fact that the initial concentration of X is uniform: its contribution to the tagging reaction is not limited by a boundary layer diffusion and is therefore independent of its diffusion coefficient. Its decrease favors C to the detriment of E. In the framework of the on-line tagging in the nanospray, these results show that the modification yield is not affected by the size of the targets (amino acids, peptides, proteins). As shown by this table, the second electrochemical reaction is negligible. As a consequence, the faradaic current generated during the spray process is totally dedicated to the electrogeneration of B. Furthermore, the current involved in the oxidation of the adduct is almost equal to zero. As the nanospray works as a controlled-current electrolytic cell,[36] the concentration of the latter can be easily calculated.[37]

4.4 Kinetic and convective aspects of the tagging

The transversal mean concentration of the 5 species is calculated at different positions along the channel (x axis) according to equation 75. These profiles are determined for different rate constants *k'*. The effect of the latter on the concentrations of X, C and E is illustrated in Figure

V-8a, b and c, respectively. As displayed in Figure V-8a, a value of $k'=10^3$ $mM^{-1}\cdot s^{-1}$ is needed for this geometry and flowing condition to obtain a complete consumption of X. In Figure V-8b, one can also see the slope increase for the C concentration immediately after the end of the electrode. This fact is easily understood since it is not consumed far from the electrode (reaction (65)) as already illustrated in Figure V-7b. In Figure V-8c, the limit of the electrochemical production is undoubtedly identified at $x/x_e=1$, but downstream the E concentration drops and does not remain stable as expected (conservation of E in the region where it does not undergo any reaction).

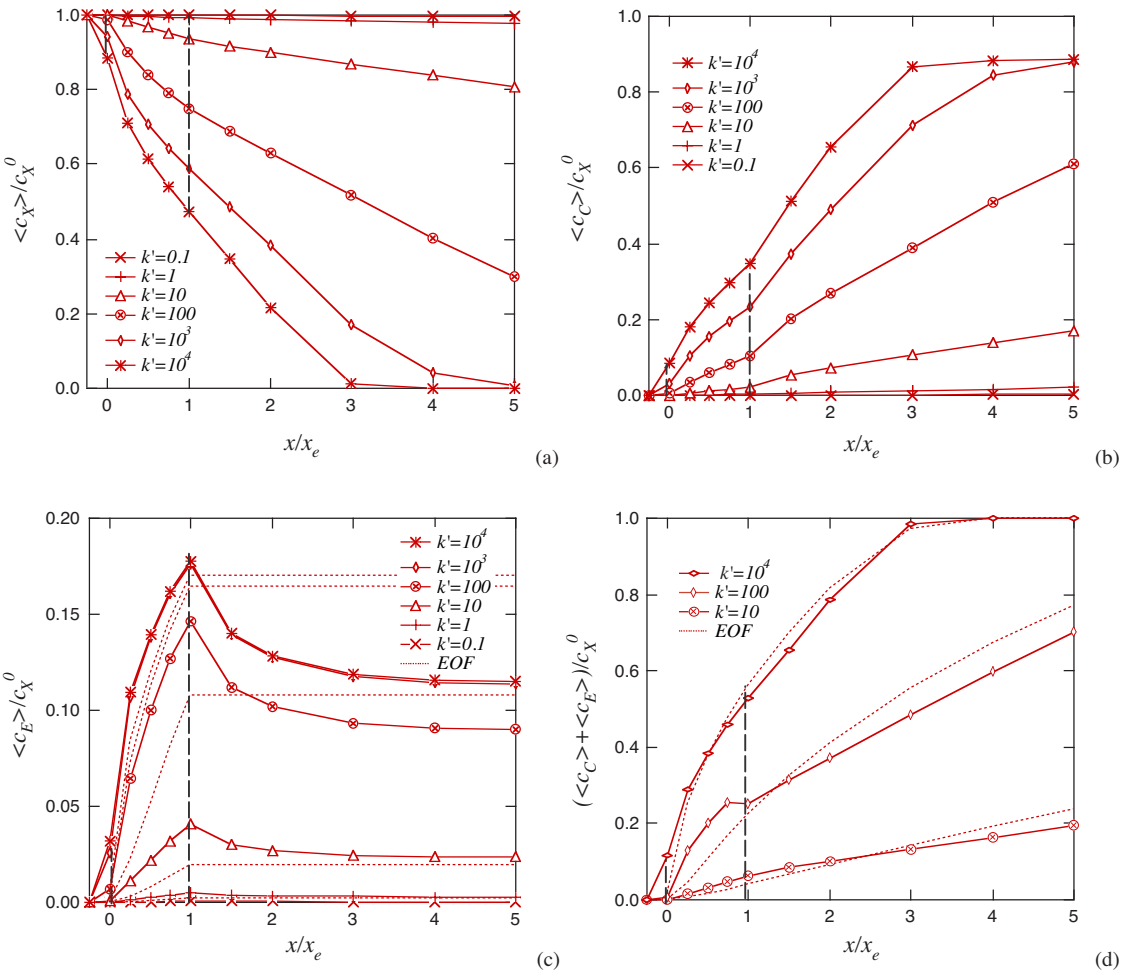

Figure V-8. *Distribution of the mean concentration of X (a), C (b), E (c) and of the total amount of adduct (d) along the x axis at different values of rate constant k' according to equation 75. Comparison between EOF (dotted curves) and PDF for the same flow rate ($V_0^{EOF}=2.67\cdot10^{-3}$ $m\cdot s^{-1}$, $V_0^{PDF}=4\cdot10^{-3}$ $m\cdot s^{-1}$, $x_e=100\mu m$, $h=20\mu m$; $c_A^0=1mM$; $c_X^0=0.01mM$; $D_i=1\cdot10^{-9}m^2\cdot s^{-1}$).*

This phenomenon is caused by the parabolic profile of the pressure driven flow (PDF), since the fluid velocity value is very low at the edges of the channel. The concentrated zone of E, surrounding the electrode, moves much slower than the center of the flow, resulting in a pseudo accumulation of E at the electrode and in a dilution effect after the microelectrode. The last effect is due to the high velocity of the arriving central part of the flow, which is free from E species. This assumption is confirmed by a calculation based on an electroosmotic flow (EOF) regime, assuming a flat velocity profile.

As illustrated in Figure V-8c, the concentration of E remains at its maximum downstream from the electrode, regardless of the rate constant. Nevertheless, the differences between the E concentration profiles obtained with PDF and EOF flows need to be unraveled. At low k' values (k'<100), the pressure flow favors the oxidation of C at the electrode over the EOF, due to the longer residence time at the electrode. When the homogeneous kinetic is faster, the influence of the residence time is damped by the depletion of X. Consequently, the post electrode dilution effect is not compensated by the increase in the residence time near the electrode. As shown in Figure V-8d, the yield of the modification, defined above as $\left(c_C + c_E\right)/c_X{}^0$, confirms the result previously described for the flow profile on the $EC_{2X}E$ mechanism (illustrated for k'=100 $mM^{-1}\cdot s^{-1}$). For $x<x_e$, B is confined to the electrode surroundings. Therefore, the production of C and E is favored in the same region, due to an increased residence time. When $x>x_e$, the unreacted B molecules diffuse towards the center of the channel and are then transported rapidly to the outlet by convection. Therefore, the time to react with X is globally reduced compared to the EOF case. This is illustrated in Figure V-8d where it can be observed that the PDF yield is lower than the EOF yield for $x>x_e$.

The influence of k' on the C and E concentration profiles is not linearly progressive, as observed in Figure V-8c. The range k'=[10-100 $mM^{-1}\cdot s^{-1}$] defines indeed a border at which reaction (65) dominates. This corresponds to the values K=0.397-K=3.97, i.e. the same range

for which the largest increase of N_{eff} is observed at equivalent flow rate (see Figure V-4b). This strong increase between k'=10 $mM^{-1}\cdot s^{-1}$ and k'=100 $mM^{-1}\cdot s^{-1}$ is also observed on the total adduct production (see Figure V-8d). To reach or exceed this "threshold" value of rate constant, one possibility is to use different probes. Indeed, experimental values of k' have already been determined in the case of the tagging of cysteines with quinonoid compounds. Roussel et al. obtained k'=0.21 $mM^{-1}\cdot s^{-1}$ for the reaction of the cysteine with electrogenerated benzoquinone,[23] while Brookes and co-workers determined k'=125 $mM^{-1}\cdot s^{-1}$ with acetamidophenol,[22] indicating a wide range of rate constants for this kind of compounds.

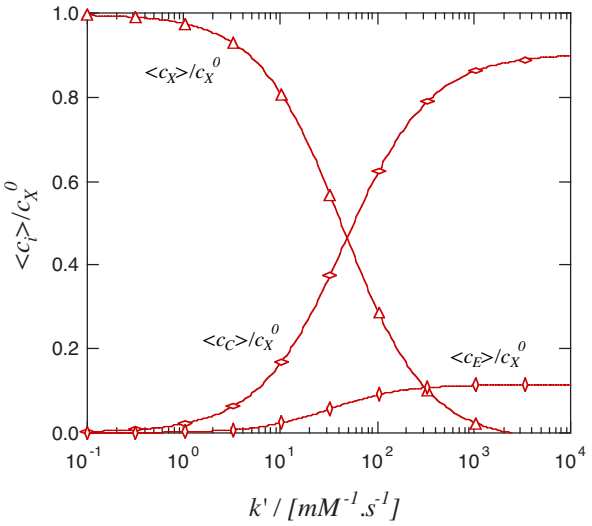

Figure V-9. *Mean concentration of X, C and E at the end of the channel* (x/x_e=5) *versus the rate constant k' (*x_e*=100 µm,* $V_0=4\cdot10^{-3}$ *m·s*$^{-1}$*, h=20 µm;* c_A^0*=1mM;* c_X^0*=0.01mM;* $D_i=1\cdot10^{-9}$ $m^2\cdot s^{-1}$*).*

The mean concentration evolution versus k' of the species X, C and E is displayed in Figure V-9 for x/x_e=5 (end of the channel). The value of k', for which the half-modification is obtained, can thus be determined. As expected, this value ($k_{1/2}$'=42 $mM^{-1}\cdot s^{-1}$) is within the range above defined, i.e. k'=[10-100 $mM^{-1}\cdot s^{-1}$]. Furthermore, in the present model, a 90% modification requires a rate constant k_{opt}'= 330 $mM^{-1}\cdot s^{-1}$. For a given geometry, this representation allows a quantification of the global tagging efficiency for different probe-target couples.

5. Conclusions

In this study, a numerical model of the electrochemically induced $EC_{2X}E$ tagging in a nanospray channel has been developed. The effect of the depletion in the target is shown to be drastic regarding the electrode current ratio N_{eff}. Furthermore, the kinetic aspects of the tagging have been investigated and the different phenomena involved in the $EC_{2X}E$ mechanism have been pointed out. It has been shown that the flow profile can modify the yield distribution along the channel due to changes in the residence time at different transversal locations. This effect is particularly marked for low rate constant on-line tagging.

To increase the yield of the electrochemical tagging regardless of the kinetic aspect, several alternative geometries could be considered, such as a metallic foil wedged between to plastic substrates having flow channels. In this way, the electrode surface would thus be doubled and the electrogenerated species could diffuse from both sides into the bulk.

It has also been demonstrated that the efficiency of this on-line reaction can be assessed for a specific probe-target system considering the geometry and flowing conditions. In the framework of a quantitative proteomics analysis, such as the ICAT technology, two electroactive probes can be chosen to tag specifically two different cell states. To infuse the different mixtures, a nanospray interface design could consist in a Y junction channel mixing downstream these two sets of on-line tagged proteins before the interface outlet. In this context, the present model allows an optimization of the conditions needed to obtain a full tagging of the two protein mixtures before mixing.

6. References

(1) Alden, J. A.; Booth, J.; Compton, R. G.; Dryfe, R. A. W.; Sanders, G. H. W. *J. Electroanal. Chem.* **1995,** *389*, 45-54.

(2) Coen, S.; Cope, D. K.; Tallman, D. E. *J. Electroanal. Chem.* **1986,** *215*, 29-48.

(3) Aixill, W. J.; Alden, J. A.; Prieto, F.; Waller, G. A.; Compton, R. G.; Rueda, M. *J. Phys. Chem. B* **1998,** *102*, 1515-1521.

(4) Alden, J. A.; Compton, R. G. *Electroanalysis* **1996,** *8*, 30-33.

(5) Amatore, C. A.; Fosset, B.; Deakin, M. R.; Wightman, R. M. *J. Electroanal. Chem.* **1987,** *225*, 33-48.

(6) Deakin, M. R.; Wightman, R. M.; Amatore, C. A. *J. Electroanal. Chem.* **1986,** *215*, 49-61.

(7) Seddon, B. J.; Girault, H. H.; Eddowes, M. J. *J. Electroanal. Chem.* **1989,** *266*, 227-238.

(8) Unwin, P. R.; Compton, R. G. *J. Electroanal. Chem.* **1988,** *245*, 287-298.

(9) Alden, J. A.; Compton, R. G. *J. Electroanal. Chem.* **1996,** *402*, 1-10.

(10) Alden, J. A.; Compton, R. G. *J. Electroanal. Chem.* **1996,** *404*, 27-35.

(11) Bidwell, M. J.; Alden, J. A.; Compton, R. G. *J. Electroanal. Chem.* **1996,** *417*, 119-128.

(12) Ball, J. C.; Compton, R. G. *Electroanalysis* **1997,** *9*, 1305-1310.

(13) Ferrigno, R.; Brevet, P. F.; Girault, H. H. *Electrochim. Acta* **1997,** *42*, 1895-1903.

(14) Ferrigno, R.; Josserand, J.; Brevet, P. F.; Girault, H. H. *Electrochim. Acta* **1998,** *44*, 587-595.

(15) Bidwell, M. J.; Alden, J. A.; Compton, R. G. *J. Electroanal. Chem.* **1996,** *414*, 247-251.

(16) Bidwell, M. J.; Alden, J. A.; Compton, R. G. *Electroanalysis* **1997,** *9*, 383-389.

(17) Compton, R. G.; Dryfe, R. A. W.; Alden, J. A.; Rees, N. V.; Dobson, P. J.; Leigh, P. A. *J. Phys. Chem.* **1994,** *98*, 1270-1275.

(18) Rees, N. V.; Alden, J. A.; Dryfe, R. A. W.; Coles, B. A.; Compton, R. G. *J. Phys. Chem.* **1995,** *99*, 14813-14818.

(19) Stevens, N. P. C.; Fisher, A. C. *J. Phys. Chem. B* **1997,** *101*, 8259-8263.

(20) Cooper, J. A.; Compton, R. G. *Electroanalysis* **1998,** *10*, 141-155.

(21) Brookes, B. A.; Lawrence, N. S.; Compton, R. G. *J. Phys. Chem. B* **2000,** *104*, 11258-11267.

(22) Brookes, B. A.; White, P. C.; Lawrence, N. S.; Compton, R. G. *J. Phys. Chem. B* **2001,** *105*, 6361-6366.

(23) Roussel, C.; Rohner, T. C.; Jensen, H.; Girault, H. H. *ChemPhysChem* **2003,** *4*, 200-206.

(24) Rohner, T. C.; Rossier, J. S.; Girault, H. H. *Electrochem. Commun.* **2002,** *4*, 695-700.

(25) Compton, R. G.; Page, D. J.; Sealy, G. R. *J. Electroanal. Chem.* **1984,** *161*, 129-145.

(26) Simulog; (www.simulog.fr) 35 Chemin du Vieux Chene 38240 Meylan Zirst - France; anne-marie.bernier@simulog.fr.

(27) Stevens, N. P. C.; Gooch, K. A.; Fisher, A. C. *J. Phys. Chem. B* **2000,** *104*, 1241-1248.

(28) Harriman, K.; Gavaghan, D. J.; Houston, P.; Suli, E. *Electrochem. Commun.* **2000,** *2*, 567-575.

(29) Newman, J. In *Electroanalytical Chemistry*; Bard, A. J., Ed.; Marcel Dekker, Inc.: New York, 1973; Vol. 6, pp 187-373.

(30) Levich, V. G. *Physicochemical Hydrodynamics*: Englwood Cliffs, 1962.

(31) Aoki, K.; Toduka, K.; Matsuda, H. *J. Electroanal. Chem.* **1987,** *217*, 33-47.

(32) Harriman, K.; Gavaghan, D. J.; Houston, P.; Kay, D.; Suli, E. *Electrochem. Commun.* **2000,** *2*, 576-585.

(33) Alden, J. A.; Compton, R. G. *J. Phys. Chem. B* **1997,** *101*, 9741-9750.

(34) Vesterberg, O.; Svensson, H. *Acta Chem. Scand.* **1966,** *20*, 820.

(35) Mengeaud, V.; Josserand, J.; Girault, H. H. *Anal. Chem.* **2002,** *74*, 4279-4286.

(36) Van Berkel, G. J.; Zhou, F. M. *Anal. Chem.* **1995,** *67*, 2916-2923.

(37) Van Berkel, G. J.; Zhou, F. M.; Aronson, J. T. *Int. J. Mass Spectr. Ion Proc.* **1997,** *162*, 55-67.

Chapter VI : Peptide on-line complexation with transition metal ions

1. Introduction

Metal ions are involved in many biological functions in proteins, especially in the catalytic processes of enzymes. They usually enhance the structural stability of the biomolecule in a required conformation for further reaction, like bringing reacting groups together into the correct relative orientation for reaction, or undergoing oxidation to insure the catalytic role of the enzyme. In most of cases, metal-ion binding to biomolecules is remarkably selective for the identity of the metal species but also their oxidation state, e.g. Fe^{3+}, Fe^{2+}.

Two analytical aspects can be considered when dealing with metal-binding proteins. The first one regards the specific interaction of metals with a known biological compound. The aim of studying these metalloproteins is too fully understand the biological role of metals and its significance from a biological point of view. The second outlook is based on the analytical utility of metal binding to proteins, which are not metalloproteins. The affinity of metals towards specific functional groups, which has not a relevant biological function, can be used to get a selection from a protein mixture. For both investigations, and since the introduction of MS and MS/MS techniques, mixtures of the biological compound of interest (proteins or peptides) and of the metal salt of interest are analyzed.

The goal of this preliminary study is to use the electrolytic behavior of a nanospray type interface to generate the metal ions directly from a sacrificial electrode. This method avoids

the use of a salt (e.g. $CuSO_4$, $AgNO_3$) to get complexes, preventing signal suppression induced by the anions introduced together with the metal ion.[1] The feasibility and the efficiency of the electrogeneration and adduct formation will be investigated for several metals and peptides, using MS and tandem MS studies.

2. Complexation

2.1 Metal-ligand interaction

The atoms or groups of atoms that are chemically bound to a metal ion are termed ligands. The number of such coordinating atoms surrounding the metal cation is called the coordination number. Metal ions act as electrophiles, seeking the possibility to share electron pairs in order to form a bond or a charge-charge interaction.

The formation of a metal complex is known to be an acid-base reaction, considering the Lewis definition. The Lewis base of a complex, which releases an electron doublet to the metal cation, is the so-called ligand. Usually, metals involved in complexation reactions are the transition metals, characterized by a certain amount of empty orbitals, particularly the d levels. When a coordination complex is formed, the atom can interact through covalent, ionic or van der Waals interactions. Unlike the alkali and alkaline-earth metals, where the bonding is predominantly electrostatic in origin, the coordination complexes of transition metals with peptides should exhibit binding with a substantial degree of covalence.[2]

The coordination type and the likely ligands depend on the intrinsic nature of the metal and the ligand, and more specifically on their respective polarizability. Ions with a low polarizability are classified as "hard", while the highly polarizable ones are termed "soft". Table VI-1 lists some ligands and metal cations. Hard bases usually coordinate with hard acids, and soft bases prefer to coordinate with soft acids. Soft acid/base coordination results in an electron pooling,

primarily in ionic or covalent bond depending on their difference in electronegativities, while hard acid/base leads primarily to electrostatic interactions.

	Cation	**Ligand**
Hard	H^+, Na^+, Li^+, K^+	ROH, $RCOO^-$, RO^-
Borderline	Zn^{2+}, Cu^{2+}, Ni^{2+}, Fe^{2+}, Fe^{3+}	Pyridine, RNH_2
Soft	Cu^+, Ag^+	RSH, RS^-, RS_2

Table VI-1. *Hard/soft classifications (Reprinted from [3]).*

2.2 Affinity chromatography

Practically speaking, metal complexation is nowadays used as an affinity tool. Immobilized Metal Ion affinity Chromatography (IMAC), also called Metal Chelate Affinity chromatography (MCAC), was first successfully demonstrated in 1975 by Porath et al. for human serum proteins.[4] To carry out an IMAC, metal ions, such as Zn^{2+}, Ni^{2+}, Cu^{2+}, are first bound to solid matrices. Stable complexation is usually obtained with histidine, tryptophan, and cysteine residues of peptides or proteins. For proteins, the efficiency of the technique can be lowered by the inaccessibility of these residues. Thus, the purification of recombinant proteins is routinely performed by the modification of the protein with a poly-histidine tag (4, 6 or 10 residues) introduced by the coding DNA strand, and subsequent IMAC with Ni^{2+} affinity.

Typically, binding occurs at neutral or slightly alkali pH, whereas desorption/elution generally occurs under acidic conditions. Once bound, the proteins can be eluted via pH or imidazole gradients. IMAC is widely used for the enrichment of phosphopeptides. Adsorption of these

post-translational modified peptides is based on the complexation between the phosphate and certain metal ions, such as Cu^{2+} or Ni^{2+} but more specifically Fe^{3+} or Ga^{3+}, the former being more selective to monophosphorylated peptides.[5] Contrary to other affinities, the complexes are formed under acidic conditions (pH ranges from 2.5 to 5.5) and broken at alkaline pH.

2.3 ESI-MS for complexes elucidation

One step forward with MS

Techniques used to study the interaction between metal ions and biological materials include Absorption Spectroscopy, Circular Dichroïsm and NMR spectroscopy. As previously mentioned, another way to study the affinity and the specificity of a complexation and the induced structural changes is to analyze by MS a mixture of the metal ion and the protein of interest. The complexation of metals with amino acids has first been introduced to enhance their ESI-MS detection. They were analyzed in the form of ternary complexes with a divalent transition metal and a neutral ligand, e.g. 2,2'-bipyridine or 1,10-phenanthroline.[6-8] The ligand was used to enhance the complexation and, in the case of a metal ion with a coordination number higher than the number of interactions with the analyte, e.g. Cu^{2+} and mono- or dipeptides, preventing the formation of neutral binary complexes.[7, 9] Metal complexation has also been explored as an alternative to protonation for ESI-MS analyses of pharmaceutical compounds.[10]

Tandem mass spectrometry of peptides

To examine the metal chelation with peptides from a structural point of view, the study of their stability and their fragmentation pattern can be helpful. Metal cations have indeed been found to direct amino acid and peptide fragmentations to provide information on both the side chains and the amino acid sequence.[11, 12]

The controlled fragmentation of ions in mass spectrometers is based on Collision Induced Dissociation (CID) technique. The CID operates with an inert gas, which will interact with the precursor (or parent) ions, characterized by a translational kinetic energy. The high-energy CID is typical for high kinetic energy precursor ions generated in magnetic deflection sector instruments and featuring few keV, while the low-energy CID (few eV) is typical for quadrupoles and ion traps.

Being more specific to ion traps, CID can take place at three different locations of the mass spectrometer, which is schemed in Appendix 3. The capillary-skimmer ion source CID occurs between the end of the heated capillary and the skimmer, modulating the potential between the heated capillary and the tube lens on one hand and the skimmer on the other. The multipole ion source CID is obtained by tuning the potential difference between the skimmer and the first multipole. Lastly, the mass analyzer CID is obtained by the modification of the resonance excitation RF voltage, which is applied between the two endcap electrodes of the trap (see appendix 3).

For the last process, the parent mass is specified and the corresponding ions gain in kinetic energy by increasing the resonance excitation RF voltage, then collide with the damping gas in the trap, dissociating in product ions. This technique is also called Tandem MS or MS/MS. The use of tandem MS in proteomics is now widespread since it makes possible to analyze complex peptide mixtures, often encountered in bottom-up approaches.

Under CID conditions, peptides fragment mostly on the peptide backbone, often with transfer of one or two hydrogens to create stable ion structures. A nomenclature system for sequence ions resulting from peptide fragmentation has been early introduced by Roepstorff et al.,[13] later completed by Biemann,[14] and is nowadays completely implemented (see Figure VI-1).

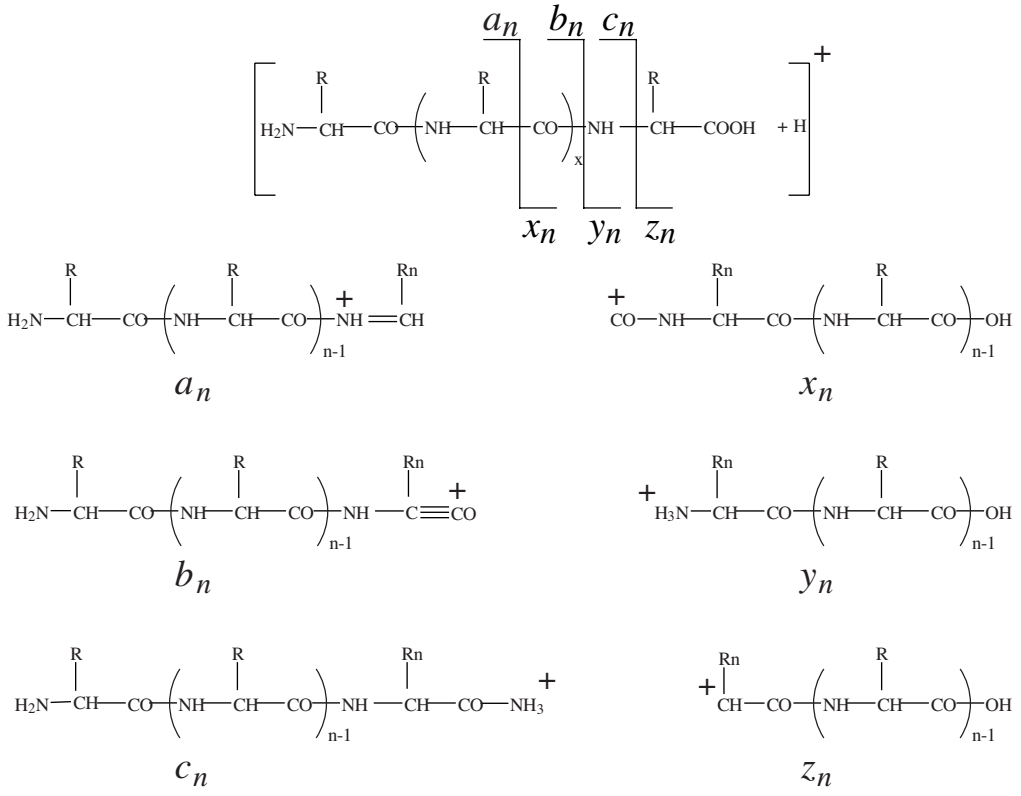

Figure VI-1. *Possible fragmentation products observed during MS/MS experiment.*

When dealing with a singly protonated precursor ion, the charge can be either retained on the fragment containing the N-terminal residue, or the C-terminus of the peptide. Thus, the detected fragment will be a **b**-type ion or a **y**-type ion respectively, both along with a neutral fragment. There are significant differences in MS/MS spectra obtained in high- and low-energy CID. In low-energy CID, **c**, **x**, **z** and **a**-type fragment ions are usually not observed, whereas ions resulting from the loss of water, ammonia, carbon monoxide are often present. Conversely, all the fragment ions described in Figure VI-1 are generated in high-energy CID.

Low-energy CID is a method of choice to get some structural information on complexes. High-energy CID might involve cleavages of the chelate structure itself or induce charge-remote reactions whose product ions would not directly reveal the precise location of the metal ion binding site.

2.4 ESI as ionization source for complex studies

The first advantage of ESI is obviously the softness of the ionization. Thus, the fragmentation can be completely controlled by the mass spectrometrist by tuning the spectrometer parameters. Secondly, in this particular study, the electrospray electrode is used as electrochemical species generator. It is worth noticing that the electrolytic behavior of the electrospray ionization has been originally demonstrated by the electrogeneration of zinc metal ions using a zinc emitter.[15] It has also been demonstrated that metal ions could be deposited on or liberated from the electrospray electrode simply by switching from negative (for the plating step) to positive mode (for the stripping step).[16] Since the current flowing out of the electrospray electrode is controlled by the droplet emission step, the amount of metal ions generated per unit time is then known by the i_{ES} current readout, which is constant under stable conditions. Therefore, the amount of cations in solution can be regulated during a same experiment by stabilization of the spray current intensity at different levels.

3. Experimental

Residues such as histidine and cysteine are considered to be better metal binding ligands than amides in peptides, and so a structure that involves a metal chelating to these groups and the neighbor amide(s) is more favorable than those involving only amide groups.[17] Therefore, Human Angiotensin II (DRVYIHPF) (Bachem, Switzerland) and a synthetic peptide (AIKCTKF) have been tested. It must be stressed out that the first one contains one histidine and the second one free cysteine, but each of them has the same C-terminal residue (phenylalanine). Peptide solutions of 50μM in 50/50 (v/v) MeOH/H_2O were freshly prepared.

The first approach of metal ion on-line complexation has been carried out using a V-shaped chip, which consists of a single microchannel (40μm x 100μm). A solution reservoir is fixed at

its inlet. The transition metal electrode is used as the only nanospray electrode. The solution infusion is therefore obtained by electroosmotic pumping. First, the chip was lined up with respect to the mass spectrometer entrance. Then, the chip reservoir was loaded with 75μl of a peptide solution. The electrode connected to the high voltage supplier was inserted into the inlet reservoir. Before use, each electrode was sanded and rinsed with ethanol and methanol. The power supply was switched on positive mode (U=3.2kV) and the acquisition was started. The chip was then moved closer to the entrance in order to generate the electrospray and thus start the complexation reaction. A nanoamperometer has been used to monitor the current and its stability. The current readout has permitted to control the interface stability, and the current was fixed to 30nA by adjusting the distance between the nanospray outlet and the MS entrance for each experiment. The control of this parameter is indeed a key point to be able to qualitatively compare the complexation reactions. Taking into account the current intensity, an equivalent of 18.5pmol of M^{2+} is generated per minute (two times higher for the silver electrode). The 1:1 metal-complexes have been studied, as well as the 2:1 metal-complexes when occurring, since the latter is poorly studied. MS/MS studies have been carried out at two levels of dissociation energy (25% and 35% normalized collision energy[3]) in order to study the complex strength, and eventually to unravel the anchoring points of the metal cation on the peptides. Different salts ($CuSO_4$, $ZnCl_2$, $NiCl_2{\cdot}2H_2O$, $FeSO_4{\cdot}7H_2O$, $FeCl_3{\cdot}6H_2O$, $AgNO_3$) have been used to check the mass shift obtained with the electrogenerated ions.

[3] The normalized collision energy is a measure of the amplitude of the resonance excitation RF voltage applied at the endcaps. The normalized collision energy scales the amplitude of the voltage to the parent mass.

4. Results

The purpose of the study is to highlight the advantages or drawbacks of using sacrificial electrodes to generate metal ions that will further react with model peptides. The mass shifts obtained with this method will be checked against those obtained with the use of salts, as well as the complexation yield.

4.1 Tandem MS on native peptides

To evaluate the influence of the complexation on the fragmentation pattern, the MS^2 spectra of the molecular ions of native peptides have first been acquired. Looking at the tandem MS spectrum of the singly charged ion corresponding to angiotensin II (see Figure VI-2), a strong $\mathbf{y_7^+}$ fragment is observed.

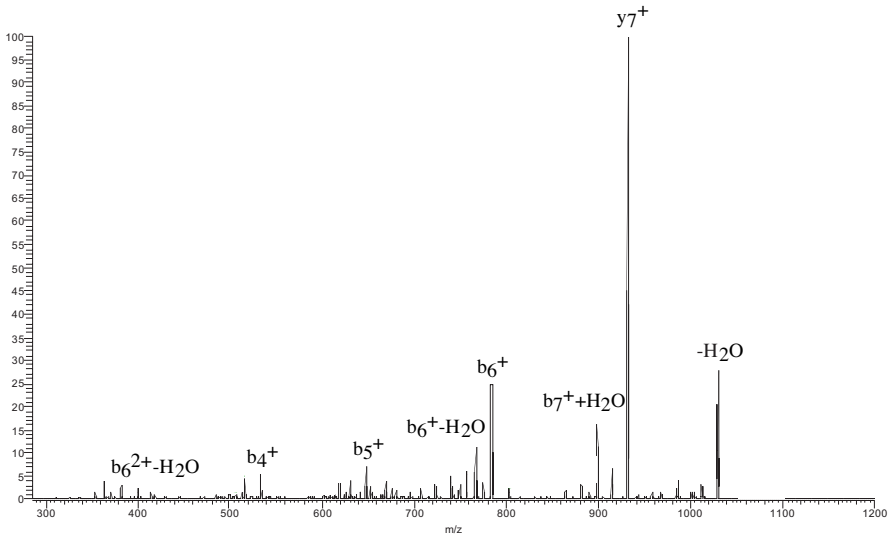

Figure VI-2. *Tandem MS on the $[M+H]^+$ (m/z 1046.2) of angiotensin II (DRVYIHPF); normalized collision energy:35%.*

This is not surprising, since the charge is preferentially on the arginine residue (basic) instead of N-terminus (aspartic acid),[18] and that the localization of the charge influences largely the fragmentation process at least for low-energy CID.[19, 20] For the same reason, a $\mathbf{b_6^+}$ fragment is

observed, resulting from a cleavage after the histidine residue. A water loss is also induced by the fragmentation, which could be induced either by the presence of aspartic acid, following the mechanism given by Schlosser et al.[21]

In the case of the cysteine-containing peptide, a strong $\mathbf{b_6^+}$ fragment is observed on the MS^2 spectrum of the peptide (see Figure VI-3), on the C-terminal side of the lysine residue. $\mathbf{b_5^+}$ is also present, confirming the charge location on the sixth residue, even if it was already demonstrated that an internal lysine residue enhances the cleavage of the amide bond in C-terminal position.[22] The fragment $\mathbf{y_5^+}$ could indicate the likely charge carrying on the first lysine, instead of the second one. A slight water loss is also induced by the fragmentation, probably due to cysteine as an interior residue.[23]

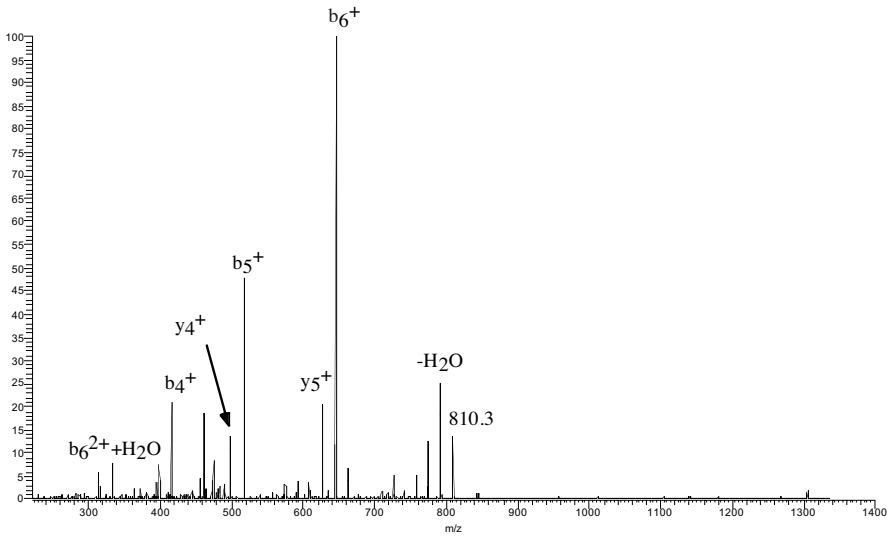

Figure VI-3. *Tandem MS on the $[M+H]^+$ (m/z 810.3) of AIKCTKF (normalized collision energy:35%).*

These spectra show that each peptide fragments with well-defined pathways, following a charge-directed fragmentation. These results will be used in order to contrast the behavior of the native peptides under fragmentation with their respective complexes. This comparison will also help to unravel the coordination of each metal on each peptide.

4.2 On-line complexation with Copper electrode

The copper complexation with proteins is well known due to the use of Biuret reagent for protein quantification using UV spectroscopy in vials or as a post-column detection for capillary electrophoresis.[24, 25] Taking advantage of the charged copper moiety and the relative stability of the complex, electrochemical detection has also been used.[26, 27] Copper has been found to complex to the amide backbone, the kinetics being dependent on the primary and secondary structures of the peptides.[25] The tandem MS complex analysis has been found to allow the distinction between isobaric (glutamine and lysine) or isomeric amino acids (leucine and isoleucine).[28]

Angiotensin II

When the copper electrode is used for electrospray ionization of the angiotensin II solution, a single complex is observed few seconds after the nanospray onset, as well as a double one, roughly one minute later, as illustrated in Figure VI-4.

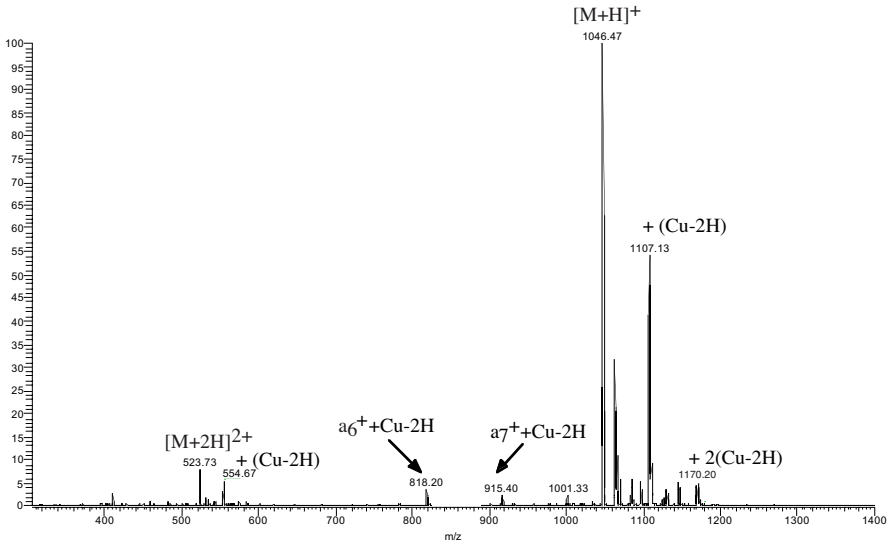

Figure VI-4. *Full scan MS from the infusion of angiotensin II using copper electrode (t=3 min).*

The shift observed due to the first addition of copper corresponds to the monoisotopic mass of the metal minus two hydrogens, which is consistent with the results obtained by Hutchens and Allen,[29] as well as Hu et al.[30] For the double adduct, the shift corresponds to 2(Cu-2H). These mass shifts have also been checked by MS analyses of a mixture of angiotensin II with $CuSO_4$ salts (data not shown), ruling out any interference due to the electrogeneration of the metal ions, such as possible generation of cuprous ions (Cu^+) and their complexation before dismutation. Therefore, the charging due to the Cu^{2+} addition is compensated by the removal of two protons.

The $\mathbf{a_6}^+$+(Cu-2H) and $\mathbf{a_7}^+$+(Cu-2H) are also generated when spraying with copper electrode, although the current has been checked to be low and stable, ruling out any fragmentation due to corona discharges. The presence of Cu^{2+} could thus induce the fragmentation, since these fragments were found to be generated also when using Cu(II) salts.

The copper-peptide complex is quite stable, as it remains the base peak at low collision energy MS/MS spectrum given in Figure VI-5a. However, it is important to notice that all the fragments present a shift of (Cu-H), instead of (Cu-2H) for the molecular ion.

The fragmentation pattern of angiotensin II is preserved when it is complexed to a copper ion, except for the $\mathbf{y_7}^+$+Cu-2H fragment, which has a somewhat lower intensity compared to the native peptide (see Figure VI-2). Besides, a strong peak corresponding to the loss of a carboxyl group is generated, becoming the base peak at higher collision energy, together with the one corresponding to the loss of a water molecule. The loss of this functional group is thus the only evidence of the structural change due to the complex formation. As pointed out by Gatlin on amino acid and peptide complexes, this loss is due to the complexation of copper at the C-terminus of the peptide.[28, 30] If the carboxyl group of the last residue is modified, no –44 loss was actually observed.

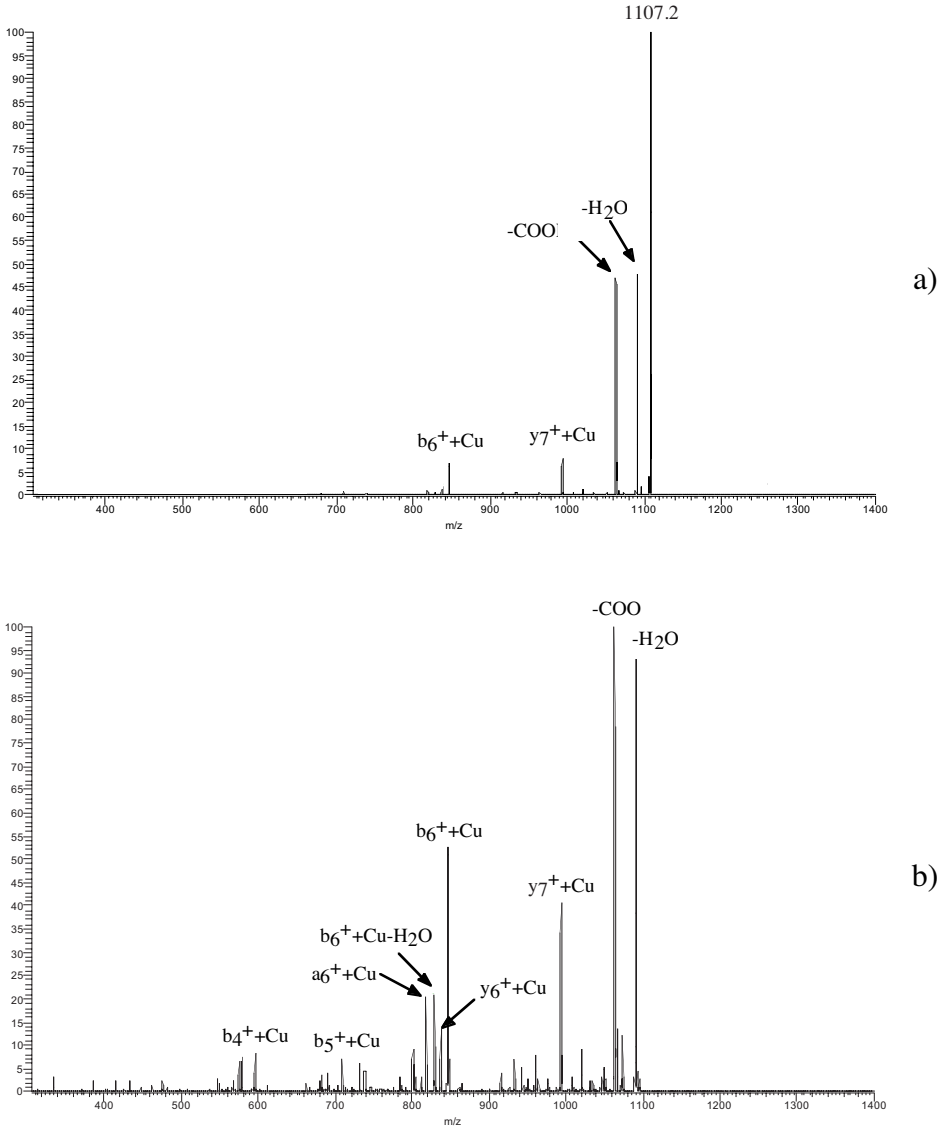

Figure VI-5. *Tandem MS spectrum on $[M+H+(Cu-2H)]^+$ (m/z 1107.2) from the infusion of angiotensin II (DRVYIHPF) using copper electrode; Collision energy: a) 25%); b) 35%. To lighten the assignment, the shift Cu-H, is only mentioned as Cu.*

When the double adduct is fragmented (data not shown), the same pattern as for the single adduct is observed. However, the single adduct is also detected as well as some of its fragments (i.e. with a (Cu-H) shift), even at low energy. The double complex is therefore less stable than the single one, probably involving electrostatic interactions. However, the shift

observed on the $\mathbf{y_6}^+$ and $\mathbf{b_6}^+$-type fragment correspond to (2Cu-3H). Thus, the complexation seems to induce some hydrogen loss during fragmentation, probably due to a rearrangement.

As underlined before, two single adduct a-type fragment are generated during the experiment. However, none of them are markedly detected when tandem MS is performed on the adduct (see Figure VI-5). This observation rules out any fragmentation induced by ESI, thus the complexation itself is directly implicated in the formation of these fragments. As already mentioned by Sigel et al., cupric ions can induce hydrolysis of the peptide backbone at acidic pH.[31] Furthermore, since the fragmentation pattern of the native peptide is roughly recovered the stability of the peptide is not changed by the complexation. Thus, the complex is tight, but complexation does not induce strong structural changes, which cause the redirection of the fragmentation.

Cysteinyl peptide

The presence of the cysteine residue seems to have a great influence on the chelation of copper on the peptide, as illustrated in Figure VI-6. A single and a double adduct are equally generated with a significant intensity, both for the singly and the doubly charged species.

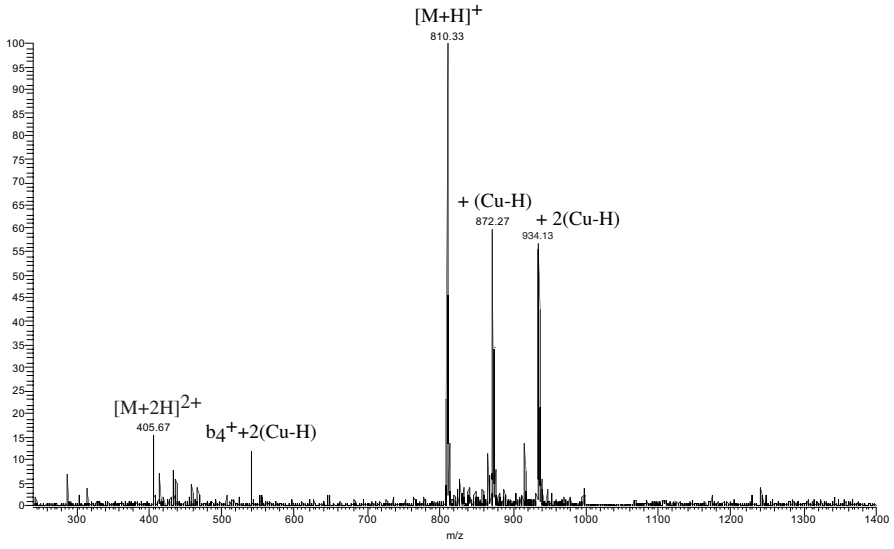

Figure VI-6. *Full scan MS from the infusion of AIKCTKF using copper electrode (t=3 min).*

Contrary to angiotensin II, the mass shift for the single-adduct corresponds here to (Cu-H). For the double addition, the mass shift corresponds to 2(Cu-H). Again, a fragment is also formed, $\mathbf{b_4}^+$+2(Cu-H), that is at the position of the cysteine residue. Since the deprotonation does not compensate the charge carried by the copper ion, the coordination through ionic or covalent bonds is likely, as well the reduction of cupric to cuprous ion (E^0=0.159V vs SHE) when complexation occurs. The reduction of Cu(II) to Cu(I) in presence of thiol moieties has already been demonstrated by several groups.[32-34]

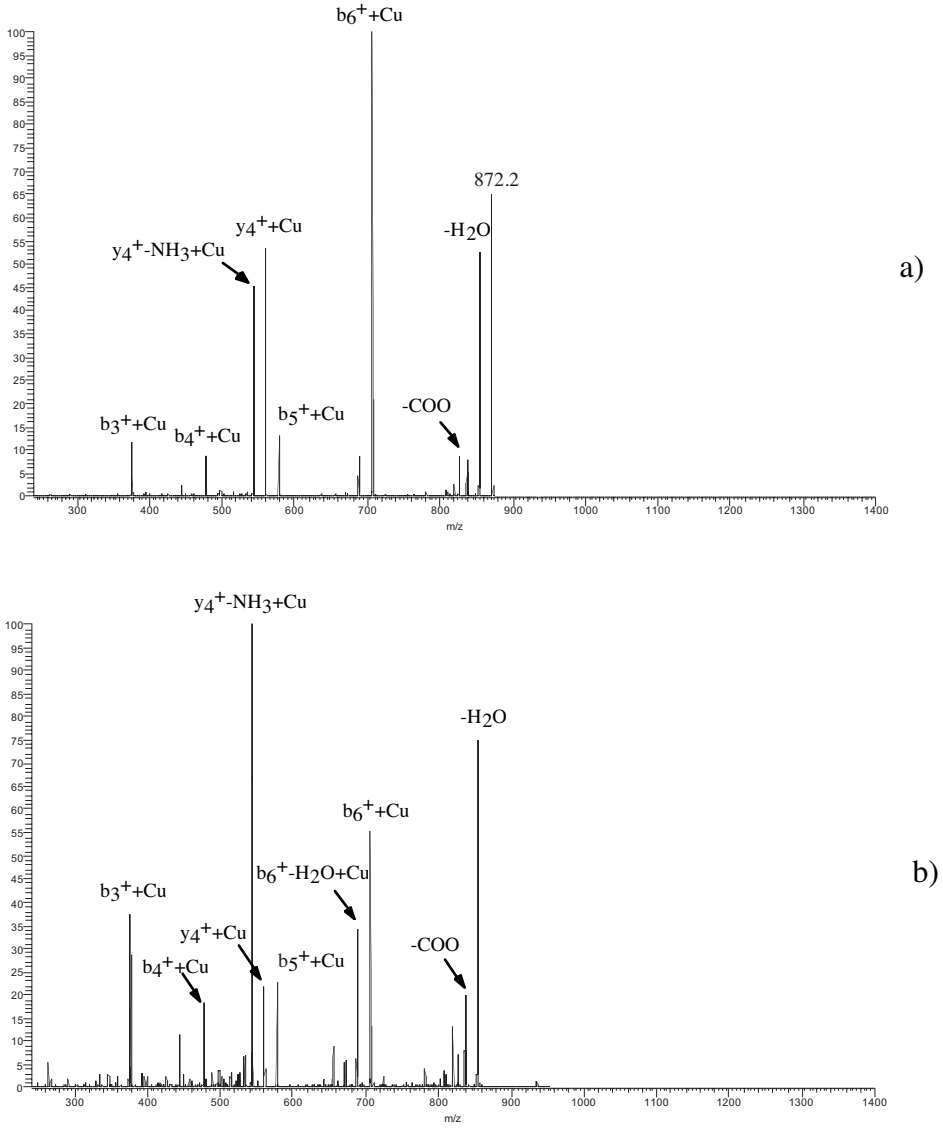

Figure VI-7. *Tandem MS spectrum on $[M+H+(Cu-H)]^+$ (m/z 872.3) from the infusion of AIKCTKF using copper electrode; Collision energy: a) 25%); b) 35%. To lighten the assignment, the shift Cu-H, is only mentioned as Cu.*

When MS/MS is performed on the single adduct (see Figure VI-7), the appearance of the $\mathbf{y_4^+}$-$\mathbf{NH_3}$+Cu-H fragment could result from the addition of copper on the cysteine side chain together with the charge carrying on the lysine residue, increasing the instability of the peptide bond. The loss of NH_3 has been already observed for peptide containing a cysteine at the N-terminal.[35] The fact that this channel is also observed in this case confirms the high strength of the copper binding to the cysteine side-chain. Due to the complexation, the $\mathbf{b_5^+}$+Cu-H fragment is less produced in favor of $\mathbf{b_3^+}$+Cu-H, i.e. at the first lysine residue, as indicated by Figure VI-7b. Compared to the native peptide, the carboxyl and water losses are more effective. Thus, the coordination to the threonine could induce an increased loss of its side chain hydroxyl group. The slight increase of loss of COO is probably due to the coordination to the last lysine residue, amplifying the COO destabilization. The complex seems to be stronger compared to the angiotensin II complex, as well as the native peptide, as illustrated by the high intensity of the corresponding at low collision energy (see Figure VI-7a).

At higher energy, the $\mathbf{y_4^+}$-$\mathbf{NH_3}$+Cu-H becomes the base peak to the detriment of $\mathbf{b_6^+}$+Cu-H fragment. Contrary to angiotensin II complex fragmentation, the shift observed for the fragments is the same as for the molecular ions, so probably the coordination does not need to get reorganized when the complex fragments. Tandem MS performed on the double copper adduct (data not shown) with low collision energy comes up with very low fragmentation of the latter, and only one abundant fragment is $\mathbf{b_6^+}$+2(Cu-H) (80% with respect to the base peak). In addition, the fragmentation peak resulting from the loss of a water molecule is very low (less than 5% of the base peak intensity) compared to the single adduct (see Figure VI-7a), probably indicative of a stabilization of threonine by a second coordination. At higher collision energy, $\mathbf{b_6^+}$+2(Cu-H) becomes the base peak and the appearance of $\mathbf{b_4^+}$+2(Cu-H) is observed but only with 12% of the base peak intensity, as well as a less intense $\mathbf{a_4^+}$+2Cu-3H and $\mathbf{b_6^+}$+H_2O+(Cu-H) (7% of base peak intensity). The double addition enhances markedly the stability of the peptide complex, particularly around the cysteine residue. Again, the shift

corresponding to the double addition is confirmed by the fragment masses, if the $\mathbf{a_4^+}$ type fragment is not taken into account.

To conclude, the copper complex is strongly coordinated to the cysteine, the other ligands involving the two lysines and the threonine residues. The double complexation increases the stability of the metal-peptide system, probably by a second coordination on the cysteine and close to threonine.

4.3 On-line complexation with Zinc electrode

Zinc occurs naturally in many metalloproteins, such as carbonic anhydrase, and several proteases and isomerases. Actually, it is known that all acid-base catalyses by metal ions in biological systems at neutral pH are catalyzed by Zn^{2+}.[36] In carbonic anhydrase, the zinc ion is coordinated to 3 histidinyl imidazole groups, and helps the reaction first by orienting the CO_2 molecule but also by rapidly converting water to hydroxide in order to get a very high local hydroxide concentration. Zinc is also involved in DNA recognition by the "zinc finger proteins": the motif of the zinc fingers is widespread in eukaryotic gene regulators, the coordination of zinc involving two histidines and two cysteines. Besides, zinc is also widely used for the purification of histidine-tagged proteins.

Angiotensin II

A strong complexation occurs on angiotensin II, as illustrated by Figure VI-8. A double adduct is also produced, even though its intensity is very weak.

The mass shifts are respectively (Zn-2H), confirmed by Hu et al. as well as Loo and co-workers,[30, 37] and 2(Zn-2H) for the single and double adducts. Contrary to the experiments with copper, no fragmentation is observed on the full scan MS spectra (see Figure VI-4).

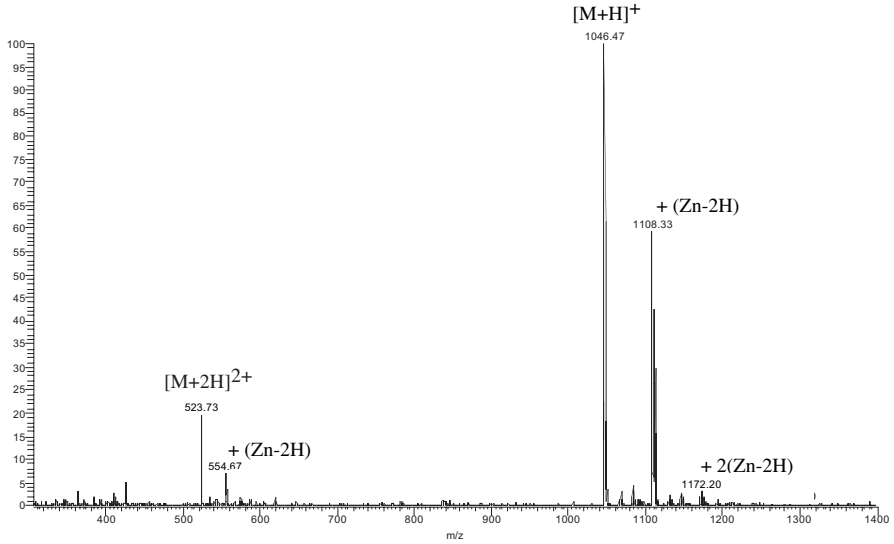

Figure VI-8. *Full scan MS from the infusion of angiotensin II using zinc electrode (t=4 min).*

When tandem MS is performed on the single adduct, the fragmentation pattern is obviously changed, and also much less complicated than for copper complex. The strong $\mathbf{y_7}^+$ fragment signal is completely inhibited by the complexation, suggesting that the charge is no longer on arginine and/or that the charge-directed fragmentation is completely inhibited. For low collision energy, only $\mathbf{b_6}^+$+Zn-2H and $\mathbf{y_6}^+$+Zn-2H fragments are produced, but the base peak corresponds to the loss of water. When the collision energy is increased, a second fragmentation point is revealed at the peptide bond between tyrosine and isoleucine, since both $\mathbf{b_4}^+$ and $\mathbf{y_4}^+$-type fragments are generated. However, it must be stressed here that the mass shift for the $\mathbf{b_4}^+$ fragment is Zn-3H, unraveling a rearrangement due to fragmentation.

When the double complex is fragmented, the loss of water is the main pathway at low and high collision energy, with low-intensity $\mathbf{b_6}^+$-type fragments as well as $\mathbf{y_6}^+$-type fragment, i.e. between arginine and valine residues. The pattern is thus quite similar to the one of the single adduct, even though no fragmentation occurs between tyrosine and isoleucine, meaning that this second coordination stabilizes the simple complex.

To summarize, the complex formed with zinc is very tight, as suggested by the rare fragments generated. The strong loss of water indicates that the sole weakness is at the hydroxyl of tyrosine. The appearance of $\mathbf{y_6^+}$-type fragment could be due to the coordination on valine. Therefore, the tetradentate zinc ion could be complexed through the VYIH sequence.

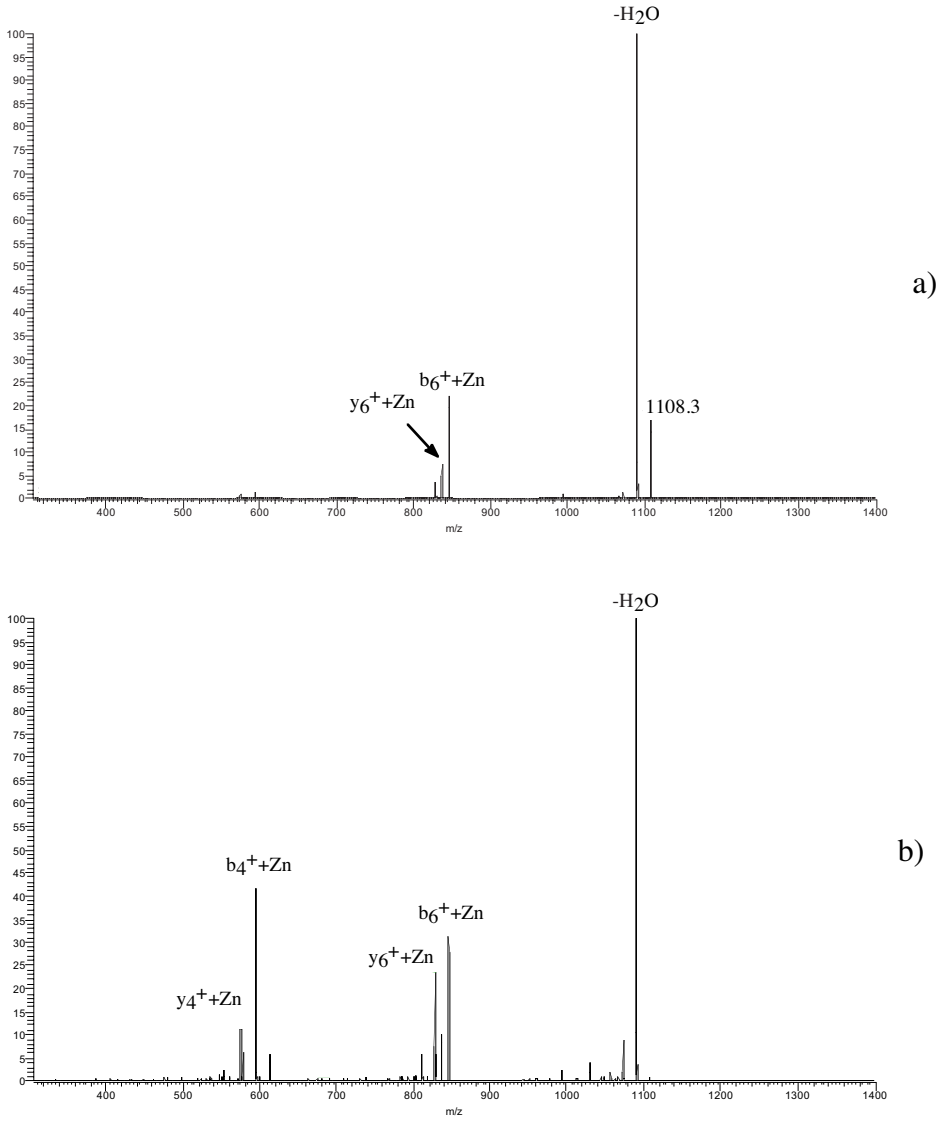

Figure VI-9. *Tandem MS spectrum on $[M+H+(Zn-2H)]^+$ (m/z 1108.3) from the infusion of angiotensin II (DRVYIHPF) using zinc electrode; Collision energy: a) 25%); b) 35%. To lighten the assignment, the shift Zn-2H, is only mentioned as Zn.*

Cysteinyl peptide

When spraying with the zinc electrode, a single and a double complex are observed as shown in Figure VI-10, the latter being lost in the background. Compared to angiotensin II, the efficiency of the tagging is quite lower. This could be due to the lower affinity of zinc (borderline Lewis acid) with cysteine (soft Lewis base).

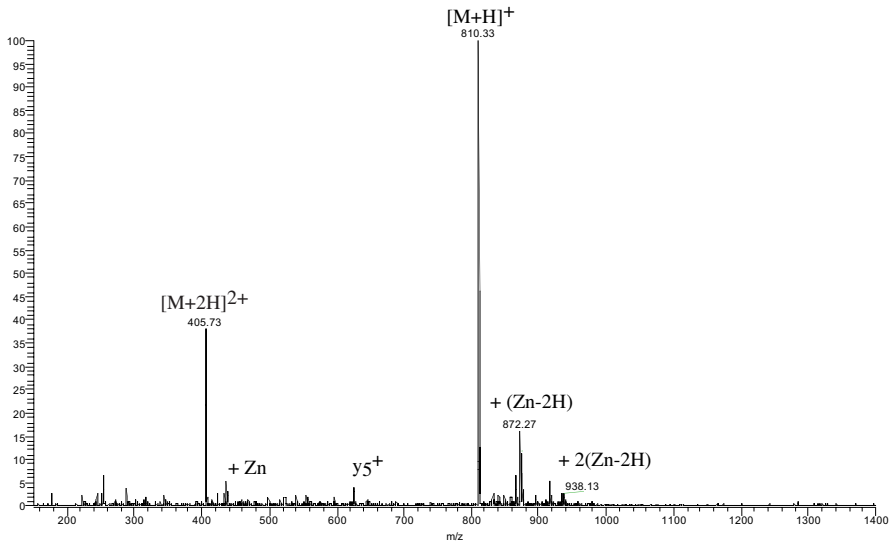

Figure VI-10. *Full scan MS from the infusion of AIKCTKF using zinc electrode (t=4 min).*

Here, the mass shift of the single adduct and the double adduct corresponds respectively to (Zn-2H) and 2(Zn-2H), as for angiotensin II.

Zinc complexes of a peptide containing cysteines have been found to have the following form:

$$\left[\mathrm{M} + x\mathrm{H} + y\mathrm{Zn} - 4y\mathrm{H}\right]^{x}$$

where x is the charge of the considered ion and y the number of zinc cations complexed to the peptide, which suggests a tetracoordinate geometry.[38] However, the tested 71-residues peptide contained two clusters of 4 cysteines. So more than the specific interaction with one cysteine residue, the zinc affinity for the cysteinyl motif has been investigated, which could explain the difference in the mass shift.

At low energy collision, the complex undergoes very low fragmentation, since the base peak remains the molecular ion (see Figure VI-11a). In addition, the $\mathbf{b_6^+}$+Zn-2H and $\mathbf{y_4^+}$+Zn-2H fragments are generated, and losses of water and of carboxyl group are also noticed, the latter being significantly higher than with the native peptide. The first fragment indicates that the charge is still carried by the lysine residue, the second one confirms this idea and also that zinc is coordinated to the cysteine residue and probably more on the C-terminus part of the peptide.

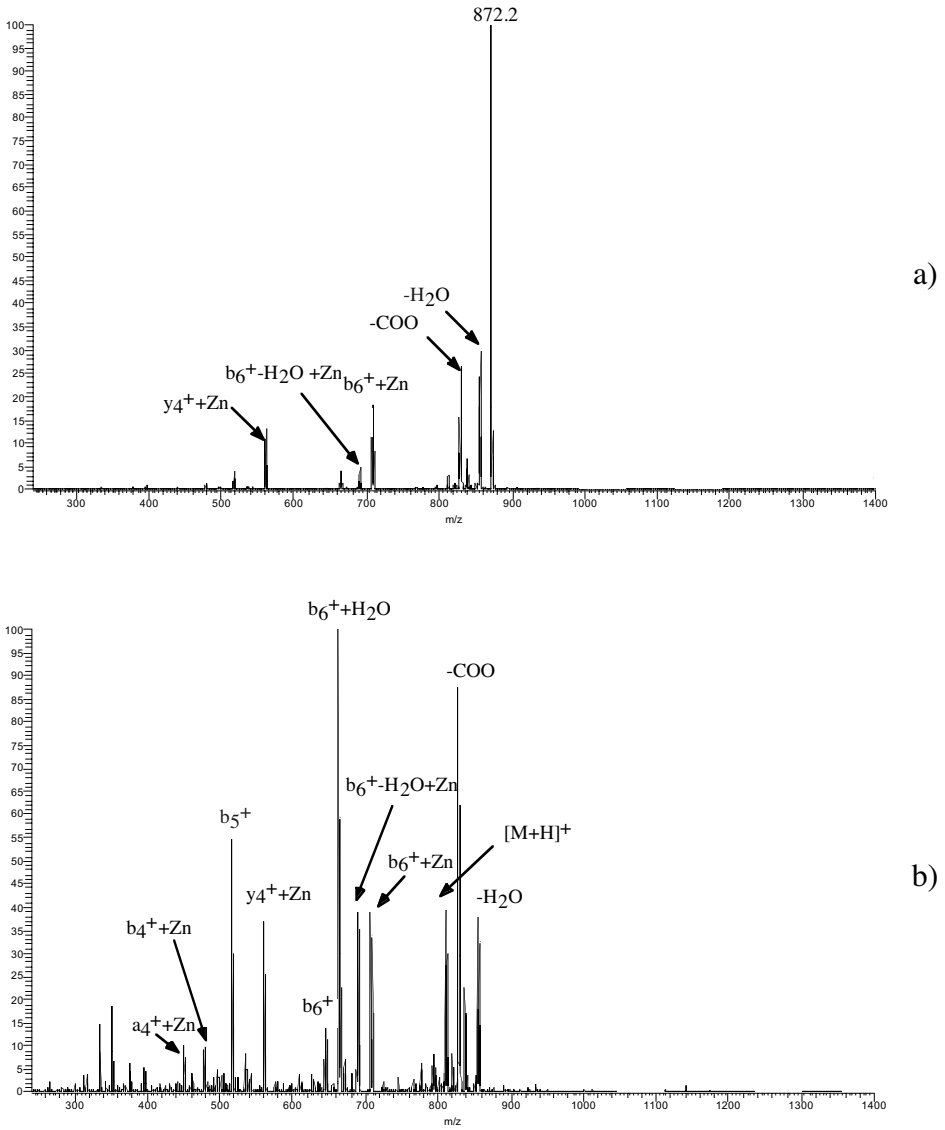

Figure VI-11. *Tandem MS spectrum on $[M+H+(Zn-2H)]^+$ (m/z 872.3) from the infusion of AIKCTKF using zinc electrode; Collision energy: a) 25%); b) 35%. To lighten the assignment, the shift Zn-2H, is only mentioned as Zn.*

At higher energy, these fragments are preserved. However, the base peak becomes ($\mathbf{b_6}^+$+H_20), a fragment coming from the native peptide, and the second most abundant is the loss of COO. The latter could indicate, as for the copper-angiotensin II complex, a coordination to the C-terminus residue (phenylalanine). The native peptide is also recovered. A comparison with the fragmentation of the latter (see Figure VI-3) shows that this pattern ($\mathbf{b_6}^+$+H_20, $\mathbf{b_5}^+$) is also obtained when the complex is broken. It is thus expected that the complexation of the peptide with Zn^{2+} is purely electrostatic and loose. In addition, the complexation does not stabilize the peptide as for copper. As indicated by the MS/MS studies, the pattern should be therefore KCT-F.

When the copper and zinc complexes are formed, their peak values (*m/z* 872.3) are the same. One way to distinguish them is to get a high-resolution mass spectrum to access to the isotopic distribution. However, with a low-resolution spectrum, a simple tandem analysis is satisfactory, since these complexes provide different fragmentation patterns (see Figure VI-7 and Figure VI-11).

4.4 On-line complexation with Nickel electrode

No biological system containing functionally significant nickel was known until 1975. Currently, four proteins or enzymatic systems are known to contain functional nickel: carbonyl dehydogenase, hydrogenases, methyl coenzyme M reductase cofactor F430, and ureases.[36] However, the redox role of nickel has been demonstrated for all these systems, except for ureases, even though it is thought that one polarizes the carbonyl group of urea while the second increases the nucleophilicity of a coordinated water molecule for further reaction on the carbonyl of urea. The high affinity of Ni^{2+} for imidazole is also widely used for affinity chromatography of histidine-containing peptides.

Angiotensin II

The complexation of Nickel with angiotensin II is markedly less efficient than with the previous metals, as illustrated by Figure VI-12. The mass shift corresponds to (Ni-2H), which indicates that the charge of the metal cation is intact. This mass shift is preserved when fragmentation is performed.

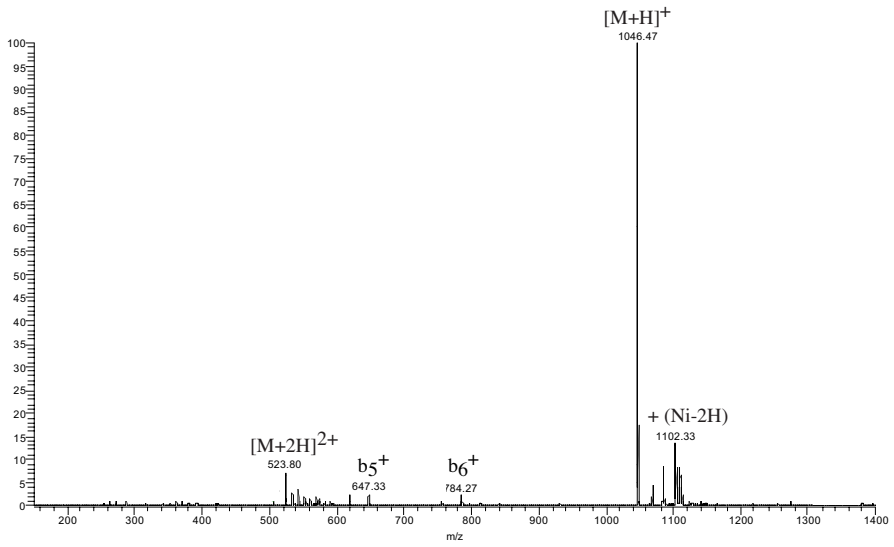

Figure VI-12. *Full scan MS from the infusion of angiotensin II using nickel electrode (t=4 min).*

At low collision energy, a strong fragmentation occurs between the tyrosine and isoleucine residues ($\mathbf{b_4}^+$+Ni-2H), as well as a less effective after histidine residue ($\mathbf{b_6}^+$+Ni-2H). The $\mathbf{b_4}^+$+Ni-type fragment has been also observed for numerous tetra and pentapeptides, indicating a square-planar coordination from the N-terminus.[39, 40]

The $\mathbf{b_6}^+$+Ni-type fragment observed reveals that probably there are two conformations for the complex: one strongly coordinated to the N-terminus and the second to the histidine side chain. The last coordination cannot involve the proline at the seventh position, since it prevents the anchoring to the peptide backbone. Therefore, the Ni^{2+} cation needs to bind to the tyrosine residue to complete the tetracoordination. However, it is also involved in the coordination to

the N-terminus. Therefore, the two coordinations cannot coexist. That is probably why a double complexation is not observed. The intense loss of water corroborates the supposition of two coordination possibilities on tyrosine.

It is worth noticing that a large amount of the intact complex is also detected, highlighting its strength. A small $\mathbf{y}_7^+$+Ni-2H is also observed, indicating that the fragmentation of the native peptide is not so affected by the complexation.

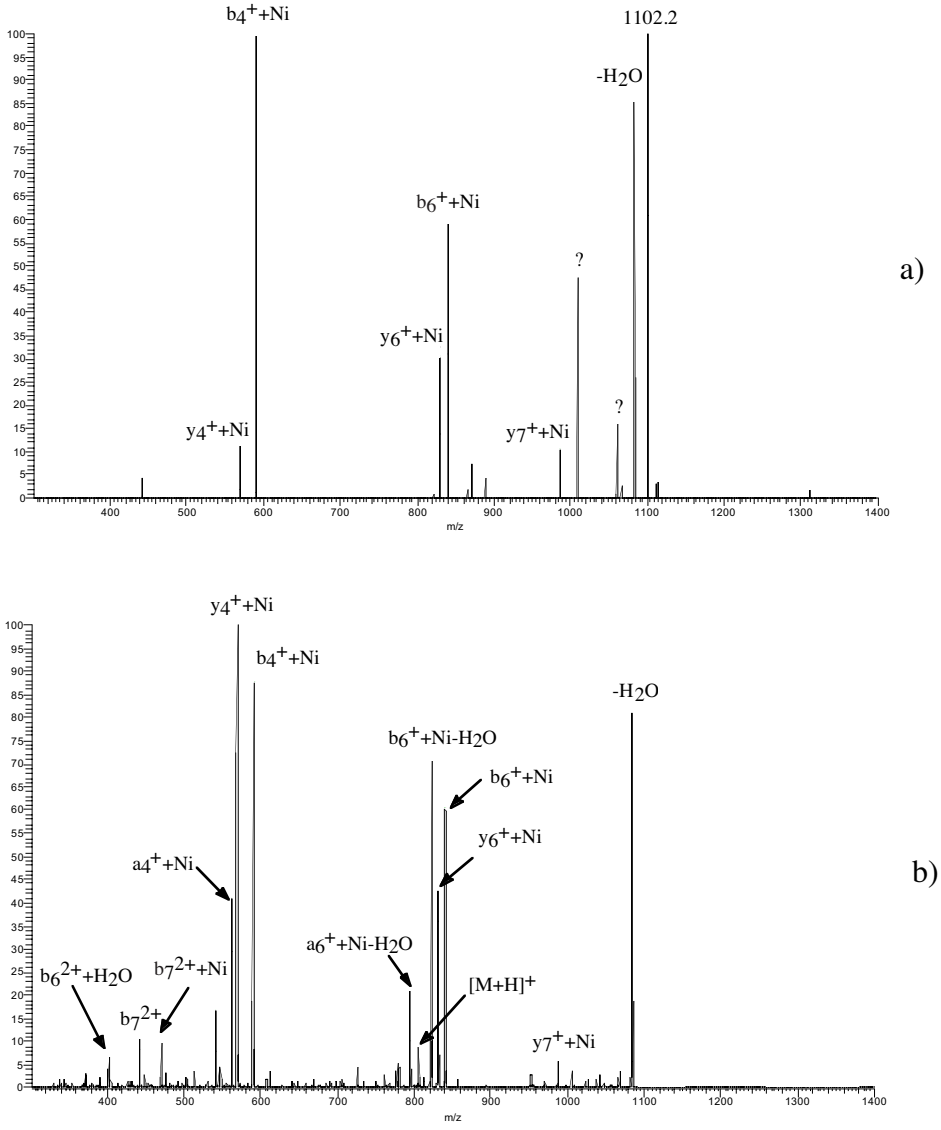

Figure VI-13. *Tandem MS spectrum on $[M+H+(Ni-2H)]^+$ (m/z 1102.3) from the infusion of angiotensin II (DRVYIHPF) using nickel electrode; Collision energy: a) 25%); b) 35%. To lighten the assignment, the shift Ni-2H, is only mentioned as Ni.*

The pattern of the zinc complex fragmentation at high energy is also observed here, suggesting similar coordination, strongly anchored to the histidine side chain (see Figure VI-9). The highest peak with a question mark could be due to the loss of the side chain of phenylalanine (mass shift=-93Da; side chain=91Da).[39, 41] It has been found to be indicative of the coordination of phenylalanine with metal ions.

At higher energy, the native peptide is recovered, as well as some of its fragments ($\mathbf{b_6^{2+}}$+H_2O, $\mathbf{b_7^{2+}}$). This is in agreement with previous results obtained by Hu and Loo.[30] Some new fragments indicating a bond breaking before the phenylalanine residue ($\mathbf{b_7^{2+}}$+Ni-2H, $\mathbf{y_7^{+}}$+Ni-2H) could come from the further fragmentation of the daughter ions, which are less stable due to the loss of phenylalanine side chain, since the corresponding peaks disappear at higher collision energy.

The major fragmentation pathways remain the same as for lower energy. The presence of the $\mathbf{y_4^{+}}$+Ni-2H and $\mathbf{b_4^{+}}$+Ni-2H fragments at higher energy confirms the dual coordination based on either the N-terminus or the histidine. The strong coordination from the N-terminus is confirmed by the investigations of Reiter et al.[39] Since the fragmentation pattern observed here is very close to the one for the zinc (see Figure VI-9), the coordination motif is probably identical, however, the stability of the Ni-complex seems to be lower according to the higher intensities of the fragments at the same collision energy and the slight recovery of the native peptide.

The complexation with the native peptide is thus presumed to be highly localized on the C-terminus side. The charge effect on the fragmentation is then preserved, except for the $\mathbf{y_7^{+}}$-type fragment, which is largely inhibited when a complex is formed. This could indicate a coordination motif between the nickel ion and the four residues tyrosine-isoleucine-histidine and phenylalanine, since no coordination can occur on the proline nitrogen.

Cysteinyl peptide

As for angiotensin II, the reaction of complexation seems very slow, since less than 7% of the peptide is converted after 3 minutes of infusion (see Figure VI-14). The associated mass shift corresponds to (Ni-2H), which indicates an electrostatic interaction only.

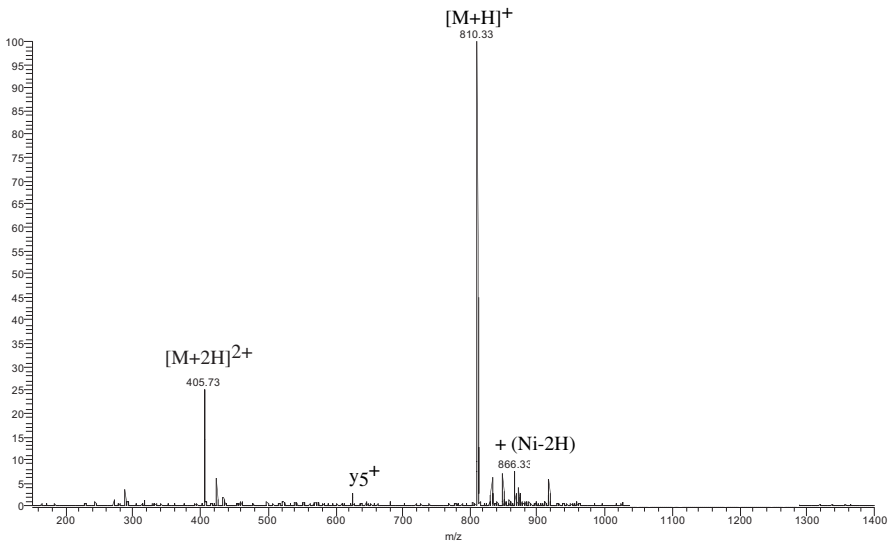

Figure VI-14. *Full scan MS from the infusion of AIKCTKF using nickel electrode (t=3 min).*

The MS/MS spectrum is quite identical to the one of zinc-peptide complex (see Figure VI-10 and Figure VI-15). However, the stability of the Ni complex is much higher than all the other metal-complexes investigated, as the intensities of the fragments are markedly reduced. It is probably more influenced by the intrinsic stability of the peptide than oriented by the complexation, as for metals already tested.

For the higher collision energy, the complex is not completely fragmented. However, the native peptide is also detected along with some fragments. The complex fragments are found to be quite identical to those of the native form, except for the carboxyl group loss. This confirms the fact that the structure of the peptide is not really affected by the complexation Furthermore, conversely to investigations on peptides complexed with Ni^{2+},[39] as well as on

angiotensin II (see Figure VI-13a), the $\mathbf{b_4^+}$ fragment is poorly generated. Therefore the cysteine residue is probably a stronger anchoring point for the metal cation, as also observed for oxidized insulin chain A.[40] The slightly higher COO loss than for the native peptide is probably due to the fact that the latter and the complex are fragmenting through this pathway.

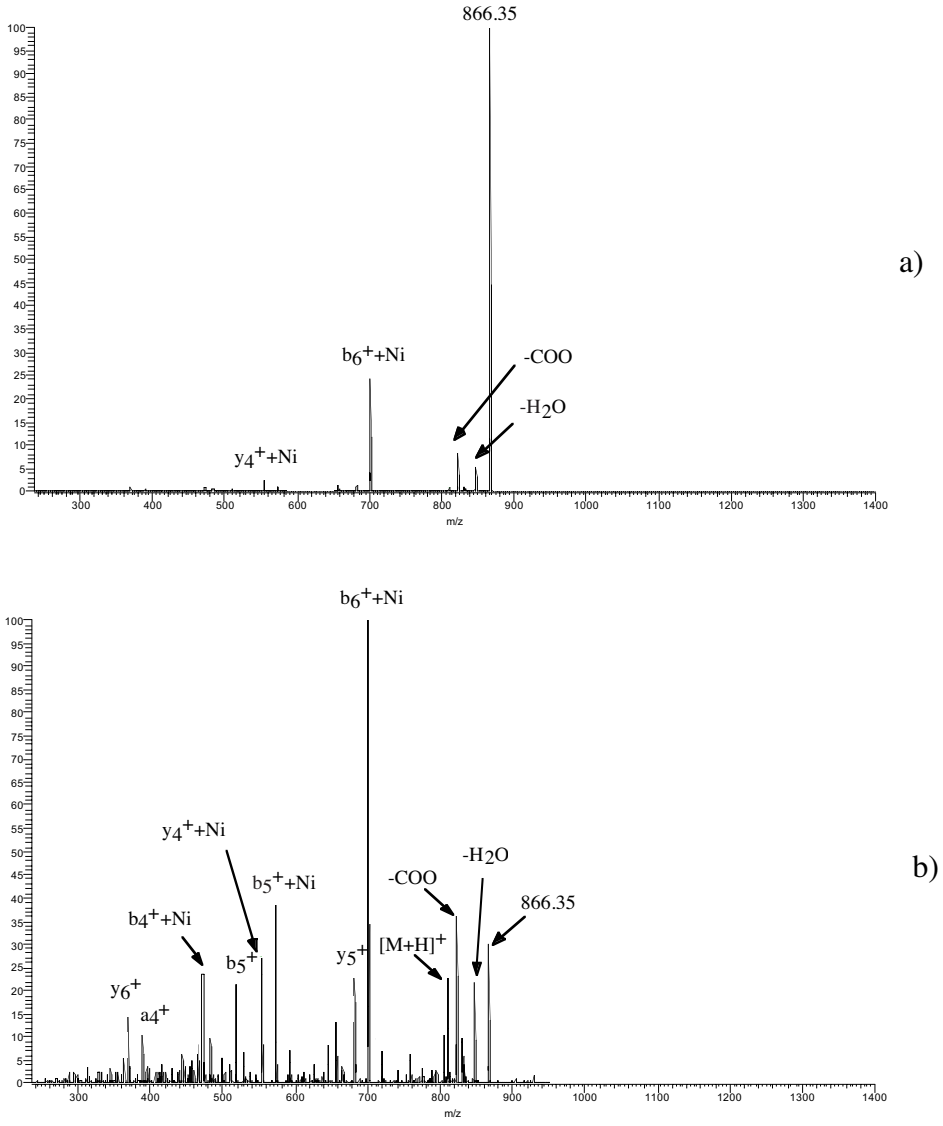

Figure VI-15. *Tandem MS spectrum on $[M+H+(Zn-2H)]^+$ (m/z 872.3) from the infusion of AIKCTKF using nickel electrode; Collision energy: a) 25%); b) 35%. To lighten the assignment, the shift Ni-2H, is only mentioned as Ni.*

4.5 On-line complexation with Iron electrode

Fe^{2+} is a borderline Lewis acid, and it can bind to both hard and soft ligands. Binding to soft ligands, however, will result in a greater degree of covalence and lead to more stable complexes. The interaction of iron ions and sulfides is common in all biological systems, and these groups are found at the active centers of a wide variety of redox and catalytic proteins.

Angiotensin II

No iron adduct was detected on angiotensin II when Fe^{2+} was already present in solution, together with a diimine ligand, namely 2,2'-bipyridyl.[9] However, with the help of iron cation electrogeneration using a rusted iron wire as electrospray electrode, Smith et al. could detect some peptide-metal ion complex in an acidic medium.[42]

The complex formation with iron is quite low, as shown in Figure VI-16. The mass shift corresponds to (Fe-2H).

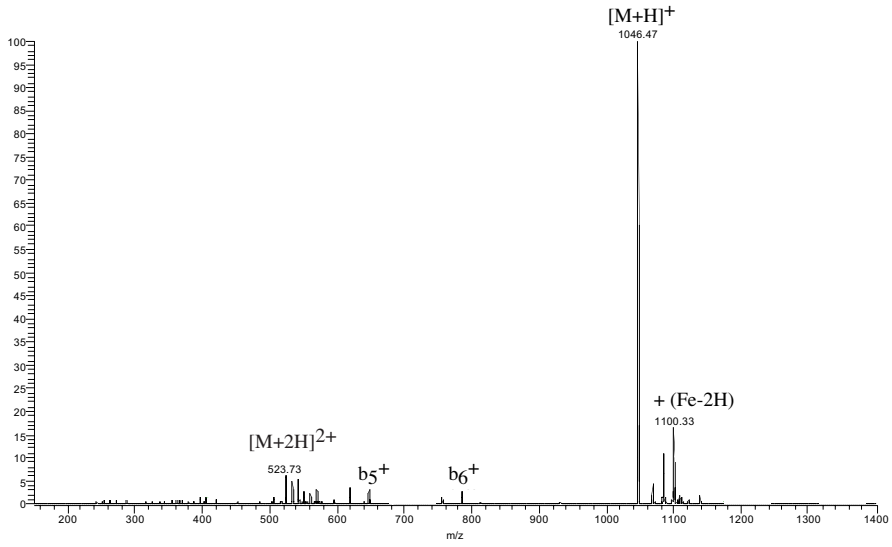

Figure VI-16. *Full scan MS from the infusion of angiotensin II using iron electrode (t=2 min).*

When fragmentation is performed on the complex, the major pathway is water loss, as illustrated in Figure VI-17. At low energy, a part of the native peptide is already recovered,

and a mixture of fragments coming from the latter as well as the adduct is observed at higher energy, but still with a low intensity. No COO loss is observed, suggesting that the coordination does not occur through the C-terminus carboxylic group.

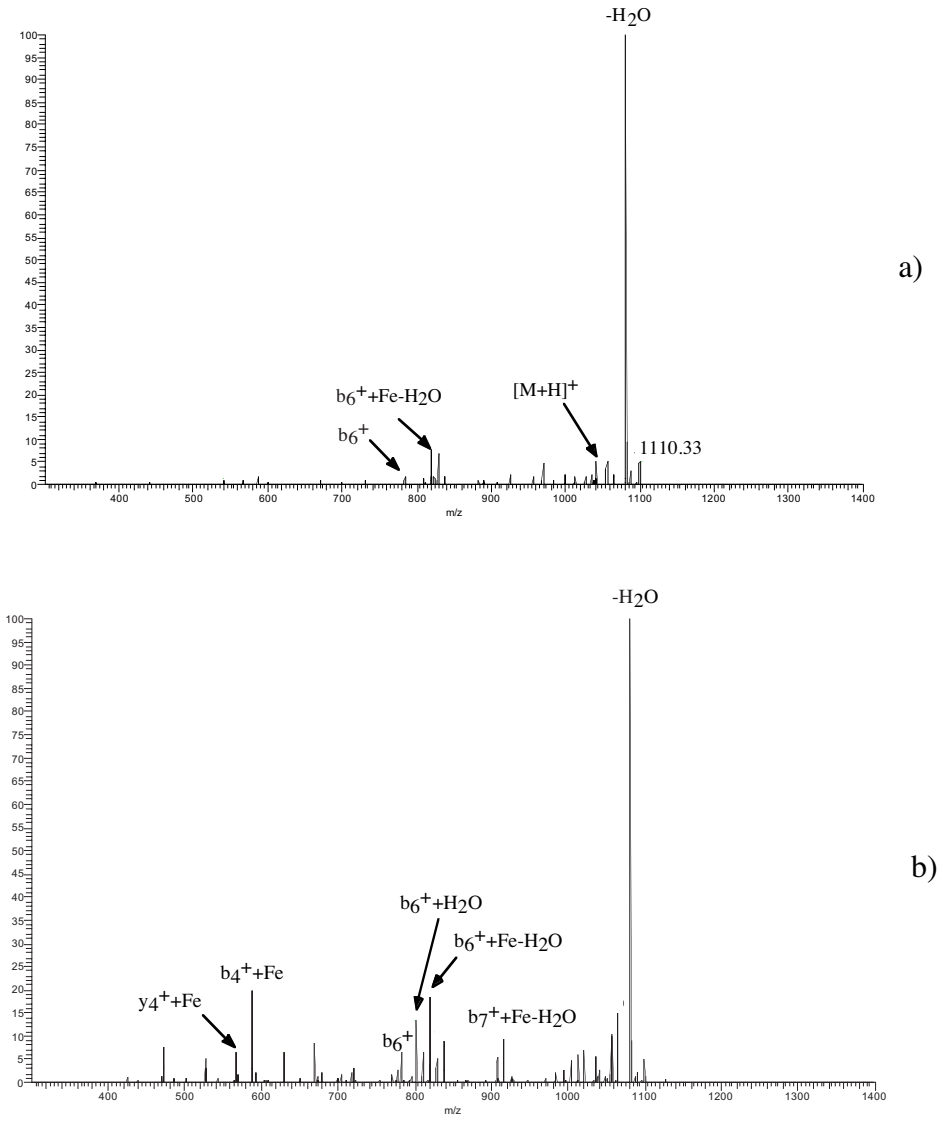

Figure VI-17. *Tandem MS spectrum on $[M+H+(Fe-2H)]^+$ (m/z 1110.33) from the infusion of angiotensin II (DRVYIHPF) using iron electrode; Collision energy: a) 25%); b) 35%. To lighten the assignment, the shift Fe-2H, is only mentioned as Fe.*

The fragmentation pattern suggests that the loss of water is induced by the coordination of iron to tyrosine, confirmed by the presence at higher energy collision of the $\mathbf{b_4}^+$ and $\mathbf{y_4}^+$-type

fragments. Except for $\mathbf{y_7}^+$-type fragment, the pattern of the native peptide is recovered. Thus, the coordination of the complex is tight, however, when it is broken, no rearrangement is possible, therefore the stabilization of the fragment occurs by the decomplexation. The coordination is likely anchored to the histidine residue, then on tyrosine, isoleucine and valine.

Cysteinyl peptide

Specific and strong interactions of iron with sulfur from the thiol group of the cysteine side-chain have been observed, demonstrated by the highly specific fragmentation, which ends up with abundant $\left[a_n - 2\mathrm{H} + \mathrm{Fe}\right]^+$ ions, where n is the position of cysteine residues in the peptide chain, characterized by a lower intensity when n increases, i.e. cysteine is more distant from the N-terminus.[43] For peptides containing 2 cysteine residues, an internal ion is also detected, resulting from the interaction of Fe and both thiols.[2]

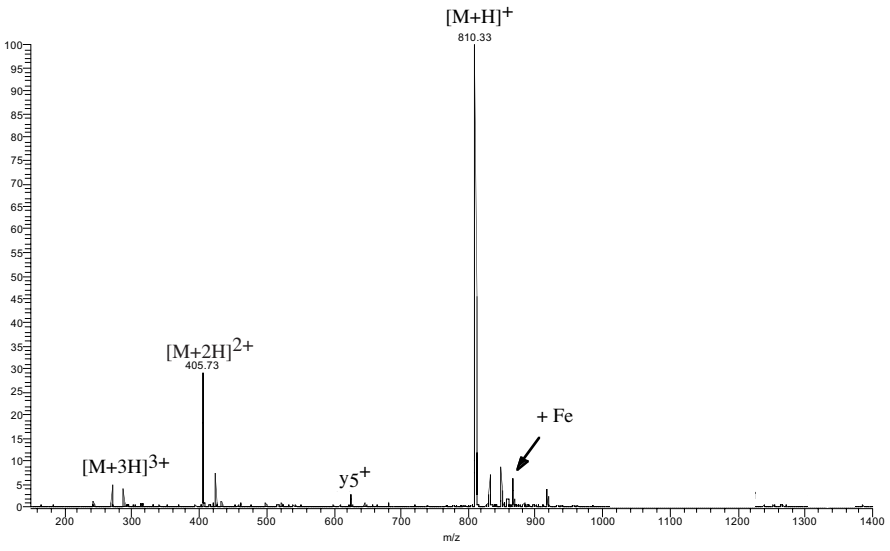

Figure VI-18. *Full scan MS from the infusion of AIKCTKF using iron electrode (t=3min).*

In this particular case, the mass shift corresponds to the monoisotopic mass of the iron, which means that the coordination is different from the one with angiotensin II. In addition, this mass

shift is not in accordance with results obtained under different conditions by Nemirovskiy et al.,[2, 43] since they reported a (Fe-H) shift for the adduct.

When fragmentation is performed on the complex, a double pattern is observed, one coming from the peptide, and its equivalent from the complex. The interaction of the metal with the peptide is too low to hinder the intrinsic stability of the peptide.

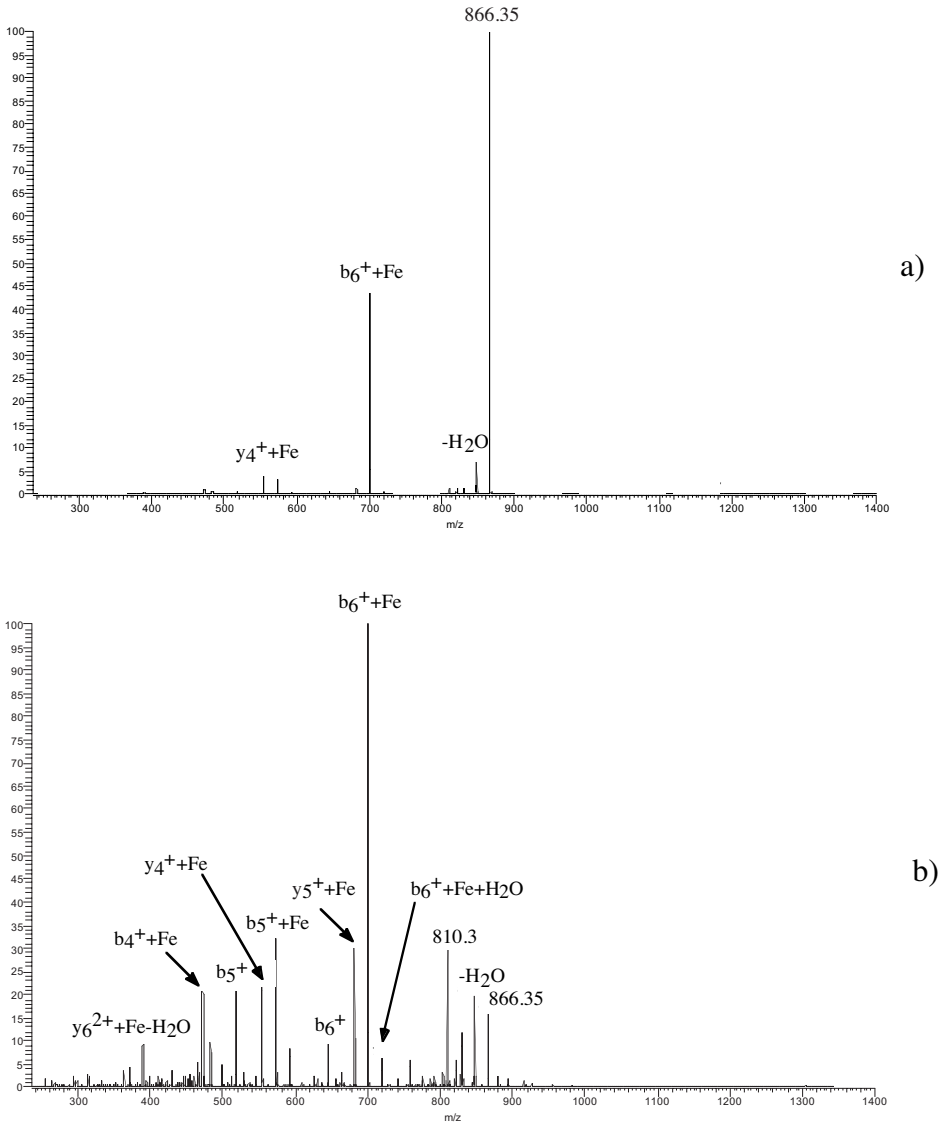

Figure VI-19. *Tandem MS spectrum on $[M+H+Fe]^+$ (m/z 866.35) from the infusion of AIKCTKF using iron electrode; Collision energy: a) 25%); b) 35%.*

It must be stressed here that the mass of this complex is the same as the Ni-peptide adduct. Whatever the energy, no real difference between the Ni and Fe complexes can be observed when Tandem MS is performed (see Figure VI-15 and Figure VI-19), except the presence of the peak corresponding to the COO loss. This is therefore the only way to distinguish the two adducts, apart from high-resolution spectra. In other words, the coordination of Nickel could involved the carboxyl group of the C-terminus of the peptide, while iron is probably coordinated to the amide of the peptide backbone.

The low efficiency of the complex formation with Fe could be related to the electrode, which was not a pure Fe electrode. A Fe reduced material should be used, or Fe should be electroplated on an inert electrode in order to get a pure Fe sacrificial layer.

Another possibility for the low efficiency is the homogeneous reaction of ferrous ion with water and oxygen (see reaction (79)), which results in the precipitation of FeOOH on the electrode,[44] i.e. rust.

$$2Fe^{2+} + 3H_2O + \frac{1}{2}O_2 \rightarrow FeOOH + 4H^+ \qquad (79)$$

This implies that the electrogeneration of Fe^{2+} for complexation should be carried out in degassed solutions to avoid any passivation of the electrode, with an electroplated channel flow cell electrode. The reaction (79) also induces a pH drop, which could result in the appearance of the $[M+3H]^{3+}$ on the spectrum (see Figure VI-18). In addition, the formation of an oxide layer decreases the surface of iron available for oxidation. Therefore, some water oxidation could also take place in order to maintain the i_{ES} level, inducing a pH drop as well. Another problem could be the reoxidation of ferrous ion to ferric ion. Since the oxidation state is increased, the coordination can be drastically modified.

To identify if the oxidation state of the iron could affect the efficiency of the complexation, $FeSO_4$ and $FeCl_3.6H_2O$ salts were successively tested, using a platinum electrode to generate the spray. However, not only the oxidation state does not dramatically change the complexation efficiency, but none of the mass shifts obtained for those complexes (Fe-2H and Fe-3H for the Fe(II)- and the Fe(III) salt, respectively) correspond to the mass shift obtained with the iron sacrificial electrode. Therefore, the complex formation by using the sacrificial electrode does not follow the same pathway. Lastly, the MS/MS spectra of the complexes obtained by addition of Fe(II) salt and with the sacrificial electrode are completely different at low and high energy. The Fe(II)-complex fragmentation presents two main peaks at low energy, corresponding to the loss of COO and water, while at high energy a second loss of water is observed in addition to the above mentioned peaks. Neither fragments from the peptide nor its corresponding molecular ion were observed. However, $\mathbf{y_4}^+$-type and $\mathbf{b_6}^+$-type fragments are generated, as for the Fe(0)-complex. Therefore, the coordination of the two considered complexes is completely different. The formation of small clusters on the electrode could explain this surprising behavior. A cyclic voltammetric study could be helpful to unravel mechanisms involved with both complexations, at least occurring in the solution phase.

4.6 On-line complexation with Silver electrode

Silver ion is not involved in any biochemical interactions, despite its use as an antibacterial agent. However, silver complexation is widely used to stain in-gel proteins. Silver(I) has indeed been found to form aqueous phase complexes with both sulfur and non-sulfur bearing peptides and proteins.[45] The abundance of the silver(I)-containing ions has been shown to be correlated to the that of the protonated ions, as the peptide length is increased. This effect is markedly enhanced for methionine-containing peptides.[45] Although methionine acts as a silver anchoring point, the Collision Induced Dissociation (CID) studies have revealed the formation of silver/peptides product ions that are free of sulfur.

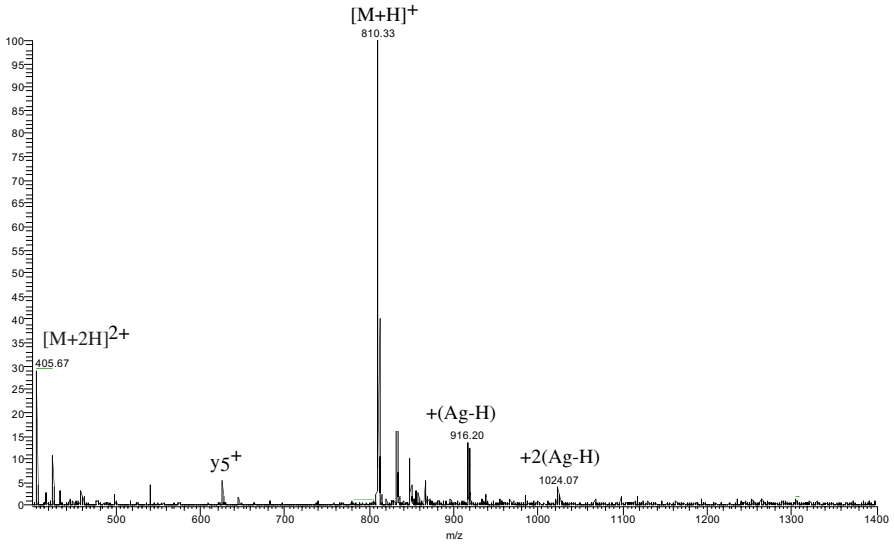

Figure VI-20. *Full scan MS from the infusion of AIKCTKF using silver electrode (t=3min).*

Nevertheless, no complexation was observed to occur with angiotensin II after 10 minutes of infusion, in agreement with the classification of hard/soft metals and ligands (see Table VI-1). With the cysteine containing peptide (AIKCTKPF), a single and a double adduct are formed, as shown in Figure VI-20. The mass shift corresponds to (Ag-H). However, it must be stressed here that no noticeable doubly-charged complex is detected. This could mean that part of the complex is formed by exchange of the proton giving a charge to the peptide with a silver ion.

The low complexation could be due to a passivation of the electrode. For instance, an oxide film Ag_2O could be generated at the electrode surface or a thin AgCl film due the presence of chloride ions as impurity, therefore preventing the silver ions to react with the peptides.

The fragmentation pattern is quite close to the one of copper (see Figure VI-7), except that the native peptide is recovered, suggesting a loose electrostatic nature of the coordination. No fragment of the latter is observed however. Nonetheless, the $\mathbf{y_4}^+$-NH_3-type fragment indicates a strong coordination with the cysteine residue as for copper. Referring to Figure VI-7, the absence of $\mathbf{b_3}^+$ and $\mathbf{b_4}^+$-type fragments at low energy (as well as $\mathbf{b_3}^+$ at high energy) is a sign of a particularly strong binding on lysine and cysteine residues.

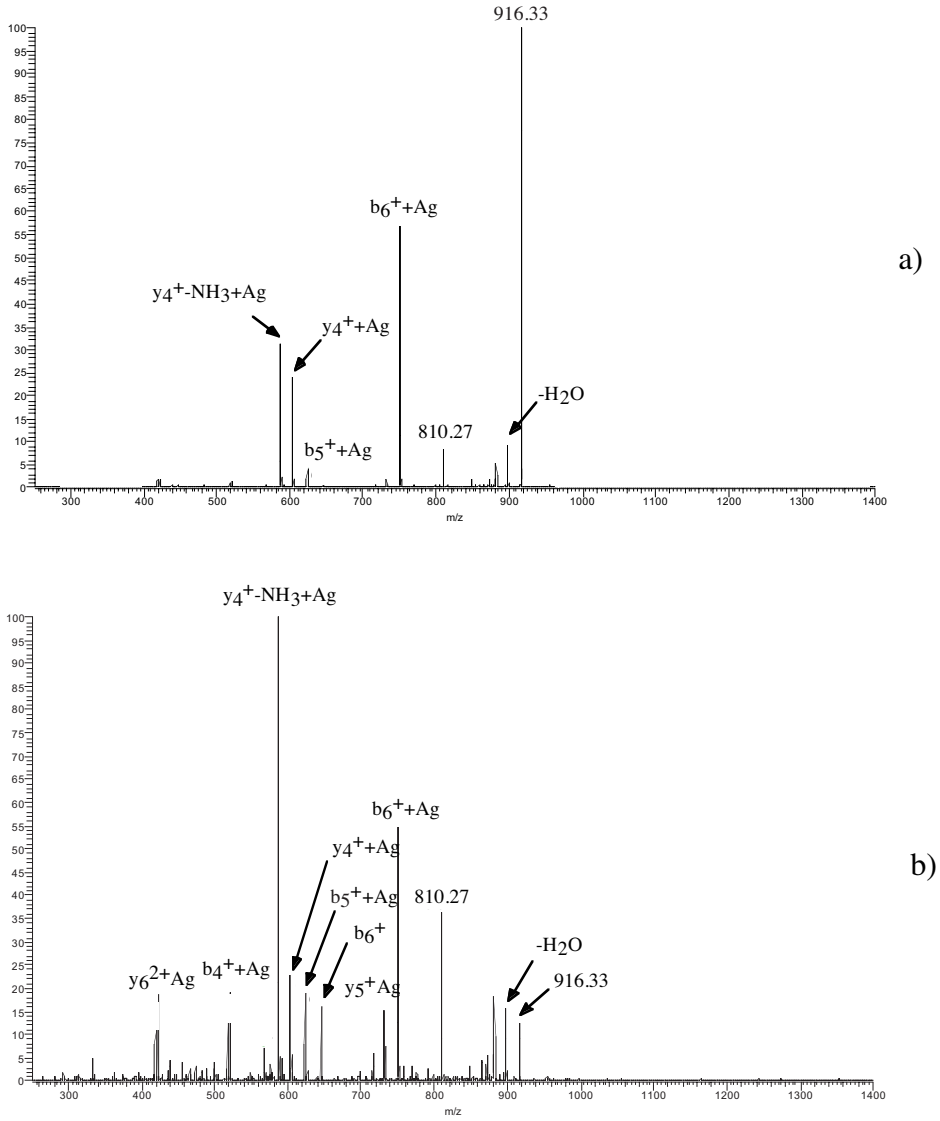

Figure VI-21. *Tandem MS spectrum on $[M+H+(Ag-H)]^+$ (m/z 916.3) from the infusion of AIKCTKF using silver electrode; Collision energy: a) 25%); b) 35%. To lighten the assignment, the shift Ag-H, is only mentioned as Ag.*

The strength of the complex is maybe lowered from the two other coordinations, due to the soft nature of silver, which reduces the chance to get strong coordination with other ligands, compared to Cu^{2+}, which is a borderline Lewis acid. The distinction between the two complexes fragmentation can be made also by the lack of COO loss, suggesting no coordination through the carbonyl of the C-terminus residue when silver is used, and a reduced water loss.

The fragmentation of the double complex results in a strong $\mathbf{b_6^+}$-type fragment, with low $\mathbf{a_4^+}$ and $\mathbf{b_4^+}$-type fragments at higher energy. This indicates that the double complex is much more tight than the single one and that the coordination stabilize much more the peptide than the first coordination, with a strong interaction with the cysteine and, the second lysine keeping the charge-induced behavior of the native peptide.

4.7 Summary and discussion

The mass shifts for every metal-ligand couple is given in Table VI-2. It has been demonstrated that the charge compensation due to metal complexation is usually enforced. The protons lost for charge compensation are likely to be different from those carrying the charge of the native peptides.[45] The deprotonation can occur at the C-terminus carboxylic group or at the phenol moiety of tyrosine residue,[46] but the most likely source is the protons from the amide groups coordinated to the metal ion.

However, the charge compensation has been found to be uncompleted for the copper and iron complexes with the cysteinyl peptide (one proton and no proton loss, respectively). Other cysteinyl-peptides should be tested in order to attribute this behavior to the only presence of this residue and/or the use of sacrificial electrode in the case of iron.

Concerning the stability of the different complexes, it has been found that the copper complexation is the strongest, since no recovery of the peptides has been observed when fragmentation is performed. Apart from the latter, the strongest complex for the angiotensin II is with iron (lowest fragment intensities), while it is with the nickel for the synthetic peptide, even though the reactions are slow. Concerning the residues, histidine seems to be the amino acid with the highest affinity for metal ions. Indeed, except for the iron, no fragment coming from the native peptide is induced by the CID of the complexes, highlighting a strong

coordination with the metal ions. This is not the case of the synthetic peptide, for which each CID on the complexes comes up with a recovery of the native molecule.

	Cu	**Zn**	**Ni**	**Fe**	**Ag**
Angiotensin II	60.95	61.90	55.83	53.82	-
AIKCTPF	61.89	61.84	55.94	55.97	105.94
Isotopic masses	62.93 64.92 (44%)	63.93 65.92 (57%)	57.93 59.93 (38%)	55.93 53.93 (6%)	106.90 108.9 (92.9%)

Table VI-2. *Mass shifts obtained with the different electrodes, with the metal isotopic masses.*

The use of MS/MS to identify the metal ion chelating with a peptide and the corresponding motif coordination has been found to be an efficient tool. Although some complexes of the peptide, such as with copper and zinc, can not be resolved in MS due to the same shift value, the fragmentation pattern allows a confident analysis of the complex. Specific losses have been found to occur under fragmentation for most of the complexes. Apart form the tyrosine and threonine, the loss of water could also come from the C-terminal amino acid because all peptides studied here contain are free of any modification.[2]

The similarity of tandem MS spectra can also help to corroborate the coordination of metal ions. Thus, the coordination of Ni to angiotensin II has been found to be strong on the histidine and on the N-terminus side. According to this observation, the coordination of zinc is confirmed on the histidine, valine and tyrosine, but also on the N-terminus.

The different tagging efficiencies have been summarized in Table VI-3, as well as the solvation time, i.e. mean lifetime of a single water molecule in the first coordination sphere of the metal ion. Apart from the amino acids affinities with the metal, the solvation time is also

relevant for the complexation. Copper is therefore the metal that has the highest apparent affinity with the peptides. Histidine is definitely a primary amino acid as an anchor for Zn, since a very high tagging yield is obtained despite the low solvation time of the metal.

	AngII+M^{a+}	**Pep+M^{a+}**	**AngII+2M^{a+}**	**Pep+2M^{a+}**	**Solvation time**
Cu^{2+}	58%	55%	5%	61%	10^{-9} s
Zn^{2+}	70%	25%	4%	5%	10^{-7}s
Fe^{2+}	9%	7%	--	--	10^{-6} s
Ni^{2+}	15%	7%	--	--	10^{-4} s
Ag^{+}	--	19%	--	6%	--

Table VI-3. *Adduct relative intensities after 5 minutes infusion (100%= native peak) for each experiment. Solvation times correspond to mean lifetimes of a single water molecule in the first coordination sphere of a given metal ion.*

For each peptide, a decrease of the signal-to-noise ratio has also been observed, particularly when the copper electrode is used, as well as the appearance of sodium and potassium adducts, which were not observed for nanospray generation with a platinum wire. Surprisingly, the same additions were observed by Jiao et al,[47] although copper salts were used. They attributed these peaks to a contamination coming from the salt sample. However, this is not likely in the sacrificial electrode case. Hence, this phenomenon could be linked to the complexation reaction.

Based on experiments done with 100μM CuSO4 mixtures, the estimated concentration of the electrogenerated ions should be somewhat lower but within the same range. This means that the position of the electrode with respect to the microchannel inlet is a key issue to get an

equivalent efficiency for the on-line complexation. Therefore, the use of embedded sacrificial microelectrode seems to be the best option to study the on-line complex formation in a reproducible manner.

The best candidates for this method are copper and zinc electrodes, which besides are the most abundant metals involved in metalloproteins. The implementation of this technique for nickel, iron and silver seems to be difficult, due to uncontrolled film formations at least for the two last metals. The low efficiency of nickel complexation has to be investigated more to rule out any hindrance from the on-line system, as well as the formation of iron-cysteinyl peptide due to its amazing behavior.

5. Conclusions

The fragmentation patterns are indicative of the complex stability and the metal ion associated can be easily identified from the pattern and/or the mass shift from the native. As a conclusion, a motif more than a amino acid could be highly specific to a metal ion, such as also demonstrated by Fenselau's group[48] as well as Volz and co-workers.[49] Copper complex on-line generation and subsequent MS/MS study could be a smart way to detect C-terminus modifications, such as amidation (characteristic feature of peptide hormones), since the loss of carboxyl group under fragmentation is inhibited by the derivatization of the C-terminus.

Using both presented configurations of the chip, a full study could also be carried out. Using the in-channel electrode chip in simple infusion configuration (pressure pumping) as presented in Chapter 4, steady states could be established and the conditions to get (or to avoid) a given modification, such as chip design could be optimized.[50] Furthermore, the carbon electrode could be plated with a chosen metal, avoiding multiple nanospray interfaces.

The chip using a wire in a low-volume reservoir, placed at a defined distance from the microchannel inlet, (electroosmotic pumping) could be used to directly monitor the complexation reaction, as already done for protein digestion or denaturation.[51] Therefore, one could get access to the kinetic of the reaction and the effect of solution composition on the formation and the stability of the non-covalent complexes, especially for natural metalloproteins. The study of argentinated complexes could also help to understand the mechanism involved in the gel silver staining. Lastly, taking advantage of the high surface-to-volume ratio of the channel flow cell, the on-line tagging of histidine and cysteine by copper could be used to get additional sequential and structural information on a protein or peptide mixture, additionally preventing any problem of signal-to-noise ratio deterioration. Finally, investigations on the efficiency of the tagging, especially pH conditions for on-line complexation should be carried out however. The complex anchor can actually change depending on the pH of the infused solution, such as for phosphorylated peptides, for which, contrary to usual IMAC, the immobilization through the phosphate groups occurs at low pH and the release when an alkaline buffer is infused.

6. References

(1) Mirza, U. A.; Chait, B. T. *Anal. Chem.* **1994,** *66*, 2898-2904.
(2) Nemirovskiy, O. V.; Gross, M. L. *J. Am. Soc. Mass Spectrom.* **1996,** *7*, 977-980.
(3) Glusker, J. P. In *Advances in Protein Chemistry*; Academic Press, 1991; Vol. 42.
(4) Porath, J.; Carlsson, J.; Olsson, I.; Belfrage, G. *Nature* **1975,** *258*, 598-599.
(5) Zhou, W.; Merrick, B. A.; Khaledi, M. G.; Tomer, K. B. *J. Am. Soc. Mass Spectrom.* **2000,** *11*.
(6) Gatlin, C. L.; Turecek, F.; Vaisar, T. *J. Mass Spectrom.* **1995,** *30*, 1605-1616.
(7) Gatlin, C. L.; Turecek, F.; Vaisar, T. *J. Mass Spectrom.* **1995,** *30*, 1617-1627.
(8) Gatlin, C. L.; Rao, R. D.; Turecek, F.; Vaisar, T. *Anal. Chem.* **1996,** *68*, 263-270.
(9) Gatlin, C. L.; Turecek, F. *J. Mass Spectrom.* **1995,** *30*, 1636-1637.
(10) Alvarez, E. J.; Brodbelt, J. S. *J. Am. Soc. Mass Spectrom.* **1998,** *9*, 463-472.

(11) Zhao, H.; Adams, J. *Int. J. Mass Spectr. Ion Proc.* **1993,** *125*, 195-205.

(12) Hu, P.; Gross, M. L. *J. Am. Soc. Mass Spectrom.* **1994,** *5*, 137-143.

(13) Roepstorff, P. *Biomedical mass spectrometry* **1984,** *11*, 601.

(14) Biemann, K. *Biomedical and Environmental Mass Spectrometry* **1988,** *16*, 99-111.

(15) Blades, A. T.; Ikonomou, M. G.; Kebarle, P. *Anal. Chem.* **1991,** *63*, 2109-2114.

(16) Van Berkel, G. J. *J. Mass Spectrom.* **2000,** *35*, 773-783.

(17) Sigel, H.; Martin, R. B. *Chem. Rev.* **1982,** *82*, 385-426.

(18) Sullards, M. C.; Reiter, J. A. *J. Am. Soc. Mass Spectrom.* **2000,** *11*, 40-53.

(19) Papayannopoulos, I. A. *Mass Spectrom. Rev.* **1995,** *14*, 49-73.

(20) Biemann, K. *Methods Enzymol.* **1990,** *193*, 351-360.

(21) Schlosser, A.; Lehmann, W. D. *J. Mass Spectrom.* **2000,** *35*.

(22) Kish, M. M.; Wesdemiotis, C. *Int. J. Mass Spectrom.* **2003,** *227*, 191-203.

(23) Reid, G. E.; Simpson, R. J.; O'Hair, R. A. J. *J. Am. Soc. Mass Spectrom.* **1998,** *9*, 945.

(24) Lacher, N. A.; Garrison, K. E.; Lunte, S. M. *Electrophoresis* **2002,** *23*, 1577-1584.

(25) Gawron, A. J.; Lunte, S. M. *Electrophoresis* **2000,** *21*, 2067-2073.

(26) Schwarz, A.; Bagel, O.; Girault, H. H. *Electroanalysis* **2000,** *12*, 811-815.

(27) Gawron, A. J.; Lunte, S. M. *Electrophoresis* **2000,** *21*, 3205-3211.

(28) Gatlin, C. L.; Turecek, F.; Vaisar, T. *J. Am. Chem. Soc.* **1995,** *117*, 3637-3638.

(29) Hutchens, T. W.; Allen, M. H. *Rapid Comm. Mass Spectrom.* **1992,** *6*, 469-473.

(30) Hu, P.; Loo, J. A. *J. Am. Chem. Soc.* **1995,** *117*, 11314-11319.

(31) Sigel, A.; Sigel, H. *Probing of proteins by metal ions and their low-molecular-weight complexes*; Marcel Dekker: New York, 2001.

(32) Katayama, A.; Kamidate, T.; Morita, M.; Watanabe, H. *Analytical Sciences* **1991,** *7*, 633-636.

(33) Brust, M.; Blass, P. M.; Bard , A. J. *Langmuir* **1997,** *13*, 5602-5607.

(34) Zhang, W. W.; Lu, C. S.; Zou, Y.; Xie, J. L.; Ren, X. M.; Zhu, H. Z.; Meng, Q. J. *J. Colloid Interface Sci.* **2002,** *249*, 301-306.

(35) O'Hair, R. A. J.; Styles, M. L.; Reid, G. E. *J. Am. Soc. Mass Spectrom.* **1998,** *9*, 1275-1284.

(36) Kendrick, M. J.; May, M. T.; PLishka, M. J.; Robinson, K. D. *Metal ions in biological systems*: Chichester, 1992.

(37) Loo, J. A.; Hu, P.; Smith, R. D. *J. Am. Soc. Mass Spectrom.* **1994,** *5*, 959-965.

(38) Allen, M. H.; Hutchens, T. W. *Rapid Comm. Mass Spectrom.* **1992,** *6*, 308-312.

(39) Reiter, A.; Adams, J.; Zhao, H. *J. Am. Chem. Soc.* **1994,** *116*, 7827-7838.

(40) Ho, Y.; Li, H.; Lu, L. *Int. J. Mass Spectrom.* **2003,** *227*, 97-109.

(41) Hu, P.; Gross, M. L. *J. Am. Chem. Soc.* **1993,** *115*, 8821-8828.

(42) Smith, A. D.; Moini, M. *Anal. Chem.* **2001,** *73*, 240-246.

(43) Nemirovskiy, O. V.; Gross, M. L. *J. Am. Soc. Mass Spectrom.* **1998,** *9*, 1285-1292.

(44) Landolt, D. In *Traite des Materiaux*; PPUR, Ed.; PPUR: Lausanne, 1993; Vol. 12, pp 316-324.

(45) Li, H.; Siu, K. W. M.; Guevremont, R.; Le Blanc, J. C. Y. *J. Am. Soc. Mass Spectrom.* **1997,** *8*, 781-792.

(46) Marzluff, E. M.; Campbell, S.; Rodgers, M. T.; Beauchamp, J. L. *J. Am. Chem. Soc.* **1994,** *116*, 7787.

(47) Jiao, C. Q.; Freiser, B. S. *J. Am. Soc. Mass Spectrom.* **1995,** *6*, 521-524.

(48) Fabris, D.; Zaia, J.; Hathout, Y.; Fenselau, C. *J. Am. Chem. Soc.* **1996,** *118*, 12242-12243.

(49) Volz, J.; Bosch, F. U.; Wunderlin, M.; Schuhmacher, M.; Melchers, K.; Bensch, K.; Steinhilber, W.; Schafer, K. P.; Toth, G.; Penke, B.; Przybylski, M. *J. Chromatogr. A* **1998,** *800*, 29-37.

(50) Van Berkel, G. J.; Asano, K. G.; Kertesz, V. *Anal. Chem.* **2002,** *74*, 5047-5056.

(51) Fligge, T. A.; Bruns, K.; Przybylski, M. *J. Chromatogr. B* **1998,** *706*, 91-100.

Chapter VII : Conclusions and perspectives

In the present work, a polymer nanospray interface for mass spectrometric analysis has been developed and characterized. The fast prototyping as well as the flexibility provided by photoablation micromachining of polymers has been used to design and fabricate a miniaturized interface having a microchannel with well-defined dimensions and an inlet reservoir. A thick-film microelectrode can easily be integrated in the microchannel, in order to apply the high voltage necessary to generate the electrospray at the outlet of the channel.

Three different designs have been used during this work: the flat-edge and the V-shaped interfaces with an embedded electrode, as well as the v-shaped nozzle using an electrode in the solution reservoir. The flat-edge interface with an embedded microelectrode is adapted to pressure-driven flows and has been found to reach low detection limit. The particularity of this interface is the presence of insulating parts surrounding the outlet of the microchannel that could induce a focalization of the current lines and therefore a higher transmission efficiency to the mass spectrometer. This design is however not well adapted to pumping by electroosmotic flow (EOF), if the interface electrode is also used to generate the EOF. Some surface treatments, such as deposition of Teflon-like polymers by Plasma Enhanced Chemical Vapor Deposition (PECVD) could help to enhance the hydrophobicity of the surface at the outlet of the nanospray, and therefore restrict the anchoring area for the Taylor cone. The V-shaped nozzle has been found to be the easiest to use, regardless of the configuration used (i.e. embedded electrode and pressure-driven flow, or in-reservoir shared electrode and EOF). This design has been found to confine the Taylor cone at the outlet, and to enhance the stability of the signal.

The intrinsic electrolytic behavior of the electrospray interfaces has been used to perform an on-line tagging of free cysteine residues on proteins. Hydroquinone has been found to be a compound of choice to specifically tag the thiol moiety of cysteines with the electrogeneration of benzoquinone. In addition to its specific reactivity, the other advantages of this quinonoid are its high stability in a degassed ESI medium, and that it is neutral, which avoids any signal suppression even at high concentrations. Besides, thanks to its low redox potential, it prevents the formation of oxygen bubbles and also the possible oxidation of the analytes.

The electrochemically induced tagging allows a modification of peptides and proteins at a post-column stage. In addition, due to its low molecular weight compared to the one of tryptic peptides or even proteins, it does not interfere in the ionization efficiency of the analyzed mixture. Finally, adjustment of the spray current to a defined level permits the calculation of the concentration of the generated probe. The low surface-to-volume ratio is a key issue in this method, since it reduces the diffusion time required for a quantitative electrochemical conversion and therefore increases the efficiency of the chemical step. The fast prototyping provided by the UV photoablation is particularly well suited for the design of the channel flow cell (length of the electrode and/or the microchannel) to optimize the yield of this on-line modification.

Cyclic voltammetric studies of the cysteine/hydroquinone system have been found to be an efficient tool to understand and get access to the chemical and electrochemical steps involved in the electrochemically induced tagging. The kinetics as well as the compounds involved in the on-line modification have been unraveled thanks to cyclic voltammetry and digital simulations.

Finite element simulations have also been performed to study the mechanisms and processes associated with on-line tagging of proteins in a channel flow cell. Several issues of this method

have been established. Firstly, the diffusion coefficient does not interfere with the tagging efficiency, meaning that no discrimination against the size of the analytes is expected. It has also been found that the flow profile is of utmost importance on the modification, due to the location of the embedded electrode at the bottom of the microchannel, particularly for large ratios of electrode length over channel length. Lastly, the kinetic rate constant of the probe/target system is obviously a key parameter, and the channel flow cell electrode, i.e. the nanospray interface, has to get an optimized geometry to reach a 100% yield for on-line modifications. The study of quinonoid compounds similar to hydroquinone, e.g. with additional functional groups to enhance the reactivity of the quinone, could permit to find an optimum compound for on-line electrochemically induced tagging of cysteines.

The final study has been devoted to the use of sacrificial electrodes to generate transition metal ions capable of reactions with peptides. The feasibility as well as the efficiency of the technique have been investigated with different metals and model peptides. The preliminary studies on the on-line complexation of peptides have shown that the electrogeneration of metal ions in the nanospray interface was satisfactorily efficient to obtain peptide complexes. Copper and zinc have been found to be the best candidates, contrary to nickel, silver, and iron for which parallel reactions occur, such as film formation on the electrode. Again, the small dimensions permit to decrease the diffusion distances, and thus the overall efficiency of the complexation is enhanced. However, some phenomena associated with the complexation need to be further investigated. The electroplating of metals on an embedded electrode in the channel or in the solution reservoir (for kinetic studies) could prevent any cross contamination due to traces of metallic impurities always present in bulk metals.

In the present work, it has been demonstrated that polymer nanospray interfaces are particularly well suited for coupling to mass spectrometers. The design of a defined microstructure is easy and the implementation of the latter to micromachining with mass-production techniques has already been performed. Apart form the hydrophobic nature of polymer substrates, the advantages of the mass production of nanospray chips are multiple. First, the chips should have highly reproducible dimensions, which is not the case of standard nanospray tips, since their opening is done by breaking their apex. Very small interferences in the reproducibility of experiments could be reached. The production of reproducible interfaces could help to improve the design, in terms of stability and/or detection limit, and to further investigate the electrospray ionization mechanisms.

Secondly, due to the low-cost of micromachining, the microchips could be disposable, limiting the problems due to cross contamination. The use of arrays of disposable microchips in an automated system could be an efficient tool for high-throughput analyses. In terms of technical developments, the fast prototyping of microstructured polymer substrates could help to get a low dead-volume liquid junction, on the same principle as standard ESI interfaces. A second microchannel could be drilled, the junction being at the outlet of the main microchannel. The mixing would thus occur in the Taylor cone. The liquid junction has indeed been found to be a useful apparatus for the coupling of chips with separation devices, such as CE or nano-LC. However, the dead-volumes induced by the plumbing are cumbersome.

The next step for the development of the on-line electrochemically induced modifications is certainly the use of high voltage potentiostat to fully control the electrochemical events on the integrated electrode. A pseudo reference electrode can be easily integrated in the microchannel, using silver/silver chloride paste or microarrays of holes connected to a

reservoir with a bulk electrode. The change of controlled-current to controlled-potential electrode will lead to a fully controlled nanospray interface.

Appendix 1: Numerical formulation

The general equation (8) can be detailed as following, by taking into account the diffusion-convection reaction equations for the 5 considered species. In order to simplify the writing, the nabla notation is used.

$$\frac{\partial c_A}{\partial t} + \nabla \cdot \left(-D_A \nabla c_A + \mathbf{V} c_A \right) = -k_{ox1} c_A + k_{red1} c_B \qquad \text{(A.1)}$$

$$\frac{\partial c_B}{\partial t} + \nabla \cdot \left(-D_B \nabla c_B + \mathbf{V} c_B \right) = +k_{ox1} c_A - k_{red1} c_B - k' c_B c_X \qquad \text{(A.2)}$$

$$\frac{\partial c_X}{\partial t} + \nabla \cdot \left(-D_X \nabla c_X + \mathbf{V} c_X \right) = -k' c_B c_X \qquad \text{(A.3)}$$

$$\frac{\partial c_C}{\partial t} + \nabla \cdot \left(-D_C \nabla c_C + \mathbf{V} c_C \right) = -k_{ox2} c_C + k_{red2} c_E + k' c_B c_X \qquad \text{(A.4)}$$

$$\frac{\partial c_E}{\partial t} + \nabla \cdot \left(-D_E \nabla c_E + \mathbf{V} c_E \right) = +k_{ox2} c_C - k_{red2} c_E \qquad \text{(A.5)}$$

where k_{ox1}, k_{ox2}, k_{red1}, k_{red2} are defined on the electrode surface only, k' being defined on all the domain. These expressions are derived in the global general form (A.8), using the Galerkin's formulation (multiplication by a second order projective function α and integration on the domain of study, Ω).

$$\iint_{\Omega} \alpha \left[\frac{\partial c_i}{\partial t} + \nabla \cdot \left(-D_i \nabla c_i + \mathbf{V} c_i \right) \pm k_{ox,red} c_{i,j} \pm k' c_i c_k \right] d\Omega = 0 \qquad \text{(A.6)}$$

The convection term is derived by taking into account the continuity equation $\nabla \cdot \mathbf{V} = 0$. By decomposing the product between α and the divergence, the second order derivative of the equation (A.6) (divergence of the gradient) becomes:

$$\alpha \nabla \cdot (-D_i \nabla c_i) = \nabla \cdot (-\alpha D_i \nabla c_i) + D_i \nabla \alpha \cdot \nabla c_i \qquad \text{(A.7)}$$

Applying (A.7) in (A.6) and using the Ostrogradsky theorem, the divergence term is rejected at the boundary (A.8), where it expresses the flux conditions of the species *i*. In the present case, this boundary condition is equal to zero (no flux at the boundaries of the domain).

$$\iint_{\Omega} \left[\alpha \frac{\partial c_i}{\partial t} + D_i \nabla \cdot \alpha \nabla c_i + \alpha \mathbf{V} \cdot \nabla c_i \pm \alpha k_{ox,red} c_{i,j} \pm \alpha k' c_i c_k \right] d\Omega = \int_{\partial\Omega} \alpha D_i \frac{\partial c_i}{\partial n} \mathbf{dl} = 0 \qquad \text{(A.8)}$$

Equation (A.8) is applied to the initial set (A.1-A.5), which is expressed in a matricial form. The steady state part of this matrix (local form for a given node) is described in (A.9) where β is the interpolation function of the unknown vector [c_A c_B c_X c_C c_E] (second order polynomial function).

The position in the matrix of the $\alpha k' \beta c_{B,X}$ terms (corresponding to the $k' c_B c_X$ in (A1.5)) is adjusted in order to maximize the weight of the diagonal of the matrix (a). It has been observed that this disposition allows the convergence of the calculations even for very low values of c_x (for which the formulation (b) doesn't reach the convergence criteria).

$D_A \nabla\alpha\cdot\nabla\beta + \alpha\mathbf{V}\cdot\nabla\beta + \alpha k_{ox1}\beta$	$-\alpha k_{red1}\beta$			
$-\alpha k_{ox1}\beta$	$D_B \nabla\alpha\cdot\nabla\beta + \alpha\mathbf{V}\cdot\nabla\beta + \alpha k_{red1}\beta + \alpha k'\beta c_X$ (a)	$\alpha k'\beta c_B$ (b)		
		$D_X \nabla\alpha\cdot\nabla\beta + \alpha\mathbf{V}\cdot\nabla\beta + \alpha k'\beta c_B$		
		$-\alpha k'\beta c_B$	$D_C \nabla\alpha\cdot\nabla\beta + \alpha\mathbf{V}\cdot\nabla\beta + \alpha k_{ox2}\beta$	$-\alpha k_{red2}\beta$
			$-\alpha k_{ox2}\beta$	$D_E \nabla\alpha\cdot\nabla\beta + \alpha\mathbf{V}\cdot\nabla\beta + \alpha k_{red2}\beta$

(A.9)

Appendix 2: Model validation

Short electrode validation

Harriman et al. result[1] for the E reaction study is taken as reference value, and the analytical approximations of Levich (A.10),[2] Newman (A.11),[3] and Aoki (A.12).[4]

$$I_0 = 0.8075 P_S^{1/3} \qquad \text{(A.10)}$$

$$I_0 = 0.8075 P_S^{1/3} + 0.7058 P_S^{-1/6} - 0.1984 P_S^{-1/3} \qquad \text{(A.11)}$$

$$I_0 = 0.8075 P_S^{1/3} + 0.4558 P_S^{-1/6} - 0.1984 P_S^{-1/3} \qquad \text{(A.12)}$$

The current values for the simulated geometry are listed in Appendix Table 1. The error compared with Harriman et al. results is –0.02%. Furthermore, apart from Levich value, the simulated current I_O is within 1% error.

	I_O /[-]	Error /[-]
Simulated value	6.59820	-
Harriman	6.599555	-0.021%
Levich [(a)]	6.409131	2.950%
Newman [(b)]	6.634661	-0.550%
Aoki [(c)]	6.545923	0.799%

Appendix Table 1. *I_0 current values (x_e=10 µm,V_0=0.5 m·s^{-1},* h=*200 µm, recess size=0.03 µm, recess mesh=0.01 µm, electrode mesh=80,* c_A^0=1mM); [(a)] *according to Equation A.10,* [(b)] *according to Equation A.11,* [(c)] *according to Equation A.12.*

The study of the E reaction allows also the evaluation of the effect of mesh parameters on the model. First, it is worth noticing that the mesh size is refined near the electrode edges (geometric progression on a 1μm path). The mesh size on the electrode edge is kept equal to the mesh size on the recess. On the center of the electrode (from 1μm to 9μm), the mesh is regular. Referring to Appendix Table 2, the size of the recess should not exceed 0.03μm (0.3% of the electrode length) if an error of less than 1% is required.

r /[μm]	*m* /[μm]	I_0 /[-]
0.03	0.01	6.59820
0.03	0.03	-0.17%
0.1	0.03	-2.55%
0.1	0.1	-2.61%

Appendix Table 2. *Effect of the recess size* r *and the recess mesh size* m *on the current value* I_0 *for a small electrode (x_e=10 µm,* V_0=0.5 m·s^{-1}, h=*200 µm, electrode mesh=80;* c_A^0=1mM).

A mesh of 0.03μm at the edges of the electrode (and on the recess) is found to be acceptable. Concerning the middle of the electrode (Appendix Table 3), there is no need to mesh in a very thin manner (20 subdivisions).

mesh number	I_O /[-]	Error /[-]
80 (0.1 μm)	6.59820	-
40 (0.2 μm)	6.60093	0.04%
30 (0.27μm)	6.60390	0.09%
20 (0.4 μm)	6.61322	0.23%

Appendix Table 3. *Effect of the electrode mesh on the current value* I_0 *for a small electrode (*x_e*=10 µm,* V_0*=0.5 m·s*$^{-1}$*,* h*=200µm, recess size=0.03 µm, recess mesh=0.01 µm;* c_A^0*=1mM).*

Long electrode validation

Due to the large size of the electrode, the effect of the recess size and the recess mesh is considerably diminished, resulting in a total error of –0.3% for a recess and a recess mesh size of 0.1μm. Furthermore, as the electrode size is increased the effect of middle electrode mesh is stronger. Nevertheless, the bigger mesh is chosen (mesh size of 4.9μm with 0.26% error on the current value I_0). Finally, the mesh at the end of the channel has been also assessed and no particular effect on the precision of the concentration values is highlighted.

References

(1) Harriman, K.; Gavaghan, D. J.; Houston, P.; Suli, E. *Electrochem. Commun.* **2000,** *2*, 567-575.

(2) Levich, V. G. *Physicochemical Hydrodynamics*: Englwood Cliffs, 1962.

(3) Newman, J. In *Electroanalytical Chemistry*; Bard, A. J., Ed.; Marcel Dekker, Inc.: New York, 1973; Vol. 6, pp 187-373.

(4) Aoki, K.; Toduka, K.; Matsuda, H. *J. Electroanal. Chem.* **1987,** *217*, 33-47.

Appendix 3: Ion trap scheme

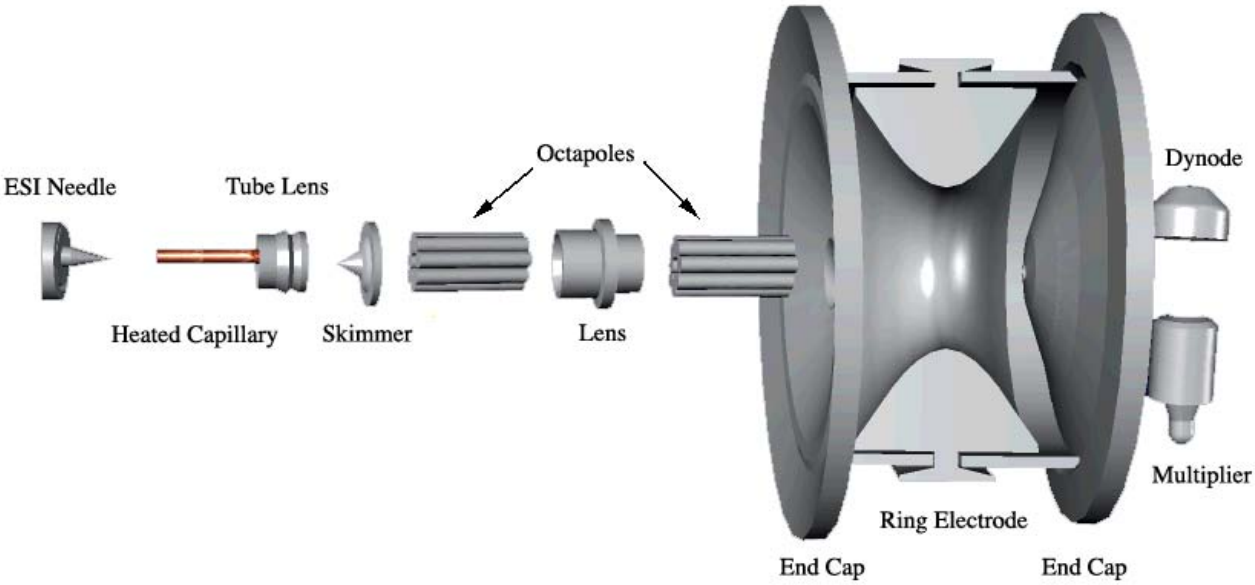

Curriculum Vitae

Name: Tatiana C. Rohner

Date of birth: 07/17/1973

Nationality and origin: French and Swiss (Altstätten, SG)

Education:

1999	Materials Science EPF Engineer. Diploma Thesis: "Mechanical Characterization of Hollow Composite Profiles Made by Bladder Inflation Molding" (Supervisor: J.-Å.E. Manson).
1995-1999	Materials Science at the Swiss Federal Institute of Technology Lausanne.
1992-1995	Microtechnology at the Swiss Federal Institute of Technology Lausanne.
1991	Scientific Baccalaureate in Marseille, France.

Publications:

1) T. C. Rohner, J. Josserand, H. Jensen, and H. H. Girault (2003). *Numerical Investigation of an Electrochemically Induced Tagging in a Nanospray for Protein Analysis*. **Analytical Chemistry**, 2065-2074.

2) C. Roussel, T. C. Rohner, H. Jensen, and H. H. Girault (2003). *Mechanistic Aspects of On-line Electrochemical Tagging of Free L-cysteine Residues during Electrospay Ionisation for Mass Spectrometry in Protein Analysis*. **ChemPhysChem**, 200-206.

3) V. Gobry, J. van Oostrum, M. Martinelli, T. C. Rohner, F. Reymond, J. S. Rossier, and H. H. Girault (2002). *Microfabricated polymer injector for direct mass spectrometry coupling*. **Proteomics**, 405-412.

4) T. C. Rohner, J. S. Rossier, and H. H. Girault (2002). *On-line electrochemical tagging of cysteines in proteins during nanospray*. **Electrochemistry Communications**, 695-700.

5) T. C. Rohner, J. S. Rossier, and H. H. Girault (2001). *Polymer microspray with an integrated thick-film microelectrode*. **Analytical Chemistry**, 5353-5357.

Patent:

J. S. Rossier, F. Reymond, H.H. Girault, T.C. Rohner, N. Lion, V. Gobry (10.10.2002). *Apparatus and method for dispensing a sample*, JY&GW Johnson: WO 02/080222 A1.

Oral presentation:

- **ANAKON 2001**, Gesellschaft Deutscher Chemiker, Fachgruppe Analytische Chemie, *Konstanz* (G); 4-7 April 2001.

Poster presentations:

- **Swiss Proteomic Society 2002 Congress: Applied Proteomics**, *Lausanne* (CH); 3-5 December 2002.
- **19th Symposium on Liquid Chromatography/Mass Spectrometry**, *Montreux* (CH); 4-8 November 2002.
- **53rd Annual Meeting of the International Society of Electrochemistry**: Electrochemistry in microscopic and molecular dimensions, *Düsseldorf* (G); 15-20 September 2002.
- **Bioinformatics and proteomics: from sequence to function**, *Lausanne* (CH); 6 December 2001.
- **Swiss Proteomic Society 2001 Congress: Functional Proteomics**, *Genève* (CH); 21-22 November 2001.
- **International Council of Electrophoresis Societies 2001: An Electrophoretic Odyssey**, *Verona* (I); 10-13 June 2001.
- **4th Lausanne Conference on Bioorganic Chemistry**, *Lausanne* (CH); 8-9 March 2001.